

SUPRAMOLECULAR ORDERING THROUGH AXIAL INTERACTIONS IN MONO
AND MIXED VALENT METELLOMESOGENIC SYSTEMS OF PLATINUM(II) AND
PLATINUM(IV)

Rachel J. Allenbaugh

A dissertation submitted to the faculty of the University of North Carolina at Chapel Hill
in partial fulfillment of the requirements for the degree of the Doctor of Philosophy in the
Department of Chemistry

Chapel Hill
2006

Approved by
Advisor: Professor Cynthia K. Schauer
Reader: Professor Wenbin Lin
Reader: Professor Joseph Templeton

© 2006
Rachel J. Allenbaugh
ALL RIGHTS RESERVED

ABSTRACT

RACHEL J. ALLENBAUGH: Supramolecular Ordering Through Axial Interactions in Mono and Mixed Valent Metallomesogenic Systems of Platinum(II) and Platinum(IV)
(Under the direction of Professor Cynthia K. Schauer)

MX chain interactions lead to formation of anisotropic materials with possible optical, semiconducting, and device miniaturization applications. These interactions are explored in a variety of Pt^{II}/Pt^{IV} systems. Platinum *N*-R-salicylaldimine complexes, Pt(sal-R)₂, are candidates for formation of MX chain materials based on their structural and electronic properties, as determined by density functional theory (DFT) calculations. The *trans* geometry of Pt(sal-*n*-Bu)₂Cl₂, determined by single-crystal X-ray diffraction (XRD), is compatible with MX chain formation. Electrochemical analysis of M(sal-R)₂ complexes results in electro-oxidative polymerization. The mechanism for polymerization is discussed. Pt(sal-R)₂ (R = *n*-Bu, *n*-Dec, Ph) complexes are determined to oxidize at less positive potentials than Ni(sal-Ph)₂ (0.66, 0.65, 0.61, and 0.59 V, respectively). DFT calculations of Pt(sal-Me)₂ and Ni(sal-Me)₂ determine a dπ* and π*(ligand) HOMO composition consistent with the observed oxidation potentials.

Platinum dialkyl-2,2'-bipyridine-4,4'-dicarboxylates (Lⁿ, n = number of carbon atoms in the alkyl chain) are analyzed for their potential to form liquid crystalline MX chain interactions. Crystal structures of PtL¹Cl₂, PtL²Cl₂, and PtL¹⁶Cl₂ are presented. The new PtLⁿCl₄ complexes (n = 10, 12, 16, 20) display smectic mesophases (30-194 °C overall). Mesophase ordering is believed to occur through π-π interactions of adjacent bipyridine

moieties. $\text{Re}(\text{CO})_3\text{L}^n\text{Br}$ and CdL^nCl_2 complexes ($n = 12, 18$) were prepared to study the tolerance of the mesophase to different metal geometries. Through optical microscopic and differential scanning calorimetry (DSC) analyses, $\text{Re}(\text{CO})_3\text{L}^{18}\text{Br}$ is determined to be mesogenic, while the Cd complexes are not.

The $\text{PtL}^{16}\text{Cl}_2/\text{PtL}^{16}\text{Cl}_4$ molecular alloy forms a Col_H mesophase. This is the first binary liquid crystalline system to include a Pt^{IV} component. DSC analyses of the enthalpy change associated with mesophase formation and XRD analyses suggest a 1:1 $\text{PtL}^{16}\text{Cl}_2/\text{PtL}^{16}\text{Cl}_4$ alloy consistent with formation of the first MX interactions in a liquid crystalline phase. Solid-state $\text{PtL}^{16}\text{Cl}_2$ and $\text{PtL}^{16}\text{Cl}_4$ complexes were characterized by luminescence spectroscopy, and both complexes demonstrates evidence of a CT lowest energy excited state consistent with DFT calculations of $\text{PtL}^{16}\text{Cl}_2$ and $\text{PtL}^{16}\text{Cl}_4$ orbital energies. The longer-lived emission from mixtures of $\text{PtL}^{16}\text{Cl}_2$ and $\text{PtL}^{16}\text{Cl}_4$ is enhanced in intensity compared to emission from the individual species. Samples that have self-assembled into the $\text{PtL}^{16}\text{Cl}_2/\text{PtL}^{16}\text{Cl}_4$ alloy do not luminesce.

ACKNOWLEDGEMENTS

First and foremost I would like to thank my family. I would like to thank my mother for supporting my sometimes insane science fantasies by subscribing to space magazines when I wanted to be an astronaut and by spending weeks in consultation with my biology teacher to get the perfect microscope when microbiology was my holy grail. Avoiding the junior chemistry set probably was safest for all concerned. I would like to thank my father for teaching me that every house should have a library and that the accumulation of books is something akin to an act of prayer. My sister has taught me that doing well rarely has to do with doing the best on the test, but rather has to do with doing the best with the situation you have. Someday, perhaps, I will learn to succeed in new situations with half the grace she has shown. My paternal grandparents introduced me to the wonders of quartz crystals, red bud leaves, and caterpillars in glass jars. My Grandpa Head taught me the value of being too stubborn to quit and too ornery to care how long it took to get there, a lesson without price in the long road to a Ph.D. My grandma supported me no matter where I went, even when she couldn't understand why I wanted to be going. Thank you all.

Since coming to UNC, I have been helped by a great many people. I am grateful to my advisor, Dr. Cynthia Schauer, who has taught me many invaluable lessons about research chemistry and in teaching. She has tirelessly responded to multiple drafts of this work, as well as having performed the molecular orbital calculations discussed herein. Dr. Pamela Visintin was of great assistance in my first three years of research. I would also like to thank the members of the Brookhart and Glish groups, specifically Dr. Desmond Kaplan, Dr. Amy

Roy, and Alison Sykes, for their help in solving all sorts of problems. Also, thank you to Jenny Ariansen and Melissa Villanueva of the Wightman group for your support and friendship. Meghan Lafferty has been the best librarian one could hope for, and a great friend.

Several people helped me with the instrumentation utilized for these experiments and/or performed data collection on instruments not available in the UNC chemistry department. Amanda Josey and Dr. James Martin and North Carolina State University provided the variable temperature X-ray diffraction data presented in this thesis. Jennifer Weinberg-Wolf, Zhongqiau Ren, and the other members of the McNeil lab at UNC provided the luminescence emission data. Dr. Matthew Kyle Brennaman worked with me to collect the emission lifetime data, and he continues to aid his expertise to my luminescence studies. Dr. Peter White performed the single crystal X-ray diffraction data collection and analyses.

Quite a few people made remarkable contributions to my life between adolescence and graduate school, but I'll stick to the highlights. Thank you to Jackie Stewart, who continues to teach the most amazing high school chemistry class I have ever seen or experienced. Without the lessons I learned at Truman State University, I never would have made it here. Thank you to the professors of the department of chemistry, especially Dr. Russell Baughman whose comments on my lab reports both kept the producers of purple ink in business and greatly enhanced my understanding of chemistry. I cannot forget the professors of the departments of art and English, who prevented me from becoming a total nerd. I never would have made my undergraduate career, much less graduate school, without the friendship and guidance of Kristen VonGruben, who managed to achieve distinction in both chemistry and decidedly liberal arts. You inspire me. Thank you to the members of the

Gamma Theta chapter of Alpha Chi Sigma you continue to be the best friends anyone could hope for. Special thanks to my undergraduate lab partner Dr. Jennifer Hargrave, D.O. Medicine's gain is chemistry's loss.

Teaching at UNC has been a wonderful experience. I would like to thank Dr. Haifa Johns for mentoring me in my first year as a teaching assistant and in many subsequent semesters teaching inorganic chemistry lab. Dr. Marcey Waters was kind enough to let me learn by doing turning over her general chemistry class to my less than experienced lecturing style. The experience was an eye-opening look at just how much effort my instructors have put into my education. Thank you. I would also like to thank my students. You all taught me far more about myself and chemistry than I can every thank you for.

To My Family

A

TABLE OF CONTENTS

	Page
LIST OF TABLES	xiv
LIST OF FIGURES	xvi
LIST OF ABBREVIATIONS AND SYMBOLS	xxiv
1. INTRODUCTION TO MX CHAIN INTERACTIONS AND LIQUID CRYSTALS.....	1
1.1 Supramolecular Ordering by Metal-Centered and Liquid Crystalline Interactions	1
1.2 MX Chain Interactions.....	4
1.2.1 Discovery and General Properties of MX Chain Interactions	4
1.2.2 Conductivity and Electrical Structure of MX Chains.....	5
1.2.3 Charged and Neutral MX Chain Systems.....	10
1.3 Liquid Crystalline Metal Complexes	12
1.3.1 Reasons for Incorporating a Liquid Crystalline System.....	12
1.3.2 Introduction to Smectic Liquid Crystals.....	13
1.3.3 Non-traditional Metallomesogens: Structure and Mesophase Formation	14
1.4 Progression and Impetus for Research.....	16
2. SYNTHESIS AND CHARACTERIZATION OF PLATINUM(II) AND PLATINUM(IV) SCHIFF BASE COMPLEXES OF SUBSTITUTED SALICYLALDIMINES.....	18
2.1 Introduction.....	18

2.2 Experimental Section	22
2.2.1 Synthetic Materials and General Procedures	22
2.2.2 Syntheses of Pt ^{II} Complexes	22
2.2.3 Syntheses of Pt ^{IV} Complexes	23
2.2.4 Syntheses of Bis(<i>N</i> -phenylsalicylaldimine)nickel(II)	25
2.2.5 Electrochemical Procedures.....	25
2.2.6 Single Crystal X-ray Diffraction Procedures.....	26
2.2.7 DFT Calculations	27
2.3 Results and Discussion	28
2.3.1 Synthesis of Ligands.....	28
2.3.2 Synthesis of Pt ^{II} Complexes.....	28
2.3.3 Synthesis of Pt ^{IV} Complexes.....	30
2.3.4 Crystal Structure of Pt(sal- <i>n</i> -Bu) ₂ Cl ₂	33
2.3.5 DFT Calculations.....	34
2.3.6 Cyclic Voltammetry of Hsal- <i>n</i> -Bu.....	41
2.3.7 Mechanism for Electrodimerization of Hsal- <i>n</i> -Bu	43
2.3.8 Cyclic Voltammetry of Ni(sal-Ph) ₂	45
2.3.9 Mechanism for the Electropolymerization of M(sal-R) ₂	48
2.3.10 Redox Potentials and Diffusion Coefficients for M(sal-R) ₂	52
2.3.11 MX Chain Self Assembly	56
2.4 Conclusions.....	57
3. COMPARISON OF THE PHASE BEHAVIOR OF DIALKYL-2,2'-BIPYRIDINE-4,4'- DICARBOXYLATO COMPLEXES OF Pt ^{II} , Pt ^{IV} , Re ^I , AND Cd ^{II} : THE EFFECTS OF AXIAL INTERACTIONS ON THE FORMATION OF MESOPHASES.....	58

3.1 Introduction.....	58
3.1.1 Secondary Interactions in MX Chain Systems and New System Design.....	58
3.1.2 Thermotropic Metallomesogens and Mesophases Ordering.....	62
3.1.3 Previously Developed Metallomesogenic Systems	66
3.2 Experimental Section.....	69
3.2.1 General Laboratory Procedures and Instrumentation	69
3.2.2 Syntheses of Ligands	70
3.2.3 Syntheses of Pt ^{II} Complexes.....	71
3.2.4 Syntheses of Pt ^{IV} Complexes.....	73
3.2.5 Syntheses of Cd ^{II} Complexes.....	75
3.2.6 Syntheses of Re ^I Complexes.....	76
3.2.7 X-ray Data Collection for PtL ¹ Cl ₂ •2CH ₂ Cl ₂ , PtL ² Cl ₂ , and PtL ¹⁶ Cl ₂ •2CHCl ₃	77
3.2.8 Variable Temperature Powder X-ray Diffraction.....	79
3.3 Results and Discussion	79
3.3.1 Syntheses.....	79
3.3.2 Structural Descriptions of PtL ¹ Cl ₂ , PtL ² Cl ₂ , and PtL ¹⁶ Cl ₂	85
3.3.3 Phase Transitions of PtL ⁿ Cl ₂ Complexes.....	89
3.3.4 Variable Temperature X-ray Diffraction of PtL ⁿ Cl ₂ Mesophases	93
3.3.5 Phase Transitions of PtL ⁿ Cl ₄ Complexes.....	97
3.3.6 Variable Temperature X-ray Diffraction of PtL ⁿ Cl ₄ Mesophases	102
3.3.7 Expansion of this System to Re and Cd Complexes.....	112
3.4 Conclusions.....	115

4. SELF-ASSEMBLY OF MX CHAINS IN LIQUID CRYSTALLINE MOLECULAR ALLOYS AND ASSEMBLY CONTROLLED LUMINESCENCE	117
4.1 Introduction.....	117
4.1.1 Proposed MX Chain Interactions in a Liquid Crystalline Phase	117
4.1.2 Previous Work with Binary Metallomesogenic Phases.....	120
4.2 Experimental.....	122
4.2.1 General Laboratory Procedures and Instrumentation	122
4.2.2 Variable Temperature Powder X-ray Diffraction.....	123
4.2.3 Luminescence Emission Measurements	123
4.2.4 Luminescence Lifetime Measurements	124
4.2.5 PtL ⁿ Cl ₂ /PtL ⁿ Cl ₄ Sample Preparation.....	124
4.2.6 DFT Calculations	125
4.3 Results and Discussion	125
4.3.1 Determination of the Mesogenic Range for PtL ⁿ Cl ₂ /PtL ⁿ Cl ₄ Molecular Alloys	125
4.3.2 Structure of the PtL ¹⁶ Cl ₂ /PtL ¹⁶ Cl ₄ Alloy Mesophase as Determined by XRD	136
4.3.3 PtL ¹⁶ Cl ₂ Absorbance Spectrum and DFT Calculations	139
4.3.4 Luminescence Spectroscopy of Pt ^{II} Complexes	146
4.3.5 PtL ¹⁶ Cl ₄ Luminescence Spectroscopy and DFT Calculations.....	151
4.3.6 Luminescence Enhancement for Non-Assembled PtL ¹⁶ Cl ₂ /PtL ¹⁶ Cl ₄ Mixture	157
4.3.7 Luminescence Quenching in PtL ¹⁶ Cl ₂ /PtL ¹⁶ Cl ₄ Molecular Alloys	159
4.3.8 Low Temperature Solid-State Luminescence.....	164
4.4 Conclusions.....	166

APPENDIX I	^1H NMR data for $\text{Pt}(\text{sal-Ph})_2$, $\text{Ni}(\text{sal-Ph})_2$, $\text{Pt}(\text{sal-Ph})_2\text{Cl}_2$, and $\text{Pt}(\text{sal-Ph})_2\text{Br}_2$	168
APPENDIX II	Differential Scanning Calorimetry Traces for Various PtL^nCl_2 , PtL^nCl_4 , CdL^nCl_2 , and $\text{Re}(\text{CO})_3\text{L}^n\text{Br}$ Complexes and $\text{PtL}^{16}\text{Cl}_2/\text{PtL}^{16}\text{Cl}_4$ Mixtures	170
APPENDIX III	X-ray Diffraction Data for Various PtL^nCl_2 and PtL^nCl_4 Complexes	177
REFERENCES.....		180

LIST OF TABLES

	Page
Table 1-1 Robin, Day and Hush Classification System	7
Table 1-2 Location of IVCT bands in solution phase UV-vis spectra for MX chains with neutral amine equatorial ligands	9
Table 1-3 Well-characterized PtX chain systems formed from neutral species.....	12
Table 1-4 Examples of square-planar metallomesogens.....	15
Table 2-1 Crystallographic information for Pt(sal- <i>n</i> -Bu) ₂ Cl ₂	27
Table 2-2 Conditions for synthesis and yields of Pt(sal- <i>n</i> -Bu) ₂	30
Table 2-3 Conditions for the reaction of Pt(sal-Ph) ₂ and CuX ₂ in refluxing 1:1 CH ₂ Cl ₂ /EtOH for 18 h to produce Pt(sal-Ph) ₂ X ₂	32
Table 2-4 Selected bond distances (Å) and angles (°) for Pt(sal- <i>n</i> -Bu) ₂ Cl ₂	34
Table 2-5 Bond distances and angles for Pt(sal-Me) ₂ (a), Pt(sal-Me) ₂ Cl ₂ (b), and Ni(sal-Me) ₂ (c) as determined by Gaussian DFT calculation compared to single crystal X-ray diffraction data for similar species	36
Table 2-6 Oxidation (E _{p,o}) and reduction (E _{p,r}) potentials (V vs Cp ₂ Fe ^{0/+}) for various metal salicylaldimine complexes, CH ₂ Cl ₂ /0.1 M TBATFB; sweep rate 200 mV/s; 1.5 mM Pt(sal- <i>n</i> -Dec) ₂ , 6.0 mM Ni(sal-Ph) ₂ , 0.57 mM Pt(sal-Ph) ₂ , 2.2 mM Pt(sal- <i>n</i> -Bu) ₂ , redox waves labeled as in Figure 2-14	52
Table 2-7 Diffusion coefficients for various species determined using the initial oxidation wave for each species	56
Table 3-1 Crystallographic information for PtL ¹ Cl ₂ •2CH ₂ Cl ₂ , PtL ² Cl ₂ and PtL ¹⁶ Cl ₂ •2CHCl ₃	78
Table 3-2 Temperatures for PtL ⁿ Cl ₄ to PtL ⁿ Cl ₂ decomposition as determined by TGA	82
Table 3-3 Selected bond angles and distances for PtL ¹ Cl ₂ , PtL ² Cl ₂ , and PtL ¹⁶ Cl ₂	86
Table 3-4 Thermal properties of the PtL ⁿ Cl ₂ complexes	92
Table 3-5 X-ray diffraction data for the PtL ¹² Cl ₂ mesophase at 115 °C, including calculated reflections for a P222 ₁ unit cell	96

Table 3-6	Thermal properties of the PtL^nCl_4 complexes	101
Table 3-7	X-ray diffraction data and proposed assignments of the reflections for the mesophase of $\text{PtL}^{12}\text{Cl}_4$ and $\text{PtL}^{16}\text{Cl}_4$ assuming a P1 unit cell	109
Table 3-8	Thermal properties of the CdL^nCl_2 and $\text{Re}(\text{CO})_3\text{L}^n\text{Br}$ complexes.....	114
Table 4-1	Stable temperature range upon heating for the CoI_H molecular alloy of 1:1 $\text{PtL}^n\text{Cl}_2/\text{PtL}^n\text{Cl}_4$ as determined by DSC.....	130
Table 4-2	Enthalpy change upon clearing for various ratios of $\text{PtL}^{16}\text{Cl}_2/\text{PtL}^{16}\text{Cl}_4$ as determined by DSC	133
Table 4-3	Enthalpy change for formation of $\text{Pt}^{16}\text{Cl}_2/\text{PtL}^{16}\text{Cl}_4$ molecular alloys.....	135
Table 4-4	Calculated and observed reflections for the $\text{PtL}^{16}\text{Cl}_2/\text{PtL}^{16}\text{Cl}_4$ molecular alloy at 110 °C	137
Table 4-5	Bond distances and angles for PtL^1Cl_2 (a) and PtL^1Cl_4 (b) as determined by Gaussian DFT calculation compared to single crystal X-ray diffraction data for similar species.....	142
Table 4-6	UV-vis absorbance maxima and molar absorptivities for $\text{PtL}^{16}\text{Cl}_2$ in CHCl_3 and calculated orbital energy differences for PtL^1Cl_2	146
Table 4-7	Solid-state emission wavelengths and lifetimes of various L^{16} , $\text{PtL}^{16}\text{Cl}_2$, and $\text{PtL}^{16}\text{Cl}_4$ samples.....	150
Table 4-8	UV-vis absorbance maxima and molar absorptivities for $\text{PtL}^{16}\text{Cl}_4$ in CHCl_3 and calculated orbital energy differences for PtL^1Cl_4	155
Table 4-9	Solid-state emission maxima of $\text{PtL}^{16}\text{Cl}_4$ and $\text{PtL}^{16}\text{Cl}_2/\text{PtL}^{16}\text{Cl}_4$ mixtures in various states of self-assembly at 30 K and $\sim 3 \times 10^{-6}$ torr, $\lambda_{\text{ex}}=514$ nm	165

LIST OF FIGURES

		Page
Figure 1-1	Examples of d^8-d^8 (left) and MX chain (right) supramolecular stacking interactions for platinum complexes.....	3
Figure 1-2	Formation of metal-halogen-metal interactions in a hexatic-columnar liquid crystalline phase; packing in the hexatic-columnar mesophase (left), interaction of the metal centers within one column (right).....	3
Figure 1-3	Proposed electronic configurations for Wolfram's red salt. The alternating $Cl-Pt^{IV}-Cl \cdots Pt^{II} \cdots$ structure (left) was determined to be correct via X-ray crystallography	5
Figure 1-4	Electronic structures of linear chains; Class I, trapped valence (a), Class II Peierls distorted system, low energy IVCT transitions (b), Class II antiferromagnetically coupled system, low energy IVCT transitions (c), Class III, electronic band structure of a partially oxidized complex such as $K_2Pt(CN)_4 \bullet Br_{0.30} \bullet 3H_2O$ (d); CB = conduction band, VB = valence band.	6
Figure 1-5	Phonon assisted electron hopping mechanism for electron conduction in PtX chain systems as proposed by Interrante and Browall; electron transfer (half arrow), vibrational motion of the bridging halogens (grey arrows). The initial oxidation may occur from either a spontaneous process or a defect site	8
Figure 1-6	Possible examples of charged $X-M^{III}-X-M^{III}-$ chains with hydrogen bonding to the counterions (left) and neutral $\cdots M^{II} \cdots X-M^{IV}-X$ chains (right); for clarity, not all counterions are shown	11
Figure 1-7	Types of mesogens; calamitic (a), discotic (b), and ionic melts (c).....	13
Figure 1-8	Nematic, smectic A, smectic C, rectangulo-columnar, and hexatic-columnar liquid crystalline phases (left to right); director (white), tilt (black).....	14
Figure 1-9	Smectic phases of polar mesogens: smectic A_1 (SmA_1), semi-bilayer smectic A (SmA_d), and bilayer smectic (SmA_2) mesophases (left to right); layer spacing (black lines).....	16
Figure 2-1	Ni, Pt^{II} , and Pt^{IV} complexes analyzed in this research.....	18
Figure 2-2	Proposed $Pt(sal-R)_2/Pt(sal-R)_2Cl_2$ MX chain interaction and electronic configuration of alternating filled and empty d orbitals; photoinduced electron transfer from Pt^{II} to Pt^{IV} (half arrow)	19

Figure 2-3	Characteristic cyclic voltammogram for electro-oxidative formation of an electroactive polymer film on the electrode surface; oxidation of the film (a), reduction of the film (b), and oxidation of monomer in solution (c). Oxidation of the monomer is irreversible, leading to the lack of reduction wave (d). Three potential cycles are shown, with the first as a thick line	21
Figure 2-4	Proton NMR spectra for Pt(sal- <i>n</i> -Bu) ₂ (top) and Pt(sal- <i>n</i> -Bu) ₂ Cl ₂ (bottom); CD ₂ Cl ₂ , 400 MHz	31
Figure 2-5	Aromatic region of the ¹ H NMR spectrum for the products of the reaction of 5 CuBr ₂ + 5 CuCl ₂ + Pt(sal-Ph) ₂ (top) and 3.8 CuBr ₂ + 16.2 CuCl ₂ + Pt(sal-Ph) ₂ (bottom); Pt(sal-Ph) ₂ Cl ₂ resonances (○), Pt(sal-Ph) ₂ Br ₂ resonances (□), overlapping resonances (■)	32
Figure 2-6	Ortep diagrams for Pt(sal- <i>n</i> -Bu) ₂ (left) and Pt(sal- <i>n</i> -Bu) ₂ Cl ₂ (right).....	33
Figure 2-7	Unit cell packing of Pt(sal- <i>n</i> -Bu) ₂ Cl ₂ showing the non-coplanar Schiff base ligands	34
Figure 2-8	Proposed MX chain formation from Pt(sal-Me) ₂ and Pt(sal-Me) ₂ Cl ₂ complexes showing the alternating filled/empty electronic structure of the d ₂₂ orbitals.....	35
Figure 2-9	Frontier orbitals for Pt(sal-Me) ₂ , Ni(sal-Me) ₂ , and Hsal-Me determined using Gaussian DFT calculations; energies in eV	38
Figure 2-10	Frontier orbitals for Pt(sal-Me) ₂ and Pt(sal-Me) ₂ Cl ₂ as determined using Gaussian DFT calculations; energies in eV	40
Figure 2-11	Cyclic voltammogram of 2.8 mM Hsal- <i>n</i> -Bu in acetonitrile/0.1 M TBATFB; sweep rate = 1 V/s, potential vs Cp ₂ Fe ^{0/+}	42
Figure 2-12	Cyclic voltammogram of 2.8 mM Hsal- <i>n</i> -Bu in acetonitrile/0.1 M TBATFB; sweep rate = 100 mV/s, potentials vs Cp ₂ Fe ^{0/+} , three cycles shown	42
Figure 2-13	Proposed mechanism for the electro-dimerization of Hsal- <i>n</i> -Bu, as extrapolated from Ohmori et al.....	44
Figure 2-14	Cyclic voltammogram of 4.2 mM Ni(sal-Ph) ₂ in CH ₂ Cl ₂ /0.1 M TBATFB; sweep rate = 200 mV/s, potentials vs Cp ₂ Fe ^{0/+} , six cycles shown; initial oxidation of Ni(sal-Ph) ₂ (A), oxidation of dimer (B), reduction of surface adsorbed species (C and D), and oxidation of the surface adsorbed polymer (E and F).....	47

Figure 2-15	Cyclic voltammogram of Pt(sal- <i>n</i> -Bu) ₂ in CH ₂ Cl ₂ /0.1 TBATFB; sweep rate = 100 mV/s, potentials vs Cp ₂ Fe ^{0/+} ; initial oxidation of Pt(sal- <i>n</i> -Bu) ₂ (A), oxidation of dimer (B), and reductions of surface adsorbed polymer (C and D).....	48
Figure 2-16	Proposed mechanism for the electro-oxidative dimerization of M(sal-R) ₂ complexes. For most species several resonance structures are possible.....	49
Figure 2-17	Proposed mechanism for the oxidative polymerization of M(sal-R) ₂ at an electrode surface. For most species several resonance structures are possible. Electroactivity is expected at more than just the polymer ends, but only those processes contributing to chain growth are shown.....	49
Figure 2-18	Diagram of the HOMO for Pt(sal-Me) ₂ and Ni(sal-Me) ₂ as determined from Gaussian DFT calculations	54
Figure 2-19	Randles-Sevcik plot for Pt(sal- <i>n</i> -Bu) ₂ . From the slope, the diffusion coefficient is determined to be 1.1 × 10 ⁻⁶ cm ² s ⁻¹	55
Figure 3-1	Diagram of the hydrogen bonding between MX chain ligands and the counterions as occurs in [Ni ^{III} (chxn) ₂ Cl](NO ₃) ₂ (chxn = 1,2-diaminocyclohexane, cyclohexane ring not shown); Ni (black), Cl (white), NO ₃ ⁻ (grey), hydrogen bonds (---), some counterions omitted for clarity	59
Figure 3-2	Method of formation for surfactant supported MX chain complexes in solution as developed by Kimizuka, Oda, and Kunitake; en = 1,2-diaminoethane	60
Figure 3-3	Initially hypothesized system for the formation of MX chain interactions in a liquid crystalline phase.....	61
Figure 3-4	Complexes synthesized for this research; L ⁿ = dialkyl-2,2'-bipyridine-4,4'-dicarboxylates, where n is the number of carbon atoms in the alkyl chain.....	61
Figure 3-5	Examples of smectic liquid crystalline phases smectic A (a), semi-bilayer smectic A (SmA _d) (b), bilayer smectic (SmA ₂) (c), and bilayer smectic C (SmC ₂) (d). Monolayer, bilayer, and semi-bilayer phases may occur for both SmA and SmC phases	62
Figure 3-6	Complimentary shape approaches where segregation of hydrophobic and hydrophilic domains engenders columnar ordering from non-discotic mesogens; single mesogens shown at top	64

Figure 3-7	Mesogenic phases showing the progression from hexatic-columnar (Col_H) through rectangulo-columnar (Col_R) and lamello-columnar (Col_L) to smectic A (SmA) mesophases as anisotropic microsegregation of the alkyl chains occurs.....	65
Figure 3-8	“V”-shaped Pt^{IV} metallomesogens.....	67
Figure 3-9	Diagram of the liquid crystalline phase of $PtL^{16}Cl_2$ (001), right, and (010), left. A $Pt^{II} \cdots Pt^{II}$ columnar interaction is shown as a space-filling model.....	68
Figure 3-10	Proton NMR spectra of L^{16} (top) and $PtL^{16}Cl_2$ (bottom); $CDCl_3$, 400 MHz. To better show the aromatic resonances, the methylene resonance has been truncated.....	80
Figure 3-11	Proton NMR spectrum of $PtL^{16}Cl_4$; $CDCl_3$, 400 MHz. To better show the aromatic resonances, the methylene resonance has been truncated.....	82
Figure 3-12	Proton NMR spectrum of $CdL^{12}Cl_2$; $CDCl_3$, 400 MHz. To better show the aromatic resonances, the methylene resonance has been truncated.....	83
Figure 3-13	$Re(CO)_3L^{18}Br$ 1H NMR aromatic region; $CDCl_3$, 400 MHz.....	85
Figure 3-14	Thermal ellipsoid plot for $PtL^{16}Cl_2$; solvent molecules removed for clarity.....	86
Figure 3-15	Crystalline packing of $PtL^{16}Cl_2$, with solvent molecules and hydrogens removed for clarity. The $Pt \cdots Pt$ interactions alternate along the axial direction.....	87
Figure 3-16	Interdigitation of the alkyl chains from the single crystal structures of $PtL^1Cl_2 \cdot 2CH_2Cl_2$ (a), PtL^2Cl_2 (b), and $PtL^{16}Cl_2 \cdot 2CHCl_3$ (c). Solvent molecules have been removed for clarity.....	88
Figure 3-17	Heating and cooling curves for $PtL^{20}Cl_2$; heating rate 10 °C/min, 2 nd heating shown, crystal (Cr), lamellar mesophase (L), isotropic liquid (I).....	89
Figure 3-18	Phase diagram for the crystal 1 to crystal 2 (◆), crystal 2 to lamellar (●) and lamellar or crystal 2 to isotropic (■) transitions of PtL^nCl_2 complexes. Data for PtL^8Cl_2 and $PtL^{22}Cl_2$ are from Pucci et al.....	91
Figure 3-19	Texture of $PtL^{20}Cl_2$ under cross-polarization. Similar textures are observed for all unsheared mesomorphic PtL^nCl_2 complexes studied here.....	93
Figure 3-20	X-ray diffraction pattern for the lamellar $PtL^{12}Cl_2$ mesophase at 115 °C.....	94

Figure 3-21	Experimental (top) and calculated (bottom) X-ray diffraction patterns for the lamellar PtL ¹² Cl ₂ mesophase at 115 °C; (100) reflection truncated to better show the low intensity reflections	96
Figure 3-22	Heating and cooling curves for PtL ²⁰ Cl ₄ ; heating rate heating rate 10 °C/min, 2 nd heating shown; crystal (Cr), lamellar mesophase (L), isotropic liquid (I)	99
Figure 3-23	Mesogenic texture of PtL ²⁰ Cl ₄ under cross-polarization. All mesogenic PtL ⁿ Cl ₄ complexes display similar texture	99
Figure 3-24	Phase diagram for the crystal 1 to crystal 2 (◆), crystal 2 to lamellar (●) and lamellar or crystal 2 to isotropic (■) transitions and the PtL ⁿ Cl ₄ to PtL ⁿ Cl ₂ decomposition (Δ) temperatures of PtL ⁿ Cl ₄ complexes.....	102
Figure 3-25	X-ray diffraction patterns for PtL ¹² Cl ₄ (top) and PtL ¹⁶ Cl ₄ (bottom) mesophases.	103
Figure 3-26	Possible packing of the metal-bipyridine moieties in PtL ⁿ Cl ₄ liquid crystalline phases, which is disfavored due to the repulsions between the chloride ligands and the 3,3' bipyridine protons	105
Figure 3-27	Partial π-π overlap in the single crystal structure of Pt(bpy)Cl ₄	106
Figure 3-28	Proposed mesophase ordering for the mesogenic PtL ⁿ Cl ₄ complexes; π-π stacking interactions (---).....	107
Figure 3-29	Experimental diffraction pattern for the PtL ¹² Cl ₄ mesophase (top) and calculated pattern (bottom) determined utilizing the simplified PtCl ₄ formula unit and P1 unit cell shown; FWHM has been modified to better match the experimental data	108
Figure 3-30	Experimental diffraction pattern for the PtL ¹⁶ Cl ₄ mesophase (top) and calculated pattern (bottom) determined utilizing the simplified PtCl ₄ formula unit and a P1 unit cell; FWHM has been modified to better match the experimental data, (001) reflection cannot be observed due to its proximity to the X-ray beam.....	111
Figure 3-31	Mesogenic texture of Re(CO) ₃ L ¹⁸ Br under cross polarization	115
Figure 4-1	Diagram of possible mesogenic phases supporting MX chain interactions; Col _L and Col _R mesophases, which differ by the strength of the correlations between layers (top), Col _H mesophase (bottom); the alkyl chains are highly disordered and are not shown	119

Figure 4-2	Representative interactions in the SmA mesophase obtained for a mixture of Au and Cu isocyanide complexes; Au ⁺ ··Au interactions are disrupted by the Cu complexes	121
Figure 4-3	Representative interactions in the Col _H mesophase obtained from a mixture of Rh and Cu heptanoate complexes; Rh and Cu complexes supramolecularly order in separate columns.....	121
Figure 4-4	DSC trace for 1:1 PtL ¹⁶ Cl ₂ /PtL ¹⁶ Cl ₄ ; 1 st heating and cooling (black), 2 nd heating and cooling (grey); phases are given for the 2 nd cycle	127
Figure 4-5	Mesogenic phases of PtL ¹⁶ Cl ₂ and PtL ¹⁶ Cl ₄ prior to shearing at 106 °C (a) and the single 1:1 PtL ¹⁶ Cl ₂ /PtL ¹⁶ Cl ₄ mesophase obtained during the second heating at 118 °C (b); under cross polarization.	127
Figure 4-6	DSC traces for 1:1 mixtures of PtL ¹² Cl ₂ /PtL ¹² Cl ₄ (top) and PtL ²⁰ Cl ₂ /PtL ²⁰ Cl ₄ (bottom); 1 st heating/cooling cycle (black), 2 nd heating/cooling cycle (grey)	130
Figure 4-7	DSC trace for 1.5:1 PtL ¹⁶ Cl ₂ /PtL ¹⁶ Cl ₄ (top) and 0.55:1 PtL ¹⁶ Cl ₂ /PtL ¹⁶ Cl ₄ (bottom) showing the new endotherm (*), which is not observed for 1:1 PtL ¹⁶ Cl ₂ /PtL ¹⁶ Cl ₄ ; 2 nd heating shown.....	132
Figure 4-8	Enthalpy change associated with formation of the Col _H alloy for various ratios of PtL ¹⁶ Cl ₂ /PtL ¹⁶ Cl ₄ as a function of the number of moles of alloy; ratio of PtL ¹⁶ Cl ₂ /PtL ¹⁶ Cl ₄ adjacent to each point.....	135
Figure 4-9	X-ray diffraction pattern for Col _H 1:1 PtL ¹⁶ Cl ₂ /PtL ¹⁶ Cl ₄ molecular alloy at 110 °C (top) and calculated powder pattern based on a P-6 unit cell of dimensions $a = b = 35.16 \text{ \AA}$, $c = 10.2 \text{ \AA}$, $\alpha = \beta = 90^\circ$, $\gamma = 120^\circ$ (bottom) showing proposed assignment of the major reflections.....	137
Figure 4-10	XRD patterns for PtL ¹⁶ Cl ₂ at 110 °C (top), PtL ¹⁶ Cl ₄ at 120 °C (middle), and the PtL ¹⁶ Cl ₂ /PtL ¹⁶ Cl ₄ Col _H alloy at 110 °C (bottom); reflections not observed for the individual complexes (*).....	138
Figure 4-11	Possible methods of formation for a Col _H mesophase of 1:1 PtL ¹⁶ Cl ₂ /PtL ¹⁶ Cl ₄ ; MX chain interactions within [PtL ¹⁶ Cl ₂ -PtL ¹⁶ Cl ₄] _m columns (left) and random distributions of individual [PtL ¹⁶ Cl ₂] _m and [PtL ¹⁶ Cl ₄] _m columns (center)	139
Figure 4-12	UV-vis absorbance spectrum for 12.5 μM PtL ¹⁶ Cl ₂ in CHCl ₃ and the d orbital diagram expected for a generic square-planar complex	141
Figure 4-13	Calculated molecular orbitals for PtL ¹⁶ Cl ₂ ; orbital energies in eV, orientation for the C _{2v} symmetry of the molecule shown.....	144

Figure 4-14	Molecular orbital diagram for PtL^1Cl_2 as determined using Gaussian; orientation at the molecule refers to the usual square-planar coordinate system.....	145
Figure 4-15	Solid-state emission spectra for $\text{PtL}^{16}\text{Cl}_4$, and $\text{PtL}^{16}\text{Cl}_2$, and 1:1 $\text{PtL}^{16}\text{Cl}_2$ and L^{16} ; $\lambda_{\text{ex}} = 514 \text{ nm}$, measured under reduced pressure (thick line), measured under ambient conditions (thin line), relative intensities are not normalized	148
Figure 4-16	Decay curve for the luminescence of $\text{PtL}^{16}\text{Cl}_2$ at room temperature (black) with the lifetime determined by fitting the curve to a biexponential decay (red); $\lambda_{\text{ex}} = 423 \text{ nm}$, $\lambda_{\text{obs}} = 614 \text{ nm}$	151
Figure 4-17	Absorbance spectrum for $8.9 \mu\text{M}$ $\text{PtL}^{16}\text{Cl}_4$ in CHCl_3 with the simplified molecular orbital diagram for a generic octahedral complex	152
Figure 4-18	Calculated molecular orbitals for PtL^1Cl_4 ; orbital energies in eV	153
Figure 4-19	Molecular orbital diagram for PtL^1Cl_2 (left) and PtL_1Cl_4 (right) as determined using Gaussian; orientation at the molecule refers to the usual square-planar coordinate system	154
Figure 4-20	Powder XRD pattern for $\text{PtL}^{16}\text{Cl}_4$ anhydrous sample (grey) and sample stored in air (black)	156
Figure 4-21	Normalized luminescence emission spectra for various heterogeneous mixtures of $\text{PtL}^{16}\text{Cl}_2$ and $\text{PtL}^{16}\text{Cl}_4$ powders; $\lambda_{\text{ex}} = 514 \text{ nm}$, $\text{PtL}^{16}\text{Cl}_4$ spectrum included for scale	157
Figure 4-22	Possible mechanism for solid-state luminescence enhancement in heterogeneous mixtures of $\text{PtL}^{16}\text{Cl}_2$ and $\text{PtL}^{16}\text{Cl}_4$ where the final step (c) is dominated by radiative emission; oxidation state after each step of the mechanism shown adjacent to the energy well.....	159
Figure 4-23	XRD patterns for the 1:1 $\text{PtL}^{16}\text{Cl}_2/\text{PtL}^{16}\text{Cl}_4$ molecular alloy; $110 \text{ }^\circ\text{C}$ (bottom), RT after the sample is heated to $130 \text{ }^\circ\text{C}$ and quenched with liquid nitrogen (top). The X-ray beam edge appears at low Q as a sharp increase in intensity. Two different instruments were utilized resulting in different minimum observable Q.....	160

Figure 4-24	Normalized room temperature emission spectra for various PtL ¹⁶ Cl ₂ and PtL ¹⁶ Cl ₄ mixtures; $\lambda_{\text{ex}} = 514 \text{ nm}$, PtL ¹⁶ Cl ₄ spectrum included for scale; samples analyzed in glass tubes under ambient conditions (thick line), samples analyzed under reduced pressure in a quartz and brass sample holder (thin line), prepared by heating fine powders to 130 °C and quenching with liquid nitrogen (quenched alloy), prepared by mixing fine powders at room temperature (mixture)	161
Figure 4-25	Solid-state emission spectra for various powders: 1:1 PtL ¹⁶ Cl ₂ and PtL ¹⁶ Cl ₄ powders mixed at RT (a), PtL ¹⁶ Cl ₂ powder (b), PtL ¹⁶ Cl ₂ heated to 130 °C and quenched with liquid nitrogen (c), and 1:1 PtL ¹⁶ Cl ₂ /PtL ¹⁶ Cl ₄ heated to 130 °C and quenched with liquid nitrogen (d, at baseline); $\lambda_{\text{ex}}=514 \text{ nm}$	162
Figure 4-26	Axial vibrational mode for quenching of the charge transfer excited state	163
Figure 4-27	Possible vibrational relaxation mechanism for solid-state luminescence quenching of the PtL ¹⁶ Cl ₂ /PtL ¹⁶ Cl ₄ molecular alloy where the final step (c) is dominated by back electron transfer	164
Figure 4-28	Low temperature solid-state emission spectra for PtL ¹⁶ Cl ₄ and various mixtures of PtL ¹⁶ Cl ₄ /PtL ¹⁶ Cl ₂ ; $\lambda_{\text{ex}} = 514 \text{ nm}$, all samples held in a brass and quartz sample holder at 30 K and 3×10^{-6} torr; prepared by heating fine powders to 130 °C and quenching with liquid nitrogen (N ₂), prepared by mixing fine powders at room temperature (RT).....	165

LIST OF ABBREVIATIONS AND SYMBOLS

°C	degrees Celsius
Ar	aromatic
Col _H	hexatic-columnar
Col _L	lamello-columnar
Col _R	rectangulo-columnar
d	doublet
DFT	density functional theory
DSC	differential scanning calorimetry
eq	equation
equiv	equivalent
Et	ethyl
eV	electron volts
FWHM	full width at half maximum
g	grams
h	hour
HOMO	highest occupied molecular orbital
Hz	hertz
<i>i</i> -Pr	isopropyl, -CH(CH ₃) ₂
IVCT	intervalence charge transfer
K	Kelvin

LUMO	lowest unoccupied molecular orbital
<i>m</i>	meta
m	multiplet
Me	methyl
mL	milliliter
mol	moles
<i>n</i> -Bu	butyl, -C ₄ H ₉
<i>n</i> -Dec	decyl, -C ₁₀ H ₂₁
nm	nanometers
NMR	nuclear magnetic resonance
ns	nanoseconds
<i>o</i>	ortho
<i>p</i>	para
p	pentet
Ph	phenyl, -C ₆ H ₅
POM	polarized optical microscopy
ppm	parts per million
q	quartet
RT	room temperature
s	singlet
SmA	smectic A
SmA _d	semi-bilayer smectic A

SmC	smectic C
t	triplet
TGA	thermogravimetric analysis
UV-vis	ultraviolet-visible
VT	variable temperature
XRD	X-ray diffraction
$\tilde{\nu}$	wavenumber, in cm^{-1}

CHAPTER I

INTRODUCTION TO MX CHAIN INTERACTIONS AND LIQUID CRYSTALS

1.1 Supramolecular Ordering by Metal-Centered and Liquid Crystalline Interactions

At first glance, bonding and chemical composition are often taken as the main determinants of a substance's characteristics and properties. Today though, the effects of weaker intermolecular interactions on material properties are being explored in force, and the number of recent books on supramolecular chemistry reflects importance of this research.^{1, 2, 3, 4, 5} Jean-Marie Lehn, who received the 1987 Nobel Prize for his work with supramolecular chemistry, defined the field as, “. . . the chemistry of the intermolecular bond, concerning the structure and functions of the entities formed by the association of two or more chemical species.”⁶ Barberá and coworkers⁷ characterized organic chemistry as living its “supramolecular epoch” in 1998, and the same may be said for inorganic chemistry. Of course, supramolecular interactions are not new. Electrostatic pairing, hydrophobic, hydrophilic, host-guest, π -stacking, Van der Waals, and hydrogen bonding interactions have helped to shape the properties of natural products long before chemists started exploring controlled supramolecular ordering for preparation of new materials.

Increasingly, supramolecular research involves exploring new frontiers including metallomesogenic chemistry – the chemistry of liquid crystalline metal complexes. Liquid

crystalline phases have properties intermediate between solid and liquid phases, and as such they are often termed mesophases. In at least one dimension of a mesophase, the molecules are disordered, giving an overall anisotropy to the mesophase and a liquid-like flow to the material. The anisotropy in structure extends to the material's optical and electronic properties. The liquid-like flow of liquid crystalline materials can allow the direction of anisotropy to be manipulated with magnetic fields and electrical currents.^{8, 9, 10} When metal complexes form liquid crystalline phases, the unique properties associated with the metal's electronic structure and coordination geometry are combined with the manipulatable anisotropy of the liquid crystal to make possible potential applications as semiconductors and in molecular electronic and optical devices.⁸

This research project set out to explore two types of platinum-based interactions: the d^8-d^8 stacking interactions common for square-planar Pt complexes and the metal-halogen-metal (or MX chain) orderings that occur for mixed Pt^{II}/Pt^{IV} systems as diagrammed in Figure 1-1. As will be discussed in Chapter 2, platinum salicylaldimine complexes were initially explored as candidates for the formation of MX chains. Research ultimately led to an intersection of liquid crystalline and metal-based supramolecular ordering through the design, synthesis, and characterization of a system incorporating MX chain interactions into a liquid crystalline phase. The system of dialkyl-2,2'-bipyridine-4,4'-dicarboxylate Pt^{II} and Pt^{IV} complexes (Figure 1-2) proved to be amenable to this goal. The figure shows a hexatic-columnar liquid crystalline mesophase (left) where the columnar ordering is provided by an MX chain (right). Each column is formed by alternating Pt^{II} and Pt^{IV} complexes. The two types of supramolecular interactions, the overall hexatic-columnar ordering of the mesophase and the MX chain orderings of the individual columns, will be treated separately in this

introduction. The MX chain systems are discussed first followed by an introduction to the properties and structures of liquid crystalline systems. The chemistry of the individual liquid crystalline Pt^{II} and Pt^{IV} complexes is discussed in Chapter 3, while Chapter 4 focuses on the analysis of the mixed valent liquid crystalline system diagrammed in Figure 1-2.

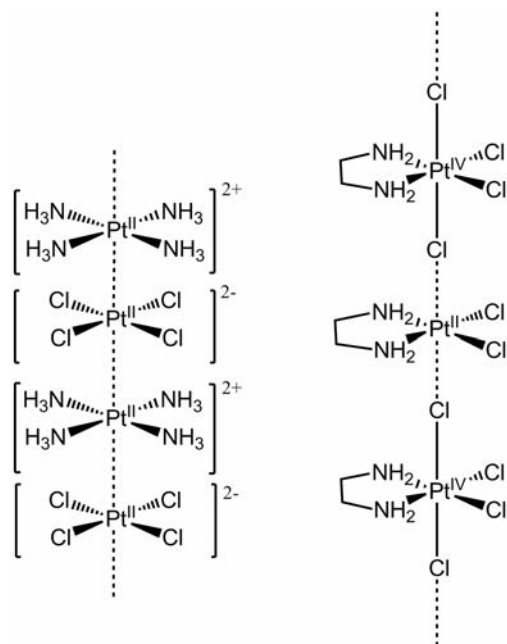


Figure 1-1. Examples of d^8-d^8 (left) and MX chain (right) supramolecular interactions for platinum complexes.

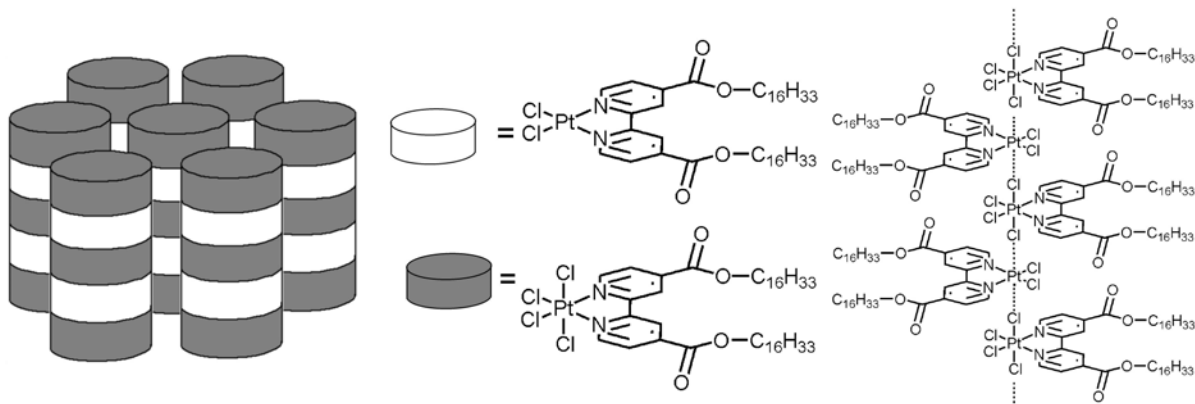


Figure 1-2. Formation of metal-halogen-metal interactions in a hexatic-columnar liquid crystalline phase; packing in the hexatic-columnar mesophase (left), interaction of the metal centers within one column (right).

1.2 MX Chain Interactions

1.2.1 Discovery and General Properties of MX Chain Interactions

So-called “one-dimensional” materials are composed of highly ordered chains of species resulting in anisotropic structures and anisotropic magnetic, intervalence charge transfer (IVCT), and optical properties.^{11, 12} This anisotropy gives rise to possible non-linear optical properties and one-dimensional electron transfer capabilities.¹³ The focus of this research is halogen-bridged transition MX chain systems.

The initial MX chain systems were synthesized and found to have deep, rich colors far before their structures were understood. Near the turn of the century, Werner¹⁴ and Wolfram¹⁵ reported the first platinum MX chain systems. Wolfram synthesized a dichromic crystal, which appeared deep red when viewed along one axis and yellow when viewed along the perpendicular axis. This dichromic behavior was especially surprising given the colors of the $[\text{Pt}(\text{etn})_4]\text{Cl}_2$ and $[\text{Pt}(\text{etn})_4\text{Cl}_2]\text{Cl}_2$ (etn = ethylamine) starting materials. The structure of Wolfram’s red salt was not determined until almost 40 years later when X-ray analysis was performed by Jensen.¹⁶

Jensen’s X-ray structure resolved the controversy over the valence of the Pt sites. The system was known to be diamagnetic, but were highly anisotropic, suggesting a chain structure consisting of either $\text{Cl}-\text{Pt}^{\text{IV}}-\text{Cl}\cdots\text{Pt}^{\text{II}}\cdots$ or $\text{Cl}-\text{Pt}^{\text{III}}-\text{Cl}-\text{Pt}^{\text{III}}-$ chains (Figure 1-3). The X-ray structural results demonstrated that a mixed valence $\text{Pt}^{\text{II}}/\text{Pt}^{\text{IV}}$ system was observed. After the determination of the mixed valent state of these materials, enthusiasm grew for the possibility of using the materials as quasi-one-dimensional semi-conductors or as molecular wires. Since then, there has been considerable research on halogen-bridged transition metal systems, and several review articles have been published.^{17, 18, 19} Despite the potential

usefulness of MX chains, the linear alignment of metal centers is largely restricted to the solid state, necessitating growth of large single crystals to maximize the size of the uniformly anisotropic structure. Uniform anisotropic domains are necessary to maximize the utility of these materials for electronic and optical applications.

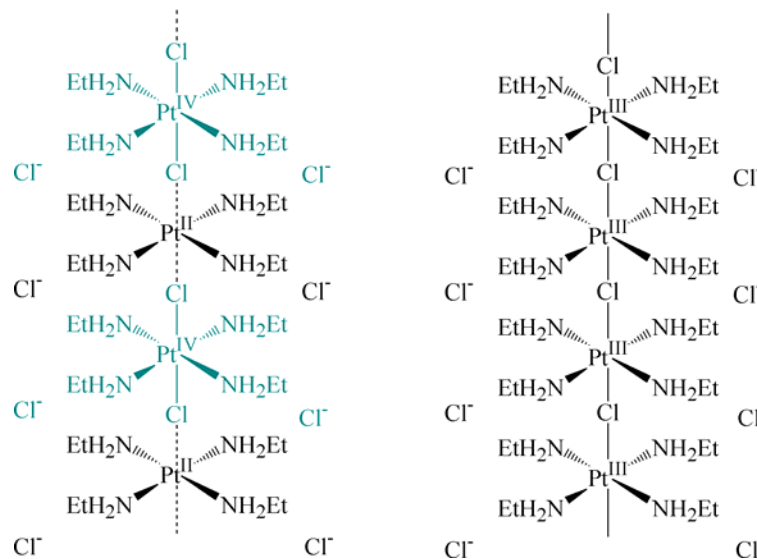


Figure 1-3. Proposed electronic configurations for Wolfram's red salt. The alternating Cl⁻-Pt^{IV}-Cl⁻···Pt^{II}··· structure (left) was determined to be correct via X-ray crystallography.¹⁶

1.2.2 Conductivity and Electrical Structure of MX Chains

Beyond anisotropy of structure, the most important consideration for formation of semi-conducting MX chain materials is a narrow band gap, which provides a low threshold for electron hopping. To meet this electronic structure requirement, a repeating structure of filled and empty sites in electronic communication is needed. This filled/empty alternation may be accomplished through either a series of alternately filled and empty orbitals (Figure 1-4, **b**), or a series of partially filled orbitals (**c** and **d**). However, if the energy for intervalence charge transfer (IVCT) from one metal center to the next is high (**a**), the materials are not useful as semi-conductors. The electronic structures of these materials are

classified according to their metal valence state in the Robin, Day, and Hush classification system (Table 1-1).^{20, 21} Class II valences are most often observed for MX chains, and the energy necessary for electron transfer from one metal center to the next is in the visible region.²²

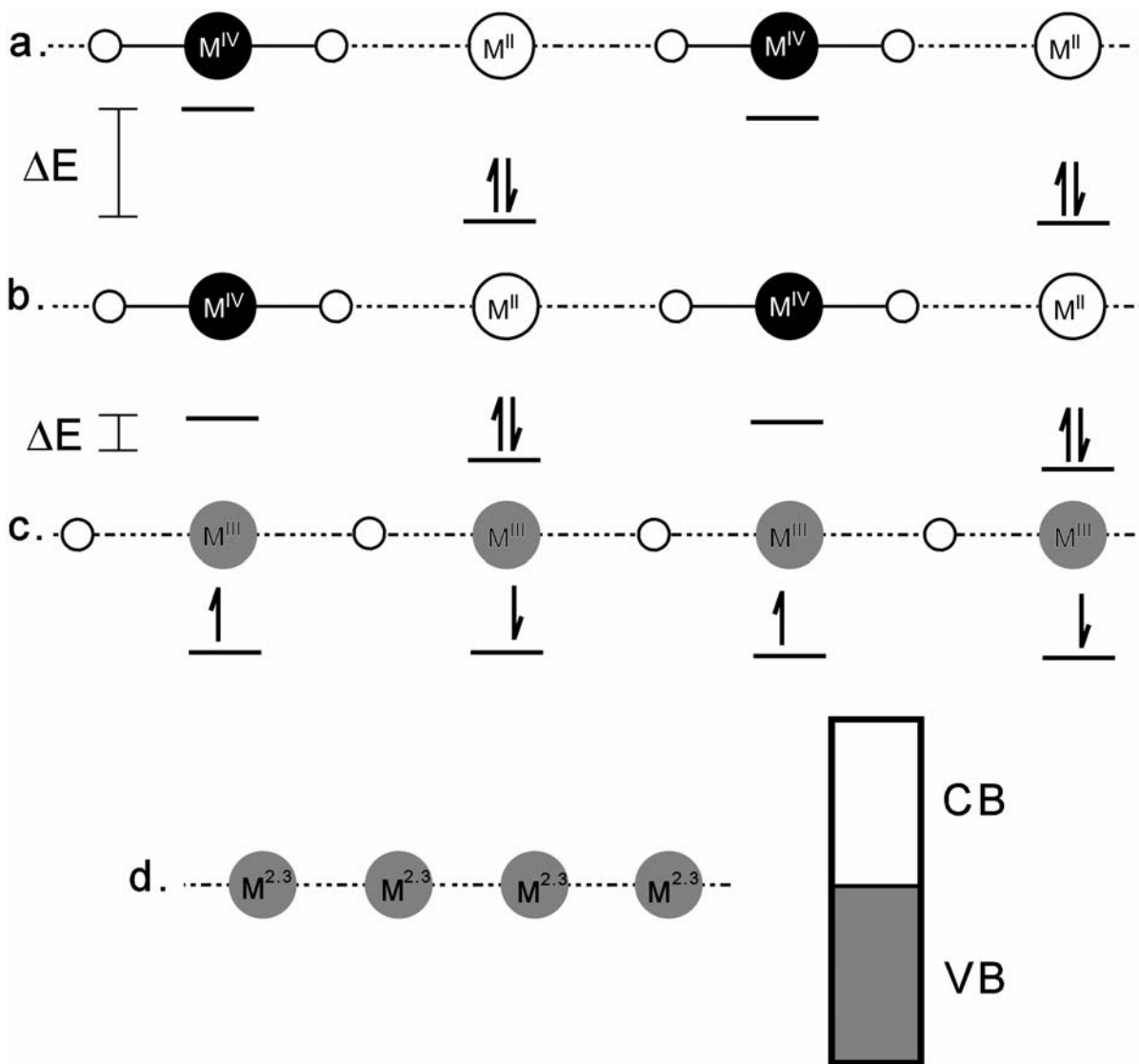


Figure 1-4. Electronic structures of linear chains; Class I, trapped valence (a), Class II Peierls distorted system, low energy IVCT transitions (b), Class II antiferromagnetically coupled system, low energy IVCT transitions (c), Class III, electronic band structure of a partially oxidized complex such as $K_2Pt(CN)_4 \cdot Br_{0.30} \cdot 3H_2O$ (d); CB = conduction band, VB = valence band.

Table 1-1. Robin, Day and Hush Classification System.^{20, 21}

Class	Valence	Example	Properties	Intervalence Transitions
I	trapped	[Cu(en) ₂][CuBr ₂] ^[a]	insulators	none or far-UV
II	low energy transitions	[Pt(en)Cl ₂][Pt(en)Cl ₄] ^[a]	insulators or semi-conductors	visible or near-UV
IIIA	delocalized in a cluster	[Nb ₆ Cl ₁₂] ²⁺	cluster compounds	$\pi \rightarrow \pi^*$ of cluster
IIIB	delocalized in linear chains	K ₂ Pt(CN) ₄ •Br _{0.30} •3H ₂ O	metallic-type conductance	band theory

^[a] en = 1,2-diaminoethane

Class II MX chain systems are of interest for the possibility of controlling the delocalization of electrons along the chain. The electrons are weakly localized, thus, ultra-violet or visible light or a relatively low electric potential may be used to move electrons along the chain axis. The conductivity perpendicular to the chain axis remains low, indicative of the one-dimensional nature of the material. Class II systems may also be characterized as Charge Density Wave (CDW) systems, in which charge may be propagated through a filled valence band ($M^{II} d_{z^2}$) to an empty conduction band ($M^{IV} d_{z^2}$).²³ As will be explained below, an electron hopping mechanism often better describes the conduction process.

The alternating $X-Pt^{IV}-X \cdots Pt^{II} \cdots$ structure is usually observed for PtX chain systems. This preference may be explained by describing the platinum MX chains as Peierls-Hubbard systems, in which the properties of the chains are determined by the balance between several factors including: electron-phonon interactions (**S**), electron transfer (**T**), and onsite and intersite Coulombic interactions (**U** and **V**, respectively).²⁴ These factors may compete or cooperate with one and other. Strong **S** and **V** interactions lead to a distortion of the bridging

halogen from the midpoint between the two metal centers and a more localized valence.²⁵ Further delocalization to a Class III system occurs when U is stronger than S . For this reason Ni (which has larger U interactions) is more likely to form anti-ferromagnetic systems (Figure 1-4 c) than Pd or Pt within the same ligand system.²⁶

Due to the alternating Pt^{II} and Pt^{IV} moieties, conductivity in PtX chain systems requires transfer of a metal center electron from Pt^{II} to Pt^{IV} through a phonon assisted hopping mechanism as proposed by Interrante and Browall (Figure 1-5).²⁷ In this process, the Pt^{II} center is oxidized to Pt^{III} with a concurrent vibrational stretching of the bridging Cl toward the Pt^{III} center (Figure 1-5 a). The Pt^{IV} center is reduced to give adjacent Pt^{III} sites (b). During the hopping portion of the mechanism, an electron from farther along the MX chain reduces the Pt^{III} center back to its initial Pt^{II} state and propagates electrons along the chain (c). The more closely the oxidation potential of the Pt^{II} species matches the reduction potential of Pt^{IV} , the more easily electrons are expected to be moved along the chain.

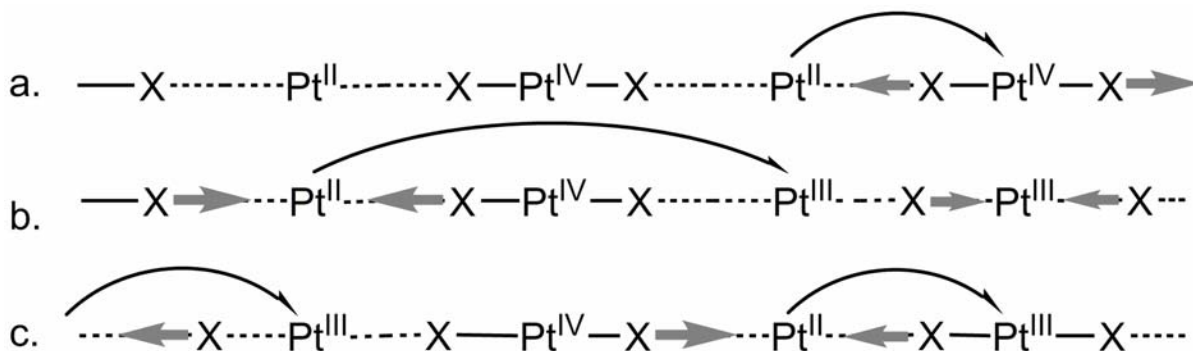


Figure 1-5. Phonon assisted electron hopping mechanism for electron conduction in PtX chain systems as proposed by Interrante and Browall²⁷; electron transfer (half arrow); vibrational motion of the bridging halogens (grey arrows). The initial oxidation may occur from either a spontaneous process or a defect site.

Interrante, Browall, and Bundy demonstrated that for many Pt and Ni MX chain systems the parallel conductivity could be 300 times the perpendicular conductivity.²⁸ From

the analysis of UV-vis spectroscopy, an IVCT band may be found for oligomeric MX chains in solution. This absorbance arises from a photo-induced electron transfer from M^{II} to M^{IV} and is an indicator of the relative conductivity of the system. Clark and coworkers have established general trends based on the identity of the bridging-halogen atom for systems utilizing neutral amine equatorial ligands (see Table 1-2).¹⁸

Table 1-2. Location of IVCT bands in solution phase UV-vis spectra for MX chains with neutral amine equatorial ligands.¹⁸

Bridging Halogen	IVCT Band (nm)
Cl	400-549
Br	424-699
I	489-1333

These changes in IVCT energy are a reflection of the MX chain structure. Complexes with axial iodine ligands tend to undergo less Peierls distortion than chloride or bromide complexes, due in part to the size of the halogen. Consequently, there is less reorganization during electron transfer and a correspondingly reduced energy requirement.²² The determining factor is the ratio (ρ) of the M^{IV} -X bond length to the $M^{II}\cdots X$ bond length. The closer ρ is to unity, the easier it is to move electrons along the chain.²³

MX chain systems may be synthesized using mixed metals. It was determined that, for a given set of ligands, the energy of the IVCT band varies $Pd^{II}/Pt^{IV} > Ni^{II}/Pt^{IV} > Pt^{II}/Pt^{IV} > Pd^{II}/Pd^{IV} > Ni/Ni$, with the Ni/Ni systems shown to be the most conductive.⁵ There are several systems where the Ni valence is +3 throughout the chain. Copper may also be utilized in Cu^{II}/Pt^{IV} systems.^{25, 29, 30} Cu^{II}/Pt^{IV} interactions are weaker than Pt^{II}/Pt^{IV} interactions leading to less conductive systems. Comparing both the metal and bridging ligand data, the most conductive systems are also those with the most electron delocalization.

Hence, the nickel-iodide chains are expected to be the most conductive (given the same equatorial ligand system).

The conductivities of MX chain systems as a function of pressure have been studied extensively. The atmospheric pressure conductivity of Wolfram's red salt is low, but the related system $[\text{Pt}(\text{en})_2^{2+}\text{-Pt}(\text{en})_2\text{Br}_2^{2+}]\text{Br}_4$ was determined to have a conductivity at atmospheric pressure of $10^{-10} \Omega^{-1}\text{cm}^{-1}$ in single crystalline samples²⁷ and up to $10^{-3} \Omega^{-1}\text{cm}^{-1}$ at 150 kbarr²⁸. Work utilizing these systems as one-dimensional conductors was largely abandoned once it was determined the pressure dependant increase in conductivity leveled off and could not be improved past the conductivities of doped polyacetylenes.³¹

1.2.3 Charged and Neutral MX Chain Systems

There has been considerable work with MX chain systems of charged metal complexes as the previous section demonstrates. The charged systems, as shown in Figure 1-6 **a**, consist of metal complexes with an overall charge and counterions. Neutral systems are prepared from neutral metal complexes in the absence of other species (Figure 1-6 **b**). Based on the characterization of existing linear chain systems, charged and neutral, several generalizations may be made with regard to the types of interactions that allow for initial solution oligomerization of MX chains and formation of solid-state one-dimensional networks. Clark and coworkers have established numerous linear chain systems based on the use of a neutral amine equatorial ligands, a platinum or nickel metal center, and bridging halogen ligands.^{17, 18} Many are amenable to growth of X-ray quality single crystals.³² In charged systems, counterions aid in the formation of the MX chains, often by hydrogen bonding to the amine ligands. However, while ideal for highly polar and hydrogen-bonding

solvents, these systems are insoluble in most organics and may show very slow dissolution in polar solvents due to the polymeric structure. These solubility properties make crystal growth difficult.

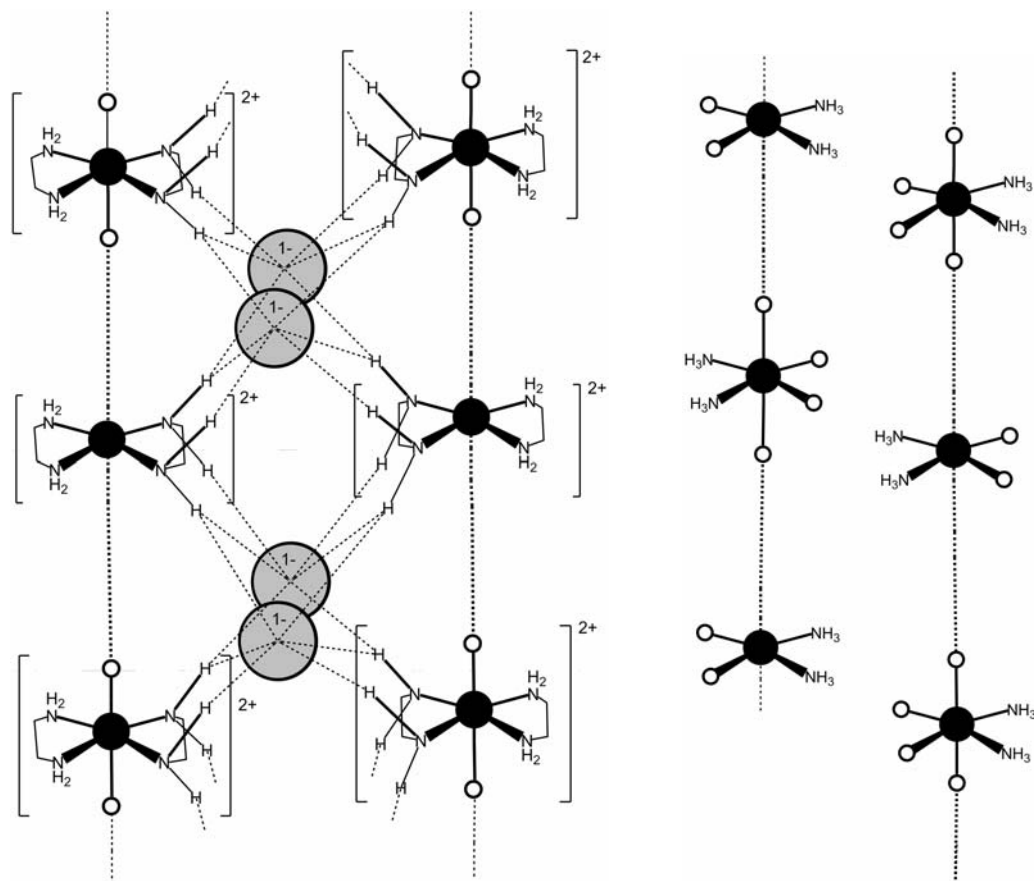


Figure 1-6. Possible examples of charged $X-M^{III}-X-M^{III}-$ chains with hydrogen bonding to the counterions (left) and neutral $\cdots M^{II}\cdots X-M^{IV}-X$ chains (right); for clarity, not all counterions are shown.

MX chains of neutral metal species (Figure 1-6 b) are often more difficult to prepare due to the lack of the secondary interactions like hydrogen bonding and solubility differences in the square-planar M^{II} and octahedral M^{IV} complexes. However, several groups have studied neutral MX chains. As shown in Table 1-3, all these species share very similar characteristics. All species have two nitrogen ligands (or a bidentate diamine ligand), and the remaining coordination sites are filled with halogen or pseudo-halogen ligands.

Table 1-3. Well-characterized PtX chain systems formed from neutral species.

Neutral PtX Chain	Method of Formation	Source
$[\text{Pt}(\text{NH}_3)_2\text{Cl}_2][\text{Pt}(\text{NH}_3)_2\text{Cl}_4]$	stoichiometric mixing	33
$[\text{Pt}(\text{NH}_3)_2\text{Br}_2][\text{Pt}(\text{NH}_3)_2\text{Br}_4]$	stoichiometric mixing	34
$[\text{Pt}(\text{en})\text{Cl}_2][\text{Pt}(\text{en})\text{Cl}_4]^b$	stoichiometric mixing	35
$[\text{Pt}(\text{en})\text{Br}_2][\text{Pt}(\text{en})\text{Br}_4]^b$	stoichiometric mixing	36
$[\text{Pt}(\text{en})\text{I}_2][\text{Pt}(\text{en})\text{I}_4]^b$	stoichiometric mixing	35
$[\text{Pt}(\text{en})(\text{SCN})_2][\text{Pt}(\text{en})(\text{SCN})_2\text{Br}_2]^b$	partial oxidation of Pt ^{II}	37
$[\text{Pt}(\text{en})(\text{SCN})_2][\text{Pt}(\text{en})(\text{SCN})_2\text{I}_2]^b$	partial oxidation of Pt ^{II}	37
$[\text{Pt}(\text{dach})\text{Cl}_2][\text{Pt}(\text{dach})\text{Cl}_4]^a$	stoichiometric mixing	38
$[\text{Pt}(\text{dach})\text{Br}_2][\text{Pt}(\text{dach})\text{Br}_4]^a$	stoichiometric mixing	38
$[\text{Pt}(\text{NH}_3)_2(\text{SCN})_2\text{I}]$	partial oxidation of Pt ^{II}	39

^a dach = 1,2-diaminocyclohexane. All isomers will form MX chains

^b en = 1,2-diaminoethane

1.3 Liquid Crystalline Metal Complexes

1.3.1 Reasons for Incorporating a Liquid Crystalline System

Analysis of the more numerous charged MX chain systems demonstrates that a secondary supramolecular interaction, such as hydrogen bonding, aids in the formation of the M-X \cdots M interactions. As will be further discussed in Chapter 3, several groups have demonstrated that supramolecular Pt^{II} \cdots Pt^{II} interactions are compatible with the formation of liquid crystalline phases, and this supramolecular interaction has been well reviewed.^{8, 10} This research expands the types of supramolecular metal-based interactions in liquid crystalline phases to the study of MX chain interactions. The anisotropic ordering of the liquid crystalline phase is proposed to aid in the formation of neutral MX chain interactions similarly to the way in which hydrogen bonding interactions aided the formation of MX chains from charged complexes. The following sections discuss how the structure of liquid crystalline molecules can be altered to control the supramolecular ordering of the mesophase.

1.3.2 Introduction to Smectic Liquid Crystals

Liquid crystalline systems are fluid phases characterized by a director which defines the average orientation of the molecules (termed mesogens). There are two major types of liquid crystals: thermotropic liquid crystals, which change phase with temperature, and lyotropic liquid crystals, which are formed by molecules in a solvent. The anisotropic molecular structures most commonly associated with formation of liquid crystalline phases are shown in Figure 1-7. The calamitic structure (a) has a rigid core and flexible alkyl chains. The discotic mesogens (b) have a thin, flat core, which may or may not be surrounded by alkyl chains. The ionic melts (c) are composed of surfactant molecules and generally monoatomic counterions. Often the alkyl chains and the rigid cores form separate domains driving formation of the mesophase.

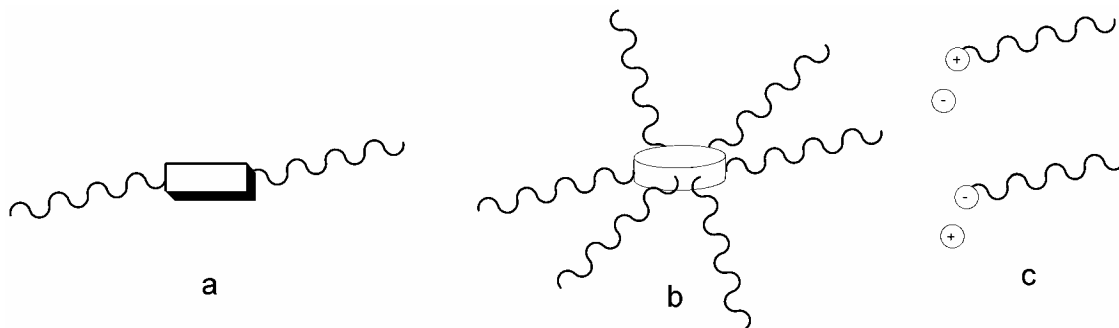


Figure 1-7. Types of mesogens; calamitic (a), discotic (b), ionic melts (c).

While molecular structure is not an absolute predictor of the type of mesophase that will form, there are some general trends. The basic types of mesophases are diagramed in Figure 1-8. For each phase, the director is shown. Nematic phases (a) can be formed by many shapes of mesogens. The director is the sole ordering parameter, and there is no positional order between mesogens. In the smectic phases (b and c), a lamellar (layered) structure is obtained with a director perpendicular to the layers. There are several

subcategories of smectic phases, with the simplest being the smectic A (SmA) and smectic C (SmC) phases. The SmA phase (**b**) is characterized by simple lamella, with the mesogens adopting an orientation on average normal to the layer plane. The SmC phase (**c**) is characterized by an average tilt of the mesogens from the normal of the layer plane. Columnar phases are generally composed of discotic mesogens which are oriented in disordered stacks. The columns may be arranged in a variety of ways, including rectangular-columnar (Col_R) and hexatic-columnar (Col_H) (**d** and **e**, respectively).

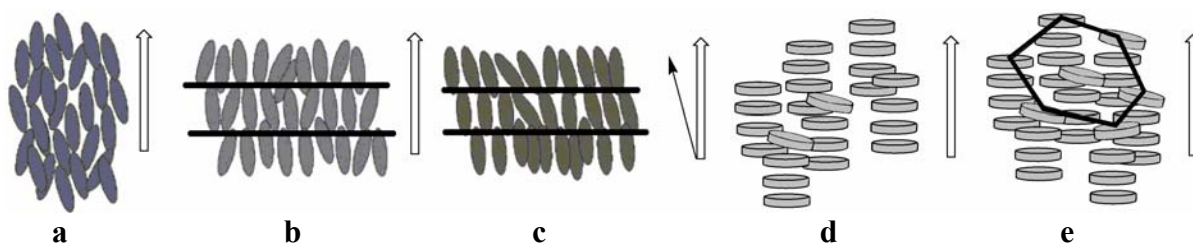


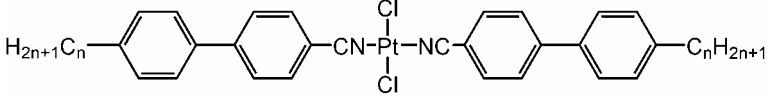
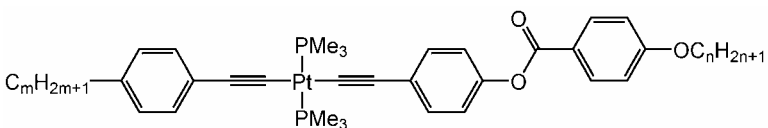
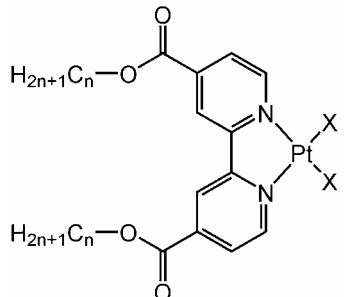
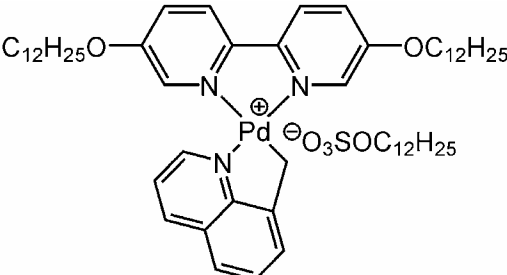
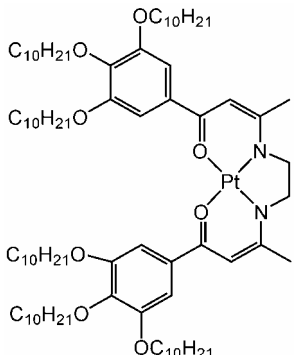
Figure 1-8. Nematic, smectic A, smectic C, rectangular-columnar, and hexatic-columnar liquid crystalline phases (left to right); director (white), tilt (black).

1.3.3 Non-traditional Metallomesogens: Structure and Mesophase Formation

Non-traditional metallomesogens may be utilized to induce formation of mesophases spreading the range from SmA to Col_H by controlling the microsegregation of the alkyl chains from the rigid core (Table 1-4).⁴⁰ Col_L phases generally occur in flat organic systems with both π - π stacking moieties and long alkyl chains, and in inorganic systems with square-planar metal centers where π - π stacking may be aided by metal-metal interactions.^{41, 42, 43, 44} Metal-centered interactions may also contribute to such well-organized intermolecular associations give rise to phases that are described as “soft crystalline phases”. Such soft crystalline phases have ordering similar to Col_H and Col_R phases, but display translational ordering of the mesogens over longer correlation distances than the liquid crystalline Col_H

and Col_R phases. Soft crystalline phases not flow freely under pressure.

Table 1-4. Examples of square-planar metallomesogens.

Example	Phase	Source
	SmA	45
	SmA _b	46
	Col _I / SmA _d	47 and this work
	Col _R	43
	Col _H	48

Less symmetrical mesogens can form even more subtle differences in ordering, often by formation of bilayer phases or other intermolecular associations of moieties. There are three main types of bilayer formation from polar mesogens, characterized by the ratio of the smectic layer spacing to the molecular length as shown in Figure 1-7.⁴⁹ The first and simplest is the SmA_1 (often just SmA) mesophase, where the layer spacing is only slightly less than the molecular length. The semi-bilayer smectic A, SmA_d , phase is characterized by a layer spacing of $1.4\text{-}1.8\times$ the molecular length.⁴⁹ The bilayer smectic A phase, SmA_2 , is characterized by a layer-spacing approximately twice the molecular length.

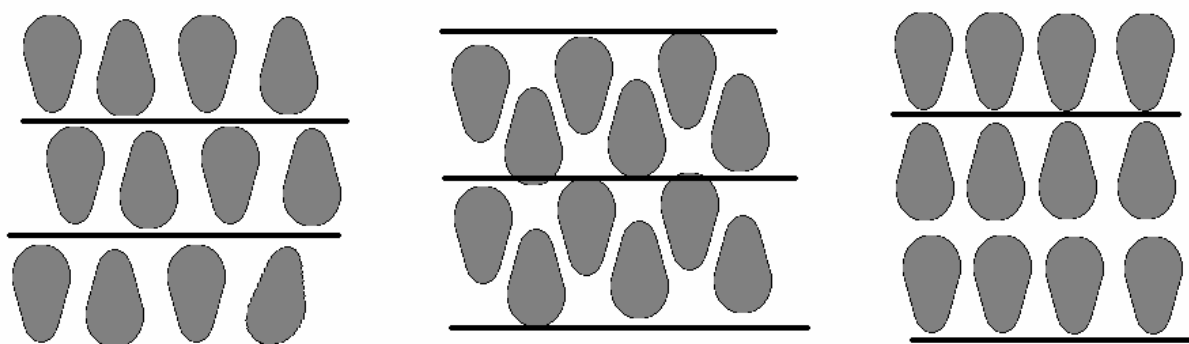


Figure 1-9. Smectic phases of polar mesogens: smectic A_1 (SmA_1), semi-bilayer smectic A (SmA_d), and bilayer smectic (SmA_2) (left to right); layer spacing (black lines).

1.4 Progression and Impetus for Research

The chapters in this dissertation roughly reflect the chronological order under which this research into supramolecular ordering progressed. Initially, a series of Pt^{II} and Pt^{IV} complexes of substituted-salicylaldimines were synthesized and characterized. Although MX chain systems were not obtained, more information was gathered on the electrochemistry and electro-oxidative polymerization of the complexes as presented in

Chapter 2. A liquid crystalline system was then designed on the belief that the mesogenic ordering could help to aid in the formation of MX chain interactions in neutral molecules. The characterization of individual dialkyl-2,2'-bipyridine-4,4'-dicarboxylate complexes of Pt^{II}, Pt^{IV}, Cd^{II}, and Re^I and their mesogenic behavior is discussed in Chapter 3. This analysis was performed to determine the candidate complexes most likely to form MX chain interactions in binary mixtures of Pt^{II} and Pt^{IV} mesogens. Chapter 4 reports the characterization of binary Pt^{II}/Pt^{IV} mesophases. A Col_H mesophase with X-ray structural characteristics compatible with formation of MX chain interactions is observed and characterized. Preliminary data on the self-assembly dependant luminescence of a binary Pt^{II}/Pt^{IV} mixture is also presented in Chapter 4.

CHAPTER II

SYNTHESIS AND CHARACTERIZATION OF PLATINUM(II) AND PLATINUM(IV) SCHIFF BASE COMPLEXES OF SUBSTITUTED- SALICYLALDIMINES

2.1 Introduction

As demonstrated in the previous chapter, the known neutral MX chain systems have two nitrogen donor and two halide or pseudo-halide equatorial ligands (see Table 1-3). In keeping with these general structural trends, the planar nature and nitrogen donor groups of Schiff base ligands made them candidates for the design of neutral MX chain systems. The imine functionalities of Schiff bases are easily modifiable, allowing for systematic study of steric and electronic effects. The Schiff base complexes synthesized for this research are given in Figure 2-1.

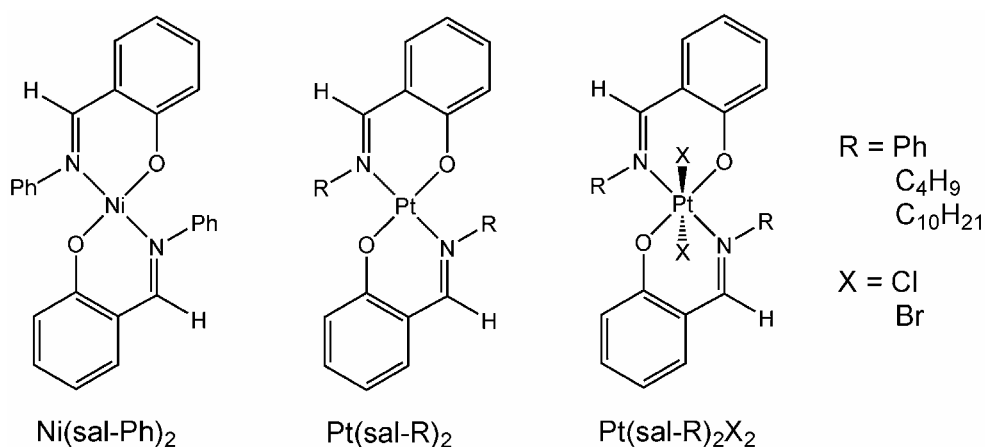


Figure 2-1. Ni, Pt^{II}, and Pt^{IV} complexes analyzed in this research.

Pt(sal-R)₂ oxidative electrochemistry was analyzed due to interest in the conductance properties of the potential Pt(sal-R)₂/Pt(sal-R)₂Cl₂ MX chain systems. Conductivity in the potential Pt(sal-R)₂/Pt(sal-R)₂Cl₂ MX chain would require transfer of a metal center electron from a filled Pt^{II} orbital to an empty Pt^{IV} orbital as discussed in Chapter 1 and shown in Figure 2-2. The more closely the oxidation potential of the Pt^{II} species matches the reduction potential of the Pt^{IV} species, the higher the conductivity of the chain is expected to be. In many MX chain systems the energy for this electron transfer is in the visible region, ~3 eV, giving deep red and green colors to many systems.^{32, 50}

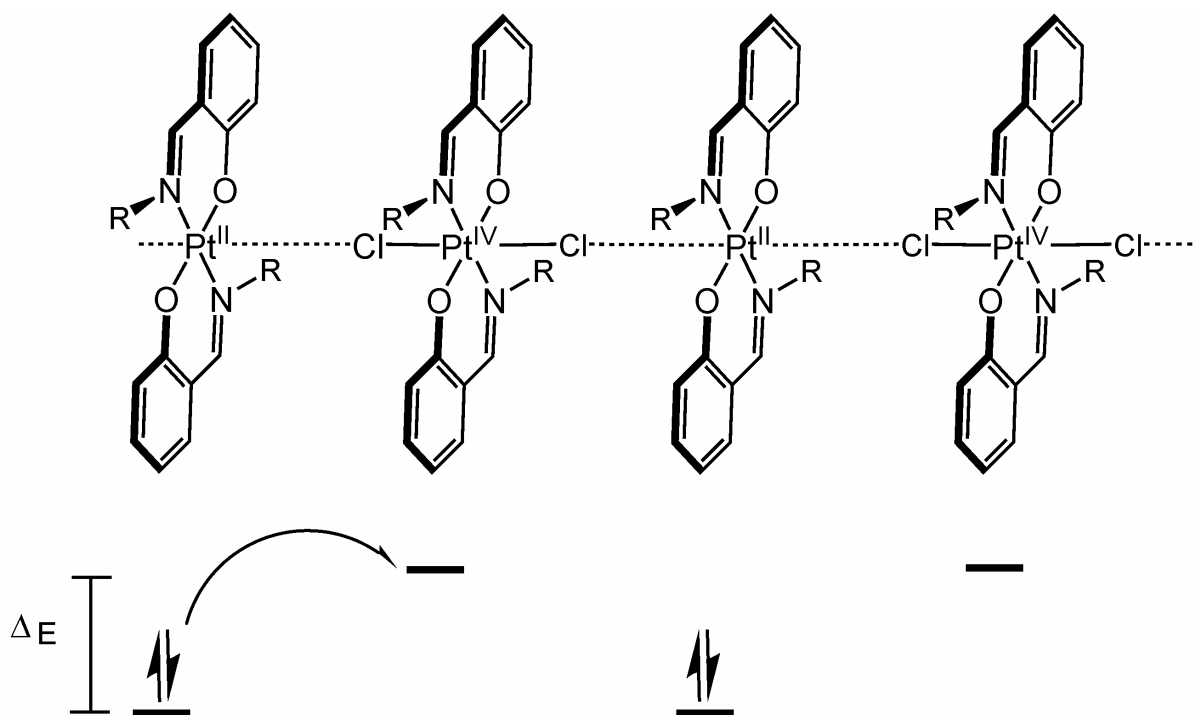


Figure 2-2. Proposed Pt(sal-R)₂/Pt(sal-R)₂Cl₂ MX chain interaction and electronic configuration of alternating filled and empty d orbitals; photoinduced electron transfer from Pt^{II} to Pt^{IV} (half arrow).

In addition to meeting the electronic requirements for MX chain formation, the complexes were also analyzed for their compatibility with structural requirements. The octahedral components of the existing neutral MX chain systems have axial halide ligands.

The single crystal structure of $\text{Pt}(\text{sal-}n\text{-Bu})_2\text{Cl}_2$ was elucidated to confirm the linear Cl-Pt-Cl arrangement desired for linear MX chain interactions.

Though ultimately unsuitable for formation of MX chain interactions, $\text{Pt}(\text{sal-R})_2$ complexes do undergo oxidative polymerization electrochemistry to form electroactive polymers on the electrode surface. The analysis of the redox potentials of the metal complexes and their electrode surface adsorbed polymers provides a complement to the data in the literature.

Oxidative electropolymerization is observed for many metal complexes with multiple aromatic Schiff base ligands. When the electropolymerization is studied via cyclic voltammetry, characteristic oxidation and reduction waves are observed as diagrammed in Figure 2-3. With each potential cycle, additional layers of polymer are deposited, and the current for the surface polymer oxidation (Figure 2-3 **a**) and reduction (**b**) waves increases. Redox couples for surface species are identifiable by their nearly identical oxidation and reduction potentials. The current associated with the oxidation of complex/monomer in solution (**c**) decreases with each cycle. The polymerization steps following the initial oxidation are rapid, resulting in an irreversible monomer oxidation and a lack of a corresponding reduction wave (**d**). The proposed mechanism for the electropolymerization will be explained further during the discussion of the voltammetric characterization of the $\text{M}(\text{sal-R})_2$ complexes.

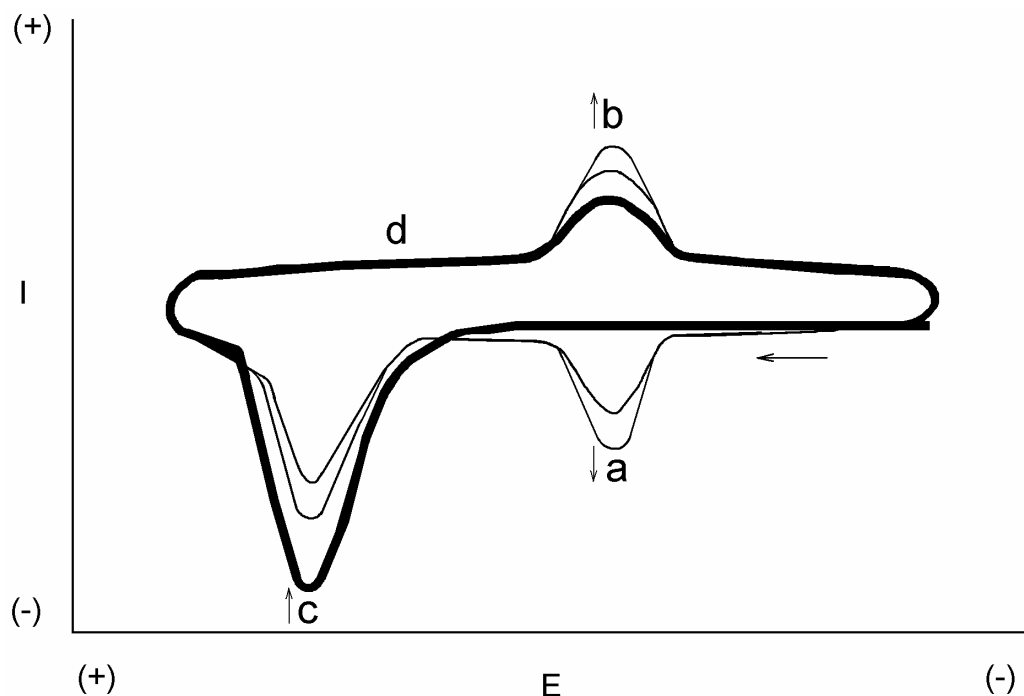


Figure 2-3. Characteristic cyclic voltammogram for electro-oxidative formation of an electroactive polymer film on the electrode surface; oxidation of the film (**a**), reduction of the film (**b**), and oxidation of monomer in solution (**c**). Oxidation of the monomer is irreversible, leading to the lack of a reduction wave (**d**). Three potential cycles are shown, with the first as a thick line.

Previous work has demonstrated that electrodes modified with electroactive metal-Schiff base polymers may be utilized in a variety of catalytic reductions including reduction of organic halides, molecular oxygen, and carbon dioxide.^{51, 52, 53, 54} Ni(salen) ($H_2\text{salen} = N,N'$ -disalicylidene-1,2-ethylenediamine) and its derivatives are most frequently utilized to produce these films, presumably due to the commercial availability of Ni(salen) and the added stability inherent in complexes of tetradentate ligands in comparison to bidentate complexes.^{55, 56} The bis(salicylaldimine) systems presented here offer more flexibility in control of the steric and electronic properties of the ligands and offer the possibility of synthesizing metal complexes with two different imine ligands.⁵⁷

2.2 Experimental Section

2.2.1 Synthetic Materials and General Procedures

Materials were purchased in reagent grade and used without further purification unless otherwise noted. All reactions involving air/moisture sensitive materials were carried out using standard Schlenk techniques. Argon was purified by passage through BASF R3-11 catalyst and 4 Å molecular sieves. Ligands *N,n*-butylsalicylaldimine, *N,n*-decylsalicylaldimine, and *N*-phenylsalicylaldimine were synthesized according to literature procedures⁵⁸ and ¹H NMR results were consistent with published data. Pt(NCPh)₂Cl₂ was either prepared via literature procedure⁵⁹ or purchased from Strem Chemical. The Pt(NCPh)₂Cl₂ produced by Strem Chemical was found to be >98% *trans* isomer. All ¹H NMR spectra were recorded on a Bruker Advance 400 MHz spectrometer using CD₂Cl₂ or CDCl₃ as the solvent. Chemical shifts are reported in ppm, using the signal from residual protonated solvent as reference. A Hewlett Packard 8452A diode array spectrometer was utilized to obtain UV-vis spectra.

2.2.2 Syntheses of Pt^{II} Complexes

General Procedure: Complexes were prepared according to the previous method from *trans*-Pt(NCPh)₂Cl₂ with modifications in work-up.⁵⁷ Crude product was extracted with hexanes overnight using a Soxhlet extractor. The sample was then concentrated for purification on a silica gel column where the desired product eluted in toluene as the first yellow band. Solvent removal yielded a bright yellow powder. Please note the comments in the discussion section on the improvements in yield obtained using *cis*-Pt(NCPh)₂Cl₂ and lower reaction temperatures.

Bis(*N,n*-butylsalicylaldimine)platinum(II): Yield: 10-25%. ¹H NMR and UV-vis analysis is in agreement with previously published results.^{57, 60} IR (KBr) $\tilde{\nu}_{\max}$: 1615.4 (C=N), 1598.0 cm⁻¹ (C-O).

Bis(*N,n*-decylsalicylaldimine)platinum(II): Yield: 8-12%. UV-vis (CHCl₃): λ_{\max} , nm (ϵ , M⁻¹cm⁻¹): 248 (32,000), 318 (13,000), 328 (13,000); 444 (4000). ¹H NMR (400 MHz, CD₂Cl₂): 0.87 (t, *J* = 6.65 Hz, 6H, CH₃), 1.26-1.45 (m, 14H, CH₂CH₂(CH₂)₇CH₃), 1.80 (p, *J* = 7.32 Hz, 4H, CH₂CH₂(CH₂)₇CH₃), 3.83 (t, *J* = 7.32 Hz, 4H, CH₂CH₂(CH₂)₇CH₃), 6.59 (t, *J* = 6.88 Hz, 2H, ArH⁴), 7.28 (dd, *J* = 7.96 Hz, *J* = 1.76 Hz, 2H, ArH⁶), 7.26-7.36 (broad, 4H, ArH⁵ and ArH³), 7.94 (s, 2H, NCH).

Bis(*N*-phenylsalicylaldimine)platinum(II): Yield: 4.2-4.9%. Analysis of UV-vis and IR spectroscopies consistent with previously published results.⁶¹ UV-vis (CHCl₃): λ_{\max} , nm (ϵ , M⁻¹cm⁻¹): 248 (28,000), 328 (13,000), 338 (13,000), 468 (4500). IR (KBr) $\tilde{\nu}_{\max}$: 1606.7 (C=N), 1580.9 cm⁻¹ (C-O). ¹H NMR (400 MHz, CD₂Cl₂): 6.08 (d, *J* = 8.7 Hz, 2H, ArH⁶), 6.52 (t, *J* = 7.4 Hz, 2H, ArH⁴), 7.21 (d, *J* = 7.5 Hz, 2H, ArH⁵), 7.27 (d, *J* = 7.8 Hz, 2H, ArH³), 7.3-7.4 (m, 6H, *o*-PhH and *p*-PhH), 7.44 (t, *J* = 7.6 Hz, 4H, *m*-PhH), 8.05 (s, 2H, NCH).

2.2.3 Syntheses of Pt^{IV} Complexes

General Procedure: Pt(sal-R)₂ (0.02-0.10 mmol) was dissolved in 10 mL chloroform that had been purged with argon for 10 minutes. In a separate flask, a tenfold excess of CuCl₂·xH₂O was dissolved in 10 mL absolute ethanol and purged for 10 min with argon. As the Pt(sal-R)₂ solution was added dropwise to the ethanol solution over 15 min, the reaction mixture changed color from dark green to brown and an orange precipitate formed. The

reaction mixture was stirred at RT for an additional 15 min. The product was collected via vacuum filtration and washed with hexanes (to remove unreacted Pt(sal-*n*-Bu)₂) and ethanol (to remove CuX and excess CuX₂). The product may be further purified by recrystallization from 1:1 CH₂Cl₂/ethanol.

Bis(*N,n*-butylsalicylaldimine)dichloroplatinum(IV): Yield: 0.025 g, 46.8%. UV-vis (CHCl₃): λ_{max}, nm (ε, M⁻¹cm⁻¹): 258 (8900), 284 (9060), 396 (3400). ¹H NMR (400 MHz, CD₂Cl₂): 1.04 (t, *J* = 7.4 Hz, 6H, CH₃), 1.50-1.59 (m, 8H, γCH₂), 2.02 (m, 4H, βCH₂), 3.95 (t, *J* = 7.7 Hz, 4H, αCH₂), 6.78 (ddd, *J* = 8.0, *J* = 7.1, *J* = 1.0, 2H, ArH⁴), 7.01 (d, *J* = 8.3 Hz, 2H, ArH⁶), 7.34 (dd, *J* = 7.9 Hz, *J* = 1.7 Hz, 2H, ArH³), 7.43 (ddd, *J* = 8.7 Hz, *J* = 7.1 Hz, *J* = 1.8 Hz, 2H, ArH⁵), 7.69 (apparent t, *J* = 52.2 Hz, 2H, NCH).

Dibromobis(*N,n*-butylsalicylaldimine)platinum(IV): Yield: 0.013 g, 18.9%. UV-vis (CH₂Cl₂): λ_{max}, nm (ε, M⁻¹cm⁻¹): 234 (30,000), 254 (57,000), 286 (16,000), 344 (1300), 400 (4400). ¹H NMR (400 MHz, CD₂Cl₂): 1.04 (t, *J* = 7.4 Hz, 6H, CH₃), 1.50-1.60 (m, 8H, γCH₂), 2.04 (p, *J* = 7.7 Hz, 4H, βCH₂), 3.95 (t, *J* = 7.5 Hz, 4H, αCH₂), 6.76 (ddd, *J* = 8.0, *J* = 7.1, *J* = 1.0, 2H, ArH⁴), 6.96 (d, *J* = 8.5 Hz, 2H, ArH⁶), 7.32 (dd, *J* = 7.9 Hz, *J* = 1.6 Hz, 2H, ArH³), 7.42 (m, *J* = 8.6 Hz, *J* = 7.0 Hz, *J* = 1.8 Hz, 2H, ArH⁵), 7.67 (apparent t, *J* = 50 Hz, 2H, NCH).

Dichlorobis(*N,n*-decylsalicylaldimine)platinum(IV): Yield: 0.60 mg, 4.5%. UV-vis (CHCl₃): λ_{max}, nm (ε, M⁻¹cm⁻¹): 250 (34,000), 276 (12,000), 396 (3100). ¹H NMR (400 MHz, CD₂Cl₂): 0.88 (t, *J* = 7.0 Hz, 6H, CH₃), 1.25-1.56 (m, 28H, CH₂CH₂(CH₂)₇CH₃), 2.03 (p, *J* = 7.4, 4H, CH₂CH₂(CH₂)₇CH₃), 3.94 (t, *J* = 7.6 Hz, 4H, CH₂CH₂(CH₂)₇CH₃), 6.78 (m, *J* = 8.0, *J* = 7.2, *J* = 1.2, 2H, ArH⁴), 7.00 (d, *J* = 8.2 Hz, 2H, ArH⁶), 7.33 (dd, *J* = 7.9 Hz, *J* = 1.4 Hz, 2H, ArH³), 7.42 (ddd, *J* = 8.6 Hz, *J* = 7.1 Hz, *J* = 1.6 Hz, 2H, ArH⁵), 7.69 (apparent

t, $J = 52$ Hz, 2H, NCH).

Dibromobis(*N,n*-decylsalicylaldimine)platinum(IV): Yield: 0.023 g, 28.7%. UV-vis (CHCl_3): λ_{max} , nm (ϵ , $\text{M}^{-1}\text{cm}^{-1}$): 252 (50,000), 286 (11,000), 402 (3400). ^1H NMR (400 MHz, CD_2Cl_2): 0.88 (t, $J = 6.7$ Hz, 6H, CH_3), 1.24-1.55 (m, 28H, $\text{CH}_2\text{CH}_2(\text{CH}_2)_7\text{CH}_3$), 2.06 (p, $J = 7.5$, 4H, $\text{CH}_2\text{CH}_2(\text{CH}_2)_7\text{CH}_3$), 3.94 (t, $J = 7.6$ Hz, 4H, $\text{CH}_2\text{CH}_2(\text{CH}_2)_7\text{CH}_3$), 6.76 (m, $J = 7.9$, $J = 6.7$, $J = 0.92$, 2H, ArH^4), 6.97 (d, $J = 8.4$ Hz, 2H, ArH^6), 7.32 (dd, $J = 7.9$ Hz, $J = 1.6$ Hz, 2H, ArH^3), 7.42 (ddd, $J = 8.6$ Hz, $J = 7.1$ Hz, $J = 1.7$ Hz, 2H, ArH^5), 7.66 (apparent t, $J = 52$ Hz, 2H, NCH).

Dibromobis(*N*-phenylsalicylaldimine)platinum(IV): Yield: trace orange solid. ^1H NMR (400 MHz, CD_2Cl_2): 6.19 (d, $J = 8.5$ Hz, 2H, ArH^6), 6.67 (ddd, 2H, $J = 8.4$ Hz, $J = 7.0$ Hz, $J = 1.04$ Hz, ArH^4), 7.3-7.7 (m, 14H, ArH^3 , ArH^5 , *o*-PhH, *m*-PhH, and *p*-PhH), 7.80 (apparent t, $J = 52$ Hz, 2H, NCH).

2.2.4 Synthesis of Bis(*N*-phenylsalicylaldimine)nickel(II)

Green crystals were prepared by modification of the literature procedure utilizing only 1 eq of Hsal-Ph, instead of 2 eq.⁶² Yield: 0.30 g, 58%. UV-vis (CHCl_3): λ_{max} , nm (ϵ , $\text{M}^{-1}\text{cm}^{-1}$): 244 (16,200), 270 (14,500), 318 (8900), 344 (8100), 648 (13). IR (KBr) $\tilde{\nu}_{\text{max}}$: 1614.5 (C=N), 1591.8 cm^{-1} (C-O).

2.2.5 Electrochemical Procedures

Acetonitrile (Aldrich, Gold Grade) was stored over 4 Å molecular sieves and used without further purification. Tetrabutylammonium tetrafluoroborate (TBATFB) was recrystallized three times from ethyl acetate/pentanes and dried under vacuum at 100 °C for

at least one day prior to use. A TBATFB concentration of 0.1 M and analyte concentrations of 0.05 to 1.0 mM were utilized. All potentials were referenced to the $\text{Cp}_2\text{Fe}^{0/+}$ couple. Ferrocene (Aldrich) was purified via sublimation prior to use and stored in a glove box. A closed electrochemical cell was utilized for all experiments, and all samples were sparged with argon prior to each experiment. Cyclic voltammetry was carried out at a glassy carbon working electrode with a Ag-wire pseudo-reference electrode and a Pt-wire counter electrode using a potentiostat/galvanostat with super-cycle built in the University of North Carolina at Chapel Hill Electronics Shop.

2.2.6 Single Crystal X-ray Diffraction Procedures

A single crystal of $\text{Pt}(\text{sal-}n\text{-Bu})_2\text{Cl}_2$ was mounted on a glass fiber and placed in the cold nitrogen stream of a Bruker SMART 1K CCD diffractometer in the omega scan mode. Data were collected at 173 K using $\text{CuK}\alpha$ radiation. The structure was solved by direct methods and anisotropically refined by full-matrix least squares. Hydrogen atoms were placed geometrically and refined isotropically using the riding-atom model. Parameters for data collection and refinement are given in Table 2-1. Thermal ellipsoid plots were produced using Ortep-3 v. 1.08.

Table 2-1. Crystallographic Information for Pt(sal-*n*-Bu)₂Cl₂.

Species	Pt(sal- <i>n</i> -Bu) ₂ Cl ₂
chemical formula	C ₂₂ Cl ₂ H ₂₈ N ₂ O ₂ Pt
formula weight	618.47
T (K)	173
wavelength (Å)	1.5418
crystal system	monoclinic
space group	C2/c
a (Å)	11.9938(4)
b (Å)	8.3349(4)
c (Å)	23.2329(10)
α (Å)	90
β (Å)	96.4430(2)
γ (Å)	90
volume (Å ³)	2307.86(17)
Z	4
D _{calc} (g/cm ³)	2.22
absorption coefficient (mm ⁻¹)	13.23
F(000)	1196.19
crystal size (mm)	0.01 × 0.01 × 0.00
2θ max (deg)	140.0
index ranges	-14 ≤ h ≤ 14, 0 ≤ k ≤ 9, 0 ≤ l ≤ 27
reflections collected	9000
significant reflections	1703
refinement method	full-matrix least-squares on F ²
data/parameters	1703/134
goodness-of-fit on F ²	1.4633
final R indices [F _o > 2.5σ(F _o)]	R = 0.037, R _w = 0.032
R indices (all data)	R = 0.051, R _w = 0.036
largest diff. peak and hole	2.080/-2.930 e Å ⁻³

$$R = (\sum |F_o| - |F_c|) / \sum |F_o|, R_w = [(\sum |F_o| - |F_c|)^2 / \sum w(|F_c|)^2]^{1/2}$$

2.2.7 DFT Calculations

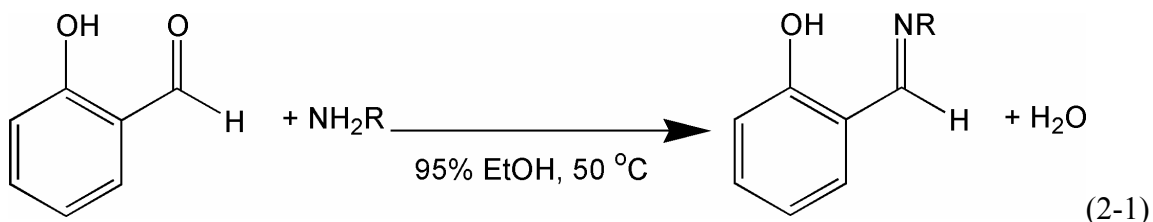
All density functional theory (DFT) calculations were performed using Gaussian 03⁶³ utilizing the methodology of Cui, Musaev, and Morokuma.⁶⁴ Geometries were optimized using B3LYP hybrid density functional theory with standard double-ζ quality basis sets, which includes lanl2dz and an effective core potential for Ni, Cl, and Pt atoms.⁶⁵ Polarization functions were included for Ni, Cl, and Pt (f, d, and f polarizations, respectively).

All other other atoms were determined utilizing D95V, instead of D95 as was utilized in the literature method.^{66, 67, 68, 69} The geometries of Ni(sal-Me)₂, Pt(sal-Me)₂, and Hsal-Me were allowed to reach an energy minimum without restricting bond lengths or angles. Molecular orbitals were visualized with GaussView 3.09.⁷⁰

2.3 Results and Discussion

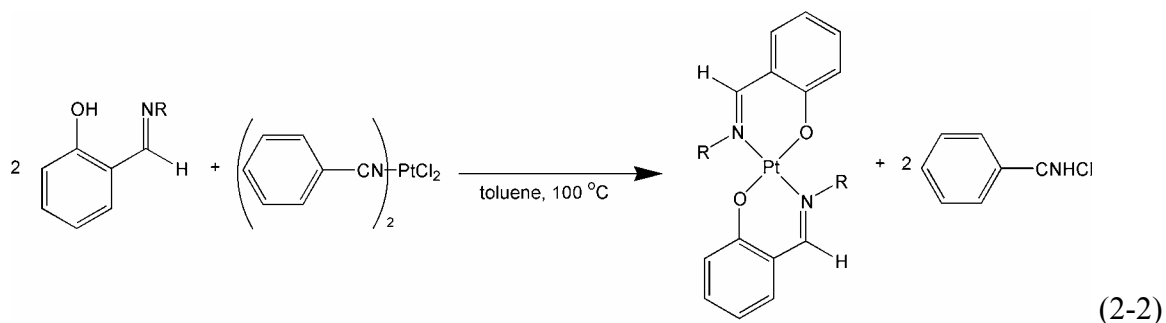
2.3.1 Synthesis of Ligands

Bidentate salicylaldimine ligands may be produced via a Schiff-base condensation reaction in essentially quantitative yield as shown in eq 2-1.⁵⁸ A wide variety of primary amines may be utilized for the reaction.



2.3.2 Synthesis of Pt^{II} Complexes

The Pt^{II} complexes were analyzed for their oxidative electrochemistry and served as a precursor for the Pt^{IV} species. Bis(benzonitrile)dichloroplatinum(II), Pt(NCPh)₂Cl₂, is reacted with Hsal-R according to a modified of a literature procedure as shown in eq 2-2 to produce Pt(sal-R)₂.⁵⁷



The previously reported synthesis of Pt(sal-*n*-Bu)₂ at 100 °C in toluene from *trans*-Pt(NCPh)₂Cl₂, reported no residual free ligand after overnight reflux, and recorded a 17% isolated yield.⁵⁷ This result could not be reproduced, as approximately two-thirds of the ligand remained unreacted after heating *trans*-Pt(NCPh)₂Cl₂ and Hsal-*n*-Bu at 100 °C in toluene for 24 h. High temperature reactions are known to give almost exclusively *trans*-Pt(NCPh)₂Cl₂, even if the *cis* isomer is initially added to the reaction mixture, due to the relatively facile thermal conversion between *cis*-Pt(NCPh)₂Cl₂ and the *trans* form. The *trans* form is produced almost exclusively by high temperature (>100 °C) synthesis, and even room temperature synthesis in excess benzonitrile produces 2.2:1 *cis/trans* isomers.⁵⁹

Various experiments on the effectiveness of *cis*- and *trans*-Pt(NCPh)₂Cl₂ for the synthesis of Pt(sal-*n*-Bu)₂ are given in Table 2-2. The *cis* isomer is much more amenable to ligand replacement. For example, refluxing two equivalents of ligand and the *trans*-Pt(NCPh)₂Cl₂ in chloroform overnight results in no reaction, while the *cis* isomer gives 62% yield by NMR spectroscopy. Overall, using lower reaction temperatures and *cis*-Pt(NCPh)₂Cl₂ as the starting material gave better yields.

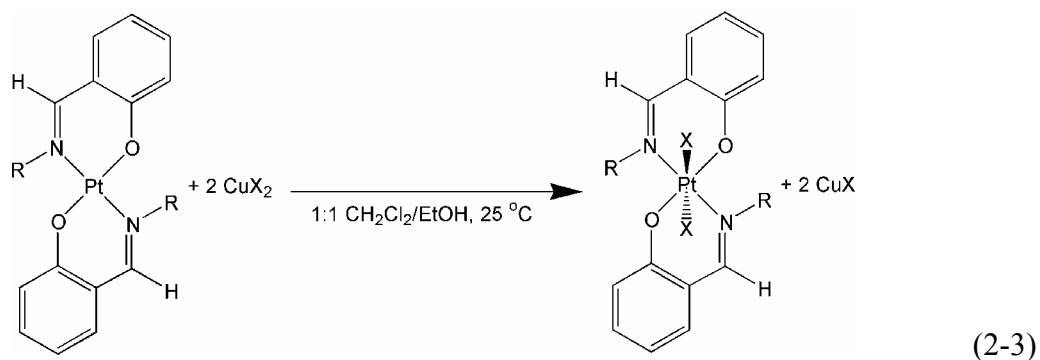
Table 2-2. Conditions for synthesis and yields of Pt(sal-*n*-Bu)₂.

Pt(NCPh) ₂ Cl ₂ Isomer	Conditions	Yield ^[a] of Pt(sal- <i>n</i> -Bu) ₂
Strem Chemicals >98% <i>trans</i>	100 °C, toluene, 18 h	11-17%
<i>cis</i>	70 °C, chlorobenzene, 18 h	54%
<i>trans</i>	reflux, CHCl ₃ , 18 h	no reaction
<i>cis</i>	reflux, CHCl ₃ , 18 h	62%
<i>trans</i>	RT, CH ₂ Cl ₂ , 4 d	3%
<i>cis</i>	RT, CH ₂ Cl ₂ , 3 d	21%

^[a] yield determined from ¹H NMR spectrum of the crude reaction mixture

2.3.3 Syntheses of Pt^{IV} Complexes

The chemical oxidation of Pt^{II} to Pt^{IV} can be accomplished with a variety of reagents. Oxidation of Pt(sal-R)₂ with an excess of X₂ in CH₂Cl₂ would be the most direct route, but the Schiff base ligands are susceptible to halogenation.⁷¹ Connelly's and Geiger's review of redox agents for organometallic chemistry points out that although copper (II) salts are not as frequently used in platinum oxidation chemistry, their one-electron oxidation chemistry and cost effectiveness make them good oxidant candidates.⁷² The oxidation of Pt^{II} 1,3-phenylenedimethanamine pincher complexes with CuX₂ has been previously demonstrated.⁷³ The Pt(sal-R)₂Cl₂ complexes are easily synthesized by oxidation of Pt(sal-R)₂ with an excess of CuX₂ according to the reaction in eq 2-3.



The production of water-soluble copper by-products, rather than copper solid, supports one-

electron oxidation chemistry. Synthesis and purification of the $\text{Pt}(\text{sal-R})_2\text{Cl}_2$ complexes may be confirmed by ^1H NMR spectroscopy (Appendix I). As shown in Figure 2-4, the resonance for the imine proton is diagnostic of the oxidation of Pt^{II} to Pt^{IV} . The resonance moves upfield and shows satellite resonances due to coupling with the 33.8% naturally abundant $^{195}\text{Pt}^{\text{IV}}$ center.

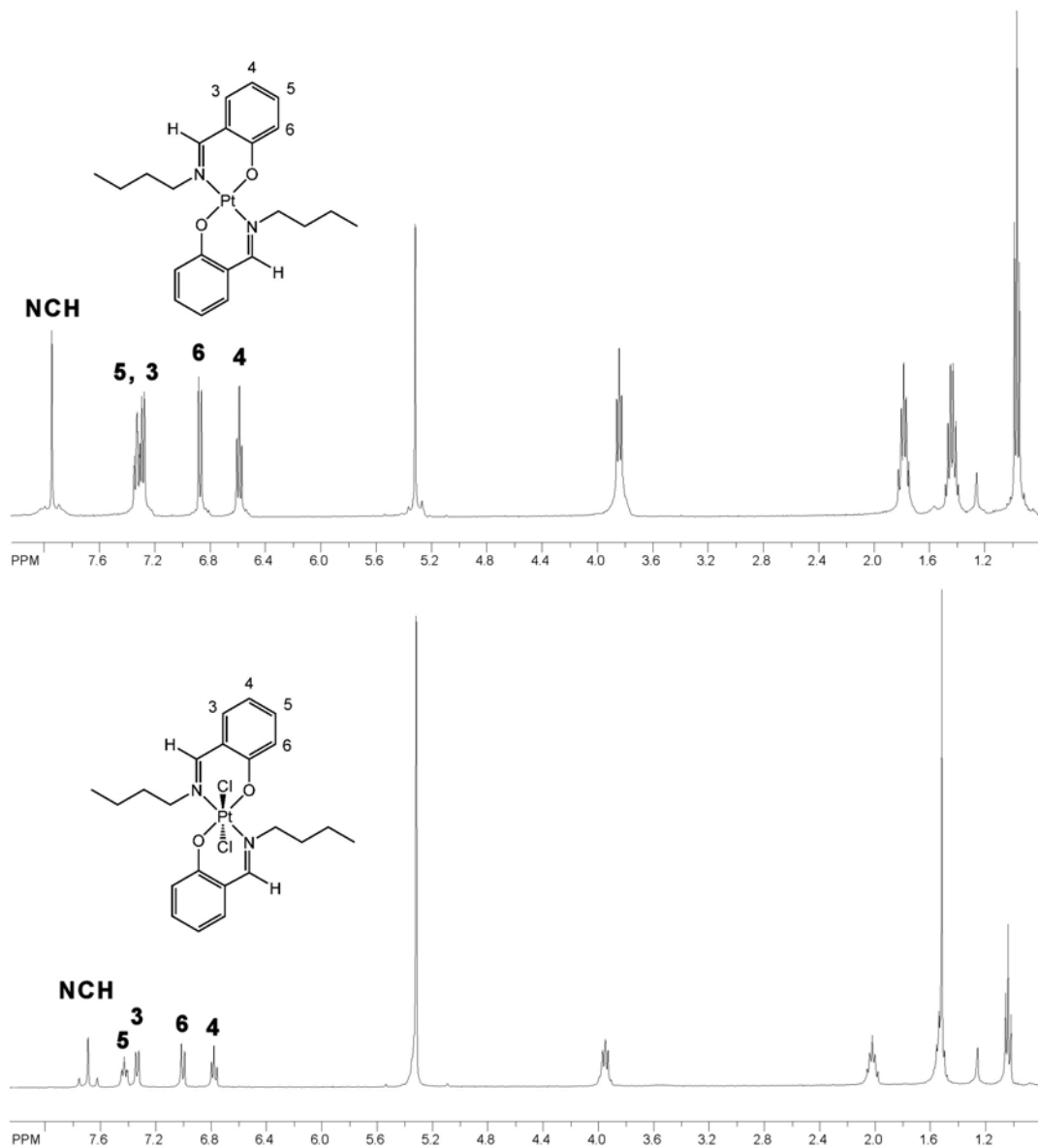


Figure 2-4. Proton NMR spectra for $\text{Pt}(\text{sal-}n\text{-Bu})_2$ (top) and $\text{Pt}(\text{sal-}n\text{-Bu})_2\text{Cl}_2$ (bottom); CD_2Cl_2 , 400 MHz.

Interestingly, combining equal equivalents of CuBr_2 and CuCl_2 in a ten-fold excess of $\text{Pt}(\text{sal-Ph})_2$ results in the production of $\text{Pt}(\text{sal-Ph})_2\text{Cl}_2$ and $\text{Pt}(\text{sal-Ph})_2\text{Br}_2$ but no $\text{Pt}(\text{sal-Ph})_2\text{BrCl}$. To further study this phenomenon, reactions were carried out as in Table 2-3. $\text{Pt}(\text{sal-Ph})_2\text{Br}_2$ and $\text{Pt}(\text{sal-Ph})_2\text{Cl}_2$ are formed exclusively, as shown in Figure 2-5, in a ratio corresponding to the initial ratio of CuBr_2 to CuCl_2 . Additional equivalents of CuX_2 do not increase the overall conversion of the reaction, which was complete by NMR spectroscopy in both cases.

Table 2-3. Conditions for the reaction of $\text{Pt}(\text{sal-Ph})_2$ and CuX_2 in refluxing 1:1 $\text{CH}_2\text{Cl}_2/\text{EtOH}$ for 18 h to produce $\text{Pt}(\text{sal-Ph})_2\text{X}_2$.

$\text{CuX}_2 : \text{Pt}(\text{sal-Ph})_2$	$\text{CuCl}_2 : \text{CuBr}_2$	$\text{Pt}(\text{sal-Ph})_2\text{Cl}_2 : \text{Pt}(\text{sal-Ph})_2\text{Br}_2$ ^[a]
10 : 1	1.1 : 1	1.2 : 1
20 : 1	4.2 : 1	4.5 : 1

^[a] Ratio determined from ^1H NMR of crude reaction mixture.

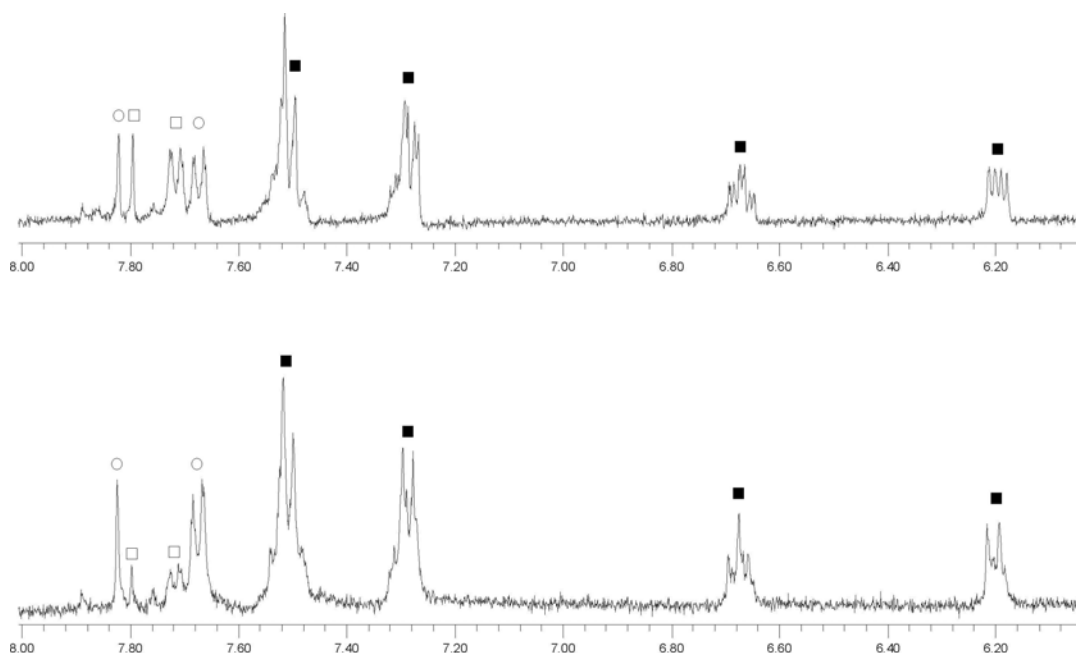


Figure 2-5. Aromatic region of the ^1H NMR spectrum for the products of the reaction of 5 $\text{CuBr}_2 + 5 \text{CuCl}_2 + \text{Pt}(\text{sal-Ph})_2$ (top) and 3.8 $\text{CuBr}_2 + 16.2 \text{CuCl}_2 + \text{Pt}(\text{sal-Ph})_2$ (bottom); $\text{Pt}(\text{sal-Ph})_2\text{Cl}_2$ resonances (\circ), $\text{Pt}(\text{sal-Ph})_2\text{Br}_2$ resonances (\square), and overlapping resonances (\blacksquare).

2.3.4 Crystal Structure of $\text{Pt}(\text{sal-}n\text{-Bu})_2\text{Cl}_2$

The structure of $\text{Pt}(\text{sal-}n\text{-Bu})_2\text{Cl}_2$ was determined by single crystal X-ray diffraction. Figure 2-6 shows the thermal ellipsoid plots of $\text{Pt}(\text{sal-}n\text{-Bu})_2\text{Cl}_2$ and the previously reported $\text{Pt}(\text{sal-}n\text{-Bu})_2$.⁵⁷ Table 2-4 gives selected bond distances and angles for $\text{Pt}(\text{sal-}n\text{-Bu})_2\text{Cl}_2$. The expected increase in the Pt-O and Pt-N bond distances upon alteration from 4-coordinate Pt^{II} to the 6-coordinate Pt^{IV} (from 1.984(3) and 2.021(3) to 1.991(4) and 2.039(4) Å, respectively) is observed. As shown in Figure 2-7, the Schiff base ligand field is non-planar in $\text{Pt}(\text{sal-}n\text{-Bu})_2\text{Cl}_2$, with both equivalent ligands tilted the same direction creating a “cup-shaped” structure. $\text{Pt}(\text{sal-}n\text{-Bu})_2$ has a more planar ligand configuration.

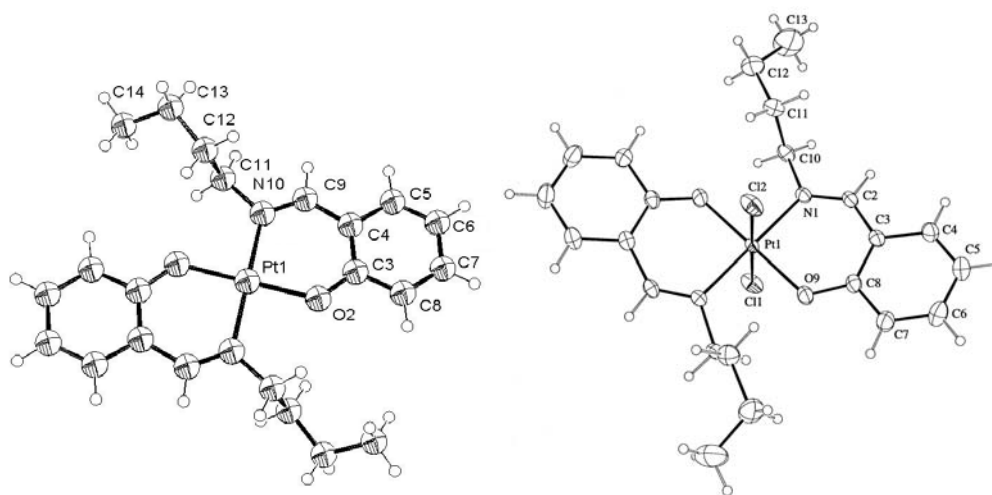


Figure 2-6. Ortep diagrams for $\text{Pt}(\text{sal-}n\text{-Bu})_2$ ⁵⁷ (left) and $\text{Pt}(\text{sal-}n\text{-Bu})_2\text{Cl}_2$ (right).

Table 2-4. Selected bond distances (Å) and angles (°) for Pt(sal-*n*-Bu)₂Cl₂.

Pt(1)-O(9)	1.991(4)	O(9)-Pt(1)-O(9a)	178.84(20)
Pt(1)-N(1)	2.039(4)	O(9)-Pt(1)-N(1)	87.50(18)
O(9)-C(8)	1.320(7)	O(9)-Pt(1)-N(1a)	92.49(18)
C(8)-C(7)	1.410(10)	O(9a)-Pt(1)-N(1a)	87.50(18)
C(7)-C(6)	1.371(10)	N(1)-Pt(1)-N(1a)	178.94(21)
C(6)-C(5)	1.392(11)	Pt(1)-O(9)-C(8)	124.4(4)
C(5)-C(4)	1.370(12)	O(9)-C(8)-C(3)	125.9(6)
C(4)-C(3)	1.408(9)	C(3)-C(2)-N(1)	128.1(5)
C(3)-C(8)	1.402(9)	C(2)-N(1)-C(10)	117.9(5)
C(3)-C(2)	1.4838(10)	Pt(1)-N(1)-C(2)	122.9(4)
C(2)-N(1)	1.277(8)	Pt(1)-N(1)-C(10)	119.2(4)
N(1)-C(10)	1.4898(8)	C(8)-C(7)-C(6)	120.8(6)
C(10)-C(11)	1.523(10)	C(8)-C(3)-C(4)	119.3(6)
C(11)-C(12)	1.524(11)	Cl(1)-Pt(1)-Cl(2)	180.0
C(12)-C(13)	1.474(13)	Cl(1)-Pt(1)-N(1)	84.47(15)
Pt(1)-Cl(1)	2.3308(24)	Cl(1)-Pt(1)-O(9)	89.42(14)
Pt(1)-Cl(2)	2.304(3)		

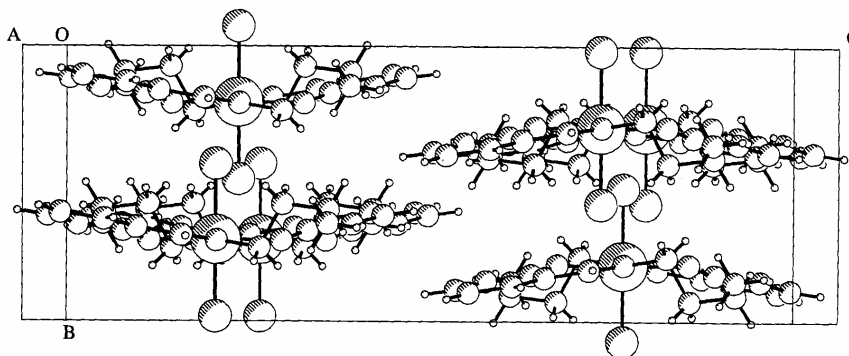


Figure 2-7. Unit cell packing of Pt(sal-*n*-Bu)₂Cl₂ showing the non-coplanar Schiff base ligand.

2.3.5 DFT Calculations

Electronic structure calculations were performed using density functional theory (DFT) to determine the relative energies of the frontier orbitals of Ni(sal-Me)₂, Pt(sal-Me)₂, and Hsal-Me. The highest occupied molecular orbital (HOMO) energies of the metal

complexes were compared to the lowest unoccupied molecular orbital (LUMO) energy calculated for $\text{Pt}(\text{sal-Me})_2\text{Cl}_2$. These calculations were performed to determine if the energy difference between the Pt^{II} and Pt^{IV} d_{z^2} orbitals was compatible with MX chain formation as is further discussed below. The d_{z^2} orbitals of a $[\text{Pt}(\text{sal-R})_2\text{-Pt}(\text{sal-R})_2\text{Cl}_2]_n$ PtX chain system are diagrammed in Figure 2-8. The methyl derivatives were utilized as a model to simplify the calculation.

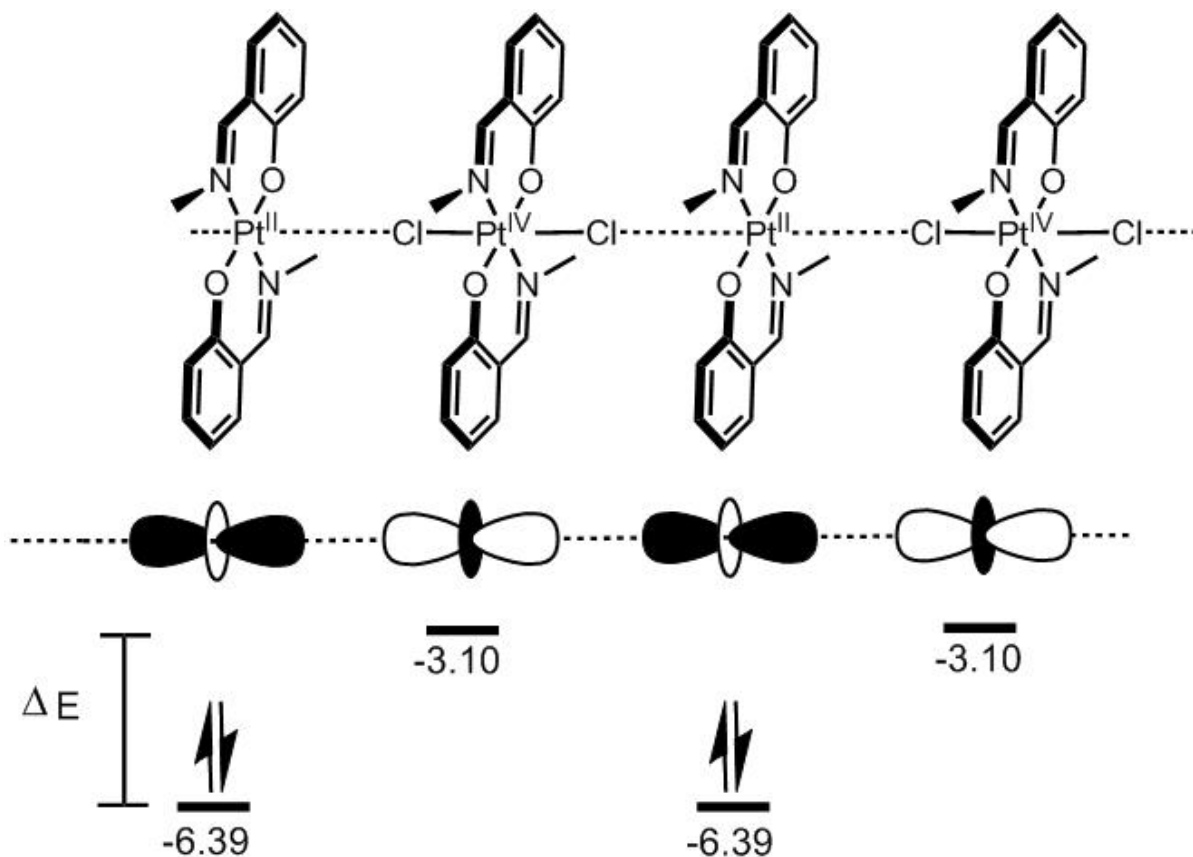


Figure 2-8. Proposed PtX chain formation from $\text{Pt}(\text{sal-Me})_2$ and $\text{Pt}(\text{sal-Me})_2\text{Cl}_2$ complexes showing the alternating filled/empty electronic structure of the d_{z^2} orbitals.

The energy minimized bond lengths and angles determined from the calculations are compared to single crystal X-ray diffraction data for similar species in Table 2-5. The minimized bond lengths and angles for $\text{Pt}(\text{sal-Me})_2$ and $\text{Pt}(\text{sal-Me})_2\text{Cl}_2$ are in good agreement

with those observed in the single crystal structures of Pt(sal-*n*-Bu)₂ and Pt(sal-*n*-Bu)₂Cl₂ (Table 2-5 **a** and **b**).⁵⁷ The calculated Pt-O and Pt-N bond distances are slightly longer (within ~0.02 Å) than observed in the crystal structures. The calculated Pt-Cl distance of 2.39 for Pt(sal-Me)₂Cl₂, which is ~0.07 Å longer than the observed Pt-Cl distance in Pt(sal-*n*-Bu)₂Cl₂, is the only substantial structural deviation between the experimental and calculated structures. The other calculated Pt bond distances were within ~0.02 Å of the observed bond lengths.

Table 2-5. Bond distances and angles for Pt(sal-Me)₂ (**a**), Pt(sal-Me)₂Cl₂ (**b**), and Ni(sal-Me)₂ (**c**) as determined by Gaussian DFT calculation compared to single crystal X-ray diffraction data for similar species.

a	Pt(sal- <i>n</i> -Bu) ₂ ^[a]	Pt(sal-Me) ₂ calculated
Pt-N (Å)	2.021(3)	2.03
Pt-O (Å)	1.984(3)	2.01
N-Pt-O, intraligand (°)	93.14(11)	92.7
N-Pt-O, interligand (°)	86.86(11)	87.3
^[a] determined by single crystal X-ray diffraction ⁵⁷		
b	Pt(sal- <i>n</i> -Bu) ₂ Cl ₂ ^[b]	Pt(sal-Me) ₂ Cl ₂ calculated
Pt-N (Å)	2.039(4)	2.05
Pt-O (Å)	1.991(4)	2.01
Pt-Cl (Å)	2.317 ^[c]	2.39
N-Pt-O, intraligand (°)	92.49(18)	93.0
N-Pt-O, interligand (°)	87.50(18)	87.7
Cl-Pt-O (°)	89.42(14)	90.0
^[b] determined by single crystal X-ray diffraction (Section 2.3.5)		
^[c] av value		
c	Ni(sal-Me) ₂ ^[d]	Ni(sal-Me) ₂ calculated
Ni-N (Å)	1.926(3)	1.95
Ni-O (Å)	1.830(2)	1.85
N-Ni-O, intraligand (°)	93.23(9)	93.0
N-Pt-O, interligand (°)	86.76(9)	87.0
^[d] determined by single crystal X-ray diffraction, data given for the Ibam polymorph, a P2 ₁ /c polymorph is also known ⁷⁴		

The gas-phase DFT calculation for Ni(sal-Me)₂ gives an energy minimized square-planar structure. Due to the possibility of both tetrahedral and square-planar geometries in crystalline Ni^{II} salicylaldimine complexes, there is some concern that a square-planar model complex may not be applicable for comparison to Ni(sal-Ph)₂. The geometries of both Ni(sal-Me)₂⁷⁴ and Ni(sal-Ph)₂⁷⁵ are nearly square-planar in the solid-state. Solution studies of Ni(sal-R)₂ complexes including Ni(sal-Ph)₂ have shown the tetrahedral/square planer equilibrium favors the square-planar conformer.^{57, 75} Even complexes like Ni(sal-*i*-Pr)₂ (tetrahedral in the solid-state⁷⁶) have a solution equilibrium favoring the square-planar geometry.^{57, 75} Ni(sal-Me)₂ is expected to be a good model of the coordination geometry of the experimentally analyzed Ni(sal-Ph)₂ complex. Good agreement is observed between the energy minimized bond distances and angles of Ni(sal-Me)₂ and those observed for single crystal structures of the complex (Table 2.5 c).

The molecular orbitals calculated for the M(sal-Me)₂ (M = Ni, Pt) complexes are shown in Figure 2-9 in comparison with the molecular orbitals calculated for the free ligand, Hsal-Me. As expected, the ligand-based HOMO and HOMO-1 orbitals of the metal complexes are at higher energy than the orbitals of the free ligand. The HOMO for Ni(sal-Me)₂ is calculated to be 0.19 eV lower in energy than the Pt(sal-Me)₂ HOMO. Consistent with the calculated square-planar geometry of the complexes, the dπ* orbitals are filled and the dσ* orbitals are vacant. Both metal complexes are calculated to have several ligand-based π* orbitals with some dπ* contribution (e.g. the HOMO and HOMO-2). The HOMO for both metal complexes is calculated to be an antibonding combination of dπ* and π* orbitals with the majority of the orbital character being π*. The composition of the HOMO is discussed in relation to the observed trends in oxidation potentials for the various M(sal-

R)₂ complexes in Section 2.3.10.

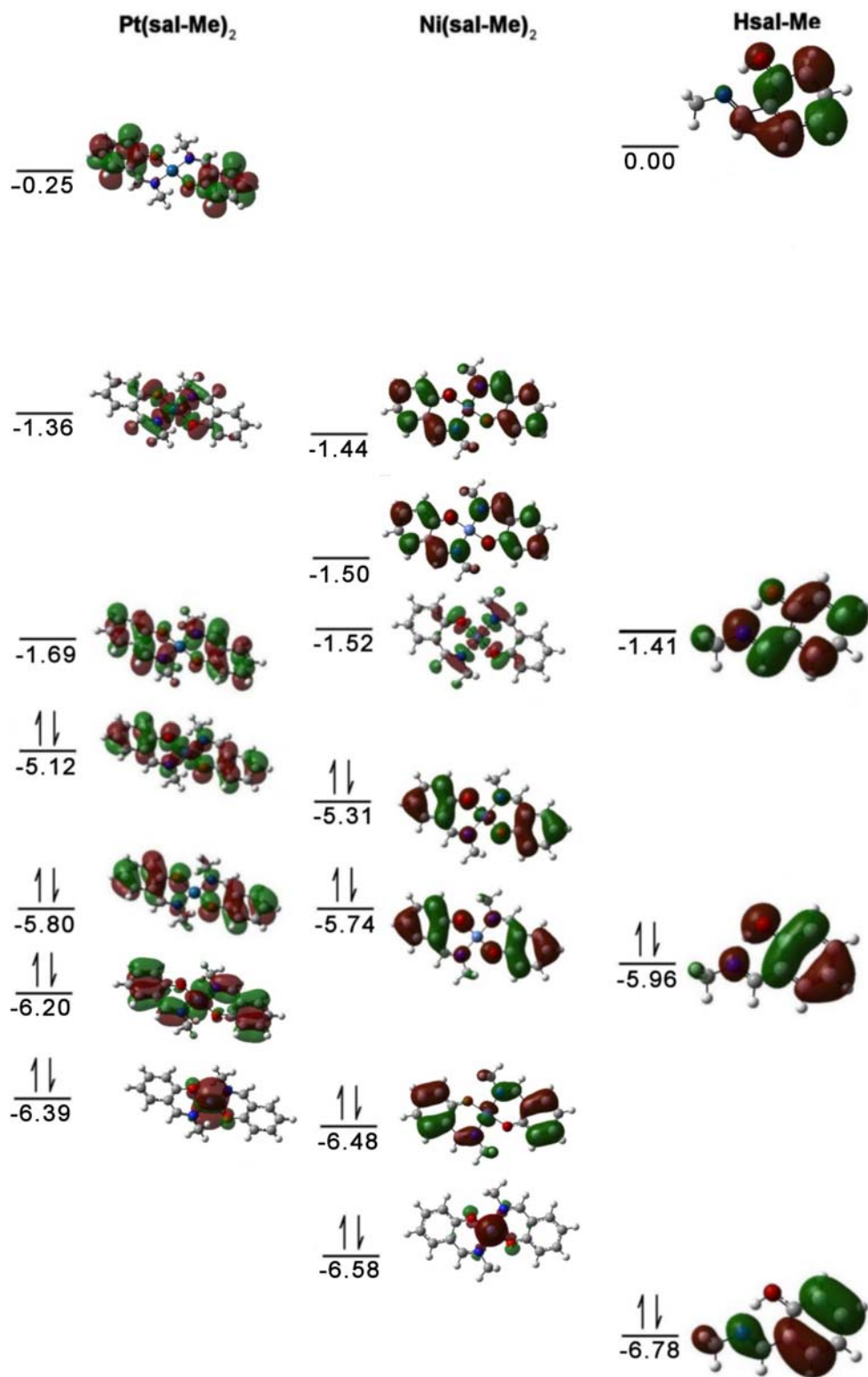


Figure 2-9. Frontier orbitals for Pt(sal-Me)₂, Ni(sal-Me)₂, and Hsal-Me determined using Gaussian DFT calculation; energies in eV.

The calculated molecular orbital energies for Pt(sal-Me)₂Cl₂ are compared with Pt(sal-Me)₂ in Figure 2-10. As discussed in Chapter 1, conduction parallel to the chain is believed to occur via a phonon assisted electron hopping mechanism involving the alternating filled and empty M^{II}/M^{IV} d_{z²} orbitals in MX chain systems.⁷⁷ The energies of the d_{z²} orbitals are calculated to be -6.39 and -3.10 eV for Pt(sal-Me)₂ and Pt(sal-Me)₂Cl₂, respectively. This 3.29 eV energy difference corresponds well to the ~1.5-2.8 eV energy for electron transfer along M^{II}⋯X-M axis determined spectroscopically for Class II MX chain complexes.^{77, 78} This correspondence is especially notable as since no correction is made for the effect of the Pt^{II}⋯Cl-Pt^{IV} interactions on the orbital energies. The Pt^{II}⋯Cl-Pt^{IV} interactions should lower the difference in d_{z²} orbital energies of the two complexes as the geometry of the Pt^{II} center is made more octahedral by the axial supramolecular interaction.

These computational results suggest that the electronic structures of the Pt(sal-R)₂ and Pt(sal-R)₂Cl₂ complexes are compatible with the known electronic characteristics of MX chain complexes. To further explore the electronic structure of these Schiff base complexes, a cyclic voltammetry study was carried out. The ligand electrochemistry was analyzed initially to help differentiate the electrochemistry of the ligand from that of the metal center in the metal complexes.

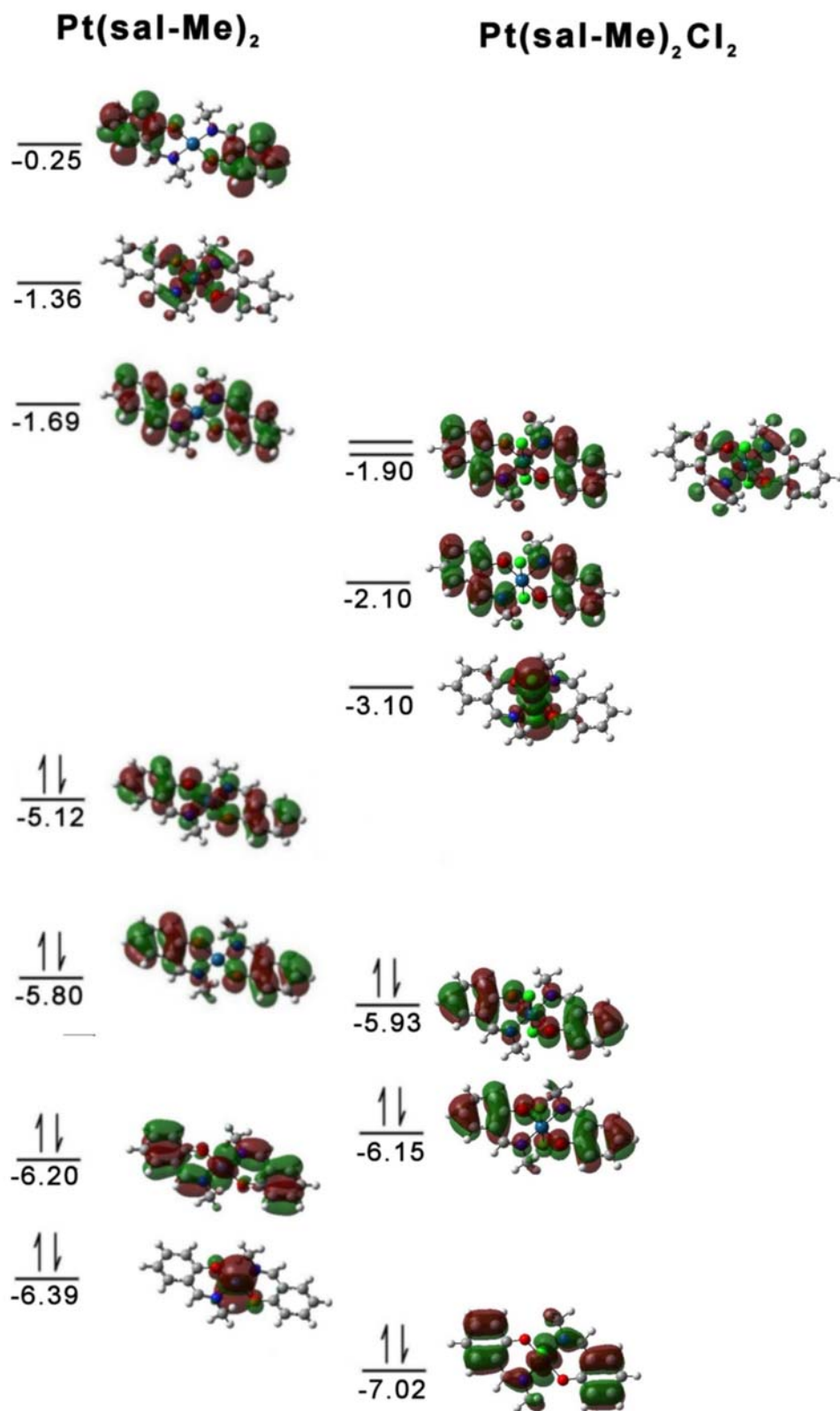


Figure 2-10. Frontier orbitals for Pt(sal-Me)₂ and Pt(sal-Me)₂Cl₂ as determined from Gaussian DFT calculations; energies in eV.

2.3.6 Cyclic Voltammetry of Hsal-*n*-Bu

The discussion of cyclic voltammetry is divided into several subsections. The electrochemical characterization of the ligand Hsal-*n*-Bu is presented in this section as a simplified system where the electro-oxidative chemistry is limited to dimerization. The cyclic voltammetry of the metal complexes and a proposed mechanism for electro-oxidative polymerization are presented in subsequent sections.

The cyclic voltammetry of Hsal-*n*-Bu was examined to enable comparison of the initial oxidation potential of the ligand to the Pt complex. In this section a general description of the voltammogram of Hsal-*n*-Bu is given. A review of the mechanism for electro-dimerization of aromatic Schiff bases as developed by Ohmori and coworkers⁷⁹ is presented in the next section, and the voltammetry of Hsal-*n*-Bu is discussed in light of the mechanism.

The voltammetric experiments for Hsal-*n*-Bu were conducted in acetonitrile, and the potential was initially scanned oxidatively. The voltammogram for one potential cycle is shown in Figure 2-11. Three irreversible oxidation waves are observed and are labeled **I**, **II**, and **III**. The initial oxidation of Hsal-*n*-Bu observed at 0.78 V at a scan rate of 1 V/s (**I**, all potentials in V vs Cp₂Fe^{0/+}) is in good agreement with the previously reported 0.74 V initial oxidation potential of Hsal-*t*-Bu.⁷⁹ Oxidation **I** (0.71 V at 100 mV/s) is slightly reversible if the voltage is reversed immediately past the oxidation potential as shown in Figure 2-12, with an $i_{p,c}/i_{p,a}$ of approximately 0.14 at 100 mV/s. The corresponding reduction wave is marked **IV** in the figure. The redox couple becomes more reversible at faster scan rates, but complete reversibility is not obtained, even at 1 V/s. The small waves, **V-VII**, in Figure 2-12 are proposed to be due to surface absorbed species produced in previous scans (vide infra).

Repeated potential scans do not result in an increase in the current for these surface redox waves.

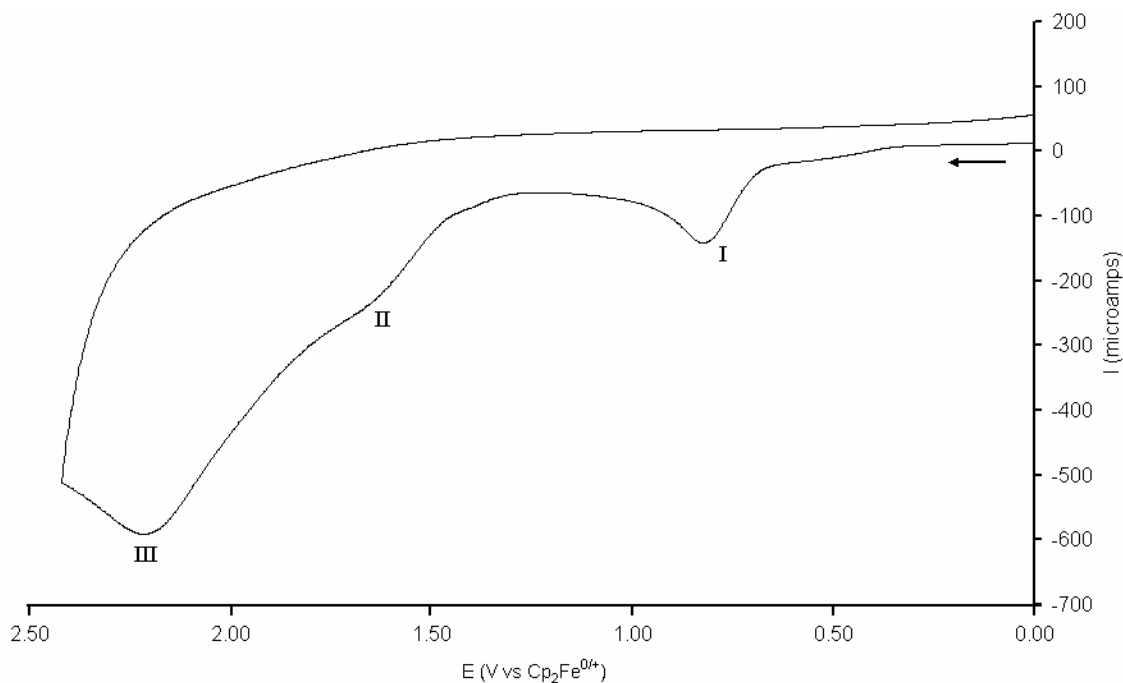


Figure 2-11. Cyclic voltammogram of 2.8 mM Hsal-*n*-Bu in acetonitrile/0.1 M TBATFB; sweep rate = 1 V/s, potentials vs $\text{Cp}_2\text{Fe}^{0/+}$.

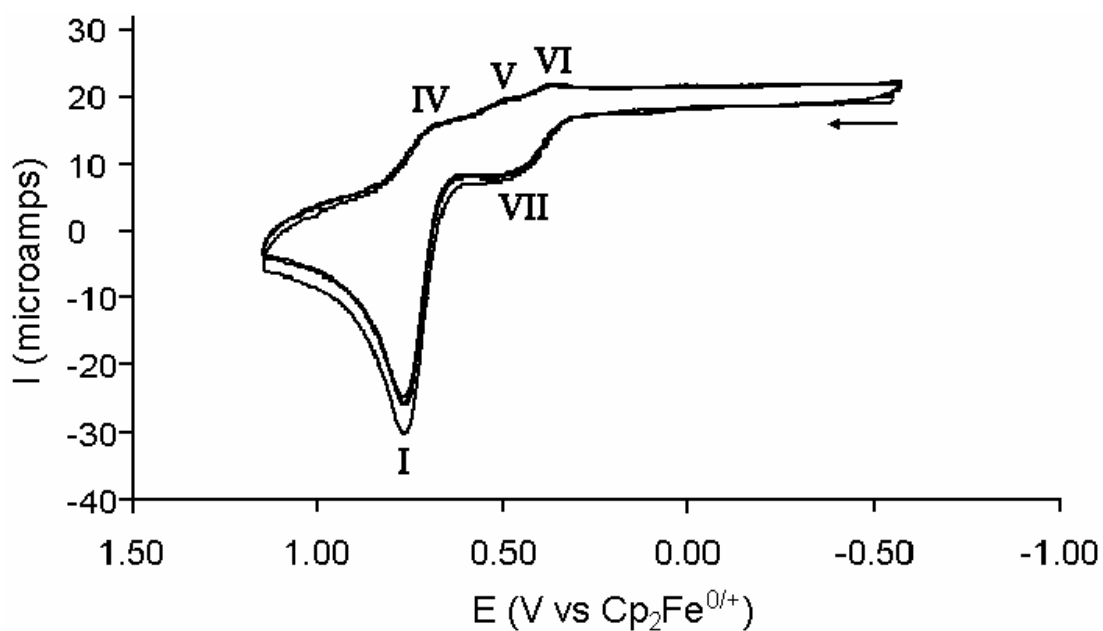
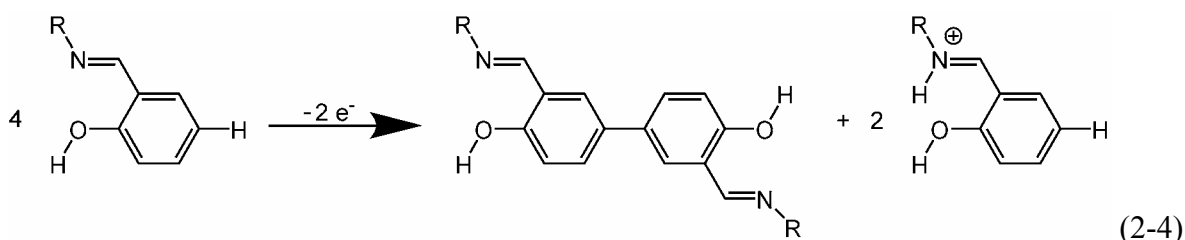


Figure 2-12. Cyclic voltammogram of 2.8 mM Hsal-*n*-Bu in acetonitrile/0.1 M TBATFB; sweep rate = 100 mV/s, potentials vs $\text{Cp}_2\text{Fe}^{0/+}$, three cycles shown.

A second oxidation wave is observed at 1.65 V (**II** in Figure 2-11) in the voltammogram of Hsal-*n*-Bu. Due to the proximity of **II** to the third oxidation wave (**III**), the reversibility of **II** was not probed. Oxidation **III** is either an oxidation of the salicylaldehyde dimer or electrolyte decomposition. Further analysis was not made due to the proximity of the electrolyte decomposition potential to **III**.

2.3.7 Mechanism for Electrodimerization of Hsal-*n*-Bu

Ohmori and coworkers previously proposed a series of ECE reactions to account for the formation of phenol dimers as a result of irreversibly oxidizing (E)-2-((alkylamino)methyl)-6-methoxyphenols.⁷⁹ The same electro-oxidative coupling chemistry is observed for Hsal-*n*-Bu according to the overall reaction in eq 2-4. The cyclic voltammetry of the ligand is simpler than that of the metal complex. The mechanism and voltammetry of oxidative dimerization may be explored without the complicating polymerization observed for the metal complexes.



The dimers resulting from the electrochemical oxidation deposit on the electrode, leading to surface oxidation and reduction waves in subsequent voltammetric cycles.

The previous work by Ohmori and coworkers and the cyclic voltammetry of Hsal-*n*-Bu may be utilized to propose a mechanism for the oxidative dimerization of Hsal-*n*-Bu as shown in Figure 2-8. The initial oxidation, **I**, is followed by a series of chemical reactions that lead to dimerization at the position *para* to the -OH group. The increased

electrophilicity of the *ortho*- and *para*-carbons (**B**, Figure 2-13) is a result of electron withdrawing effect of the cation. Although the *ortho*-carbon is expected to be activated by the electron-withdrawing effect, no evidence for *ortho-para* or *ortho-ortho* coupling has been observed either with $M(\text{sal-R})_2$ complexes or with the free ligands.^{79, 80, 81} The oxidative coupling mechanism requires the ligand to act as a base and deprotonate the dimer forming $\text{H}_2\text{sal-}n\text{-Bu}^+$ (**D**, Figure 2-13). The second oxidation wave (**II**) in the Hsal-*n*-Bu voltammogram is assigned to the oxidation of a dimer. It is not known at this time if the dimer is protonated; the neutral dimer is shown in Figure 2-13.

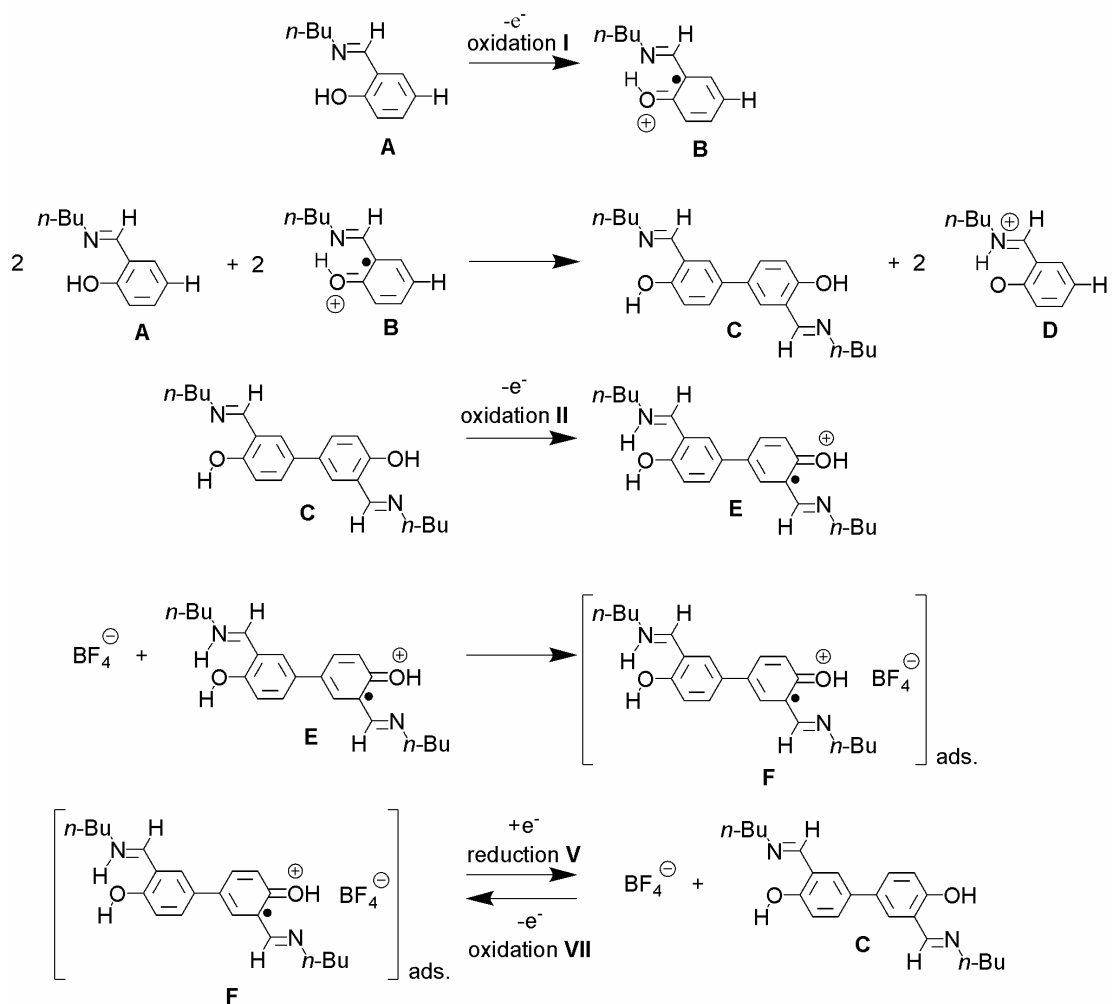


Figure 2-13. Proposed mechanism for the electrodimersization of Hsal-*n*-Bu, as extrapolated from Ohmori et al.⁷⁹

The main surface adsorbed species is the cationic radical dimer (**F**, Figure 2-13), which gives reduction and oxidation waves (**V** and **VII** in Figure 2-12) at the same potential. Because further polymerization does not occur, there is no increase in the current for **V** and **VII** over multiple potential cycles. The reductive electrochemistry is made more complicated by the number of different radical species (**B**, **E**, and protonated forms thereof, Figure 2-13), which could all potentially adsorb to the electrode. Indeed, this may explain the small reduction wave (**VI**) observed in Figure 2-12. Further investigation is required to definitively identify all surface adsorbed species.

The electrochemistry of Hsal-*n*-Bu provides a simplified system for examining the oxidative coupling chemistry that produces the polymeric linkages in the electropolymerization of the metal complexes. The coupling mechanism of loss of two electrons and two protons is also expected to occur for the metal complexes.

2.3.8 Cyclic Voltammetry of Ni(sal-Ph)₂

Prompted by the desire to determine which metal complexes would potentially give the most conductive MX chain system, the goal of the voltammetric analysis was to determine the initial oxidation potentials of the metal complexes. The one-dimensional electron hopping mechanism of conduction requires oxidation of a Pt^{II} site by an adjacent Pt^{IV} site. Pt^{II} complexes lower oxidation potentials are expected to give more facile movement of electrons along the MX chain. The oxidative chemistry of the ligand proved to be a complicating factor, because it gives rise to irreversible oxidations and fouling of the electrode.

This section gives a general overview of the M(sal-R)₂ and analogous complexes

previously studied by other groups. The cyclic voltammetry of Ni(sal-Ph)₂ is presented as an example of M(sal-R)₂ electrochemistry. Then, a possible mechanism for the electro-oxidative polymerization is discussed. Finally, trends in the oxidation and reduction potentials observed for various metal complexes are presented.

Relatively few Ni complexes with bidentate salicylaldimine ligands have been studied electrochemically.^{54, 82, 83, 84} The naphthyl Schiff base derivatives have been examined as have Co and Cu salicylaldimine complexes.^{82, 85, 86, 87, 88} The electropolymerization of Pt(sal-R)₂, and the effects of the imine functionalization on oxidation potential have not been analyzed previously. The electrochemistry of Ni(sal-Ph)₂ has not been previously reported.

Due to the greater separation between oxidative waves and the resulting simplification of the voltammogram, the cyclic voltammetry of Ni(sal-Ph)₂ will be discussed as a representative example of the M(sal-R)₂ complexes. The limited solubilities of the M(sal-R)₂ complexes in other solvents resulted in the use of methylene chloride as the electrochemical solvent. Figure 2-14 shows the voltammogram for Ni(sal-Ph)₂ when the potential is cycled from -1 to 1 V (vs Cp₂Fe^{0/+}) six times. The initial sweep (shown as the thickest line in Figure 2-14) has two irreversible oxidative waves (**A** and **B**). Under experimental conditions, the initial oxidation step is essentially irreversible for Ni(sal-Ph)₂, even at 1 V/s when the voltage is reversed just past the oxidation potential. The reductive waves (**C** and **D**) on the return sweep occur with significantly reduced current intensity compared to the oxidative waves. Subsequent cycles (progressively thinner lines in Figure 2-14) show two surface redox couples (**E/D** and **F/C**) and a decrease in the oxidative current for **A** and **B**.

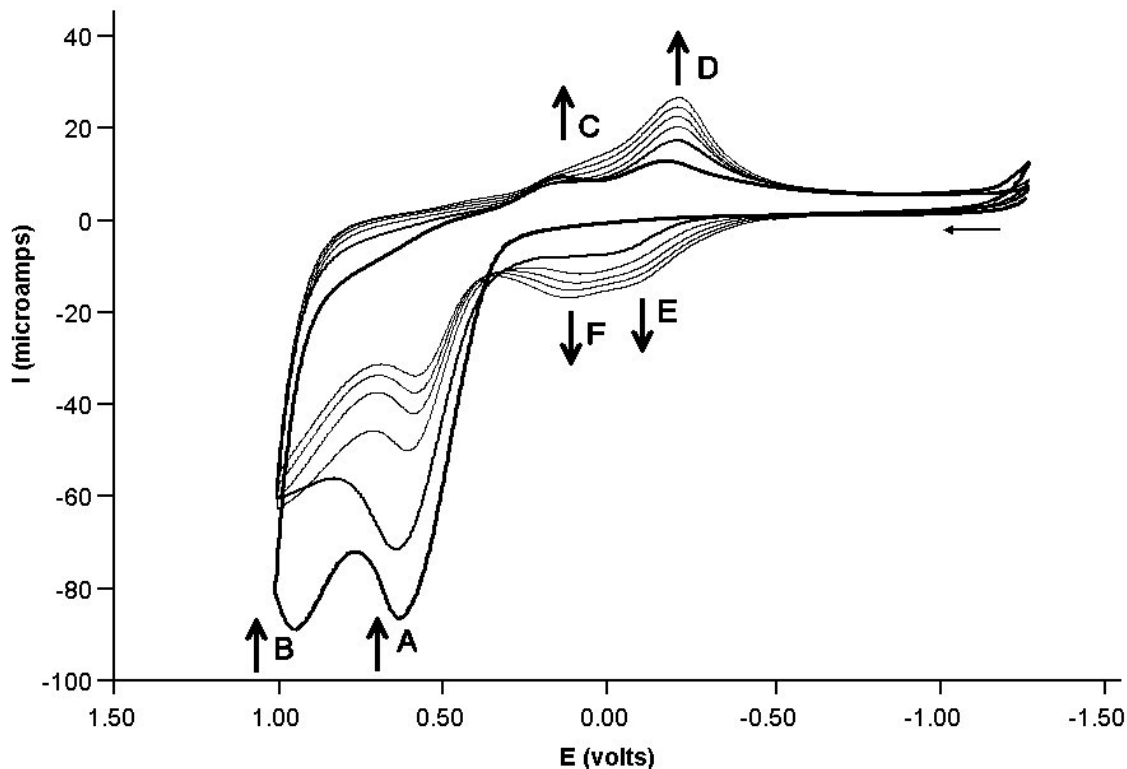


Figure 2-14. Cyclic voltammogram of 4.2 mM Ni(sal-Ph)₂ in CH₂Cl₂/0.1 M TBATFB; sweep rate = 200 mV/s, potentials vs Cp₂Fe^{0/+}; six cycles shown; initial oxidation of Ni(sal-Ph)₂ (A), oxidation of dimer (B), reduction of surface adsorbed polymer (C and D), and oxidation of surface adsorbed polymer (E and F).

Figure 2-15 shows the voltammogram for Pt(sal-*n*-Bu)₂ in CH₂Cl₂ after one oxidative/reductive cycle. Three oxidations are observed for Pt(sal-*n*-Bu)₂ between 0.5 and 1.5 V. The proximity of the first and second oxidation waves in the Pt^{II} complexes (A and B, Figure 2-15) prevented analysis of the reversibility of the initial oxidation. The proximity of the third oxidation wave (cut off in the figure) made analysis of the electropolymerization chemistry difficult, due to a decrease in the electroactivity of the film when the potential is scanned past the potential of the third oxidation. Overoxidation of the polymer film irreversibly produces ketone moieties, which has been observed by several groups to reduce the electroactivity of the polymer film.⁵⁶ For these reasons, extensive analysis of repeated

voltammetric cycles was not made for the Pt complexes.

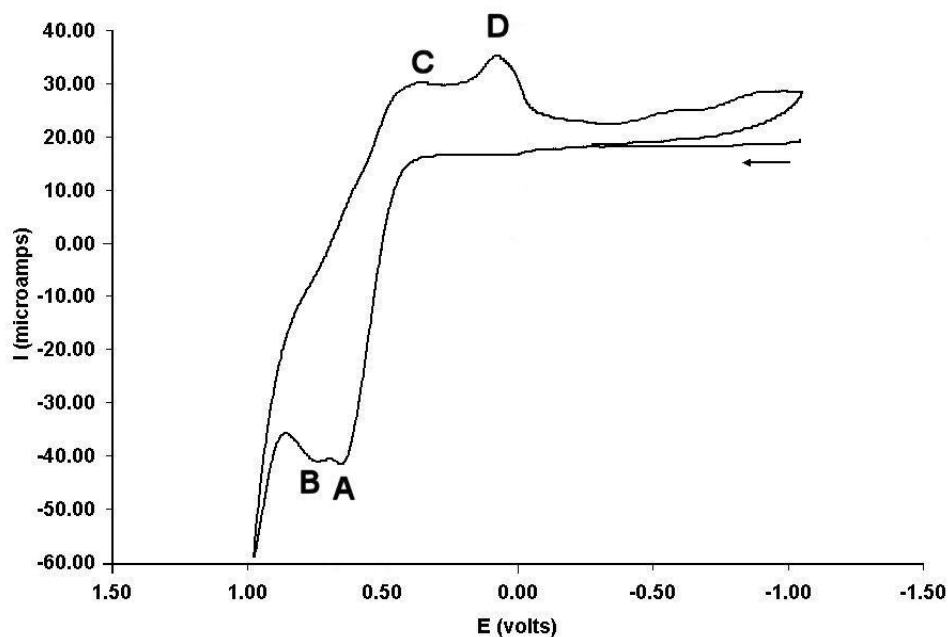


Figure 2-15. Cyclic voltammogram of Pt(sal-*n*-Bu)₂ in CH₂Cl₂/0.1 M TBATFB; sweep rate = 100 mV/s, potentials vs Cp₂Fe^{0/+}; initial oxidation of Pt(sal-*n*-Bu)₂ (A), oxidation of dimer (B), reduction of surface adsorbed polymer (C and D).

2.3.9 Mechanism for the Electropolymerization of M(sal-R)₂

Several groups have characterized the films produced from the electropolymerization of aromatic Schiff base complexes. Goldsby and coworkers⁸⁹ first proposed oxidative *para-para* phenol coupling for the surface polymerization of Ni(salen), and the composition of the resulting film was studied both by Vilas-Boas and coworkers⁹⁰ and by Audebert and coworkers.^{81, 91, 92} From this research, and in conjunction with the mechanism for electro-oxidative coupling of Schiff bases as put forth by Ohmori and coworkers,⁷⁹ a mechanism for the electropolymerization is given in two parts. The proposed mechanism for formation of a metal complex dimer, analogous to the ligand dimer oxidative coupling Hsal-*n*-Bu, is given in Figure 2-16 and Figure 2-17 gives the proposed polymerization cycle.

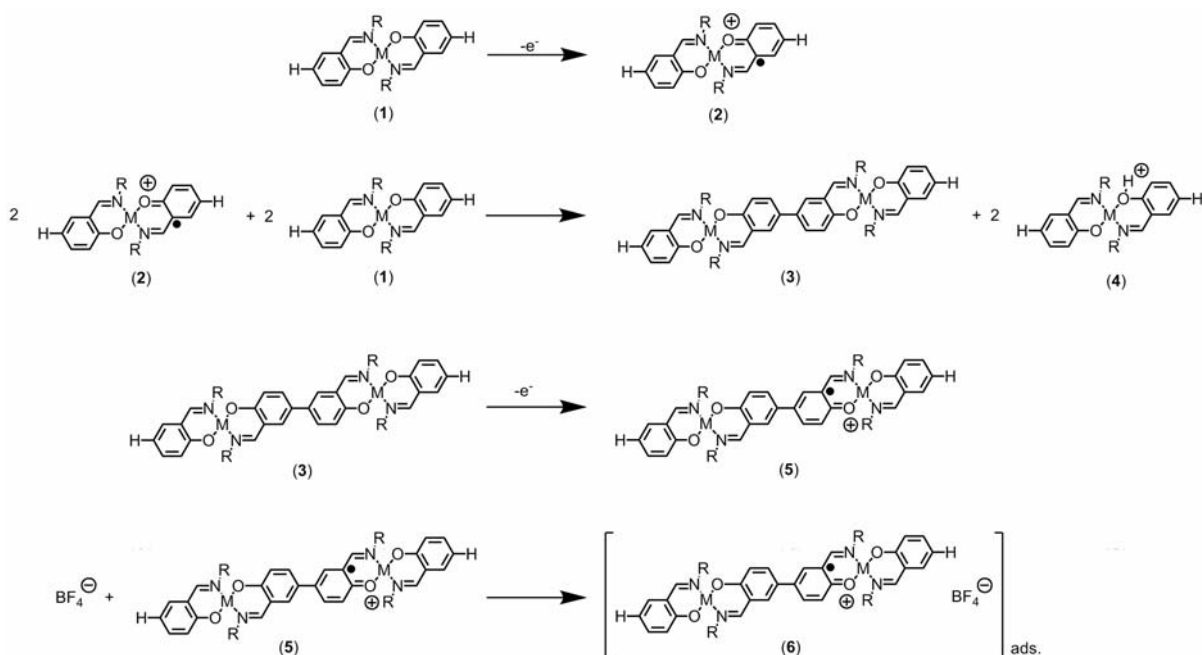


Figure 2-16. Proposed mechanism for the electro-oxidative dimerization of $\text{M}(\text{sal-R})_2$ complexes. For most species several resonance structures are possible.

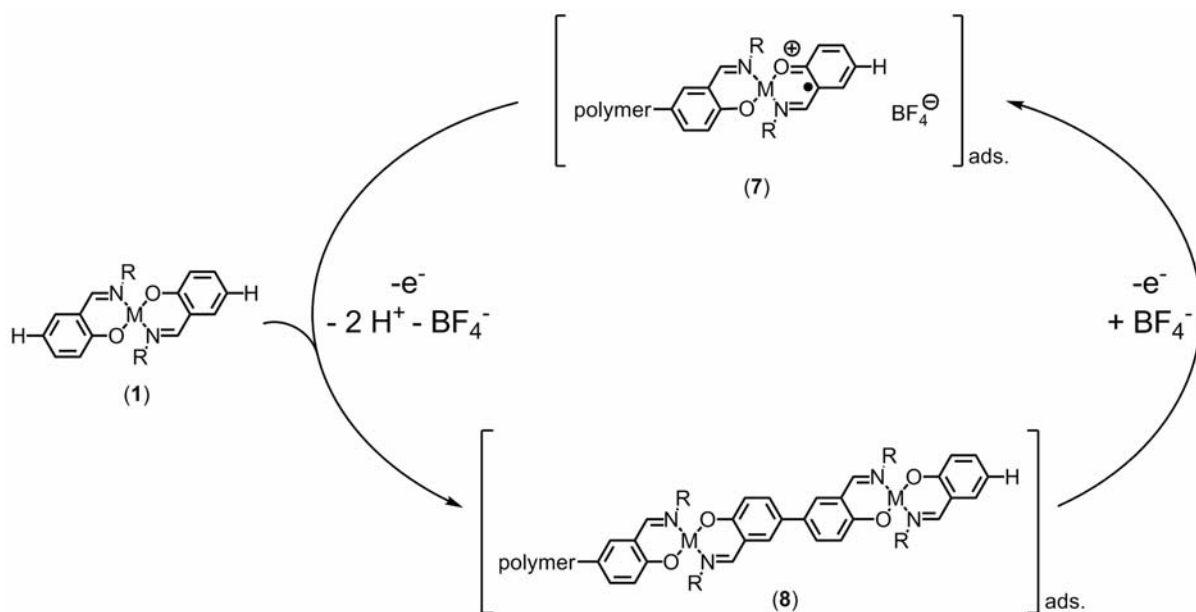


Figure 2-17. Proposed mechanism for the oxidative polymerization of $\text{M}(\text{sal-R})_2$ at an electrode surface. For most species several resonance structures are possible. Electroactivity is expected at more than just the polymer ends, but only those processes contributing to chain growth are shown.

The coupling chemistry reflected in the first cycle of the Ni(sal-Ph)₂ voltammogram is analogous to the oxidative coupling chemistry observed for Hsal-*n*-Bu. The initial oxidation of M(sal-R)₂ could potentially occur at the ligand or at the metal center, but the thermodynamic product is a ligand-based radical cation for most cases studied. In Ni(salen) and its derivatives, the Ni^{III} state can be stabilized by good donor solvents (e.g. pyridine, DMSO, DMF), preventing polymerization. In poor donor solvents, such as methylene chloride utilized in this study, the ligand-based radical cation is observed.^{80, 89, 93} The ligand-based radical (**2**, Figure 2-16) is the thermodynamic product of the oxidation in methylene chloride and is shown in the first step of the mechanism.

The cyclic voltammetry of Ni(sal-Ph)₂ can be explained utilizing the mechanism in Figure 2-16. The first oxidation (**A**, Figure 2-14) corresponds to the electrochemical oxidations of Ni(sal-Ph)₂ (**1**→**2**, Figure 2-16). The second electrochemical oxidation in the Ni(sal-Ph)₂ voltammogram occurs at 0.87 V and corresponds to the oxidation a dimer to a dimer radical (**3**→**5**). The second oxidation is suspected to be ligand based, due to the 0.87 V oxidation potential of the Ni species compared to the ~1 V potential of the Pt analogue. The Ni(sal-Ph)₂ species is expected to have at least some Ni^{III}-L character, which would make ligand based oxidation more facile than in a Pt-L⁺ species.

A two electron, two proton process gives oxidative coupling to produce a dimer (**3**, Figure 2-16) during the initial oxidative sweep. It is not known at this time where the protonation equilibrium for **3** lies, so the second oxidation wave (**B**, Figure 2-14) may be for a charged species. As the radical species (**6**) adsorbs onto the electrode surface, a robust film forms, which thickens as the polymer chains grow during repeated potential cycles according to the chain growth mechanism shown in Figure 2-17.

The surface polymer contributes to more complicated subsequent voltammetric cycles. The growth of the polymer at the surface results in surface redox waves after the first oxidative scan. Two new oxidation waves (**E** and **F**, Figure 2-14) appear at less positive potentials than the initial oxidation (**A**). These oxidation waves correspond to oxidation of multiple moieties in the polymer chain, not just the growing chain ends. While a variety of species, including Ni(salen), demonstrate multiple oxidations attributable to surface polymerized species, most only exhibit one reduction for the surface adsorbed species.^{51, 80, 89} However, as can be seen from the results with Ni(salen), the absence or presence of multiple oxidation peaks depends on the experimental conditions and the nature of the fairly uncontrolled polymerization, as well as the initial species polymerized.^{80, 89, 90, 94, 95, 96} For this reason, the multiple polymerization redox couples of Ni(sal-Ph)₂ and other complexes analyzed are proposed to be due to various moieties in different environments (e.g. end or middle of polymer, straight or twisted segments).⁹³

The conductance properties of Ni(salen) films have been studied extensively, and it has been shown by ESR and in situ IR spectroscopies that in the oxidized chain (**7**, Figure 2-17), the charge carriers include both a phenyl-based cation radical and a radical with a metal contribution delocalized over the Ni-O moiety.⁹⁰ The coulometric experiments of Vilas-Boas and coworkers demonstrated an average of two positive charges are delocalized over three monomers at potentials positive of the second oxidation for Ni(salen). Similar experiments with the 1,1,2,2-tetramethyl-1,2-ethylenediimine analogue showed one positive charge delocalized over each monomer, consistent with the mechanism shown.⁹⁷

2.3.10 Redox Potentials and Diffusion Coefficients of $M(\text{sal-R})_2$

Having examined the electrochemistry of a representative example in detail, general trends may be extracted by examining data for a variety of metal complexes. The oxidation and reduction potentials for various metal salicylaldimine complexes are given in Table 2-5. In the table, E_p values are compared rather than $E_{1/2}$ due to the irreversibility of many steps. As the waves are relatively sharp and uniform (except for **F**), E_p should give a good indication of relative redox potentials. This method has been utilized previously to study Ni(salen) and its derivatives.⁸⁹

Table 2-6. Oxidation ($E_{p,o}$) and reduction ($E_{p,r}$) potentials (V vs $\text{Cp}_2\text{Fe}^{0/+}$) for various metal salicylaldimine complexes, $\text{CH}_2\text{Cl}_2/0.1 \text{ M TBATFB}$; sweep rate 200 mV/s; 1.5 mM Pt(sal-*n*-Dec)₂, 6.0 mM Ni(sal-Ph)₂, 0.57 mM Pt(sal-*n*-Ph)₂, 2.2 mM Pt(sal-*n*-Bu)₂, redox waves labeled as in Figure 2-14.

Species	First Cycle				Second Cycle
	A $E_{p,o}$ (V)	B $E_{p,o}$ (V)	C $E_{p,r}$ (V)	D $E_{p,r}$ (V)	F $E_{p,o}$ (V)
Pt(sal-Ph) ₂	0.61	1 ^[a]	0.48	-0.26	0.12
Ni(sal-Ph) ₂	0.59	0.87	0.15	-0.20	0.12
Pt(sal- <i>n</i> -Bu) ₂	0.66	0.75	0.34	0.066	0.32
Pt(sal- <i>n</i> -Dec) ₂	0.65	0.74	0.43	0.15	0.25

^[a] estimate of a very broad wave

Previous work with a variety of metal Schiff base complexes has assigned the initial site of oxidation to the metal, which is followed by an intramolecular electron transfer from the ligand to the metal to give the ligand-based cation radical responsible for the polymerization chemistry.^{55, 80, 89} Analysis of planar Ni^{II} chelate complexes by various groups has shown the initial oxidation is metal centered.⁹⁶ Kotovoca and Sima showed that initial oxidation potentials for Ni and Cu complexes of substituted N,N'-ethylenebis(monooxo-R-acetoimines) demonstrated both ligand and metal dependence,

supporting oxidation from an orbital with metal d-character.⁹⁸ The 0.73 V initial oxidation potential of Hsal-*n*-Bu (200 mV/s) is more positive than the initial oxidation potentials of the complexes. This 0.73 V oxidation potential is consistent with metal complex oxidation from an orbital with d-character, and the relative energies calculated for the Hsal-Me and M(sal-Me)₂ HOMOs. The oxidation of Ni(sal-Ph)₂ occurs at lower potentials than the Pt analogue. However, the 0.59 V potential for Ni(sal-Ph)₂ and the 0.61 V potential of Pt(sal-Ph)₂ are more similar than would normally be expected for metal based oxidation.

The molecular orbital calculations present a reasonable explanation for the observed similarity in oxidation potentials. The HOMO Ni(sal-Me)₂ is calculated to have a 0.19 eV lower energy than the HOMO of Pt(sal-Me)₂ (Figure 2-8). In both cases the HOMO has both metal d π^* and ligand π^* character as diagrammed in Figure 2-18. The dominant character of the orbital is ligand π^* and the similar orbital energies correlate well with the observed similarity of the oxidation potentials for Pt(sal-Ph)₂ and Ni(sal-Ph)₂ (0.61 and 0.59 V, respectively). The observed less positive oxidation potential of Ni(sal-Ph)₂ is opposite of the potentials expected based on the calculated orbital energies. The relatively slight deviation from the modeled orbital energies may be due to the square-planar/tetrahedral equilibrium of Ni(sal-Ph)₂ in non-polar solvents.⁷⁵

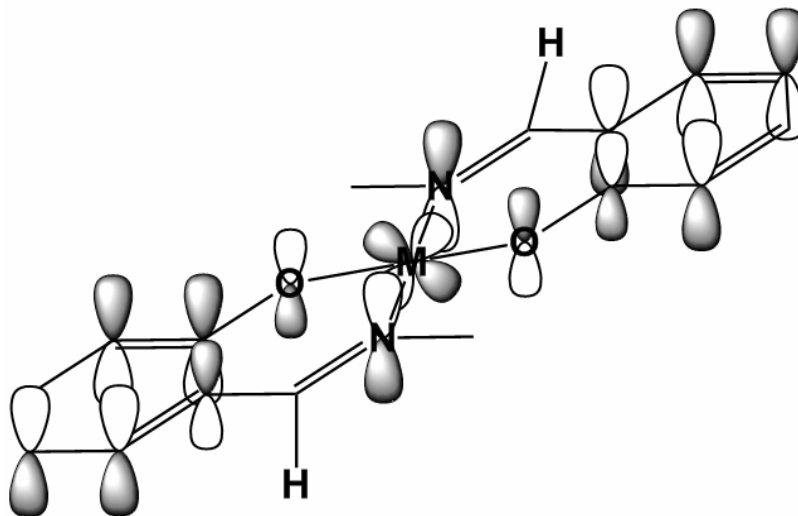


Figure 2-18. Diagram of the HOMO for Pt(sal-Me)₂ and Ni(sal-Me)₂ as determined from Gaussian DFT calculations.

The initial oxidation potential is also affected by the substituent on the imine ligand. The HOMO has a significant nitrogen component, which is consistent with this observation. The *n*-Dec and *n*-Bu complexes give similar initial oxidation potentials (0.65 and 0.66 V respectively), while Pt(sal-Ph)₂ oxidizes at 0.61 V. The second oxidations also occur at lower potentials for the metal complexes than for Hsal-*n*-Bu. A comparison of the second oxidation potentials also demonstrates a dependence of the oxidation potential on the both metal center and the imine substituent. The alkyl substituted species undergo a second oxidation at similar potentials, 0.75 and 0.74 V for Pt(sal-*n*-Bu)₂ and Pt(sal-*n*-Dec)₂ respectively. The aromatic species oxidize at more positive potentials, consistent with better aromatic stabilization of the phenyl substituted species (**3**, Figure 2-16).

The diffusion coefficients for the ligand Hsal-*n*-Bu and the metal complexes were determined to explore the molecular properties affecting the cyclic voltammetry. By measuring the peak currents as a function of scan rate, diffusion coefficients can be estimated using the Randles-Sevcik eq (2-5) for irreversible oxidations 25 °C, where *n* is the number of

electrons in the process, A is the electrode area, C° is the bulk concentration of analyte, and v is the scan rate.

$$i_p = 2.99 \times 10^5 n (\alpha n)^{1/2} A D^{1/2} C^\circ v^{1/2} \quad (2-5)$$

The transfer coefficient, α , is a measure of the symmetry barrier for electron transfer. As α is normally between 0.3 and 0.7, it will be estimated at 0.5 for this work. The values for $D^{1/2}C$ can then be determined from the slope of a plot of i_p vs $2.99 \times 10^5 A v^{1/2} C^\circ$ as shown in Figure 2-19 for Pt(sal-*n*-Bu)₂. Due to instrumental limitations in determination of the i_p values, the diffusion coefficients given here have a large degree of error. Thus, the values in Table 2-6 should be taken as informative only of the order of magnitude expected. Ni(salen) and Cu(salen) derivatives were previously determined to have diffusion coefficients of 4.2-6.6 $\times 10^{-6}$ cm²/s in DMF.⁹⁹

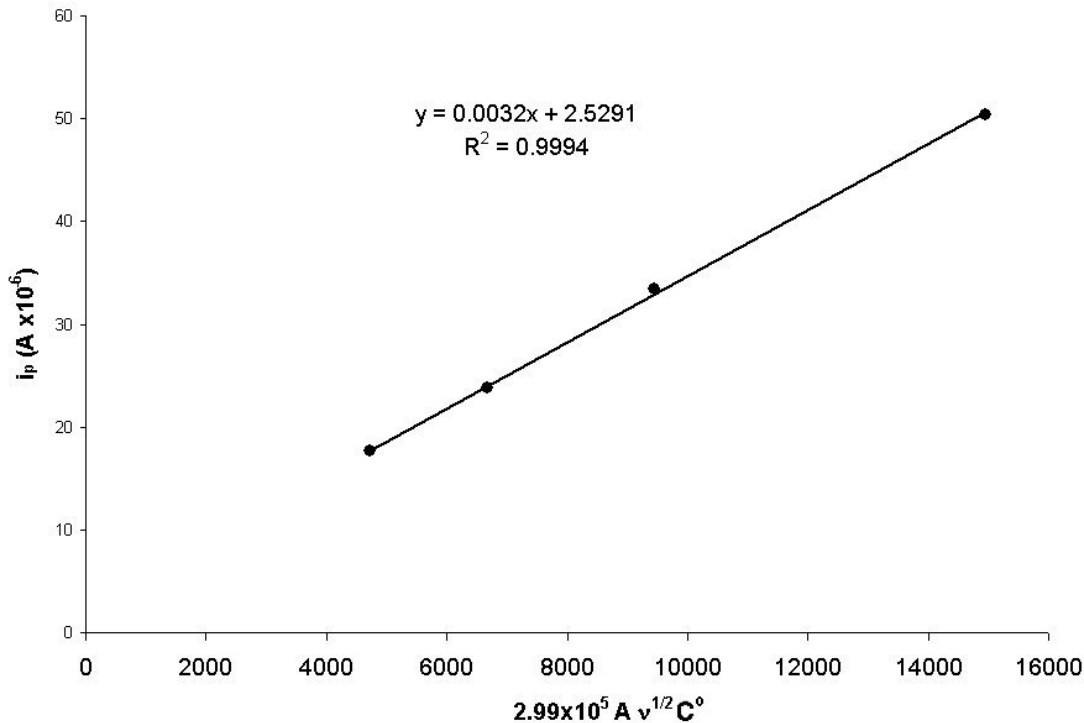


Figure 2-19. Randles-Sevcik plot for Pt(sal-*n*-Bu)₂. From the slope, the diffusion coefficient is determined to be 1.1×10^{-6} cm² s⁻¹.

Table 2-7. Diffusion coefficients for various species determined using the initial oxidation wave for each species.

Species	Solvent/Electrolyte	$D^{1/2}C$ (mol s ^{-1/2} cm ⁻²)	D (cm ² s ⁻¹)
Hsal- <i>n</i> -Bu	MeCN/0.1 M TBATFB	4.4×10^{-9}	4.9×10^{-6}
Pt(sal- <i>n</i> -Bu) ₂	MeCN/0.1 M TBATFB	4.5×10^{-9}	1.1×10^{-6}
Pt(sal- <i>n</i> -Dec) ₂	CH ₂ Cl ₂ /0.1 M TBATFB	4.1×10^{-9}	1.5×10^{-6}
Ni(sal-Ph) ₂	CH ₂ Cl ₂ /0.1 M TBATFB	10.6×10^{-9}	6.5×10^{-6}

2.3.11 MX Chain Self Assembly

Self-assembly of MX chains can potentially be initiated by several methods, as was discussed in Chapter 1. Controlled partial oxidation of Pt(sal-*n*-Bu)₂ by CuCl₂ in CH₂Cl₂ was attempted. However, this route was unsuccessful due to the tendency of Pt(sal-*n*-Bu)₂Cl₂ to precipitate from solution preventing co-crystallization. For this reason, Pt(sal-*n*-Bu)₂ and Pt(sal-*n*-Bu)₂Cl₂ were synthesized separately and then combined in stoichiometric amounts using a variety of recrystallization methods. In all cases, Pt(sal-*n*-Bu)₂Cl₂ precipitated first, or amorphous material came out of solution. There is no evidence, either by UV-vis or NMR spectroscopies, of initial formation of MX chains in solution.

Pt(hfac)₂ and Pt(acac)₂ (hfac⁻ = hexafluoroacetylacetonate, acac⁻ = acetylacetonate) were studied as alternative sources of Pt^{II}. As neutral species, they have solubilities compatible with Pt(sal-*n*-Bu)₂Cl₂. Additionally, the acetylacetonate ligands are more electron-withdrawing than the deprotonated salicylaldimines, potentially making the Pt^{II} center in a these complexes a better acceptor of electron donation from the bridging chlorines. However, none of these systems were amenable to crystallization, and no MX chain formation in solution was observed by NMR or UV-vis spectroscopies.

2.4 Conclusions

Though ultimately not useful for preparation of MX chain systems, new Pt(sal-R)₂X₂ complexes were prepared and characterized, and the single crystal structure of Pt(sal-*n*-Bu)₂Cl₂ was determined. The electropolymerization of Pt(sal-R)₂ produced previously uncharacterized surface adsorbed polymers. These polymers were compared to Ni(sal-Ph)₂ polymers. Aromatic imine substituents were found to lead to less positive initial oxidation potentials than aliphatic substituents. The Ni and Pt complexes oxidized at surprisingly similar potentials, consistent with the ligand π^* and metal $d\pi^*$ character determined by DFT calculations for the HOMO of similar species.

The next chapter discusses the proposed solution to the inability to form MX chain interactions with these Schiff base complexes. Ligands which provide a secondary ordering interaction (e.g. hydrophobic interactions) compatible with linear supramolecular ordering of the metal centers are expected to be more amenable to both MX chain formation and analysis of other axial ordering forces. Further research utilizing long chain dialkyl-2,2'-bipyridine-4,4'-dicarboxylate ligands is expected to give better secondary support to axial interactions in both Pt^{II} and Pt^{IV} complexes.

CHAPTER III

COMPARISON OF THE PHASE BEHAVIOR OF DIALKYL-2,2'- BIPYRIDINE-4,4'-DICARBOXYLATO COMPLEXES OF Pt^{II}, Pt^{IV}, Re^I, AND Cd^{II}: THE EFFECTS OF AXIAL INTERACTIONS ON THE FORMATION OF MESOPHASES

3.1 Introduction

3.1.1 Secondary Interactions in MX Chain Systems and New System Design

The previous chapter demonstrated that while the Pt(sal-R)₂ and Pt(sal-R)₂Cl₂ complexes are compatible with the chemical characteristics of the existing neutral MX chain systems, MX chains are not observed for those species. In MX chain systems of charged metal complexes there is often a secondary interaction, such as hydrogen bonding between the ligand and counterion (Figure 3-1), that helps to support the MX chain.^{32, 50} Kimizuka and coworkers demonstrated that surfactant molecules aid in the formation of MX chain interactions in solution (Figure 3-2).^{100, 101} In Kimizuka's system, the secondary support for the chain is provided by a cylindrical reverse micelle. To engineer a secondary supramolecular ordering into a neutral MX chain system, amphiphilic metal complexes could also potentially be utilized. The micro-segregation of the various domains within the amphiphile engenders the potential for ordering, especially at the interfaces of the domains.

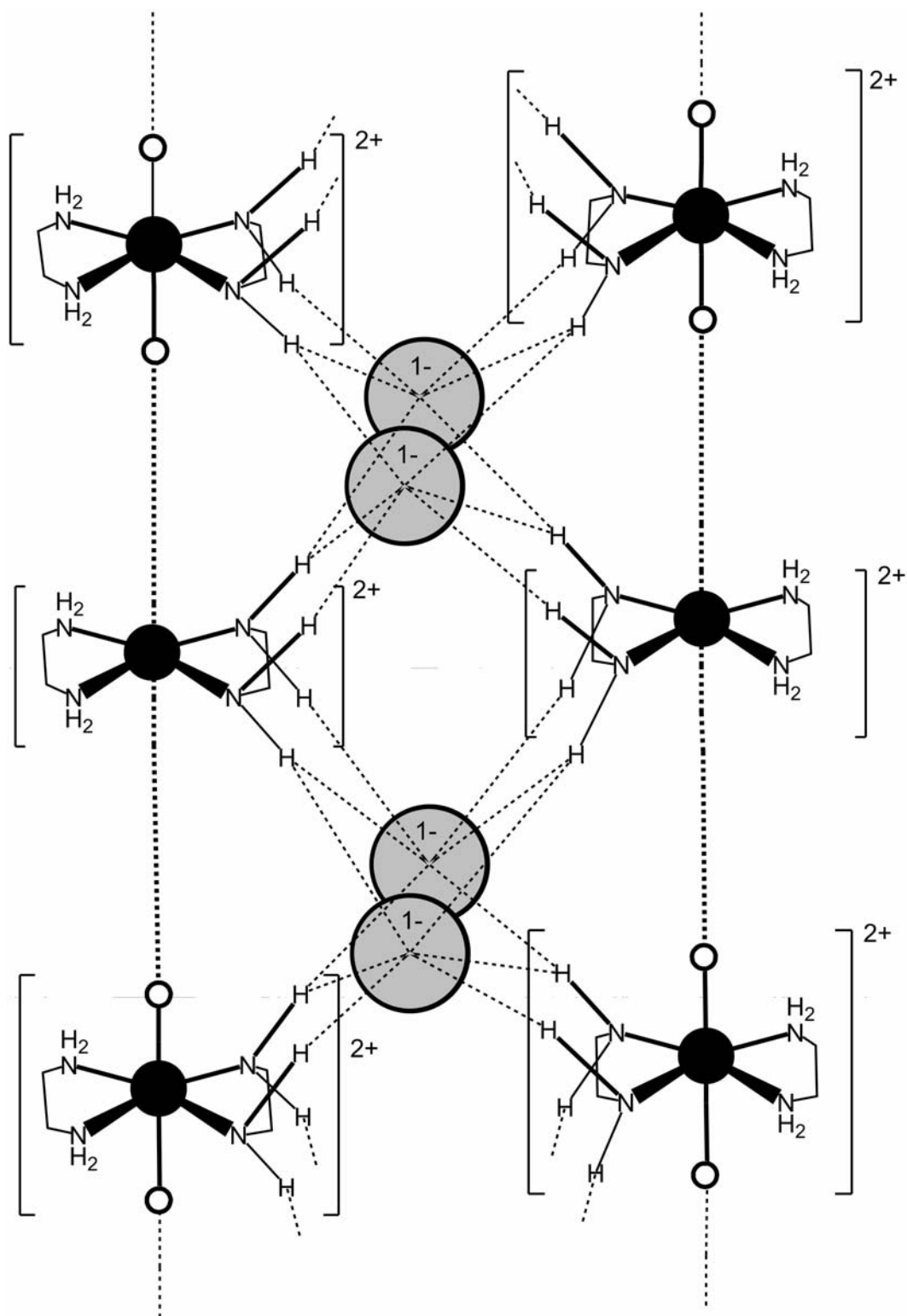


Figure 3-1. Diagram of the hydrogen bonding between MX chain ligands and counterions as occurs in $[\text{Ni}^{\text{III}}(\text{chxn})_2\text{Cl}](\text{NO}_3)_2$ (chxn = 1,2-diaminocyclohexane, cyclohexane ring not shown); Ni (black); Cl (white); NO_3^- (grey); hydrogen bonds (---), some counterions omitted for clarity

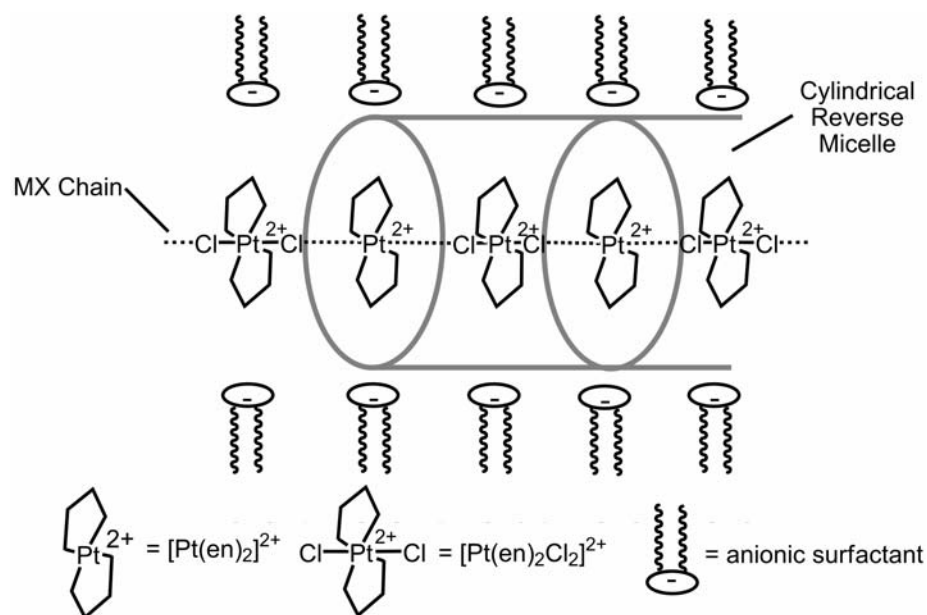


Figure 3-2. Method of formation for surfactant supported MX chain complexes in solution as developed by Kimizuka, Oda, and Kunitake¹⁰¹; en = 1,2-diaminoethane.

Kimizuka's surfactant system has an axially ordered metal-aromatic domain, which is micro-segregated from the alkyl chain domain, similar to the structure of many smectic liquid crystals. The hydrophobic packing of the alkyl chains helps to pre-organize the metal centers into domains where axial interactions between metal complexes may occur. More specific methods for controlling liquid crystalline ordering through molecular design are discussed below.

The hypothesized formation of an MX chain interaction in a mesogenic phase is shown in Figure 3-3. This is the first time that formation of MX chain interactions has been proposed in a mesogenic phase. Liquid crystalline systems provide a potential means of introducing an ordered and easily self-assembled mesophase. Unlike the tedious crystal growth process needed to produce large single crystals, ordered domains self-assemble in liquid crystalline systems and many systems are amenable to ordering by outside magnetic or

electrical fields. The proposed system utilizes dialkyl-2,2'-bipyridine-4,4'-dicarboxylato metal complexes due to the ability to control the mesogenic temperature range with alkyl chain length, and the layered ordering as previously established by Pucci and coworkers.^{47, 103} The complexes synthesized and characterized for this research are given in Figure 3-4. This chapter focuses on the characterization of individual metallomesogens. Chapter 4 presents the analyses of mixed-valent, binary mixtures of metallomesogens. This chapter begins with a short review of the ordering forces which drive mesophase formation, due to the importance of these interactions in supporting axial ordering.

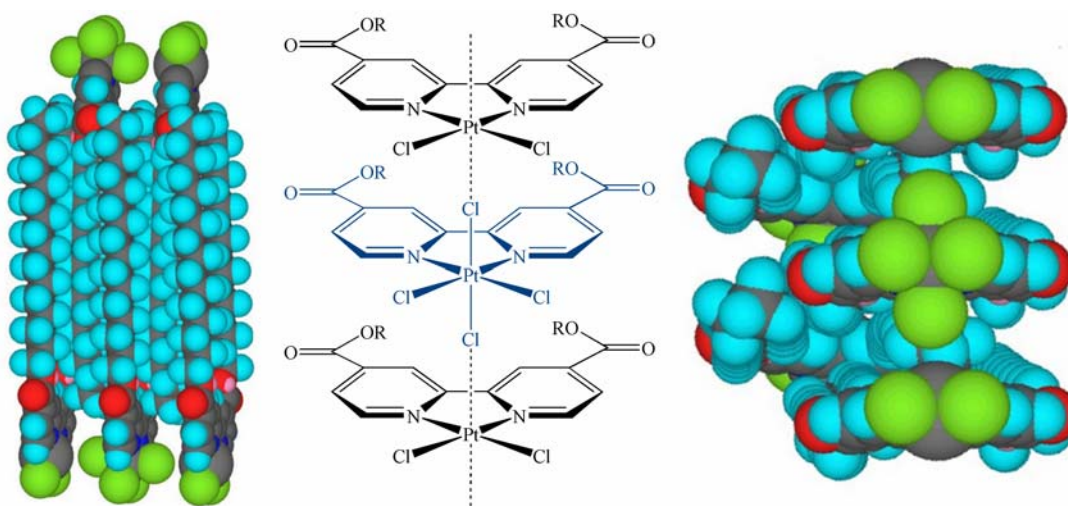


Figure 3-3. Initially hypothesized system for the formation of MX chain interactions in a liquid crystalline phase.

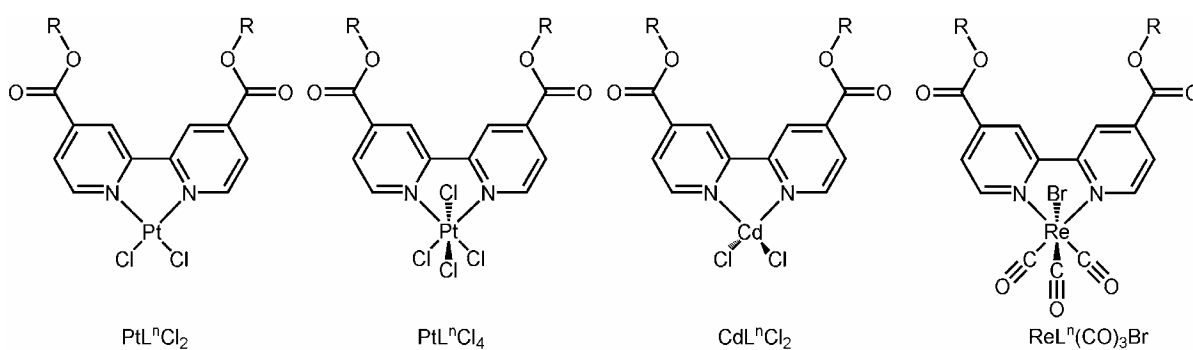


Figure 3-4. Complexes synthesized for this research. L^n = dialkyl-2,2'-bipyridine-4,4'-dicarboxylate where n is the number of carbon atoms in the alkyl chain.

3.1.2 Thermotropic Metallomesogens and Mesophase Ordering

Liquid crystals are characterized as having a state intermediate between solid and liquid, with at least one dimension of short-range positional ordering of the species. This research focuses on thermotropic liquid crystalline phases, consisting of neat samples which change phase with temperature. In order to form metal-based supramolecular interactions, a layered mesophase which was known to support Pt^{II} d⁸-d⁸ interactions at the edges of the layers was explored for its potential to similarly support MX chain interactions.

Smectic, or layered mesophases, are characterized by a director, which is taken to be perpendicular to the layer plane. Due to the fluidity of the mesophase, complexes may move into and out of the smectic layers easily. There are several sub-categories of smectic phases as shown in Figure 3-5. The smectic layers may be composed of monolayers (**a**), bilayers (**c** and **d**), or have semi-bilayer ordering (**b**).

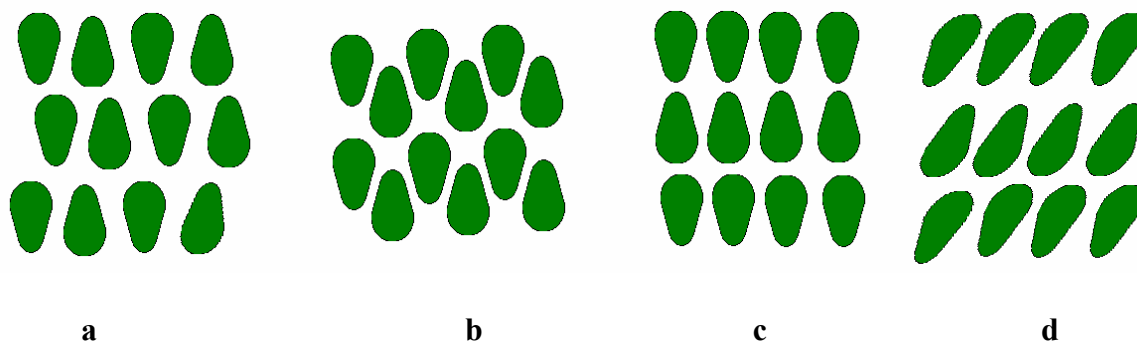


Figure 3-5. Examples of smectic liquid crystalline phases, smectic A (SmA) (**a**), semi-bilayer smectic A (SmA_d) (**b**), bilayer smectic A (SmA₂) (**c**), and bilayer smectic C (SmC₂) (**d**). Monolayer, bilayer, and semi-bilayer phases may occur for both SmA and SmC phases.

The formation of a mesophase is influenced by the shape, rigidity, and amphiphilicity of a molecule. The intermolecular forces that drive mesophase formation include

incompatibility of molecular shapes, micro-segregation due to the amphiphilicity of mesogens, and steric optimization.¹⁰⁴ Some amphiphilic ligands are themselves mesogenic, while others form mesophases only when a metal center links two non-mesogenic ligands or when metal coordination enforces rigidity.⁸

There are several “standard shapes” for complexes or molecules that are expected to have thermotropic liquid crystalline phases, as discussed in Chapter 1. Smectic phases are generally produced by calamitic liquid crystals, which have a long rigid core and flexible “tails”. These are often associated with the smectic A (SmA) and smectic C (SmC) phases (Figure 3-5, **a** and **d** respectively). Sanidic mesogens are similar, but with an emphasis on a flat, rigid core, which may lead to the formation of biaxial phases, where rotation of the mesogens about their director is hindered.^{105, 106} Discotic, or disc-shaped, mesogens are less associated with smectic phases than they are with columnar ones, though as will be explained below, columnar and smectic ordering are not mutually exclusive.

Correlated columnar ordering in the presence of smectic layers will be a focus of this chapter. The dialkyl-2,2'-bipyridine-4,4'-carboxylate complexes in this research do not readily fall into any of the traditional categories of mesogens. However, intermolecular interactions may also be utilized to form liquid crystalline phases from non-traditional mesogens (e.g. not calamitic or discotic), and axial interactions may induce more ordered mesophases, including biaxial phases.^{8, 10, 41, 43, 44} Examples of this so-called complimentary shape approach for engendering liquid crystalline behavior from non-traditional mesogens are given in Figure 3-6. Mesogens with asymmetrically distributed alkyl chains may form bilayer smectic phases (Figure 3-6, **a**). So-called tapered or wedge-shaped mesogens utilize a combination of molecular shape and polar/polarizable endgroups to form columnar phases

(b).^{107, 108} Metallomesogens, though not of a typical discotic shape, may be utilized to form correlated columnar phases, which rely on axial metal-metal interactions to coordinate two or more complimentary shaped complexes into a single disc-shaped unit with columnar ordering (a and c).^{48, 109, 110, 111}

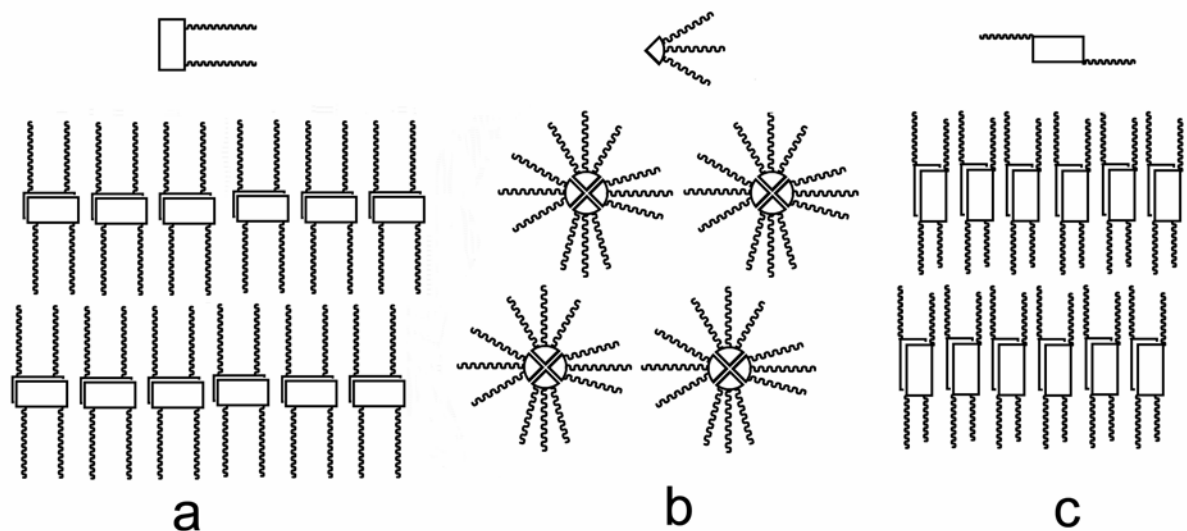


Figure 3-6. Complimentary shape approaches where segregation of hydrophobic and hydrophilic domains engenders columnar ordering from non-discotic mesogens; single mesogens shown at top.

Non-traditional mesogens may be utilized to induce formation of phases ranging from hexatic-columnar (Col_H) to smectic A (SmA) by controlling the micro-segregation of the alkyl chains from the rigid core and the degree to which the cores themselves segregate as in Figure 3-7.⁴⁰ The lamello-columnar (Col_L) phase is biaxial, yet still maintains a true liquid crystalline phase, while the Col_R phase demonstrates a slight modification in one dimension of the mesogen and a higher ordering of the mesophase. This trend demonstrates the strong effects even minor derivatization of the mesogen may have on the mesophase.

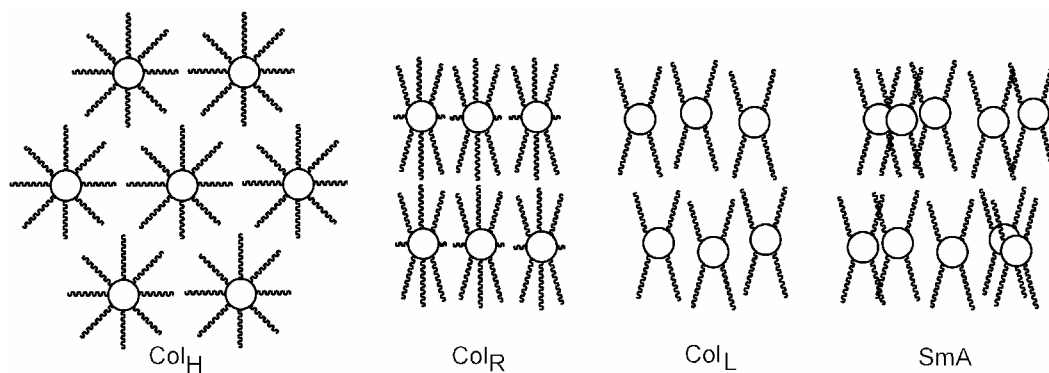


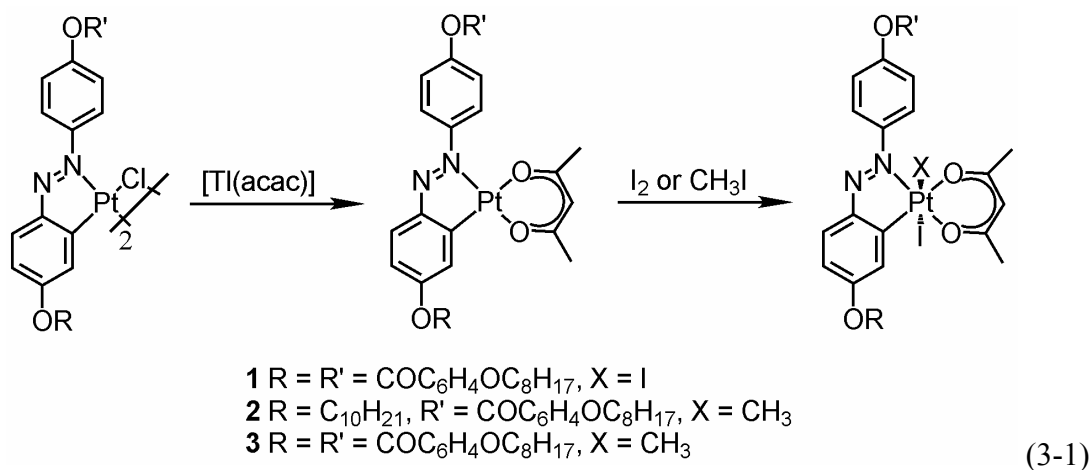
Figure 3-7. Mesogenic phases showing the progression from hexatic-columnar (Col_H) through rectangular-columnar (Col_R) and lamello-columnar (Col_L) to smectic A (SmA) mesophases as anisotropic microsegregation of the alkyl chains occurs.

If the mesophase is more highly ordered it may be considered soft crystalline. The soft crystalline phases are distinguished from true liquid crystalline phases by their resistance to flow under pressure, the temperature hysteresis upon transition to and from the mesophase as observed by differential scanning calorimetry (DSC), and by the generally sharper and more numerous reflections observed by X-ray diffraction.^{48, 112, 113}

Incorporation of a metal introduces the possibility of unique “metal-centered” optical biaxiality whereby alignment of the metal-centers increases ordering of the mesophases beyond that found in the free ligand.^{41, 43, 44, 114} The unique shapes, colors, and luminescent properties inherent in metal-ligand chemistry allow for exciting possibilities in molecular electronics, conductors, and new optical devices when they are incorporated into liquid crystalline systems. This is particularly true of platinum-bipyridine systems, whose interesting luminescent and photochemical properties have already been studied in the solid and liquid states by numerous groups.^{115, 116, 117}

3.1.3 Previously Developed Metallomesogenic Systems

In recent years, a variety of metallomesogens have been explored and a number of recent review articles are available.^{8, 10, 112, 118} The work with octahedral and tetrahedral mesogens forming smectic phases^{119, 120} has been more limited, as has the work with Pt^{IV} metallomesogens.^{121, 122, 123} Due to relative rarity of the Pt^{IV} mesophases, they will be discussed first. In 1999, Ghendini and coworkers showed that Pt^{II} mesogens could be modified as shown in eq 3-1 to give the first mesogenic Pt^{IV} complexes.¹²¹



The Pt^{IV} mesophases are similar to their Pt^{II} counterparts, with the exception of the appearance of a more highly ordered smectic phase for **3** than for the nematic Pt^{II} analogue. In general, the increase in the steric bulk upon oxidation reduces the melting temperature. This work was expanded by modifying the acetylacetonate ligand to produce liquid crystalline tropolonate, 8-hydroxyquinolate, and hexafluoroacetylacetonate derivatives.¹²²

Beagley and coworkers took a slightly different synthetic route by first oxidizing [Pt(Me)₂(COD)] (COD = 1,5-cyclooctadiene) and then reacting the Pt^{IV} complex with 4-alkoxy-4'-stilbazole ligands, which have already been demonstrated to confer liquid

crystallinity in a variety of complexes.¹²³ The complexes are unique for their pronounced “V”-shape (Figure 3-8).

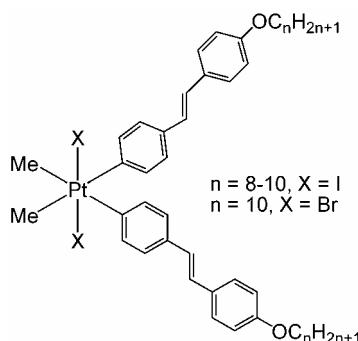


Figure 3-8. “V”-shaped Pt^{IV} metallomesogens.¹²³

There are several varieties of metallomesogenic Pt^{II} complexes, some of which are reviewed in Table 1-4 (Chapter 1). Due to the focus on bipyridine derivatives, only those complexes are discussed here. Pucci and coworkers proposed that in dialkyl-2,2'-bipyridine-4,4'-dicarboxylato metal systems, the presence of weak d^8-d^8 axial interactions perpendicular to the hydrophobic layers leads to the formation of mesophases that have both Col_L and semi-bilayer smectic A (SmA_d) characteristics (Figure 3-9). The SmA_d packing is caused by the hydrophobic interdigitation of the alkyl chains to produce alternating layers of aliphatic and aromatic domains. The columnar interactions, responsible for the Col_L characterization of the phase, are between Pt^{II} centers perpendicular to the interdigitated alkyl chains. Some debate persists as to whether hydrophobic packing of the long alkyl (semi-bilayer smectic order) or the $M^{II} \cdots M^{II}$ interactions (columnar ordering) dominate the phase behavior of the platinum species. A comparison of the phase behavior of various dialkyl-2,2'-bipyridine-4,4'-dicarboxylato complexes presents an opportunity to study the affects of intermolecular metal-metal and π - π stacking interactions on mesogenic phase formation. This research also

enables analysis of the $\text{Pt}^{\text{II}}\text{-Pt}^{\text{II}}$ and $\text{Pt}^{\text{IV}}\text{-Pt}^{\text{IV}}$ interactions that may hinder formation of $\text{Pt}^{\text{II}}\text{-Pt}^{\text{IV}}$ interactions in the binary systems of interest. Re and Cd derivatives were examined to further investigate the role of the metal center on mesophase formation. The Cd derivatives were analyzed to determine if an extended Cd- μCl -Cd framework, as had been previously observed for $[\text{CdCl}_2(\text{bpy})]_n$ ¹²⁴, could be observed in a liquid crystalline phase. The octahedral $\text{Re}(\text{CO})_3\text{L}^n\text{Br}$ derivatives were examined to determine if the increase in the headgroup size would affect mesophase formation.

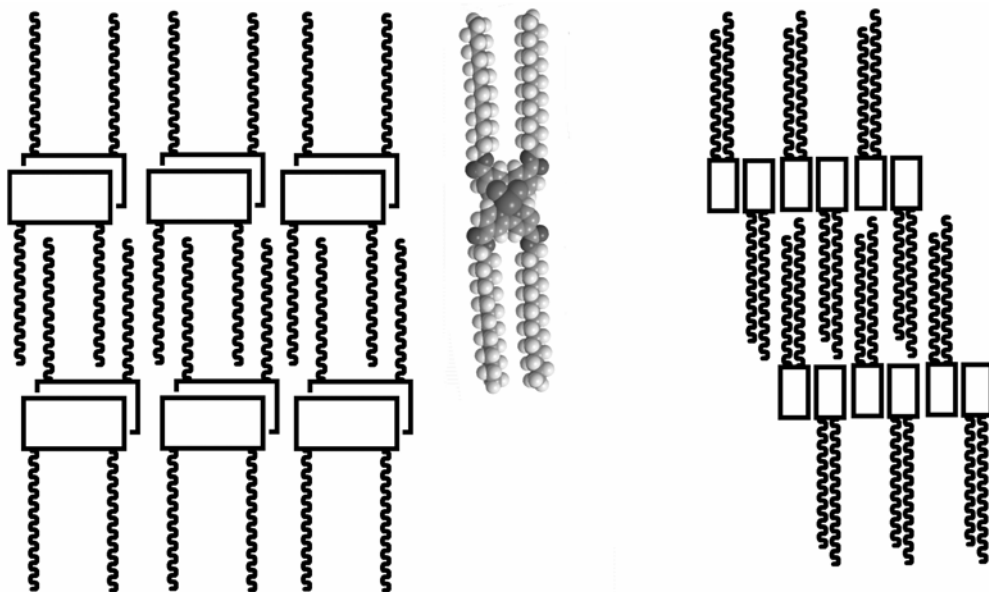


Figure 3-9. Diagram of the liquid crystalline phase of $\text{PtL}^{16}\text{Cl}_2$ (001), right, and (010), left. A $\text{Pt}^{\text{II}}\cdots\text{Pt}^{\text{II}}$ columnar interaction is shown as a space-filling model.

3.2 Experimental Section

3.2.1 General Laboratory Procedures and Instrumentation

PtCl₂, CdCl₂, Na₂PtCl₆•6H₂O, 4,4'-dimethyl-2,2'-bipyridine and various alcohols were obtained from Sigma-Aldrich and used without further purification. Re(CO)₅Br was available from previous research in our group. Ligands dimethyl-2,2'-bipyridine-4,4'-dicarboxylate¹²⁵ (L¹), diethyl-2,2'-bipyridine-4,4'-dicarboxylate¹²⁶ (L²), dioctyl-2,2'-bipyridine-4,4'-dicarboxylate¹⁰³ (L⁸), dihexadecyl-2,2'-bipyridine-4,4'-dicarboxylate¹⁰³ (L¹⁶), and dioctadecyl-2,2'-bipyridine-4,4'-dicarboxylate¹²⁷ (L¹⁸) were synthesized according to literature procedure, and ¹H NMR analysis was in agreement with previously published results. Synthesis of didodecyl-2,2'-bipyridine-4,4'-dicarboxylate¹²⁸ (L¹²) was previously reported in the literature, but as ¹H NMR was not provided, that data is given below. All ligands were purified by triple recrystallization from hot ethanol. Toluene was freshly distilled from Na and benzophenone. Methylene chloride was freshly distilled and passed through an alumina column under dry argon prior to use.

Proton NMR spectra were recorded on a Bruker 400 MHz spectrometer in CDCl₃ or CD₂Cl₂ solution and referenced to TMS. Elemental analyses were performed at Atlantic Microlabs, Norcross VA. Textures of the mesophases were analyzed using a Nikon Microphot-FX polarizing microscope equipped with a Mettler Toledo FP90 processor controlled RP82HT heating stage. Optical micrographs were obtained using a Sony SSC-C374 CCD IRIS camera and Roxio Videowave image capture. Transition temperatures and enthalpies were measured using a Seiko SSC/5200 Differential Scanning Calorimeter with a standard heating and cooling rate of 10 °C/min. In cases where two transitions occurred <10 °C apart, a heating and cooling rate of 5 °C/min was utilized to give slightly better peak

definition. Two or more heating/cooling cycles were performed on each sample. Transition temperatures and enthalpies are taken from the second heating/cooling cycle. Decomposition temperatures were determined using a Perkin-Elmer Pyris 1 Thermal Gravimetric Analyzer with a heating rate of 5 °C/min.

3.2.2 Syntheses of Ligands

2,2'-bipyridine-4,4'-dicarboxylate, L₀: The synthesis of L₀ was performed by modifying the reported method by using sodium dichromate.¹⁰³ The ¹H NMR (DMSO-d₆) spectrum was in accordance with the literature.¹²⁹ The product was dried under vacuum over P₂O₅ for a minimum of two weeks and used without further purification.

General Procedure for Ligand Synthesis: The syntheses of long alkyl chain ligands, Lⁿ, were performed in a similar manner, based on literature procedure.¹⁰³

didecyl-2,2'-bipyridine-4,4'-dicarboxylate, L¹⁰: Yield: 0.3477 g, 58%. ¹H NMR (400 MHz, CDCl₃, δ): 8.95 (d, *J* = 1.3 Hz, 2H, ArH^{3,3'}), 8.87 (d, *J* = 5.0 Hz, 2H, ArH^{6,6'}), 7.90 (dd, *J* = 5.0 Hz, *J* = 1.6 Hz, 2H, ArH^{5,5'}), 4.39 (t, *J* = 6.9 Hz, 4H, -OCH₂CH₂CH₂(CH₂)₆CH₃), 1.81 (p, *J* = 7.4 Hz, 4H, -OCH₂CH₂CH₂(CH₂)₆CH₃), 1.45 (m, 4H, -OCH₂CH₂CH₂(CH₂)₆CH₃), 1.26 (m, 24H, -OCH₂CH₂CH₂(CH₂)₆CH₃), 0.88 (t, *J* = 7.0 Hz, 6H, -OCH₂CH₂CH₂(CH₂)₆CH₃). Anal. Calcd. for C₃₂H₄₈N₂O₄: C, 73.23; H, 9.24; N, 5.34. Found: C, 73.04; H, 9.17; N, 5.31.

didodecyl-2,2'-bipyridine-4,4'-dicarboxylate, L¹²: Yield: 0.1641 g, 63%. ¹H NMR (400 MHz, CDCl₃, δ): 8.95 (s, 2H, ArH^{3,3'}), 8.87 (d, *J* = 5.0 Hz, 2H, ArH^{6,6'}), 7.90 (dd, *J* = 5.0 Hz, *J* = 1.5 Hz, 2H, ArH^{5,5'}), 4.39 (t, *J* = 6.7 Hz, 4H, -OCH₂CH₂CH₂(CH₂)₈CH₃), 1.81 (p,

$J = 7.0$ Hz, 4H, $-\text{OCH}_2\text{CH}_2\text{CH}_2(\text{CH}_2)_8\text{CH}_3$), 1.45 (m, 4H, $-\text{OCH}_2\text{CH}_2\text{CH}_2(\text{CH}_2)_8\text{CH}_3$), 1.26 (m, 32H, $-\text{OCH}_2\text{CH}_2\text{CH}_2(\text{CH}_2)_8\text{CH}_3$), 0.88 (t, $J = 6.6$ Hz, 6H, $-\text{OCH}_2\text{CH}_2\text{CH}_2(\text{CH}_2)_8\text{CH}_3$).

diicosanyl-2,2'-bipyridine-4,4'-dicarboxylate, L₂₀: Icosanol was dried over P₂O₅ in a vacuum desiccator for 2 weeks prior to use. Yield: 1.2123 g, 91.2%. ¹H NMR (400 MHz, CDCl₃, δ): ¹H 8.95 (d, $J = 1.4$ Hz, 2H, ArH^{3,3'}), 8.86 (d, $J = 5.0$ Hz, 2H, ArH^{6,6'}), 7.90 (dd, $J = 5.0$ Hz, $J = 1.6$ Hz, 2H, ArH^{5,5'}), 4.39 (t, $J = 6.8$ Hz, 4H, $-\text{OCH}_2\text{CH}_2\text{CH}_2(\text{CH}_2)_{16}\text{CH}_3$), 1.81 (p, $J = 7.0$ Hz, 4H, $-\text{OCH}_2\text{CH}_2\text{CH}_2(\text{CH}_2)_{16}\text{CH}_3$), 1.45 (m, 4H, $-\text{OCH}_2\text{CH}_2\text{CH}_2(\text{CH}_2)_{16}\text{CH}_3$), 1.25 (m, 64H, $-\text{OCH}_2\text{CH}_2\text{CH}_2(\text{CH}_2)_{16}\text{CH}_3$), 0.88 (t, $J = 6.7$ Hz, 6H, $-\text{OCH}_2\text{CH}_2\text{CH}_2(\text{CH}_2)_{16}\text{CH}_3$). Anal. Calcd. for C₅₂H₈₈N₂O₄: C, 77.54; H, 11.04; N, 3.48. Found: C, 77.17; H, 11.05; N, 3.47.

3.2.3 Syntheses of Pt^{II} Complexes

General procedure for Synthesis of Pt^{II} Complexes: In a condenser-equipped Schlenk flask under Ar, PtCl₂ (0.1 g, 0.38 mmol) was relaxed in toluene (25 mL) until a clear orange solution was obtained. A solution of 1 equiv of ligand in toluene (10-20 mL) was added to the reaction mixture. The mixture was refluxed for 18 h, cooled to 0 °C and filtered to remove any solid. Toluene was removed to give an orange solid. Products were purified by recrystallization from CHCl₃/ethanol or by flash chromatography on silica gel using chloroform as the elutant.

dichloro(dimethyl-2,2'-bipyridine-4,4'-dicarboxylato)platinum(II), PtL¹Cl₂: Due to the insolubility of L¹ in toluene, this reaction was carried out in 1:1 (v/v) CH₂Cl₂/EtOH. Yield: 0.0486 g, 55.5%. Proton NMR analysis was in agreement with the literature.¹³⁰

dichloro(diethyl-2,2'-bipyridine-4,4'-dicarboxylato)platinum(II), PtL²Cl₂: Due to the insolubility of L₂ in toluene, this reaction was carried out in 1:1 (v/v) CH₂Cl₂/EtOH. Yield: 0.0265 g, 36%. Proton NMR analysis was in agreement with the literature.¹³¹

dichloro(didecyl-2,2'-bipyridine-4,4'-dicarboxylato)platinum(II), PtL¹⁰Cl₂: Yield: 0.394 g, 38%. ¹H NMR (400 MHz, CDCl₃, δ): 9.99 (dd, *J* = 6.1 Hz, 2H, ArH^{6,6'}), 8.60 (s, 2H, ArH^{3,3'}), 8.11 (d, *J* = 6.0 Hz, *J* = 1.6 Hz, 2H, ArH^{5,5'}), 4.47 (t, *J* = 6.8 Hz, 4H, -OCH₂CH₂CH₂(CH₂)₆CH₃), 1.86 (p, *J* = 7.2 Hz, 4H, -OCH₂CH₂CH₂(CH₂)₆CH₃), 1.46 (m, 4H, -OCH₂CH₂CH₂(CH₂)₆CH₃), 1.28 (m, 24H, -OCH₂CH₂CH₂(CH₂)₆CH₃), 0.88 (t, *J* = 6.4 Hz, 6H, -OCH₂CH₂CH₂(CH₂)₆CH₃). Anal. Calcd. for C₃₂Cl₂H₄₈N₂O₄Pt: C, 48.6; H, 6.10; N, 3.5; Cl, 8.97. Found: C, 48.86; H, 6.15; N, 3.45; Cl, 8.82.

dichloro(didodecyl-2,2'-bipyridine-4,4'-dicarboxylato)platinum(II), PtL¹²Cl₂: Yield: 0.546 g, 34%. Proton NMR analysis agrees with that previously published in the literature.¹³²

dichloro(dihexadecyl-2,2'-bipyridine-4,4'-dicarboxylato)platinum(II), PtL¹⁶Cl₂: Yield: 0.0095 g, 44.4%. Proton NMR analysis was found to be in agreement with previously published values.⁴⁷

dichloro(diicosanyl-2,2'-bipyridine-4,4'-dicarboxylato)platinum(II), PtL²⁰Cl₂: Yield: 0.0648 g, 47%. ¹H NMR (400 MHz, CDCl₃, δ): 9.99 (d, *J* = 5.6 Hz, 2H, ArH^{6,6'}), 8.59 (d, *J* = 1.3 Hz, 2H, ArH^{3,3'}), 8.13 (dd, *J* = 6.2 Hz, *J* = 1.5 Hz, 2H, ArH^{5,5'}), 4.47 (t, *J* = 6.9 Hz, 4H, -OCH₂CH₂(CH₂)₁₇CH₃), 1.85 (p, *J* = 7.1 Hz, 4H, -OCH₂CH₂(CH₂)₁₇CH₃), 1.25 (m, 68H, -OCH₂CH₂(CH₂)₁₇CH₃), 0.88 (t, *J* = 6.5 Hz, 6H, -OCH₂CH₂(CH₂)₁₇CH₃). Anal. Calcd. for C₅₂Cl₂H₈₈N₂O₄Pt: C, 58.3; H, 8.3; N, 2.62; Cl, 6.62. Found: C, 58.78; H, 8.15; N, 2.76; Cl, 6.54.

3.2.4 Syntheses of Pt^{IV} Complexes

General Procedure for Synthesis of Pt^{IV} Complexes: Under an argon atmosphere, Na₂PtCl₆•6H₂O (0.1 g, 0.18 mmol) and 1 equiv of ligand were placed in a Schlenk flask. Dried methylene chloride (20-30 mL) was injected into the flask to give an orange reaction mixture. After 30 min, the reaction mixture began to turn yellow and a light-colored precipitate formed. Under static argon pressure, the solution was stirred at room temperature for 3 d. The reaction mixture was filtered, and removal of solvent yielded a yellow solid, which was washed with hexanes (3×20 mL) and cold abs. ethanol (3×20 mL). The product may be further purified by recrystallization from toluene or ethanol/chloroform.

tetrachloro(dimethyl-2,2'-bipyridine-4,4'-dicarboxylato)platinum(IV), PtL¹Cl₄:

Yield: 0.1337 g, 55.5%. ¹H NMR (400 MHz, CD₂Cl₂, δ): 9.89 (apparent td, *J* = 25.9 Hz, *J* = 6.1 Hz, 2H, ArH^{6,6'}), 8.95 (d, *J* = 1.52 Hz, 2H, Ar^{3,3'}), 8.44 (dd, *J* = 6.0 Hz, *J* = 1.8 Hz, 2H, Ar^{5,5'}), 4.10 (s, 6H, Me). Anal. Calcd. for C₁₄Cl₄H₂₁N₂O₄Pt: C, 27.6; H, 1.99; N, 4.60; Cl, 23.3. Found: C, 27.66; H, 1.94; N, 4.48; Cl, 23.46.

tetrachloro(diethyl-2,2'-bipyridine-4,4'-dicarboxylato)platinum(IV), PtL²Cl₄:

Yield: 0.0648 g, 47.1%. ¹H NMR (400 MHz, CDCl₃, δ): 9.98 (apparent td, *J* = 25.8 Hz, *J* = 5.9 Hz, 2H, ArH^{6,6'}), 8.92 (d, *J* = 1.48 Hz, 2H, Ar^{3,3'}), 8.43 (dd, *J* = 6.0 Hz, *J* = 1.7 Hz, 2H, Ar^{5,5'}), 4.61 (q, *J* = 7.2 Hz, 4H, -CH₂CH₃), 1.52 (t, *J* = 7.2 Hz, 6H, -CH₂CH₃). Anal. Calcd. for C₁₆Cl₄H₁₆N₂O₄Pt: C, 30.2; H, 2.54; N, 4.40; Cl, 22.3. Found: C, 30.45; H, 2.54; N, 4.30; Cl, 22.42.

tetrachloro(dioctyl-2,2'-bipyridine-4,4'-dicarboxylato)platinum(IV), PtL⁸Cl₄:

Yield: 0.0450 g, 31.4%. ¹H NMR (400 MHz, CDCl₃, δ): 10.00 (apparent td, *J* = 26.2 Hz, *J* = 6.0 Hz, 2H, ArH^{6,6'}), 8.92 (d, *J* = 1.6 Hz, 2H, ArH^{3,3'}), 8.43 (dd, *J* = 6.0 Hz, *J* = 1.7 Hz, 2H,

ArH^{5,5'}), 4.54 (t, $J = 6.8$ Hz, 4H, -OCH₂CH₂(CH₂)₅CH₃), 1.87 (p, $J = 7.4$ Hz, 4H, -OCH₂CH₂(CH₂)₅CH₃), 1.31 (m, 20H, -OCH₂CH₂(CH₂)₅CH₃), 0.89 (t, $J = 6.8$ Hz, 6H, -OCH₂CH₂(CH₂)₅CH₃). Anal. Calcd. for C₂₈Cl₄H₄₀N₂O₄Pt: C, 41.74; H, 5.02; N, 3.48. Found: C, 41.20; H, 5.06; N, 3.23.

tetrachloro(didecyl-2,2'-bipyridine-4,4'-dicarboxylato)platinum(IV), PtL¹⁰Cl₄:

Yield: 0.0410 g, 37.8%. ¹H NMR (400 MHz, CDCl₃, δ): 9.90 (apparent td, $J = 25.7$ Hz, $J = 6.1$ Hz, 2H, ArH^{6,6'}), 8.91 (d, $J = 1.4$ Hz, 2H, ArH^{3,3'}), 8.42 (dd, $J = 6.0$ Hz, $J = 1.7$ Hz, 2H, ArH^{5,5'}), 4.52 (t, $J = 6.8$ Hz, 4H, -OCH₂CH₂CH₂(CH₂)₆CH₃), 1.87 (p, $J = 7.8$ Hz, 4H, -OCH₂CH₂CH₂(CH₂)₆CH₃), 1.46 (m, 4H, -OCH₂CH₂CH₂(CH₂)₆CH₃), 1.28 (m, 24H, -OCH₂CH₂CH₂(CH₂)₆CH₃), 0.87 (t, $J = 6.7$ Hz, 6H, -OCH₂CH₂CH₂(CH₂)₆CH₃). Anal. Calcd. for C₃₂Cl₄H₄₈N₂O₄Pt: C, 44.60; H, 5.63; N, 3.25; Cl, 16.46. Found: C, 44.88; H, 5.86; N, 3.32; Cl, 16.40.

tetrachloro(didodecyl-2,2'-bipyridine-4,4'-dicarboxylato)platinum(IV),

PtL¹²Cl₄: Yield: 0.1009 g, 61.8%. ¹H NMR (400 MHz, CDCl₃, δ): 9.99 (apparent td, $J = 26.0$ Hz, $J = 6.0$ Hz, 2H, ArH^{6,6'}), 8.91 (d, $J = 1.3$ Hz, 2H, ArH^{3,3'}), 8.43 (dd, $J = 6.0$ Hz, $J = 1.7$ Hz, 2H, ArH^{5,5'}), 4.54 (t, $J = 6.8$ Hz, 4H, -OCH₂CH₂CH₂(CH₂)₈CH₃), 1.87 (p, $J = 7.3$ Hz, 4H, -OCH₂CH₂CH₂(CH₂)₈CH₃), 1.46 (m, 4H, -OCH₂CH₂CH₂(CH₂)₈CH₃), 1.28 (m, 32H, -OCH₂CH₂CH₂(CH₂)₈CH₃), 0.88 (t, $J = 7.0$ Hz, 6H, -OCH₂CH₂CH₂(CH₂)₈CH₃). Anal. Calcd. for C₃₆Cl₄H₅₆N₂O₄Pt: C, 47.11; H, 6.16; N, 3.05; Cl, 15.45. Found: C, 47.34; H, 6.26; N, 3.00; Cl, 15.15.

tetrachloro(dihexadecyl-2,2'-bipyridine-4,4'-dicarboxylato)platinum(IV),

PtL¹⁶Cl₄: Yield: 0.0095 g, 44.4%. ¹H NMR (400 MHz, CDCl₃, δ): 10.0 (apparent td, $J = 28.0$ Hz, $J = 5.6$ Hz, 2H, ArH^{6,6'}), 8.92 (d, $J = 1.1$ Hz, 2H, ArH^{3,3'}), 8.43 (dd, $J = 5.7$ Hz, $J =$

1.7 Hz, 2H, ArH^{5,5'}), 4.54 (t, $J = 7.7$ Hz, 4H, -OCH₂CH₂CH₂(CH₂)₁₂CH₃), 1.87 (p, $J = 7.0$ Hz, 4H, -OCH₂CH₂CH₂(CH₂)₁₂CH₃), 1.47 (m, 4H, -OCH₂CH₂CH₂(CH₂)₁₂CH₃), 1.27 (m, 48H, -OCH₂CH₂CH₂(CH₂)₁₂CH₃), 0.88 (t, $J = 6.6$ Hz, 6H, -OCH₂CH₂CH₂(CH₂)₁₂CH₃). Anal. Calcd. for C₄₄Cl₄H₇₂N₂O₄Pt: C, 51.3; H, 7.06; N, 2.72; Cl, 13.8. Found: C, 51.67; H, 7.08; N, 2.71; Cl, 13.41.

tetrachloro(diicosanyl-2,2'-bipyridine-4,4'-dicarboxylato)platinum(IV),

PtL²⁰Cl₄: Yield: 0.0513 g, 36.6%. ¹H NMR (400 MHz, CDCl₃, δ): 10.00 (apparent td, $J = 26.0$ Hz, $J = 6.0$ Hz, 2H, ArH^{6,6'}), 8.91 (d, $J = 1.4$ Hz, 2H, ArH^{3,3'}), 8.43 (dd, $J = 6.0$ Hz, $J = 1.7$ Hz, 2H, ArH^{5,5'}), 4.54 (t, $J = 6.8$ Hz, 4H, -OCH₂CH₂(CH₂)₁₇CH₃), 1.87 (p, $J = 7.2$ Hz, 4H, -OCH₂CH₂(CH₂)₁₇CH₃), 1.26 (m, 68H, -OCH₂CH₂(CH₂)₁₇CH₃), 0.88 (t, $J = 6.6$ Hz, 6H, -OCH₂CH₂(CH₂)₁₇CH₃). Anal. Calcd. for C₅₂Cl₄H₈₈N₂O₄Pt: C, 54.67; H, 7.78; N, 2.45; Cl, 12.41. Found: C, 54.27; H, 7.74; N, 2.62; Cl, 12.56.

3.2.5 Syntheses of Cd^{II} Complexes

General Procedure: The CdLⁿCl₂ complexes were synthesized using the same procedure as the PtLⁿCl₂ complexes, with the exception of acetonitrile being utilized as the solvent. Products were obtained as white crystalline powders. Purification may be made by recrystallization from hot ethanol/hexanes.

dichloro(diethyl-2,2'-bipyridine-4,4'-dicarboxylato)cadmium(II),

CdL²Cl₂: Yield: quantitative. IR (KBr) $\tilde{\nu}_{\max}$: 1730.2 cm⁻¹ (C=O). ¹H NMR (400 MHz, DMSO-d₆, δ): 8.89 (d, $J = 4.9$ Hz, 2H, ArH^{6,6'}), 8.86 (s, 2H, ArH^{3,3'}), 7.89 (d, $J = 4.5$, 2H, ArH^{5,5'}), 4.40 (q, $J = 7.1$ Hz, 4H, -OCH₂CH₃), 1.86 1.39 (t, $J = 7.2$ Hz, 6H, -OCH₂CH₃).

Anal. Calcd. for $C_{16}Cl_2H_{16}N_2O_4Cd$: C, 39.73; H, 3.34; N, 5.79; Cl, 14.66. Found: C, 38.29; H, 3.26; N, 5.54; Cl, 15.63.

dichloro(didodecyl-2,2'-bipyridine-4,4'-dicarboxylato)cadmium(II), $CdL^{12}Cl_2$:

Yield: 61.7%. IR (KBr) $\tilde{\nu}_{max}$: 1724.2 cm^{-1} (C=O). 1H NMR (400 MHz, $CDCl_3$, δ): 9.37 (d, $J = 5.0$ Hz, 2H, $ArH^{6,6'}$), 8.78 (s, 2H, $ArH^{3,3'}$), 8.14 (d, $J = 5.1$, 2H, $ArH^{5,5'}$), 4.45 (t, $J = 6.8$ Hz, 4H, $-OCH_2CH_2(CH_2)_9CH_3$), 1.84 (p, $J = 7.1$ Hz, 4H, $-OCH_2CH_2(CH_2)_9CH_3$), 1.26-1.84 (m, 36H, $-OCH_2CH_2(CH_2)_9CH_3$), 0.87 (t, $J = 6.3$ Hz, 6H, $-OCH_2CH_2(CH_2)_9CH_3$). Anal. Calcd. for $C_{36}Cl_2H_{56}N_2O_4Cd$: C, 56.57; H, 7.40; N, 3.67; Cl, 9.28. Found: C, 56.47; H, 7.49; N, 3.51; Cl, 9.42.

dichloro(dioctadecyl-2,2'-bipyridine-4,4'-dicarboxylato)cadmium(II),

$CdL^{18}Cl_2$: Yield: 56.7%. 1H NMR (400 MHz, $CDCl_3$, δ): 9.37 (d, $J = 4.2$ Hz, 2H, $ArH^{6,6'}$), 8.80 (s, 2H, $ArH^{3,3'}$), 8.16 (dd, $J = 0.56$ Hz, $J = 5.4$, 2H, $ArH^{5,5'}$), 4.45 (t, $J = 6.8$ Hz, 4H, $-OCH_2CH_2(CH_2)_{15}CH_3$), 1.84 (p, $J = 7.1$ Hz, 4H, $-OCH_2CH_2(CH_2)_{15}CH_3$), 1.22-1.58 (m, 60H, $-OCH_2CH_2(CH_2)_{15}CH_3$), 0.87 (t, $J = 6.6$ Hz, 6H, $-OCH_2CH_2(CH_2)_{15}CH_3$). Anal. Calcd. for $C_{48}Cl_2H_{80}N_2O_4Cd$: C, 61.81; H, 8.66; N, 3.00; Cl, 7.60. Found: C, 60.25; H, 8.40; N, 2.91; Cl, 7.63.

3.2.6 Syntheses of Re^I Complexes

General Procedure: All Re complexes were synthesized according to literature procedure¹³³ using toluene instead of benzene as the solvent. The reaction mixture was allowed to stir at 60 °C for 1-2 d.

bromotricarbonyl(didodecyl-2,2'-bipyridine-4,4'-dicarboxylato)rhenium(I),

$Re(CO)_3L^{12}Br$: Yield: 14.0%. IR (KBr) $\tilde{\nu}_{max}$: 2031, 1937, 1885 cm^{-1} (C≡O), 1724 cm^{-1}

(C=O). ^1H NMR (400 MHz, CDCl_3 , δ): 9.28 (t, $J = 5.8$ Hz, 2H, $\text{ArH}^{6,6'}$), 8.89 (s, 2H, $\text{ArH}^{3,3'}$), 8.13 (ddd, $J = 1.4$ Hz, $J = 4.2$, $J = 5.1$, 2H, $\text{ArH}^{5,5'}$), 4.54 (t, $J = 6.8$ Hz, 4H, $-\text{OCH}_2\text{CH}_2(\text{CH}_2)_9\text{CH}_3$), 1.90 (p, $J = 7.1$ Hz, 4H, $-\text{OCH}_2\text{CH}_2(\text{CH}_2)_9\text{CH}_3$), 1.3-1.4 (m, 36H, $-\text{OCH}_2\text{CH}_2(\text{CH}_2)_9\text{CH}_3$), 0.94 (t, $J = 6.6$ Hz, 6H, $-\text{OCH}_2\text{CH}_2(\text{CH}_2)_9\text{CH}_3$).

bromotricarbonyl(dioctadecyl-2,2'-bipyridine-4,4'-dicarboxylato)rhenium(I),

$\text{Re}(\text{CO})_3\text{L}^{18}\text{Br}$: Yield: 5.1%. IR (KBr) $\tilde{\nu}_{\text{max}}$: 2031, 1937, 1885 cm^{-1} (C \equiv O), 1718 cm^{-1} (C=O). ^1H NMR (400 MHz, CDCl_3 , δ): 9.22 (d, $J = 5.8$ Hz, 2H, $\text{ArH}^{6,6'}$), 8.83 (s, 2H, $\text{ArH}^{3,3'}$), 8.07 (ddd, $J = 1.5$ Hz, $J = 4.2$, $J = 5.3$, 2H, $\text{ArH}^{5,5'}$), 4.48 (t, $J = 6.9$ Hz, 4H, $-\text{OCH}_2\text{CH}_2(\text{CH}_2)_{15}\text{CH}_3$), 1.84 (p, $J = 6.9$ Hz, 4H, $-\text{OCH}_2\text{CH}_2(\text{CH}_2)_{15}\text{CH}_3$), 1.2-1.5 (m, 60H, $-\text{OCH}_2\text{CH}_2(\text{CH}_2)_{15}\text{CH}_3$), 0.88 (t, $J = 7.1$ Hz, 6H, $-\text{OCH}_2\text{CH}_2(\text{CH}_2)_{15}\text{CH}_3$).

3.2.7 X-ray Data Collection for $\text{PtL}^1\text{Cl}_2 \cdot 2\text{CH}_2\text{Cl}_2$, PtL^2Cl_2 and $\text{PtL}^{16}\text{L}_2 \cdot 2\text{CHCl}_3$

Crystals were mounted on a glass fiber and placed in the cold nitrogen stream of a SMART 1K CCD diffractometer. Data were collected at 173 K using $\text{MoK}\alpha$ radiation and processed with SAINT. The structure was solved by direct methods (program SIR92) and anisotropically refined by full-matrix least squares (program CRYSTALS). Hydrogen atoms were placed geometrically and refined isotropically using the riding-atom model. Parameters for data collection and refinement are given in Table 3-1. Thermal ellipsoid plots were produced using Ortep-3 v. 1.08.

Table 3-1. Crystallographic information for PtL¹Cl₂•2CH₂Cl₂, PtL²Cl₂ and PtL¹⁶Cl₂•2CHCl₃.

Species	PtL ¹ Cl ₂ •2CH ₂ Cl ₂	PtL ² Cl ₂	PtL ¹⁶ Cl ₂ •2CHCl ₃
chemical formula	C ₁₅ Cl ₄ H ₁₄ N ₂ O ₄ Pt	C ₁₆ Cl ₂ H ₁₆ N ₂ O ₄ Pt	C ₄₆ Cl ₈ H ₇₄ N ₂ O ₄ Pt
formula weight	623.19	566.32	1197.81
T (K)	173	173	173
wavelength (Å)	0.71073	0.71073	0.71073
crystal system	monoclinic	triclinic	triclinic
space group	<i>P</i> 2 ₁ / <i>c</i>	<i>P</i> -1	<i>P</i> -1
a (Å)	17.2723(16)	9.1145(4)	7.2871(5)
b (Å)	6.7511(7)	14.6632(7)	11.8947(8)
c (Å)	17.6663(17)	15.2749(7)	31.3949(20)
α (Å)	90	61.445(3)	94.642(4)
β (Å)	115.134(6)	82.988(3)	90.283(4)
γ (Å)	90	94.057(3)	95.377(4)
volume (Å ³)	1865.0(3)	1777.33(14)	2700.2(3)
Z	4	4	2
D _{calc} (g/cm ³)	2.22	2.116	1.473
absorption coefficient (mm ⁻¹)	8.121	8.19	3.02
F(000)	1184	1076.65	1220.31
crystal size (mm)	0.01 × 0.01 × 0.30	0.20 × 0.01 × 0.01	0.20 × 0.05 × 0.01
2θ max (deg)	27.0	50.0	50.00
index ranges	-22 ≤ <i>h</i> ≤ 19, 0 ≤ <i>k</i> ≤ 8, 0 ≤ <i>l</i> ≤ 22	-10 ≤ <i>h</i> ≤ 10, 0 ≤ <i>k</i> ≤ 17, -15 ≤ <i>l</i> ≤ 18	-8 ≤ <i>h</i> ≤ 8, 0 ≤ <i>k</i> ≤ 14, -37 ≤ <i>l</i> ≤ 37
reflections collected	4073	12756	30704
significant reflections	4073	4759	6523
refinement method	full-matrix least-squares on <i>F</i> ²	full-matrix least-squares on <i>F</i> ²	full-matrix least-squares on <i>F</i> ²
data/parameters	4073/236	4759/451	6523/550
goodness-of-fit on <i>F</i> ²	0.907	1.0618	1.2060
final R indices [<i>F</i> _o > 2.5σ(<i>F</i> _o)]	<i>R</i> = 0.049, <i>R</i> _w = 0.106	<i>R</i> = 0.031, <i>R</i> _w = 0.034	<i>R</i> = 0.052, <i>R</i> _w = 0.051
R indices (all data)	<i>R</i> = 0.0503, <i>R</i> _w = 0.107	<i>R</i> = 0.048, <i>R</i> _w = 0.037	<i>R</i> = 0.096, <i>R</i> _w = 0.132
largest diff. peak and hole	4.68/-2.62 e Å ⁻³	1.360/-0.980 e Å ⁻³	2.160/-1.610 e Å ⁻³

$$R = (\sum |F_o| - |F_c|) / \sum |F_o|, R_w = [(\sum |F_o| - |F_c|)^2 / \sum w(|F_c|)^2]^{1/2}$$

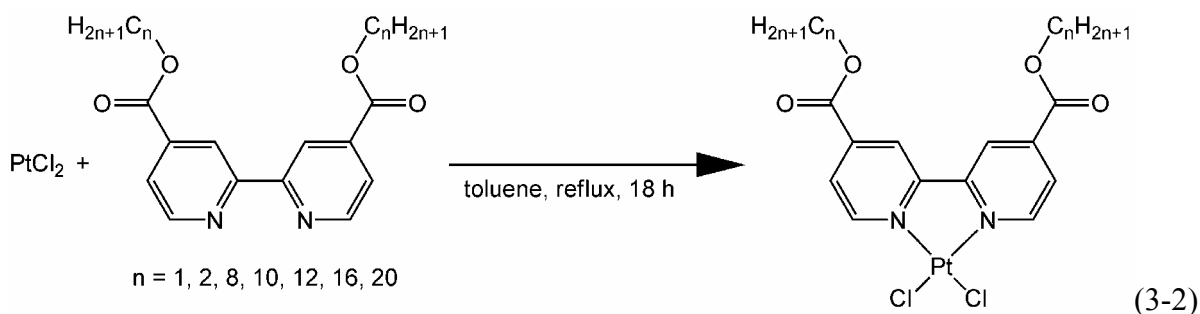
3.2.8 Variable Temperature Powder X-ray Diffraction

Finely powdered samples were placed in 0.7 mm Pyrex capillary tubes and mounted on a rotating goniometer in the monochromated $\text{CuK}\alpha$ beam of an INEL CCD spectrometer with CPS-120 detector. The instrument and beamstop were carefully aligned to give the maximum possible low-angle range (approximate minimum 2θ , $1.1\text{-}2^\circ$). Temperature was monitored via an Omega thermocouple attached to the sample capillary and maintained using a home-built forced air furnace. Temperature measurements were corrected using the known transition temperatures of an external silicon standard. Samples were allowed to equilibrate for at least 30 min prior to data collection.

3.3 Results and Discussion

3.3.1 Syntheses

The PtL^nCl_2 complexes can be readily prepared by the reaction of PtCl_2 with the corresponding bipyridine ligand in refluxing toluene (eq 3-2).



Both bis(benzonitrile)dichloroplatinum(II) and PtCl_2 may be used as the platinum starting material for these complexes, but PtCl_2 was preferred as it was more readily separated from the desired product. The reaction is easily monitored by ^1H NMR, as the $\text{H}^{6,6'}$ proton resonance shifts downfield by ~ 1 ppm upon coordination of the metal, as shown in Figure 3-10.

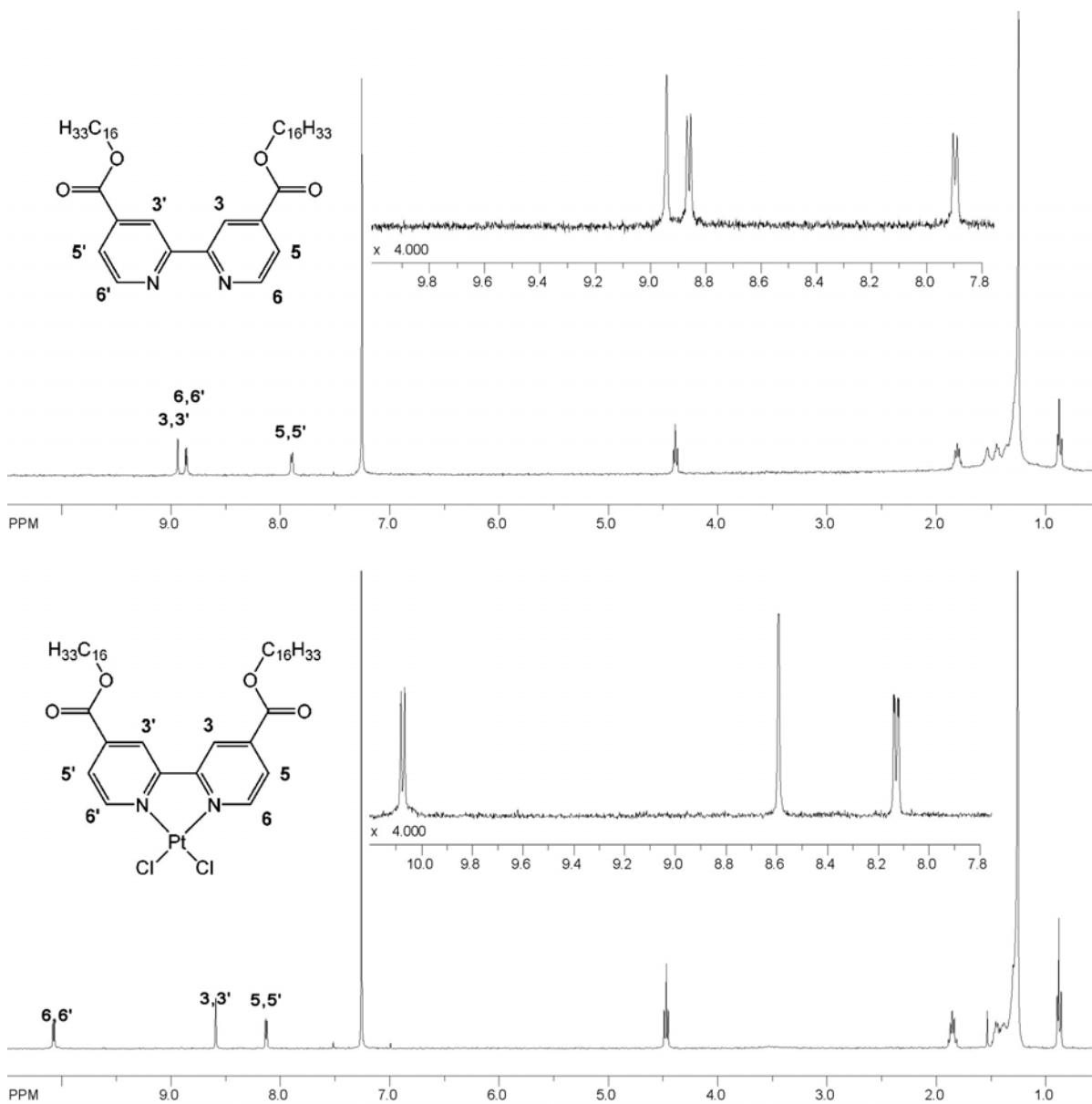
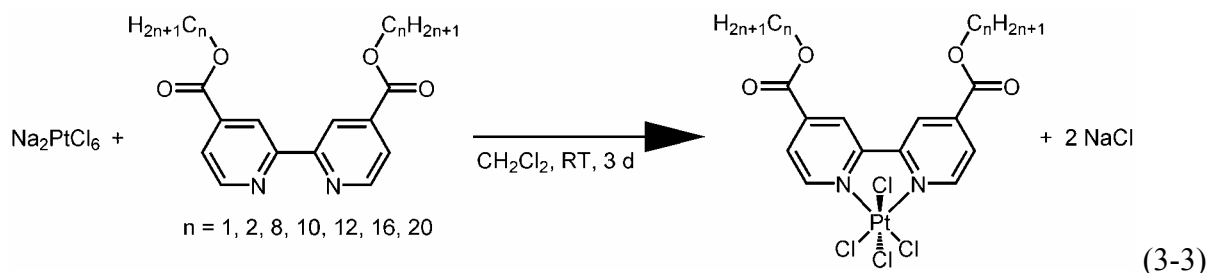


Figure 3-10. Proton NMR spectra of L^{16} (top) and $PtL^{16}Cl_2$ (bottom); $CDCl_3$, 400 MHz. To better show the aromatic resonances, the methylene resonance has been truncated.

The syntheses of the Pt^{IV} complexes are carried out using $Na_2PtCl_6 \cdot 6H_2O$ and the desired bipyridine ligand at room temperature (eq 3-3).



These reactions were complicated by the very facile reduction of the Pt^{IV} complexes to the corresponding Pt^{II} species. Using $\text{H}_2\text{PtCl}_6 \cdot 6\text{H}_2\text{O}$ as a starting material also led to formation of $\text{PtL}^{\text{n}}\text{Cl}_2$, as did the use of solvents such as ethyl acetate and methylene chloride, which had not been treated to remove trace amounts of acid and water.¹²³ Use of Na_2PtCl_6 as the starting material minimized the production of $\text{PtL}^{\text{n}}\text{Cl}_2$. Trace amounts of $\text{PtL}^{\text{n}}\text{Cl}_2$ ($n \geq 8$) may be removed by washing the product with cold hexanes. $\text{PtL}^{\text{n}}\text{Cl}_4$ is also soluble in hexanes, resulting in some product loss. Attempts at fractional recrystallization were unsuccessful due to difficulties in obtaining crystalline materials from these long alkyl chain species.

Both thermal and photochemical reduction are possible for $\text{Pt}(\text{bpy})\text{Cl}_4$.^{123, 134} Via thermogravimetric analysis (TGA), thermal decomposition of $\text{PtL}^{\text{n}}\text{Cl}_4$ was determined to occur through the loss of chlorine gas at $\sim 270^\circ\text{C}$ (Table 3-2) to form $\text{PtL}^{\text{n}}\text{Cl}_2$, as has been previously observed in the decomposition of $\text{Pt}(\text{bpy})\text{Cl}_4$.¹³⁴ The temperatures at which decomposition occurs are largely independent of alkyl chain length after accounting for the 50°C range over which significant weight loss was observed to occur during analysis. No photochemical reduction was observed to occur by ^1H NMR analysis during the synthesis of $\text{PtL}^{\text{n}}\text{Cl}_4$ in methylene chloride or during bench top storage of the isolated products over 6 months.

Table 3-2. Temperatures for PtLⁿCl₄ to PtLⁿCl₂ decomposition as determined by TGA.

Species	Temperature (°C)
PtL ² Cl ₄	299
PtL ⁸ Cl ₄	283
PtL ¹⁰ Cl ₄	272
PtL ¹² Cl ₄	264
PtL ¹⁶ Cl ₄	254
PtL ²⁰ Cl ₄	277

Successful isolation of PtLⁿCl₄ was determined by ¹H NMR analysis and confirmed by elemental analysis. Characteristic satellites were observed for the H^{6,6'} resonances of the PtLⁿCl₄ complexes due to H^{6,6'}-¹⁹⁵Pt^{IV} coupling (Figure 3-11). Coupling to ¹⁹⁵Pt was not apparent in the ¹H NMR spectra of the PtLⁿCl₂ complexes.

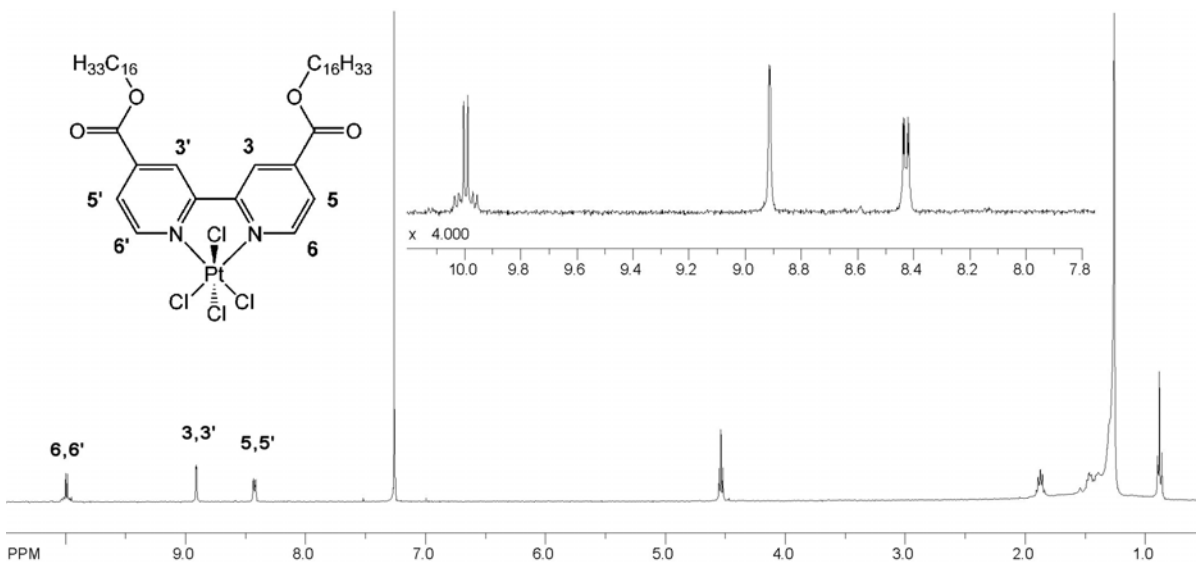
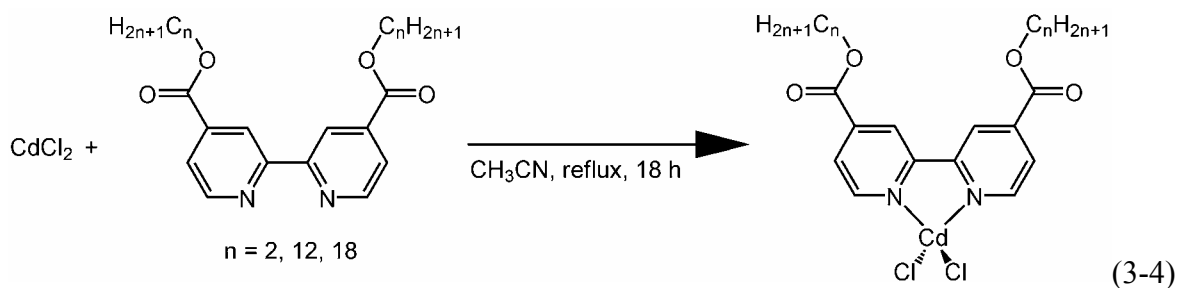


Figure 3-11. Proton NMR spectrum of PtL¹⁶Cl₄; CDCl₃, 400 MHz. To better show the aromatic resonances, the methylene resonance has been truncated.

The Cd analogues were synthesized from CdCl₂ in acetonitrile solution (eq 3-4).



The CdLⁿCl₂ complexes were characterized by ¹H NMR spectroscopy. The ¹H NMR spectra (Figure 3-12) are similar to those obtained for PtLⁿCl₂ complexes, though the H^{6,6'} resonances are not shifted as far downfield.

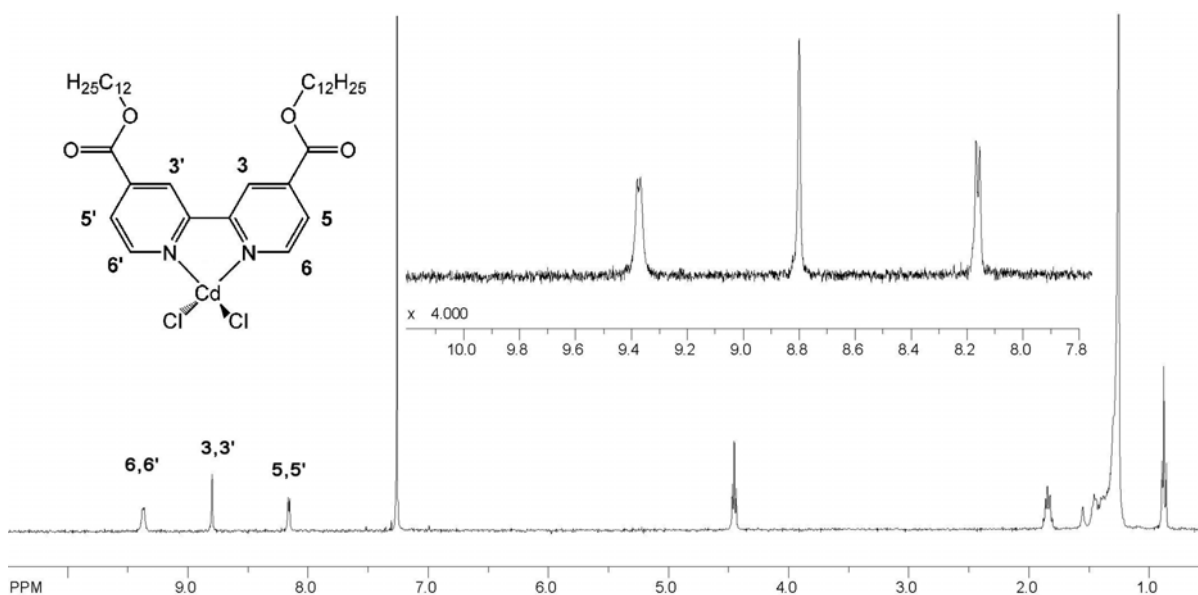
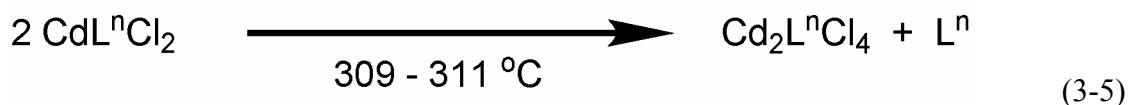


Figure 3-12. Proton NMR spectrum of CdL¹²Cl₂; CDCl₃, 400 MHz. To better show the aromatic resonances, the methylene resonance has been truncated.

Synthesis of CdLⁿCl₂ complexes should not be carried out in alcohol solvents such as methanol or ethanol, to avoid as the possibility of exchanging the ester groups on the bipyridine ligand. Products synthesized in ethanol gave ¹H NMR spectra consistent with

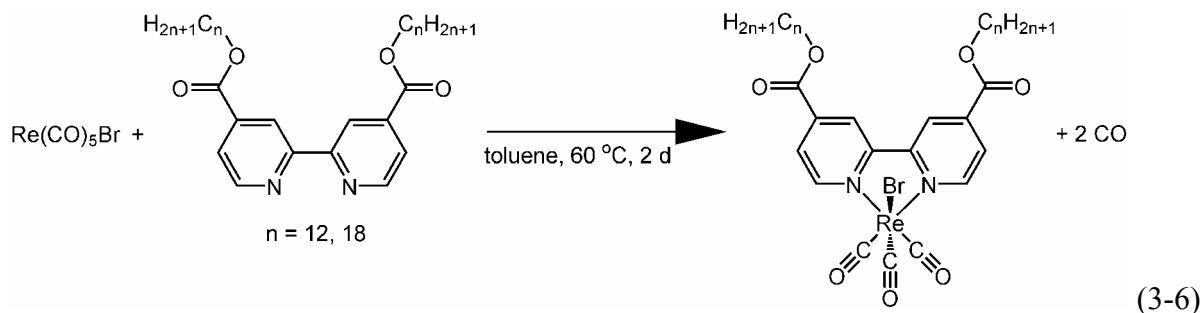
formation of asymmetric complexes in which one of the desired long alkyl esters had been exchanged for an ethyl ester.

Thermal decomposition of CdL^nCl_2 resulted in loss of one ligand for every two complexes to produce a bright pink liquid according to eq 3-5.



A previous X-ray crystallographic analysis of a similar system has shown that extended networks with bridging doubly monodentate bipyridine ligands are possible.¹³⁵

The $\text{Re}(\text{CO})_3\text{L}^n\text{Br}$ complexes were synthesized from $\text{Re}(\text{CO})_5\text{Br}$ according to eq 3-6 in a modification of the literature procedure for the synthesis of $\text{Re}(\text{CO})_3(\text{bpy})\text{Cl}$.¹³³



It was found that synthesis of the long alkyl chain $\text{Re}(\text{CO})_3\text{L}^n\text{Br}$ complexes took longer for complete conversion than for the unsubstituted bipyridine analogues. The ^1H NMR analysis of these complexes is complicated by the lack of a C_2 axis in the molecule. The ring protons are symmetry equivalent but not magnetically equivalent resulting in apparent triplets for the aromatic resonances (Figure 3-13). This inequivalency is documented in the literature for $\text{Re}(\text{CO})_3(\text{bpy})\text{Br}$.¹³⁶

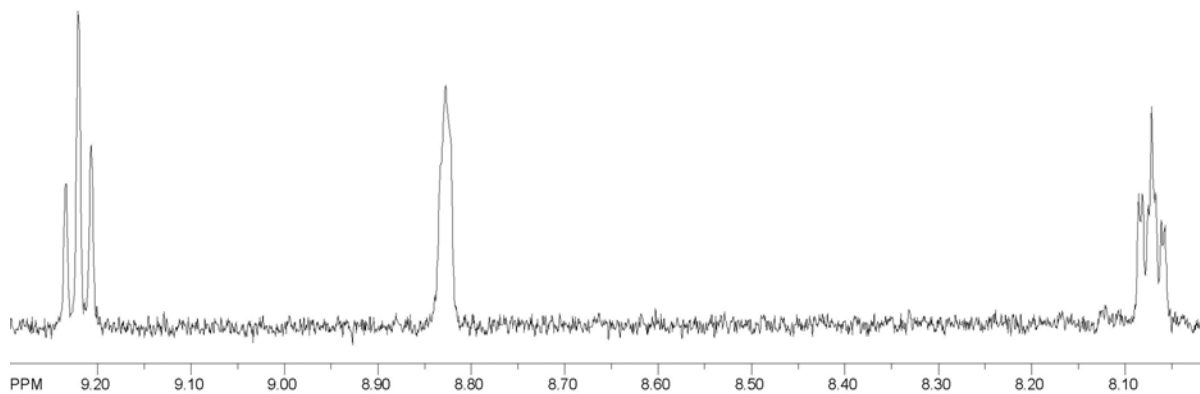


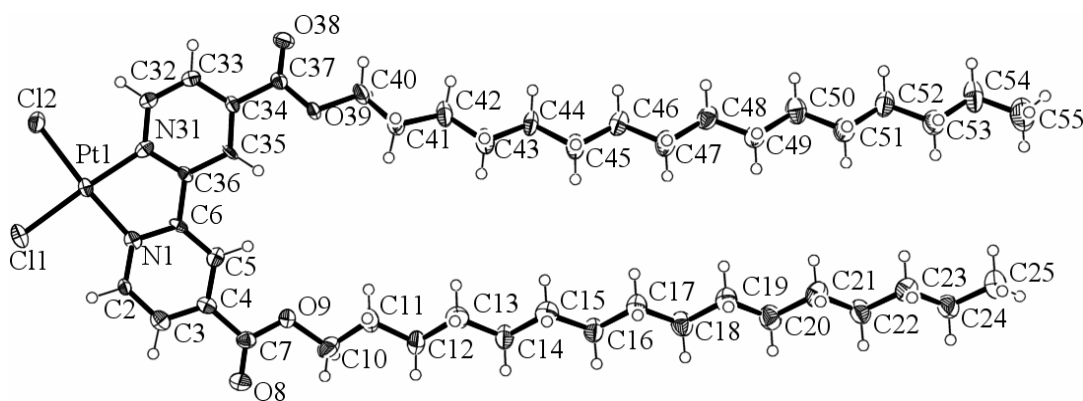
Figure 3-13. $\text{Re}(\text{CO})_3\text{L}^{18}\text{Br}$ ^1H NMR aromatic region; CDCl_3 , 400 MHz.

3.3.2 Structural Descriptions of PtL^1Cl_2 , PtL^2Cl_2 and $\text{PtL}^{16}\text{Cl}_2$

Single crystal X-ray diffraction (XRD) analysis of $\text{PtL}^{16}\text{Cl}_2$ was performed to compare the crystalline packing with the mesophase packing, which was determined from XRD patterns of the liquid crystalline phase. Selected bond distances and angles are given in Table 3-3. Figure 3-14, a thermal ellipsoid plot of $\text{PtL}^{16}\text{Cl}_2$, gives the numbering scheme utilized in the table. $\text{PtL}^{16}\text{Cl}_2$ crystallizes isomorphically with the Pd analogue.⁴⁷

Table 3-3. Selected bond angles and distances for PtL¹Cl₂, PtL²Cl₂ and PtL¹⁶Cl₂.

Species	PtL ¹ Cl ₂ •2CH ₂ Cl ₂	PtL ² Cl ₂	PtL ¹⁶ Cl ₂ • 2CHCl ₃
Pt-Pt (Å)	3.467(17)	5.58(21)	4.678(24)
		4.456(21)	3.432(24)
		3.441(21)	
Pt(1)-Cl(1) (Å)	2.2980(17)	2.2952(21)	2.3011(24)
Pt(1)-Cl(2) (Å)	2.2996(17)	2.2992(20)	2.2906(24)
Pt(1)-N(1) (Å)	2.013(6)	2.022(6)	2.001(7)
Pt(1)-N(31) (Å)	2.005(6)	2.002(6)	1.985(7)
Cl(1)-Pt(1)-Cl(2)	88.44(6)	89.21(8)	89.48(9)
N(1)-Pt(1)-N(31)	80.4(3)	80.46(24)	81.1(3)
N(1)-Pt(1)-Cl(1)	95.42(19)	95.25(18)	95.57(22)
N(1)-Pt(1)-Cl(2)	176.08(18)	175.50(19)	174.76(21)
N(31)-Pt(1)-Cl(1)	175.78(18)	175.65(17)	176.65(22)
N(31)-Pt(1)-Cl(2)	95.79(19)	95.09(17)	93.78(22)
Pt(2)-Cl(1) (Å)		2.2911(17)	
Pt(2)-Cl(2) (Å)		2.3008(18)	
Pt(2)-N(1) (Å)		2.025(6)	
Pt(2)-N(31) (Å)		2.011(5)	
Cl(1)-Pt(2)-Cl(2)		89.26(6)	
N(1)-Pt(2)-N(31)		80.69(22)	
N(1)-Pt(2)-Cl(1)		95.20(16)	
N(1)-Pt(2)-Cl(2)		175.29(16)	
N(31)-Pt(2)-Cl(1)		175.89(16)	
N(31)-Pt(2)-Cl(2)		94.85(16)	

**Figure 3-14.** Thermal ellipsoid plot for PtL¹⁶Cl₂; solvent molecules removed for clarity.

Analyses of PtL¹Cl₂ and PtL²Cl₂ were made to determine if hydrophobic interdigitation of the alkyl chains (as found in PtL¹⁶Cl₂) would be significant for very short

chains. To discuss the structures, the descriptor “in-plane” is used to refer to the plane of the bipyridine ligand, and axial is used to describe the direction perpendicular to the ligand. In the red polymorph of $\text{Pt}(\text{bpy})\text{Cl}_2$ as well as $\text{PtL}^{16}\text{Cl}_2$ crystals, the complexes orient so that all species align in-plane along the same direction (Figure 3-15).^{137, 138} In PtL^1Cl_2 crystals, the methyl esters of adjacent bipyridine ligands do not interdigitate, but short alkyl chains of PtL^2Cl_2 do begin to interdigitate as shown in Figure 3-16.

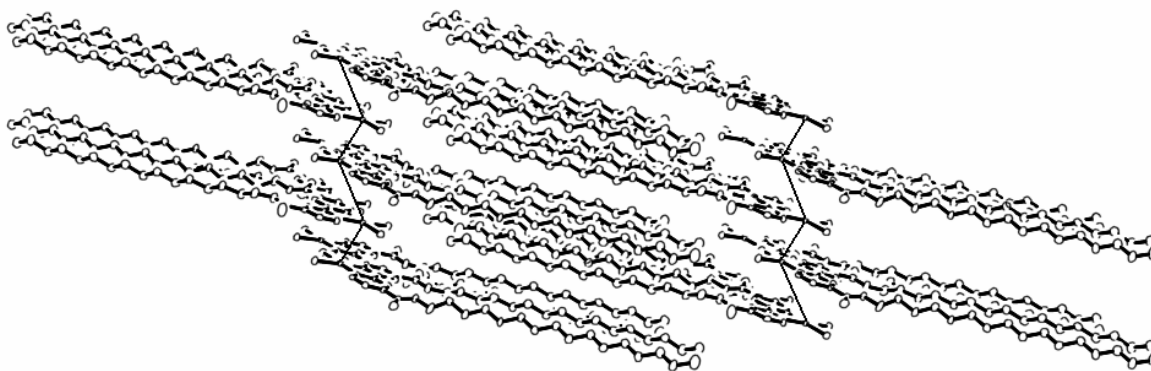


Figure 3-15. Crystalline packing of $\text{PtL}^{16}\text{Cl}_2$; solvent molecules and hydrogens removed for clarity. The $\text{Pt}\cdots\text{Pt}$ interactions alternate along the axial direction.

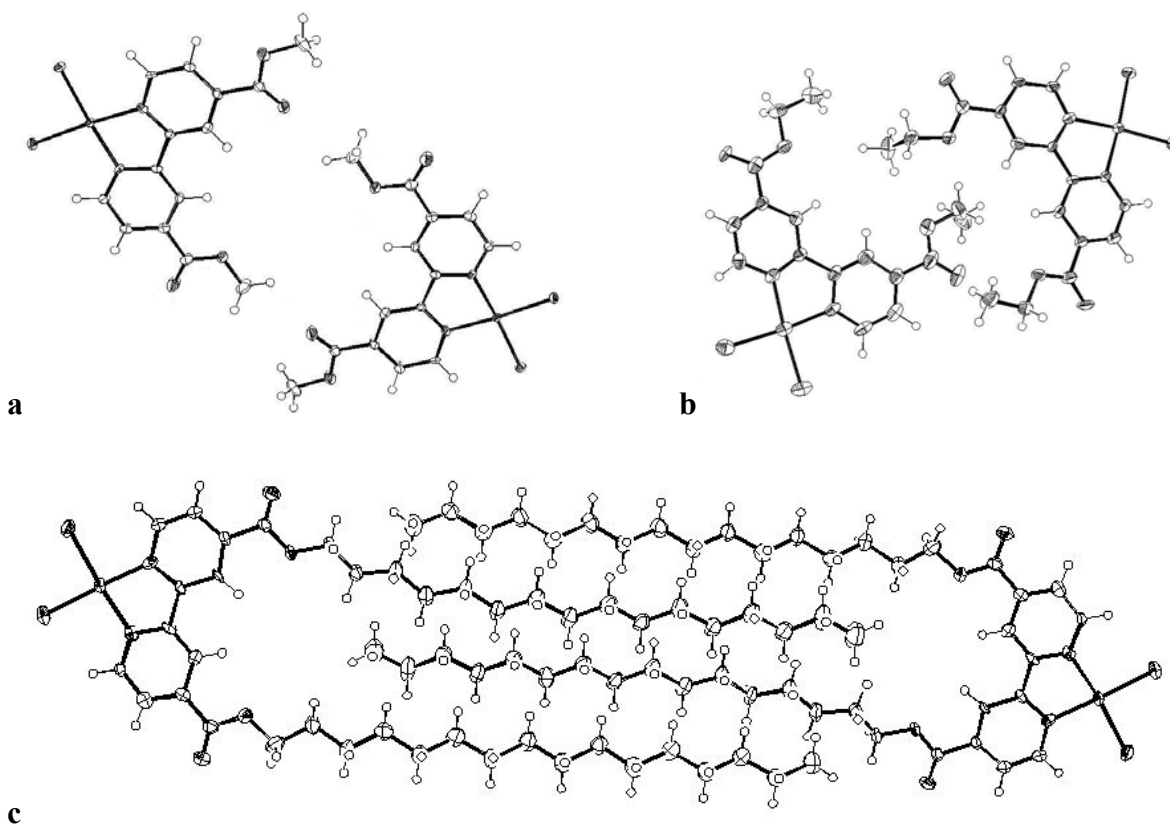


Figure 3-16. Interdigitation of the alkyl chains from the single crystal structure of $\text{PtL}^1\text{Cl}_2 \cdot 2\text{CH}_2\text{Cl}_2$ (a), PtL^2Cl_2 (b), and $\text{PtL}^{16}\text{Cl}_2 \cdot 2\text{CHCl}_3$ (c). Solvent molecules have been removed for clarity.

In all three cases, the complexes align in an head-to-head fashion offset along the axial direction as shown in Figure 3-12 resulting in a “zig-zag” chain of Pt-Pt interactions. The Pt-Pt-Pt angles are 153.62° and 127.27° for PtL^1Cl_2 and $\text{PtL}^{16}\text{Cl}_2$, respectively. These angles are intermediate between the Pt-Pt-Pt angle of the red (161.18°) and yellow (110.68°) polymorphs of $\text{Pt}(\text{bpy})\text{Cl}_2$.^{137, 138} The structure of PtL^2Cl_2 varies markedly from PtL^1Cl_2 and $\text{PtL}^{16}\text{Cl}_2$, presumably due to the absence of solvation, and has two Pt-Pt-Pt angles: 122.43° and 94.93° . Three Pt-Pt distances are obtained due to “dimers” interspersed with single PtL^2Cl_2 moieties. The single moiety is rotated to fill some of the space, which is filled with solvent in the PtL^1Cl_2 and $\text{PtL}^{16}\text{Cl}_2$ crystals.

3.3.3 Phase Transitions of PtL^nCl_2 Complexes

Differential scanning calorimetry, DSC, is utilized to determine the temperatures at which phase changes occur and the associated enthalpy changes. The transition temperatures and enthalpies are governed by dispersive forces (e.g. dynamic motion of the melted alkyl chains) and the attractive forces (e.g. dipolar, hydrophobic and Pt-Pt interactions).

As the DSC traces for all the mesogenic PtL^nCl_2 complexes ($n = 10, 12, 16, 20$) are similar (Appendix II). $PtL^{20}Cl_2$ will be discussed as a representative example. During the second heating of $PtL^{20}Cl_2$, there are a series of closely spaced first-order endotherms from ~ 50 - 60 °C, corresponding to various melting rearrangements of the alkyl chains (Figure 3-17). The rearrangement of the alkyl chains results in the formation of a second crystalline phase upon heating. By integrating the area above the endotherm, the change in enthalpy associated with the transition is obtained. Transitions with larger enthalpies correspond to greater structural rearrangements from the previous phase.

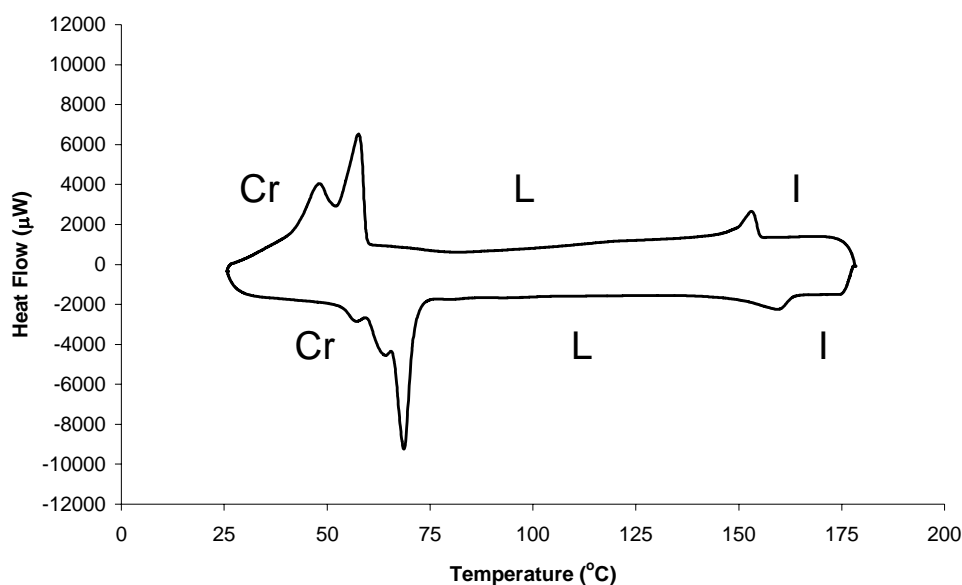


Figure 3-17. Heating and cooling curves for $PtL^{20}Cl_2$; heating rate 10 °C/min, 2nd heating shown, crystal (Cr), lamellar mesophase (L), isotropic liquid (I).

In the DSC trace for $\text{PtL}^{20}\text{Cl}_2$ shown above, an endotherm is observed at 64 °C, and the sample transitions from a crystalline solid (Cr) to a liquid crystal (Col_L). Due to the proximity of this transition to the crystalline rearrangement transition and the relatively small enthalpy change (7.6 kJ/mol) for formation of a smectic phase, the liquid crystalline phase is expected to be very similar in structure to the crystalline phase. The $\text{PtL}^{20}\text{Cl}_2$ mesophase clears, forming an isotropic liquid (I), at 155 °C. Upon cooling, the exotherm observed at 150 °C corresponds to an increase in ordering upon formation of the liquid crystalline phase from the isotropic liquid. The sample crystallizes at 55.7 °C, and undergoes some solid-state rearrangements on cooling, as evidenced by the multiple exotherms for crystalline to crystalline transitions.

PtL^nCl_2 complexes with a variety of alkyl chain lengths were synthesized. Figure 3-18 charts the variation in transition temperatures for the PtL^nCl_2 complexes with chain length. In Figure 3-18 the mesogenic phase is described as lamellar for reasons that will be explained in the X-ray diffraction discussion below. Table 3-4 summarizes the thermal behavior of the PtL^nCl_2 complexes. The enthalpy changes associated with the crystalline rearrangements increase with the alkyl chain length for the PtL^nCl_2 ($n = 8, 10, 12, 16, 20$) complexes. This larger enthalpy change for longer alkyl chains is consistent with the assignment of the transition as a Cr1 to Cr2 transition involving alkyl chain rearrangement. Comparison of the values for the PtL^nCl_2 ($n = 8, 10, 12, 16, 20$) complexes with PtL^2Cl_2 is difficult because of the different solid-state structure observed for PtL^2Cl_2 as were described above. The enthalpy changes associated with the Cr to L and I to L transitions are relatively uniform at 5-8 kJ/mol. This relatively large enthalpy change is more typically associated

with formation of smectic mesophases than the 1-2 kJ/mol values expected for the transitions to and from a nematic mesophase.

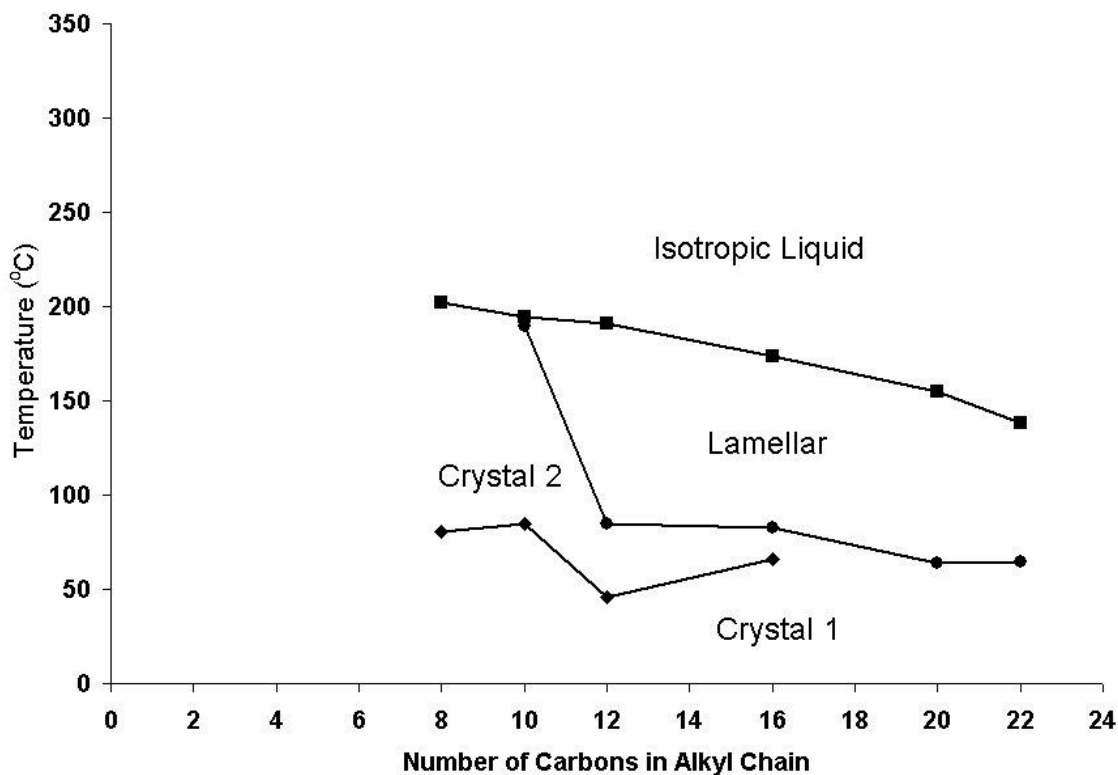


Figure 3-18. Phase diagram for the crystal 1 to crystal 2 (♦), crystal 2 to lamellar (●) and lamellar or crystal 2 to isotropic (■) transitions of PtL^nCl_2 complexes. Data for PtL^8Cl_2 and $\text{PtL}^{22}\text{Cl}_2$ are from Pucci et al.⁴⁷

Table 3-4. Thermal properties of the PtLⁿCl₂ complexes.

PtL ⁿ Cl ₂	Transition ^[a]	Temperature (°C)	Enthalpy (kJ/mol)
PtL ¹ Cl ₂	decomposition	312	---
PtL ² Cl ₂	Cr1 to Cr2 ^[b]	296.3	44.9
	decomposition	335.0	---
PtL ⁸ Cl ₂ ^[c]	Cr1 to Cr2	80.9	3.8
	Cr2 to I	202.4	11.4
	I to Cr2	201.7	11.0
	Cr2 to Cr1	57.8	8.9
PtL ¹⁰ Cl ₂	Cr1 to Cr2	84.5	6.0
	Cr2 to L	189.8	6.3
	L to I	194.6	4.7
	I to L	190.3	4.7
	LC to Cr2	184.8	4.4
	Cr2 to Cr1	59.4	5.5
PtL ¹² Cl ₂	Cr1 to Cr2	46.1	5.7
	Cr2 to L	84.5	6.8
	L to I	190.9	16.3
	I to L	186.1	15.9
	L to Cr1	61.3	5.0
PtL ¹⁶ Cl ₂	Cr1 to Cr2	66.0	25.2
	Cr2 to L	82.6	6.4
	L to I	173.8	16.3
	I to L	170.2	11.3
	L to Cr2	55.5	5.5
	Cr2 to Cr1	27.7	24.3
PtL ²⁰ Cl ₂	Cr1 to L	64.2	44.0
	L to I	155.1	7.6
	I to L	149.9	6.7
	L to Cr2	55.7	16.3
	Cr2 to Cr1	50.7	29.8

^[a] Cr1: crystal 1; Cr2: crystal 2; L: lamellar; I: isotropic liquid

^[b] data from the 1st heating curve due to decomposition

^[c] data obtained from Pucci et al.⁴⁷

Pucci and coworkers previously studied PtL¹⁶Cl₂ and did not report a Cr1 to Cr2 transition upon heating, though the reverse transition was reported upon cooling.⁴⁷ However,

variable temperature XRD analysis of $\text{PtL}^{16}\text{Cl}_2$ showed that the reflections broadened from 60-70 °C (Appendix III), and a first order transition was observed in the DSC trace at 66 °C. These results support a crystalline rearrangement (Cr1 to Cr2 transition) upon heating. The other transition temperatures and enthalpies for $\text{PtL}^{16}\text{Cl}_2$ were in good agreement with the previously reported values.

All the Pt^{II} mesogenic phases displayed the same type of birefringent texture under optical analysis. Although a mosaic texture may be obtained from thin samples which have been sheared considerably, the fine texture shown in Figure 3-19 was most often observed.

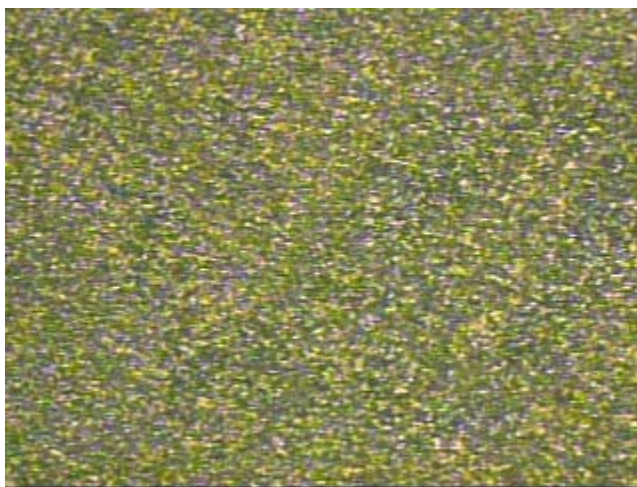


Figure 3-19. Texture of $\text{PtL}^{20}\text{Cl}_2$ under cross-polarization. Similar textures are observed for all unsheared mesomorphic PtL^nCl_2 complexes studied here.

3.3.4 Variable Temperature X-ray Diffraction of PtL^nCl_2 Mesophases

Analysis of the $\text{PtL}^{12}\text{Cl}_2$ mesophase by XRD provides for an informative comparison both to the previously reported $\text{PtL}^{16}\text{Cl}_2$ complex⁴⁷ and to the $\text{PtL}^{12}\text{Cl}_4$ complex, which will be discussed in the next section. The XRD pattern for $\text{PtL}^{12}\text{Cl}_2$ at 115 °C is shown in Figure 3-20. The diffraction pattern is plotted as intensity vs the magnitude of the scattering vector,

Q, for easier comparison of data taken using different radiation wavelengths. Q is defined in eq 3-7.

$$|\mathbf{Q}| \equiv Q = \frac{4\pi \sin\Theta}{\lambda} \quad (3-7)$$

A series of four evenly-spaced low angle reflections are observed in the diffraction pattern and are assigned as the (100), (200), (300) and (400) reflections. The *a*-dimension is dictated by the phase separation of the metal-aromatic domain from the alkyl chains to form smectic layers.^{49, 139} From these reflections, a layer spacing of 29.3 Å may be calculated. The expected molecular length for PtL¹²Cl₂ is ~21 Å, giving a ratio of layer spacing to molecular length of 1.4. This is within the 1.4-1.8 range normally expected for semi-bilayer smectic phases.⁴⁹

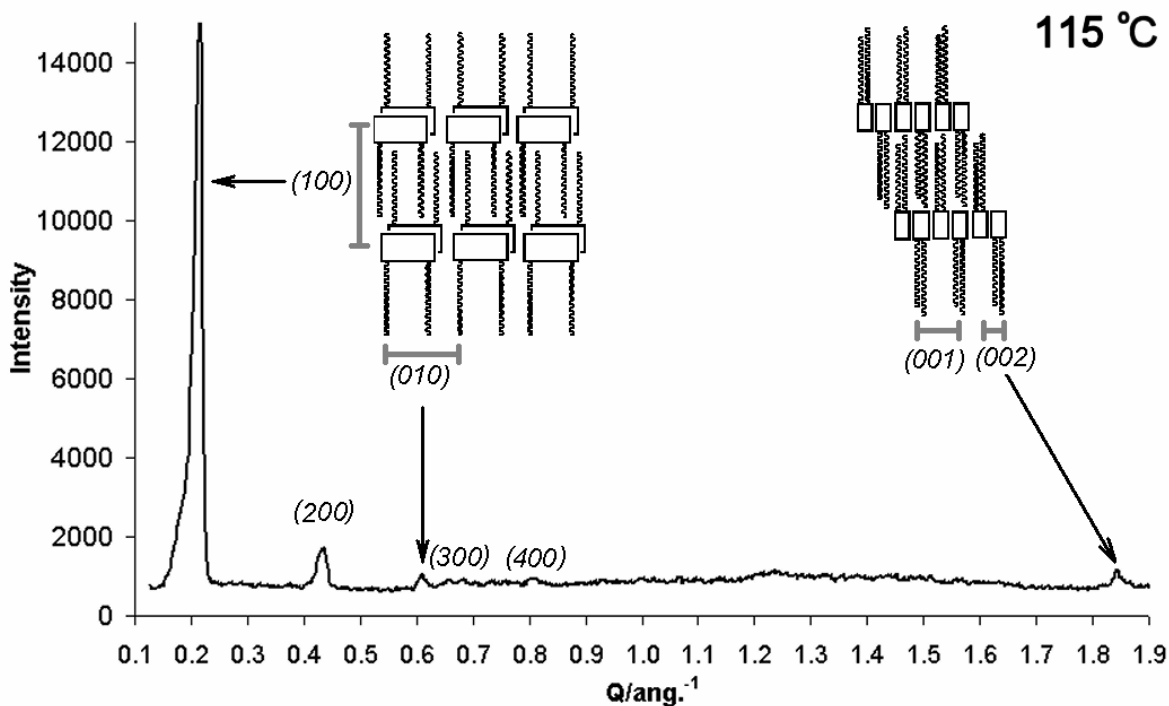


Figure 3-20. X-ray diffraction pattern for the lamellar PtL¹²Cl₂ mesophase at 115 °C.

There are also two sharp reflections corresponding to d -spacings of 10.3 and 3.4 Å respectively in the XRD pattern for the PtL¹²Cl₂ mesophase. The former is the (010) reflection, and corresponds to the in-plane Pt-Pt distance due to the positions of the Pt centers within the unit cell. The reflection for the 3.4 Å d -spacing is the (002) reflection. The (001) reflection is expected to be systematically absent due to the screw-axis relating the mesogens along the axial dimension in the P222₁ unit cell. The unit cell packing is diagramed in Figure 3-20. The broad reflection centered at 1.29 Å⁻¹ corresponds to liquid-like hydrophobic packing of the alkyl chains.

A simulated diffraction pattern may be calculated using the unit cell dimensions $a = 29.3$ Å, $b = 10.3$ Å, $c = 6.8$ Å, $\alpha = \beta = \gamma = 90^\circ$, and a P222₁ unit cell as shown in Figure 3-21. The formula unit has been simplified to contain only a Pt atom. While the unit cell contents will affect the intensities of the reflections, the positions of reflections and systematic absences are unaffected.¹⁴⁰ The calculated and observed d -spacings and assignments of the reflections are given in Table 3-5. The apparent absence of several calculated reflections is expected due to the very short range ordering of the mesophase in comparison to the nearly infinite long range ordering of a calculated powder pattern. Correlation distance, the distance over which translational ordering of the moieties is maintained, is inversely proportional to the peak width of the reflections.⁴⁹ At very short correlation distances, like those expected for the short-range-ordering in the b and c dimensions, the reflections broaden until they are no longer apparent. The low angle reflections, corresponding to the quasi-long range ordering of the smectic layers, are expected to have a progressively greater broadening for the higher order reflections.⁴⁹ Consistent with this explanation, the (100) and (200)

reflections are observed as distinct peaks, and only broad baseline reflections are observed at the expected position for the (300) and (400) reflections.

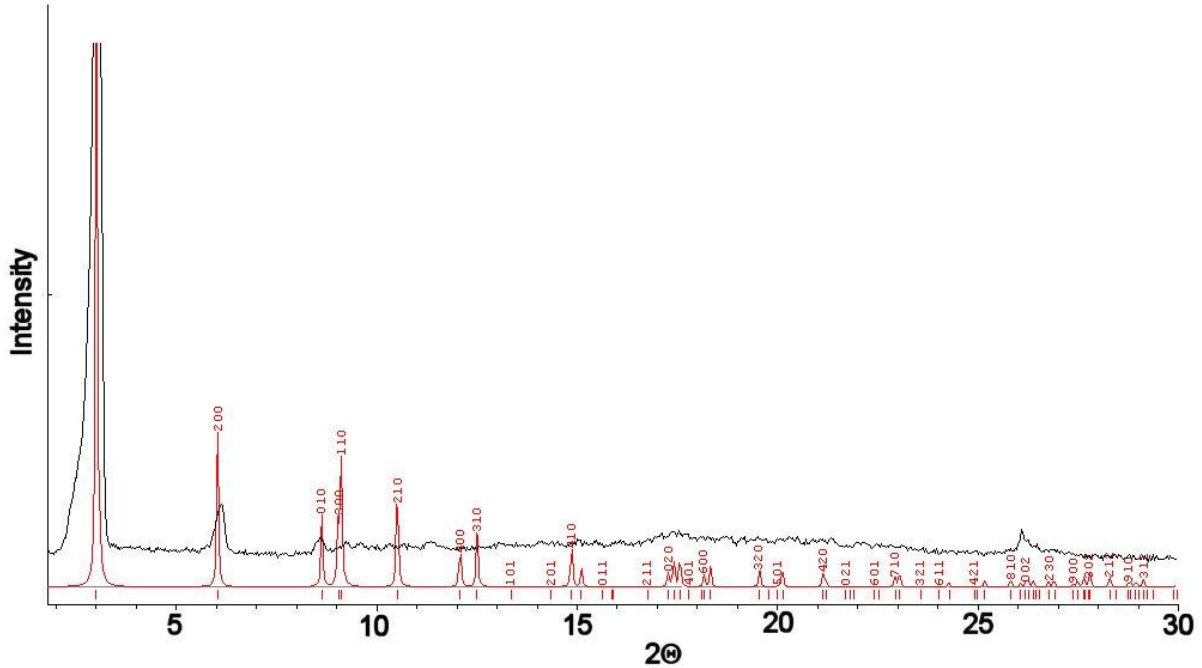


Figure 3-21. Experimental (top) and calculated (bottom) X-ray diffraction pattern for the lamellar PtL¹²Cl₂ mesophase at 115 °C; (100) reflection has been truncated to better show the low intensity reflections.

Table 3-5. X-ray diffraction data for PtL¹²Cl₂ mesophase at 115 °C, including calculated reflections for a P222₁ unit cell.

Q (Å ⁻¹)	d _{meas.} (Å)	d _{calc.} (Å)	hkl
0.21	29.9	29.3	100
0.44	14.3	14.7	200
0.61	10.3	10.3	010
0.66	9.5	9.8	300
0.68	9.2	9.7	110
0.81	7.8	7.3	400
1.24	5.1	5.1	020
1.29		4.9 (broad)	
1.84	3.4	3.4	002

L: $a= 29.3 \text{ \AA}$, $b= 10.3 \text{ \AA}$, $c= 6.8 \text{ \AA}$, $\alpha= 90^\circ$, $\beta= 90^\circ$, $\gamma= 90^\circ$.

Pucci and coworkers previously described the mesogenic phases of $\text{PtL}^{16}\text{Cl}_2$, $\text{PtL}^{22}\text{Cl}_2$, and the Pd analogues as having both SmA_d and Col_L characteristics, and termed the phase lamellar (L).^{47, 103} The analysis of the $\text{PtL}^{12}\text{Cl}_2$ mesophase is in agreement with this result and is further confirmed by comparison of the single crystal structure and calculated powder patterns. The Pt-Pt distance was determined by Pucci et al. to be 3.4 Å, a result confirmed by our work.⁴⁷ This average Pt-Pt distance is actually shorter than the 3.432(24) and 4.678(24) Å distances obtained from the single-crystal structure of $\text{PtL}^{16}\text{Cl}_2 \cdot 2\text{CHCl}_3$. The relative sharpness⁴⁹ of the 3.4 Å reflection suggests quasi-long range columnar ordering compatible with a characterization of Col_L for the phase, while the (100), (200), (300), and (400) progression of reflections and a layer spacing of 29.3 Å is consistent with the SmA_d characterization.

Cocker and Bachman reported the phase behavior of several 4,4'-dialkyl derivatives of $[\text{M}(\text{bpy})(\text{S}_2\text{C}_6\text{H}_4)]$ (where M = Ni, Pt, and bpy = 2,2'-bipyridine).¹¹³ Although very similar in structure and headgroup axial dimension to the PtL^nCl_2 complexes reported here, the additional aromatic ligand on the metal center leads to a much more organized mesophase. This greater degree of organization is presumably due to the increased π - π stacking interactions and/or the increased disc-shape of the aromatic core. A Col_H soft crystalline phase was obtained for the $[\text{M}(\text{bpy})(\text{S}_2\text{C}_6\text{H}_4)]$ complexes rather than a true liquid crystalline phase.

3.3.5 Phase Transitions of PtL^nCl_4 Complexes

Despite the small change in overall structure, the addition of axial chlorine ligands and the resulting increase in the axial dimension of the headgroup to ~ 7 Å significantly

affects the mesomorphic properties of PtL^nCl_4 . PtL^nCl_4 complexes ($n = 10, 12, 16, 20$) display a mesogenic phase with melting and clearing temperatures lower than those observed for the corresponding PtL^nCl_2 complexes. As a representative example, the DSC trace for $\text{PtL}^{20}\text{Cl}_4$ is given in Figure 3-22. Upon heating, an endothermic crystalline to crystalline transition is observed at 71 °C and a crystalline to liquid crystalline transition endotherm is observed at 80 °C. Due to the proximity of these two transitions, they are not well resolved, but the sample is not observed to shear under pressure during optical analysis until ~80 °C. Shearing under pressure is considered a requirement for a phase to be a true liquid crystalline phase rather than a soft crystalline phase. The sample becomes an isotropic liquid at 155 °C. A uniform mesophase which shears under pressure is obtained at 102 °C upon cooling. The cooling behavior of the samples is complicated by a tendency towards formation of glassy domains, but a crystallization exotherm is observed at 61 °C. The solid-state rearrangement transitions occur over a broader temperature range, but the overall enthalpy change for the rearrangements is approximately the same on heating and cooling, characteristic of thermally stable, reversible rearrangements.

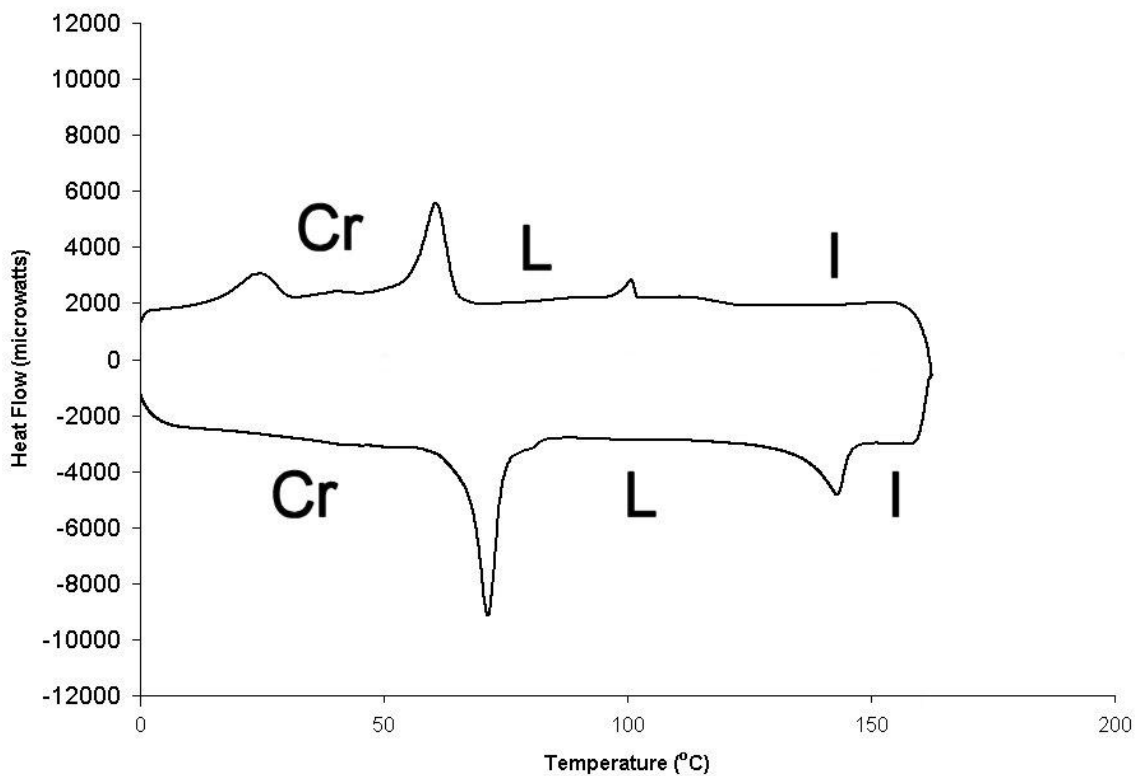


Figure 3-22. Heating and cooling curves for $\text{PtL}^{20}\text{Cl}_4$; heating rate $10\text{ }^\circ\text{C}/\text{min}$; 2nd heating shown; crystal (Cr), lamellar mesophase (L), isotropic liquid (I).

The mesogenic PtL_nCl_4 complexes have a significantly different texture under cross-polarization (Figure 3-23) than their Pt^{II} counterparts. This morphology is not readily characterized as corresponding to any of the standard textures in the literature.¹⁴¹



Figure 3-23. Mesogenic texture of $\text{PtL}^{20}\text{Cl}_4$ under cross-polarization. All mesogenic PtL^nCl_4 complexes display similar texture.

By far the most striking change upon addition of axial ligands is the increased supercooling observed in the DSC traces when comparing forward and reverse temperatures for the mesogenic to isotropic transition; though supercooling is, in part, controlled by cooling rate. The transition temperatures and enthalpy changes associated with those transitions for PtL^nCl_4 complexes are given in Table 3-6. This large degree of supercooling is more characteristic of transitions involving crystalline or soft crystalline phases.⁴⁸ Though easily deformable, the mesogenic phases of the PtL^nCl_4 complexes do not flow freely. This behavior also supports the PtL^nCl_4 mesogenic phase having some soft crystalline character. An additional difference between the PtL^nCl_4 complexes and their Pt^{II} analogues is the lack of alkyl chain length dependence for the PtL^nCl_4 clearing temperature as shown in Figure 3-24.

Table 3-6. Thermal properties of the PtLⁿCl₄ complexes.

PtL ⁿ Cl ₄	Transition ^[a]	Temperature (°C)	Enthalpy (kJ/mol)
PtL ² Cl ₄	Cr1 to Cr2 ^[b]	259.0	79.9
PtL ⁸ Cl ₄	Cr1 to Cr2	25.5	0.5
	Cr2 to I	127.7	2.9 ^[a]
	I to Cr2	118.8	3.0 ^[a]
	Cr2 to Cr1	9.0	0.4
PtL ¹⁰ Cl ₄	Cr1 to Cr2	79.6	0.7
	Cr2 to L	116.2	0.3
	L to I	148.5	14.8 ^[a]
	I to L	127.4	14.9 ^[a]
	L to Cr2	105.9	0.3
	Cr2 to Cr1	58.3	0.4
PtL ¹² Cl ₄	Cr1 to Cr2	18.2	12.2
	Cr2 to L	30.2	0.3
	L to I	147.9	17.8
	I to L	117.6	11.3
	L to Cr2	26.2	0.3
	Cr2 to Cr1	14.4	11.3
PtL ¹⁶ Cl ₄	Cr1 to Cr2	57.7	26.1
	Cr2 to L	68.6	0.4
	L to I	142.7	14.7
	I to L	102.9	14.1
	L to Cr2	55.0	0.02
	Cr2 to Cr1	49.1	27.2
PtL ²⁰ Cl ₄	Cr1 to Cr2	70.7	42.4
	Cr2 to L	79.6	2.8
	L to I	141.3	17.4
	I to L	101.2	7.5
	L to Cr2	61.4	18.4
	Cr2 to Cr1	25.7	16.0

[a] Due instrumental difficulties in proximity to the temperature for decomposition of PtLⁿCl₄ to PtLⁿCl₂, this value is estimated.

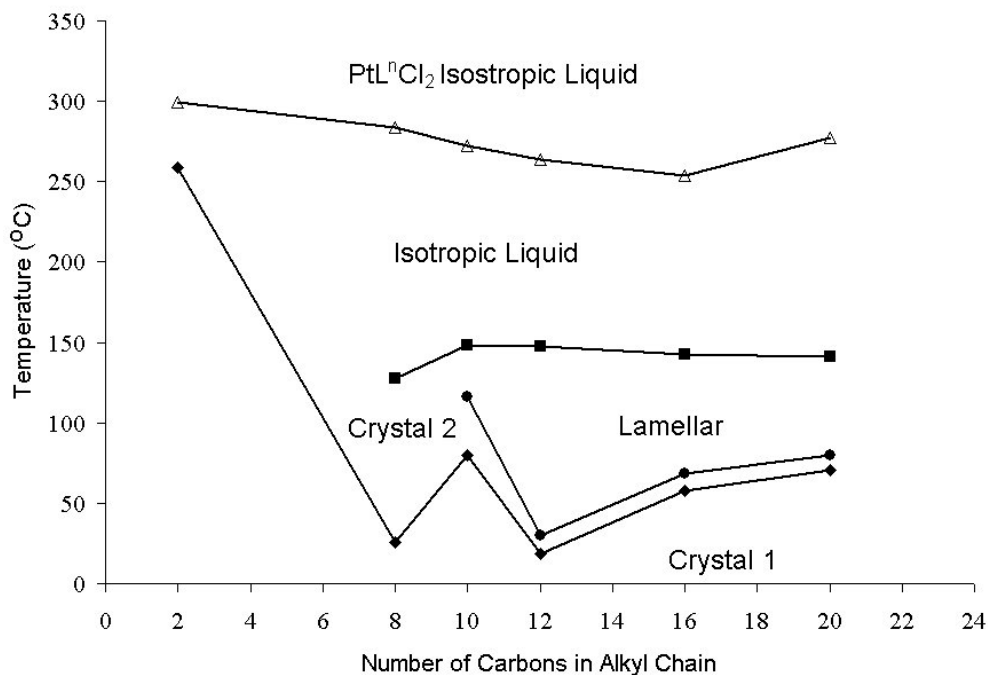


Figure 3-24. Phase diagram for the crystal 1 to crystal 2 (◆), crystal 2 to lamellar (●), and lamellar or crystal 2 to isotropic (■) transitions and the PtLⁿCl₄ to PtLⁿCl₂ decomposition (Δ) temperatures of PtLⁿCl₄ complexes.

3.3.6 Variable Temperature X-ray Diffraction of PtLⁿCl₄ Mesophases

To clarify the nature of the mesophase, XRD analysis was performed on Pt^{IV} complexes of two different alkyl chain lengths: PtL¹²Cl₄ and PtL¹⁶Cl₄. Because these two species form the same phase, the affect of increased alkyl chain length on the unit cell dimensions may be utilized to identify reflections. The XRD patterns for PtL¹²Cl₄ and PtL¹⁶Cl₄ are shown in Figure 3-25. As with the Pt^{II} analogues, there are layered hydrophobic and metal-aromatic domains. The presence of liquid-like alkyl chain interactions in a hydrophobic domain is confirmed by broad reflection at $\sim 1.3 \text{ \AA}^{-1}$ in the XRD pattern for both the Pt^{II} and Pt^{IV} mesophases.

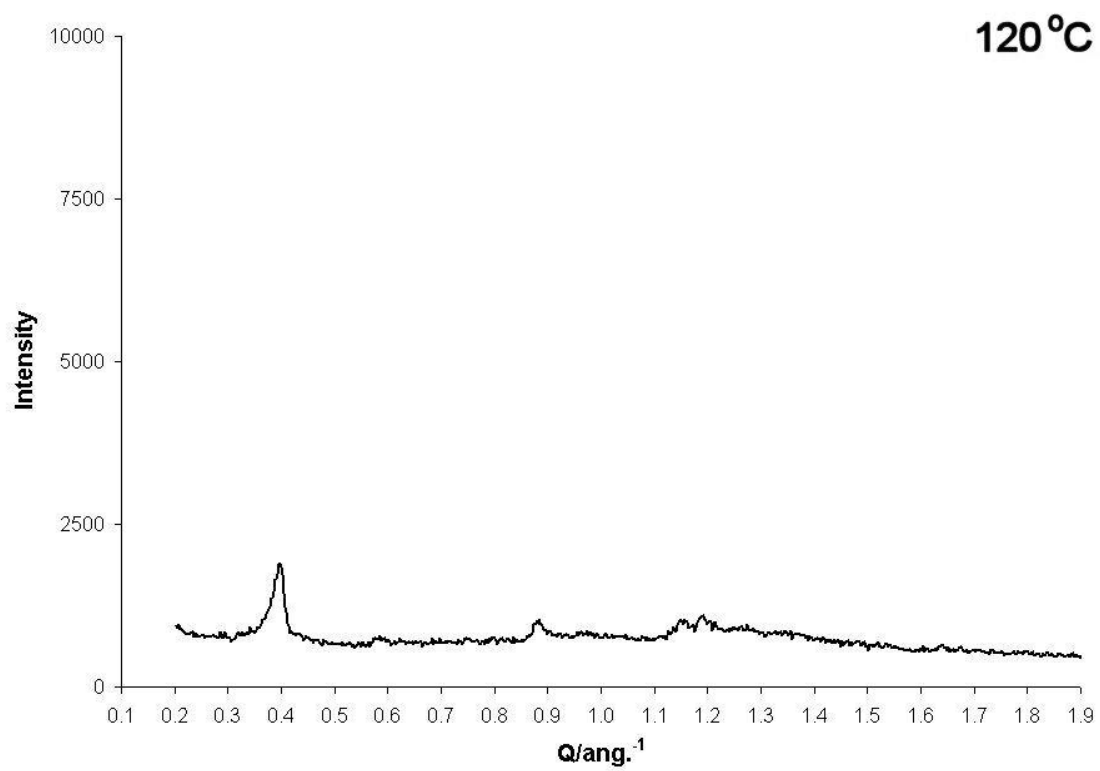
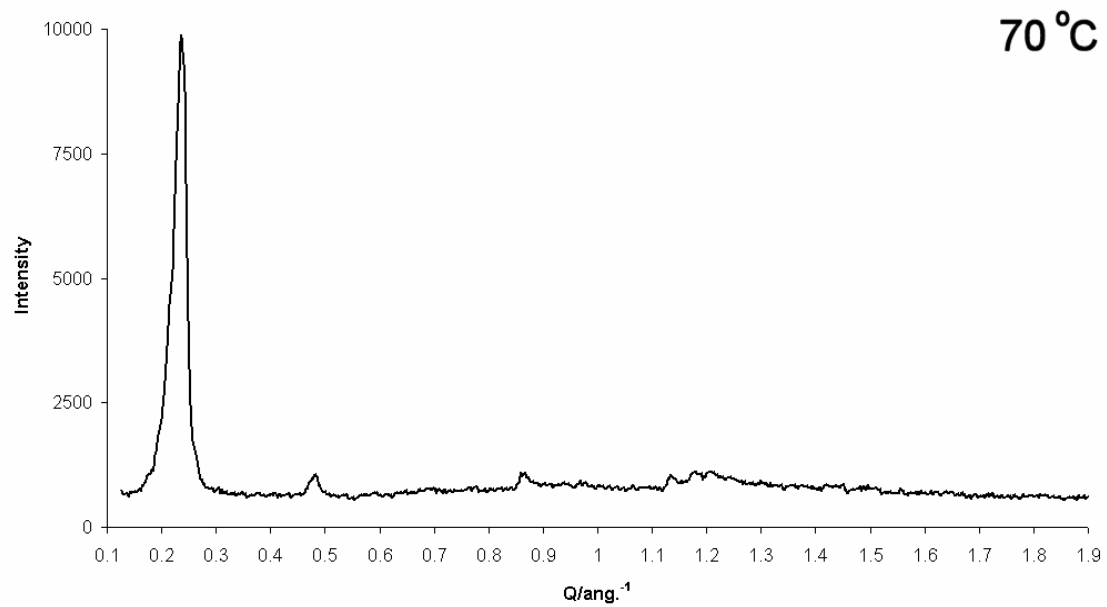


Figure 3-25. X-ray diffraction patterns for PtL¹²Cl₄ (top) and PtL¹⁶Cl₄ (bottom) mesophases.

The intense fundamental reflections for PtL¹²Cl₄ and PtL¹⁶Cl₄ demonstrate chain length dependence, and the positions and intensities of these peaks support assignment as (001) and (002) reflection from a lamellar phase. The PtL¹⁶Cl₄ (001) reflection is too close to the X-ray beam to be observed. In hexatic phases, the sharp low angle reflections positions correspond to the progression: 1, (1/2)^{1/2}, (1/3)^{1/2}, 1/2.⁴⁹ This progression is not observed here. However, the reflections are compatible with smectic as well as Col_L and Col_R phases.

As determined from the XRD pattern, the PtL¹⁶Cl₄ mesophase has a layer spacing of 31.7 Å. The molecular length of Pt¹⁶Cl₄, the same as that of PtL¹⁶Cl₂, is ~28 Å. For PtL¹²Cl₄, the dimensions are 26.0 Å and ~21 Å for the layer spacing and molecular length, respectively. The 1.1-1.2 ratio of layer spacing to molecular length is below the 1.4-1.8 expected for SmA_d mesophases.⁴⁹ The layer spacings are significantly smaller than those of the analogous Pt^{II} mesophases.

To account for this decrease in layer spacing, two different models were analyzed. In the first model, the packing of the PtLⁿCl₄ mesophase was explored as a perturbation of the PtLⁿCl₂ mesophase, taking into account the increased steric bulk of the PtLⁿCl₄ headgroup. In the second model, the packing of the PtLⁿCl₄ headgroup was based on the crystalline packing of Pt(bpy)Cl₄, with appropriate modifications to account for the smectic layering caused by the long alkyl chains. Due to the complexity of the diffraction pattern and the inability to definitively assign reflections as (h00) or (0k0) based solely on a one-dimensional diffraction patterns (Figure 3-25), the packing of the headgroups in this lamellar mesophase cannot be definitively determined.

To pack untilted $\text{PtL}^{12}\text{Cl}_4$ moieties with fully extended alkyl chains into smectic layers of 26 Å spacing, both the alkyl chains and the bipyridine moieties would need to be interdigitated as shown in Figure 3-26. Systems with this type of interdigitated columnar interaction are not common, but have been previously observed the V=O moieties of oxovanadium liquid crystals.¹⁴² The axially interdigitated arrangement is sterically crowded for the PtL^nCl_4 complexes, with the axial chlorides of one complex expected to interact with the bipyridine ring 3,3' hydrogens of the next complex.

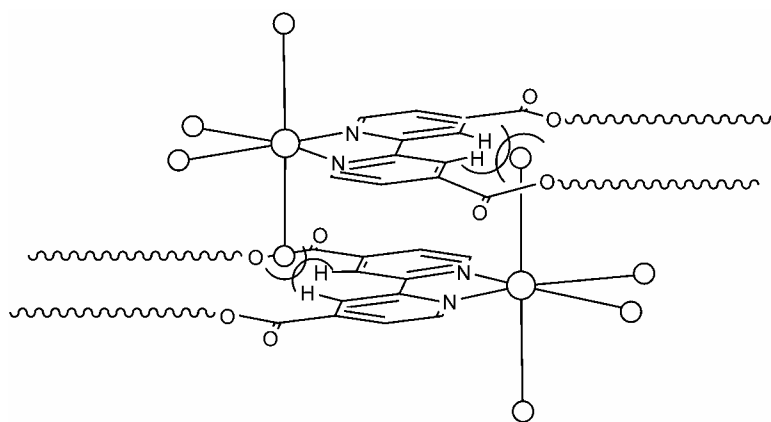


Figure 3-26. Possible packing of the metal-bipyridine moieties in PtL^nCl_4 liquid crystalline phases, which is disfavored due to the repulsions between the chloride ligands and the 3,3' bipyridine protons.

The directly overlapped bipyridine rings arrangement in Figure 3-26 resulting from the interdigitated axial chlorides would promote π - π stacking along a screw axis; however, no reflections corresponding to this dimension are observed in the XRD pattern. The observation of a reflection corresponding to a ~ 3.5 Å spacing, often a (020) reflection, is well supported in the literature, even in cases where the overlap of the bipyridine rings is not complete or symmetrical.^{41, 42, 142, 143} However, this lack of an observed screw axis may be due to formation of “dimers”, which results in two alternating intermolecular distances along the *b*-dimension of the unit cell.

The second model explored for the interactions in the PtL^nCl_4 mesophases is based on the structure of crystalline $\text{Pt}(\text{bpy})\text{Cl}_4$. This approach to modeling mesophase structure was successful for $\text{PtL}^{16}\text{Cl}_2$, where the *a*- and *b*-dimensions for the model were based on the intermolecular interactions of the Pt^{II} -bipyridine headgroup in the crystal structures of $\text{PtL}^{16}\text{Cl}_2$ and red $\text{Pt}(\text{bpy})\text{Cl}_2$.¹³⁷ Analogously, the intermolecular interactions crystalline $\text{Pt}(\text{bpy})\text{Cl}_4$ may analyzed to asses potential supramolecular ordering interactions between adjacent Pt^{IV} -bipyridine moieties in PtL^nCl_4 . In crystalline $\text{Pt}(\text{bpy})\text{Cl}_4$, a partial π - π stacking overlap of adjacent bipyridine rings is observed with a spacing of 3.79 Å (Figure 3-27).¹⁴⁴ This π - π stacking interaction can be expected to occur in PtL^nCl_4 mesophase provided it does not interfere with the hydrophobic packing of the alkyl chains. As shown in the proposed structure in Figure 3-28, the π - π stacking interaction and the interdigitated tilted alkyl chains are compatible both with each other and with the *c*-spacing dimension observed in the XRD pattern.

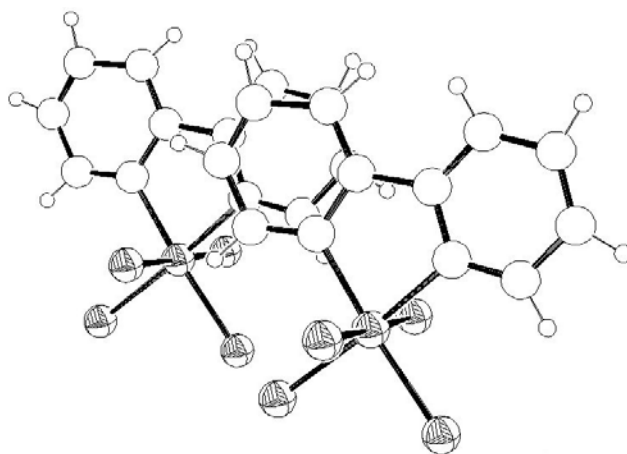


Figure 3-27. Partial π - π overlap in the single crystal structure of $\text{Pt}(\text{bpy})\text{Cl}_4$.¹⁴⁴

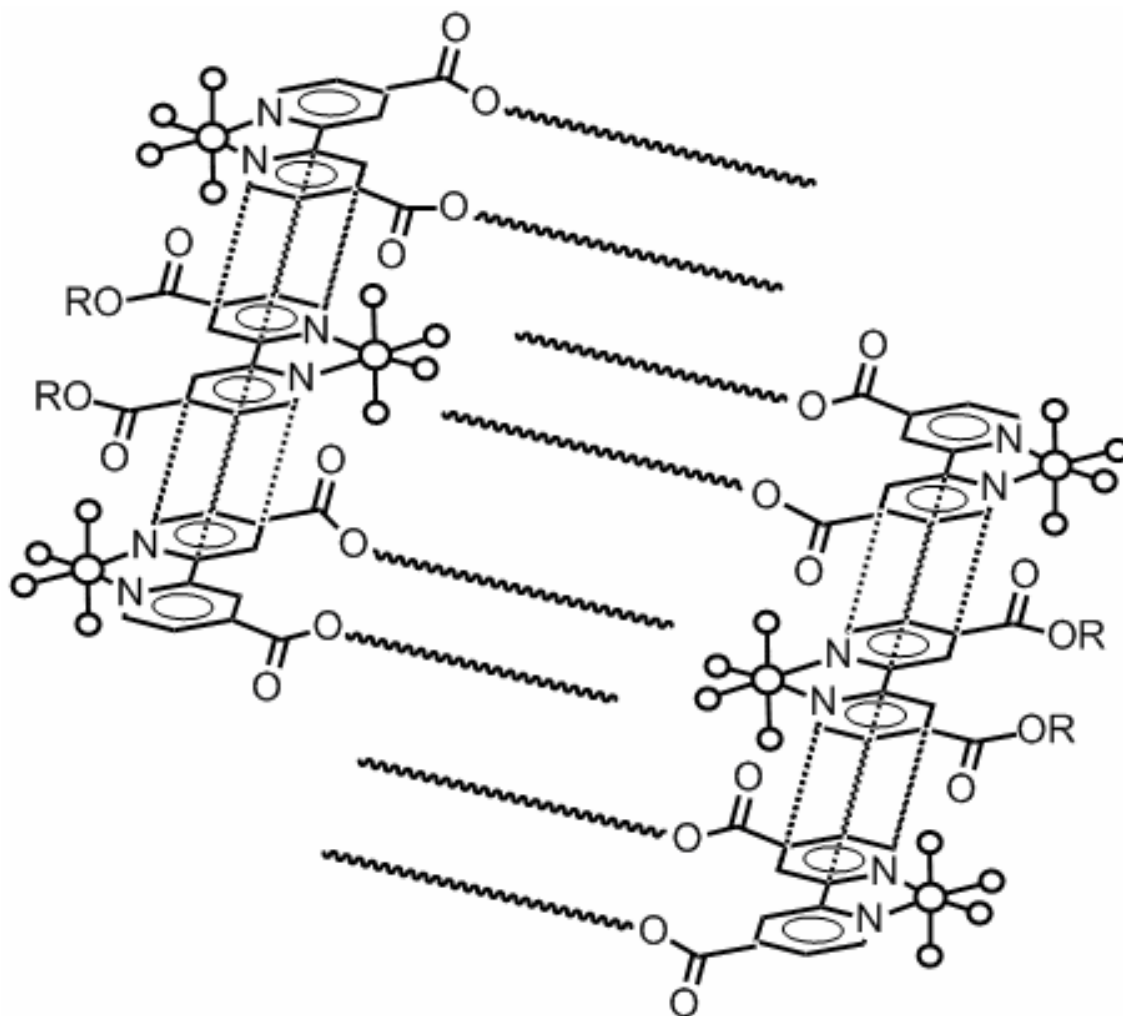


Figure 3-28. Proposed mesophase ordering for the mesogenic $\text{PtL}^{12}\text{Cl}_2$ complexes; π - π stacking interactions (---).

Using the simplified formula unit of PtCl_4 and in a P1 unit cell of dimensions $a = 11.8 \text{ \AA}$, $b = 7.8 \text{ \AA}$, $c = 26.1 \text{ \AA}$, $\alpha = \beta = 90^\circ$, $\gamma = 109.4^\circ$, a powder pattern for $\text{PtL}^{12}\text{Cl}_2$ was calculated and compared to the experimental results (Figure 3-29). In the calculated pattern, the full-width-at-half-maximum (FWHM) of the reflections has been broadened to better match the experimental data. As shown in Table 3-7, good agreement is obtained between the positions of calculated reflections and the observed reflections for the $\text{PtL}^{12}\text{Cl}_2$ mesophase.

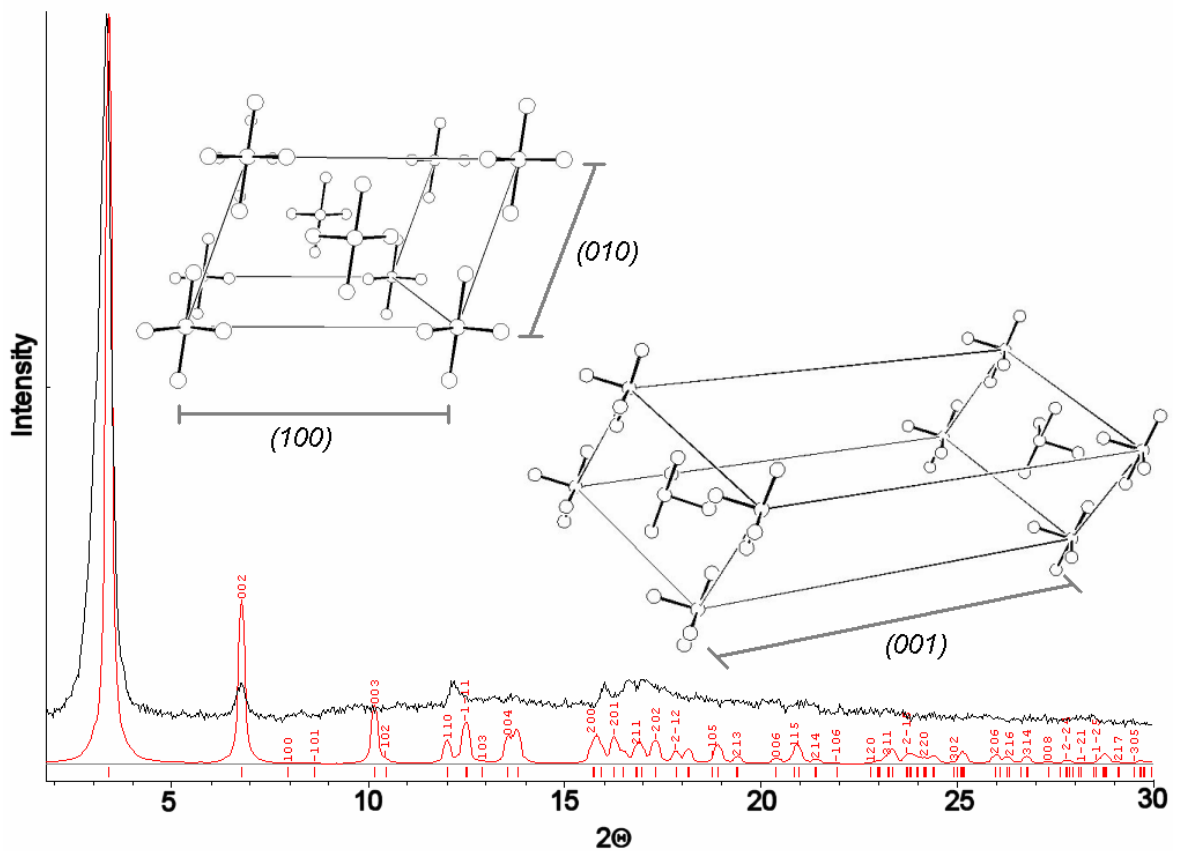


Figure 3-29. Experimental diffraction pattern for PtL¹²Cl₂ (top) and calculated pattern (bottom) determined utilizing the simplified PtCl₄ formula unit and P1 unit cell shown; FWHM of the calculated pattern has been modified to better match the experimental data.

Table 3-7. X-ray diffraction data and proposed assignment of reflections for the mesophases of PtL¹²Cl₄ (top) and PtL¹⁶Cl₄ (bottom) assuming a P1 unit cell.

Q (Å ⁻¹)	d _{meas.} (Å)	d _{calc.} (Å)	hkl
0.24	26.1	26.1	001
0.48	13.0	13.1	002
0.87	7.3	7.4	110
1.13	5.5	5.6	200
1.18	5.3	5.4	210, -201
1.21	5.2	5.1	-202
1.35		4.7 (broad)	
L: $a= 11.8 \text{ \AA}$, $b= 7.8 \text{ \AA}$, $c= 26.1 \text{ \AA}$, $\alpha= \beta= 90^\circ$, $\gamma= 109.4^\circ$.			

Q (Å ⁻¹)	d _{meas.} (Å)	d _{calc.} (Å)	hkl
0.40	15.8	15.8	002
0.88	7.1	7.4	110
1.16	5.4	5.4, 5.5	210, 201
1.19	5.3	5.3	202
1.35		4.6 (broad)	
L: $a= 11.8 \text{ \AA}$, $b= 7.8 \text{ \AA}$, $c= 31.7 \text{ \AA}$, $\alpha= \beta= 90^\circ$, $\gamma= 109.4^\circ$.			

The tilted unit cell, which allows for π - π interactions between the bipyridine rings, accounts for another of the differences between the XRD patterns for PtL¹²Cl₄ and PtL¹²Cl₂, which has an orthorhombic unit cell. In the a -direction, the most striking change from the XRD pattern for PtL¹²Cl₂ is the absence of a reflection corresponding to the $\sim 10 \text{ \AA}$ spacing associated with the regular spacing of the Pt-bipyridine moieties in an orthorhombic unit cell. Such an absence would occur if the PtL¹²Cl₄ mesophase was not biaxial, due to free rotation of the PtL¹²Cl₄ complexes around their long axes. Free rotation does not seem likely given the steric barrier imposed by the interaction between the axial chloride and bipyridine ligands. Rotational disorder in PtLⁿCl₄ phase seems more unlikely than in PtLⁿCl₂ phases, where rotational disorder is not observed. The absence of a reflection corresponding to $\sim 10 \text{ \AA}$ can more probably be explained by the tilted unit cell, which reduces the intensity

expected for the (100) reflection. The calculated diffraction pattern for an orthorhombic unit cell, as was consistent with the diffraction pattern of PtLⁿCl₂, does not fit with the XRD pattern observed for PtL¹²Cl₄, even when the large FWHM of the reflections is taken into account.

The presence of supramolecular ordering interactions other than hydrophobic packing of the alkyl chains (e.g. the proposed π - π stacking between the bipyridine rings) is suggested by the alkyl chain length independence of mesophase clearing temperatures. If the smectic layering prevented isotropic behavior below the clearing temperature of the PtLⁿCl₄ complexes, a chain length dependence should be observed for clearing temperatures. The clearing enthalpy changes for the PtLⁿCl₄ complexes are also more uniform over a range of alkyl chain lengths than the clearing enthalpies for the PtLⁿCl₂ mesophases. The lack of chain length dependence for the enthalpy change supports a supramolecular ordering not related to the alkyl chain packing, such as the proposed π - π stacking between the bipyridine rings. The possibility of some steric interaction of the Pt^{IV}-bipyridine moieties cannot be completely discounted. However, there are no readily apparent complementary shape interactions to strongly interlock adjacent octahedral metal centers.

The π - π stacking model also allows a simple explanation for the decrease in smectic layer spacing when compared to the analogous Pt^{II} species. The alkyl chains are tilted relative to the smectic layer director. In fact, the single crystal structure of PtL¹⁶Cl₂, which has alkyl chains tilted from the smectic layer director, has a *c*-spacing of 31.4 Å. The PtL¹⁶Cl₄ mesophase has a very similar 31.7 Å *c*-spacing. This tilt of the hydrophobic domain controls packing along the *c*-direction, while the π - π stacking interactions of the bipyridine rings controls packing in the *a* and *b* directions. The XRD pattern for PtL¹⁶Cl₄ is compared

to the pattern calculated for a P1 unit cell of dimensions $a = 11.8 \text{ \AA}$, $b = 7.8 \text{ \AA}$, $c = 31.7 \text{ \AA}$, $\alpha = \beta = 90^\circ$, $\gamma = 109.4^\circ$ in Figure 3-30. As with $\text{PtL}^{12}\text{Cl}_4$, the modeled XRD pattern is in good agreement with the experimentally observed reflections for the $\text{PtL}^{16}\text{Cl}_4$ mesophase. However, without further two-dimensional X-ray diffraction analysis of aligned samples, it is not possible to definitively assign the ordering of the mesophase beyond characterizing it as lamellar. Both this model and the previous model with its axially interdigitated adjacent chloride ligands are compatible with the available data and point to π - π stacking interactions as a source of intermolecular ordering.

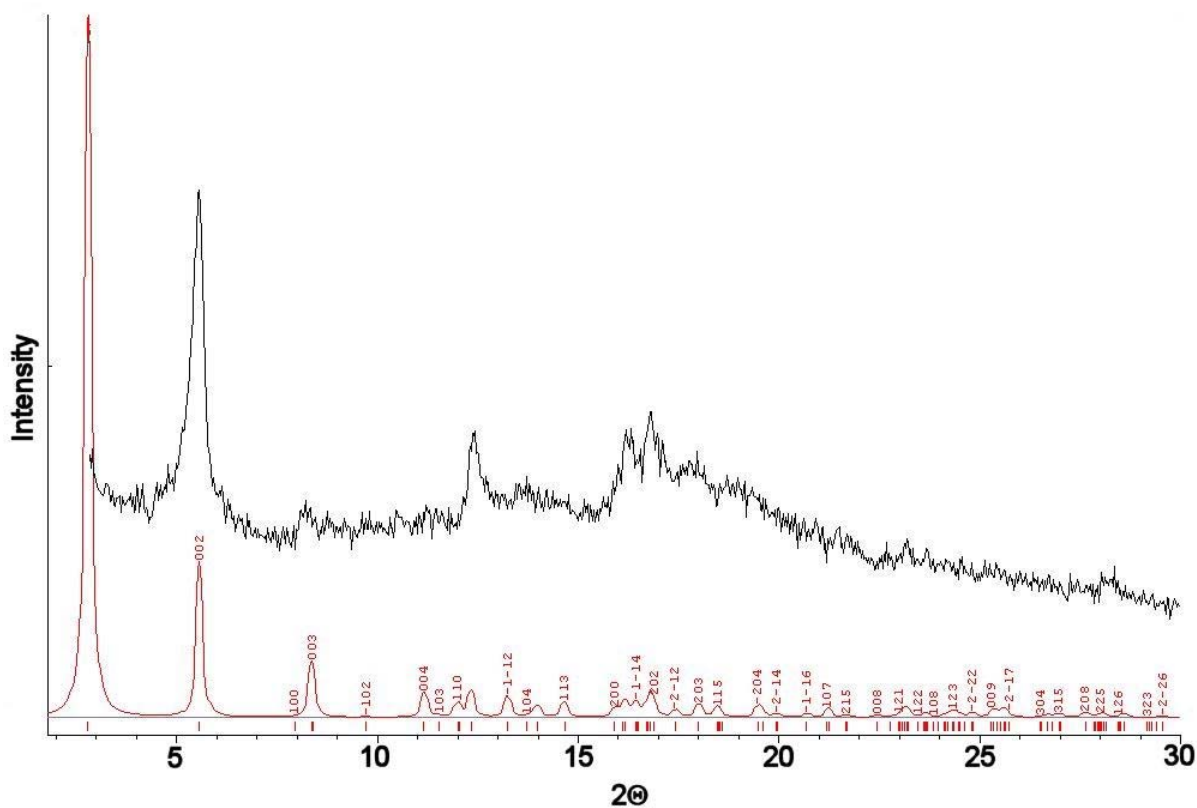


Figure 3-30. Experimental diffraction pattern for $\text{PtL}^{16}\text{Cl}_4$ (top) and calculated pattern (bottom) determined utilizing the simplified PtCl_4 formula unit and P1 unit cell; FWHM of the calculated pattern has been modified to better match the experimental data, (001) reflection cannot be observed due to its proximity to the X-ray beam.

Regardless of the exact packing arrangement of the headgroups, the lack of higher order reflections for the smectic layer spacing from the PtL^nCl_4 mesophases, compared to the observed (004) reflection of the Pt^{II} mesophases, suggest a longer correlation distance for the Pt^{II} mesophases. This longer Pt^{II} layer correlation distance may also be reflected in the comparatively lower transition temperatures of the Pt^{IV} mesophases. The smectic layer correlation distance only applies to the smectic layering, largely caused by the alkyl chains, and does not reflect the headgroup interactions between two adjacent PtL^nCl_4 complexes. The correlations between adjacent complexes appear to be stronger for the PtL^nCl_4 mesophases as evidenced by the observed $(h0l)$ and $(hk0)$ reflections.

In the absence of a single crystal structure for comparison, the π - π stacking model is consistent with the XRD pattern and the physical properties of the PtL^nCl_4 mesophases. There are several structural arrangements by which adjacent moieties could form π - π interactions. Two of these arrangements have been discussed here, and both are compatible with the observed diffraction pattern for the overall lamellar mesophase. Further analysis by two-dimensional XRD is necessary to further elucidate the headgroup packing. To date, all attempts to recrystallize PtL^nCl_4 have resulted in small crystals unsuitable for single crystal diffraction analysis.

3.3.7 Expansion of this System to Re and Cd Complexes

To examine the robustness of the mesophase formed from the alkyl-bipyridine complexes and to test the compatibility of the mesophase with different sizes and shapes of headgroups, Cd and Re analogs were synthesized. The Zn analogues, ZnL^nCl_2 ($n = 8, 16, 22$), with a tetrahedral metal centers were previously synthesized by Pucci and coworkers and

found to be non-mesogenic.⁴⁷ ZnL^nCl_2 complexes transition from crystalline solid to isotropic liquid without decomposition. Transition temperatures and enthalpies for the Re and Cd complexes are given in Table 3-8. The CdL^nCl_2 complexes ($n = 2, 12, 18$) are also non-mesogenic. The X-Cd-X angle is expected to be increased in comparison to analogous Zn complexes as demonstrated in previous crystallographic analyses of Cd bipyridine complexes.^{124, 145, 146, 147, 148} In some $Cd(bpy)Cl_2$ analogues, most notably those synthesized by hydrothermal methods, the Cd centers are octahedral due to formation of extended networks of bridging chloride ligands.¹²⁴

Table 3-8. Thermal properties of the CdL^nCl_2 and $\text{Re}(\text{CO})_3\text{L}^n\text{Br}$ complexes.

Species	Transition ^[a]	Temperature (°C)	Enthalpy (kJ/mol)
CdL^2Cl_2	decomposition	310.6	---
$\text{CdL}^{12}\text{Cl}_2$	Cr1 to Cr2	16.4	30.1
	Cr2 to Cr3	112.6	13.2
	Cr3 to Cr2	109.5	12.8
	Cr2 to Cr1	3.9	30.2
	decomposition	308.8	---
$\text{CdL}^{18}\text{Cl}_2$	Cr1 to Cr2	78.8	43.6
	Cr2 to Cr3	96.4	20.0
	Cr3 to Cr2	89.8	21.1
	Cr2 to Cr1	55.4	45.7
	decomposition	308.8	---
$\text{Re}(\text{CO})_3\text{L}^{12}\text{Br}$	Cr1 to Cr2	58.2	22.8
	Cr2 to Cr3	94.8	4.5
	Cr3 to I	121.5	21.5
	I to Cr4 ^[b]	85.3	20.7
	Cr4 ^[b] to Cr1	49.1	14.2
$\text{Re}(\text{CO})_3\text{L}^{18}\text{Br}$	Cr1 to Cr2	91.3	32.1
	Cr2 to Cr3 ^[c]	104.1	35.4
	Cr3 to L	112.7	34.1
	L to I	117.4	24.7
	I to Cr4 ^[b]	86-94	18.9
	Cr4 ^[b] to Cr1	73-79	47.9
	decomposition	340.3	---

^[a] Cr1: crystal 1; Cr2: crystal 2; Cr3: crystal 3; Cr4: crystal 4; L: lamellar; I: isotropic liquid

^[b] It is not known at this time whether the crystalline phase formed on cooling, Cr4, is the same as one of the crystalline phases formed upon heating.

^[c] This crystalline solid to crystalline solid transition is exothermic.

The Re complexes proved more amenable to formation of liquid crystalline phases. Bromotricarbonyl(dialkyl-2,2'-bipyridine-5,5'-carboxylato)rhenium(I) complexes, with the long-chain alkyl substituents in the 5,5' rather than 4,4' positions on the bipyridine ring, have

previously been shown to be thermotropic metallomesogens.^{149, 150} Both SmC mesophases with with monolayer smectic ordering and nematic mesophases were observed.

The liquid crystalline texture of $\text{Re}(\text{CO})_3\text{L}^{18}\text{Br}$, shown in Figure 3-31, is similar to that of the PtL^nCl_4 complexes in its almost metallic appearance under cross-polarization and fine texture. Further analysis will need to be carried out to determine if the structure of the mesophase is indeed similar to PtL^nCl_4 .

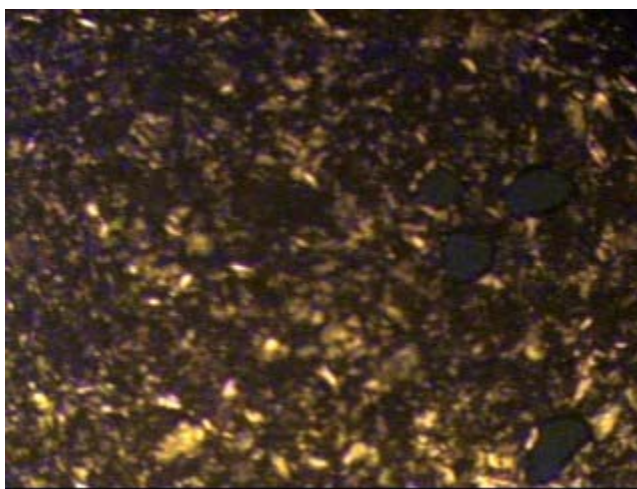


Figure 3-31. Mesogenic texture of $\text{Re}(\text{CO})_3\text{L}^{18}\text{Br}$ under cross-polarization.

3.4 Conclusions

Single crystal structures for $\text{PtL}^1\text{Cl}_2 \cdot 2\text{CH}_2\text{Cl}_2$, PtL^2Cl_2 and $\text{PtL}^{16}\text{Cl}_2 \cdot 2\text{CHCl}_3$ were elucidated, and the effects of intermolecular hydrophobic interactions in dictating the structure were discussed. The phase behavior of several mesogenic PtL^nCl_2 complexes was presented to compliment the data already found in the literature. The Pt^{II} complexes demonstrate hydrophobic domains and axially interacting Pt-Pt centers oriented along a screw axis. Both PtL^nCl_2 and PtL^nCl_4 complexes display layered mesophases, for $n = 10, 12,$

16, and 20. The Pt^{IV} complexes display a tilted phase which is dominated by the effects of π - π stacking between adjacent bipyridine moieties. These Pt^{IV} complexes are among a very few Pt^{IV} complexes displaying mesogenic behavior. The formation of Re(CO)₃LⁿBr mesophases shows that this mesogenic system of partial π - π stacking interactions may be amenable to incorporation of a variety of octahedral metal centers and pseudo-halogen ligands. The strong smectic order and the presence of axial ordering at the edges of the smectic bilayers makes these mesogens strong candidates for the formation of MX chain interactions in mixed Pt^{II}/Pt^{IV} metallomesogenic systems.

CHAPTER IV

SELF-ASSEMBLY OF MX CHAINS IN LIQUID CRYSTALLINE MOLECULAR ALLOYS AND ASSEMBLY CONTROLLED LUMINESCENCE

4.1 Introduction

4.1.1 Proposed MX Chain Interactions in a Liquid Crystalline Phase

In the previous chapter, systems with secondary interactions that aided the formation of the desired $M^{II}\cdots X-M^{IV}$ MX chain interactions (e.g. hydrogen bonds between ligands and counterions^{32, 50} and surfactant domains in reverse micelles^{100, 101}) were discussed. To engineer a secondary supramolecular ordering into a neutral MX chain system, a binary metallomesogenic phase of Pt^{II} and Pt^{IV} dialkyl-2,2'-bipyridine-4,4'-dicarboxylate complexes was proposed. This is both the first proposed system for MX chain interactions in a liquid crystalline phase and the first binary system utilizing Pt^{IV} metallomesogens.

The liquid crystalline system provides a means of self-assembling aligned MX chains more easily than by single crystal growth and with larger domains than are observed in solution systems. The advantages of PtL^nCl_2 and PtL^nCl_4 complexes (see Figure 3-1 for structures) include the ability to control the mesogenic temperature range with alkyl chain length and the ability to induce self-assembly of the binary mesophase from the isolated complexes due to the overlapping liquid crystalline ranges of isolated species with the same alkyl chain length.

The syntheses of metallomesogenic PtL^nCl_2 and PtL^nCl_4 complexes were presented in Chapter 3, as was the structural characterization of their mesophases. The mesogenic PtL^nCl_2 complexes demonstrate a phase with both SmA_d and Col_L characteristics as was previously reported in the literature.^{47, 103} The PtL^nCl_4 ($n = 10, 12, 16, 20$) mesophases demonstrated a tilted semi-bilayer mesophase with soft crystalline characteristics. Data suggest that in mesogenic PtL^nCl_2 complexes, axial ordering in the liquid crystalline phase resulted from Pt-Pt interactions, while for PtL^nCl_4 complexes, π - π interactions between the bipyridine ligands dominated the ordering. The presence of Pt-Pt and π - π axial interactions is promising for formation of other axial interactions including the desired MX chain interactions in binary $\text{PtL}^n\text{Cl}_2/\text{PtL}^n\text{Cl}_4$ mesophases. However, if the $\text{Cl-Pt}^{\text{IV}}\text{-Cl}\cdots\text{Pt}^{\text{II}}$ interactions are weaker than the Pt-Pt and π - π interactions between the respective PtL^nCl_2 and PtL^nCl_4 complexes, MX chains will not form.

There are several possible liquid crystalline phases that are compatible with formation of MX chain interactions of the type $[\text{PtL}^n\text{Cl}_2\text{-PtL}^n\text{Cl}_4]_m$ at the edges of aliphatic layers. The hypothesized MX chain interaction in a mesogenic phase is shown in Figure 4-1 (right). In each of the mesophases, the columnar ordering is driven by the formation of MX chain interactions, but there are several possibilities for the relative positions of the columns within the mesophase. The first two phases, lamello-columnar (Col_L) and rectangulo-columnar (Col_R) mesophases, are both characterized by a rectangular unit cell and differ in the strength of the correlations between layers. The Col_L mesophase does not display correlations between layers, while the Col_R mesophase will display rectangular-type positional correlations between layers. The structure of these two phases is similar over the short correlation distance of two layers, and so they are represented with the same figure (Figure 4-

1, top). The third mesophase (Figure 4-1, bottom) is the hexatic-columnar (Col_H) phase, which is characterized as having hexagonal short-range positional ordering within the layers. In all three phases, the alkyl chains have a disordered liquid-like hydrophobic packing. In the Col_H mesophase, the alkyl chains are symmetrically distributed around the columns, while in the Col_L and Col_R phases, the alkyl chains are asymmetrically distributed to form layers. It is expected that formation of MX chain interactions would lead to higher ordering in the $[\text{PtL}^n\text{Cl}_2\text{-PtL}^n\text{Cl}_4]_m$ mesophase than is found in the mesophase of the individual complexes, because the MX chain would increase the strength of the columnar interactions.

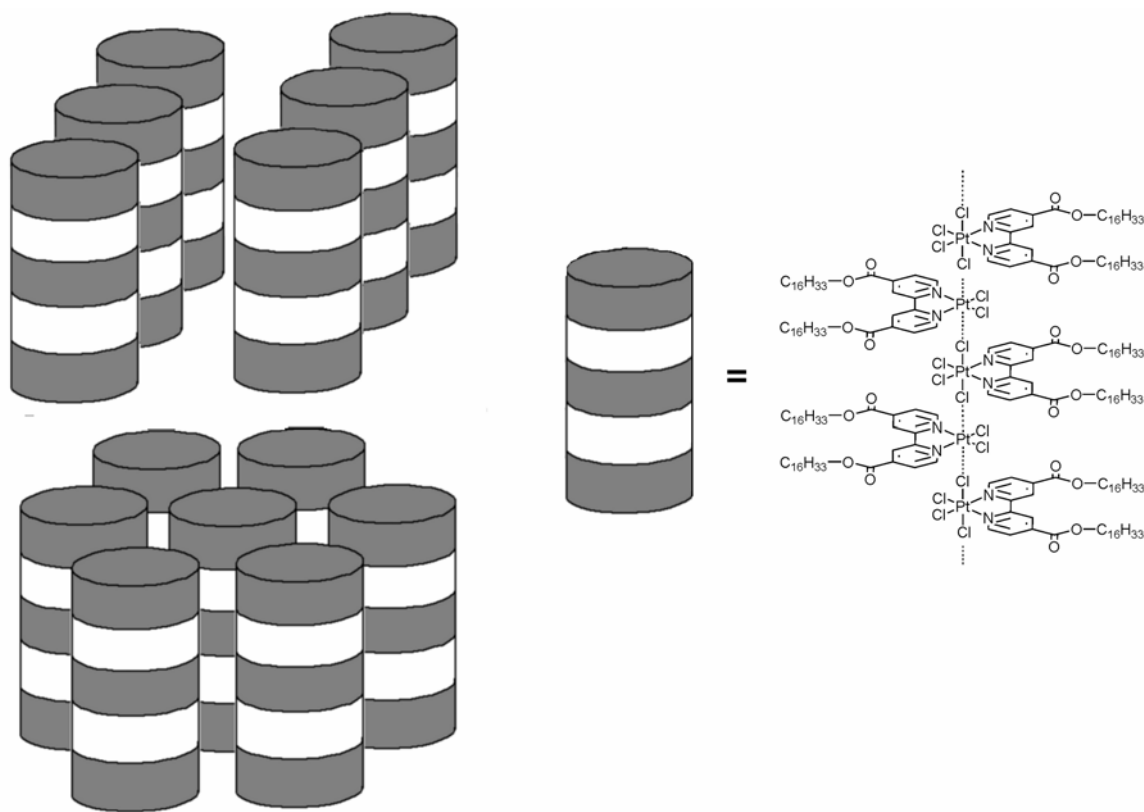


Figure 4-1. Diagram of possible mesogenic phases supporting MX chain interactions; Col_L and Col_R mesophases, which differ by the strength of correlations between layers (top), Col_H mesophase (bottom); the alkyl chains are highly disordered and are not shown.

4.1.2 Previous Work with Binary Metallomesogenic Phases

There is relatively little work in the literature on mixtures of metal complexes which form a single mesogenic phase. The existing binary systems may be divided into two general categories. The first type of binary metallomesogenic phase is comprised of two complexes with the same metal center but different ligands.^{151, 152, 153} These include binary mesophases of $\text{PtCl}_2(\text{H}_2\text{C}=\text{CHC}_m\text{H}_{2m+1})(\text{NC}_5\text{H}_4\text{R})$ complexes having different alkyl chain lengths and Pd isocyanate mixtures varying both in chain length and ligand structure.^{154, 155} In both cases, the binary phase is less ordered than the pure mesophase of at least one of the components.

The second type of metallomesogenic mixture is the “liquid crystalline molecular alloy”. This term was coined by Ballesteros, Coco, and Espinet to describe a single mesophase composed of two (or more) complexes with different metal centers.¹⁵⁶ The molecular alloys are distinguished from “mixed M-M’ metallomesogens”, which consist of multiple metal centers in a single mesogenic molecule.¹⁵⁷ Most of the previously characterized molecular alloy mesophases are so-called “salt-melts” of mono-ionic cations or NH_4^+ and carboxylic acid surfactants. These mesophases demonstrate smectic ordering controlled by cation radius and alkyl chain length.^{158, 159}

Molecular alloy mesophases formed from components that demonstrate axial interactions in their pure mesophases are most relevant to the formation of MX chain mesophases. Cu and Au isocyanide complexes may be mixed in ratios $\geq 30\%$ Au to give a SmA mesophase where the non-mesogenic Cu complex reduces the ordering of the mesophase and partially disrupts the axial $\text{Au}\cdots\text{Au}$ interactions (Figure 4-2).¹⁵⁶ In mixtures of Cu and Rh heptanoate complexes, a Col_H mesophase of randomly distributed columns of

Cu or Rh mesogens is obtained so the axial ordering of the $[(\text{CH}_3(\text{CH}_2)_n\text{CO}_2)_2\text{Rh}]_2$ dimers is not lost (Figure 4-3).¹⁶⁰

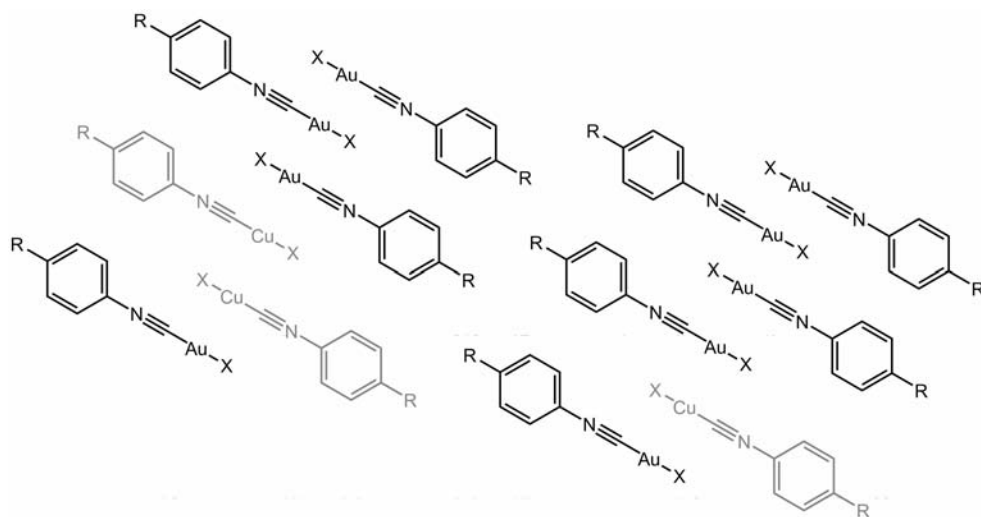


Figure 4-2. Representative interactions in the SmA mesophase obtained for a mixture of Au and Cu isocyanide complexes;¹⁵⁶ Au...Au interactions are disrupted by the Cu complexes.

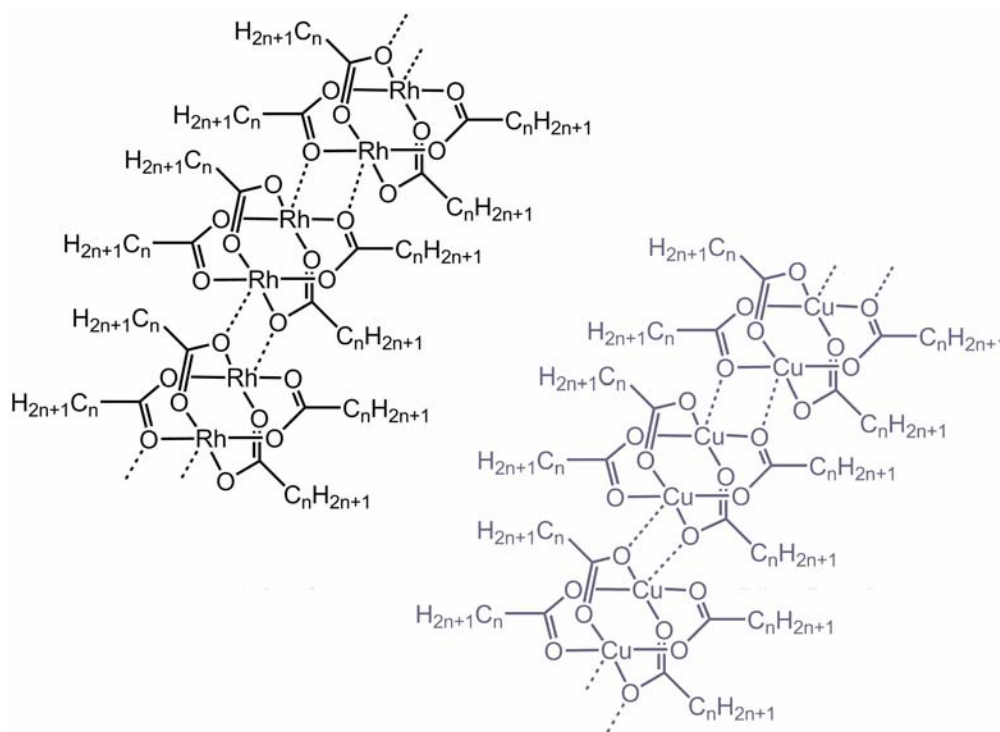


Figure 4-3. Representative interactions in the Col_H mesophase obtained from a mixture of Rh and Cu heptanoate complexes;¹⁶⁰ Rh and Cu complexes supramolecularly order in separate columns.

To form MX chains in the mesogenic phase, formation of a hexatic phase of randomly distributed columns of $[\text{PtL}^n\text{Cl}_2]_m$ and $[\text{PtL}^n\text{Cl}_4]_m$, similar to the results obtained for Rh/Cu heptanoate alloy, must be avoided. The possibility of forming a randomly distributed phase of $[\text{PtL}^n\text{Cl}_2]_m$ and $[\text{PtL}^n\text{Cl}_4]_m$ columns is further discussed in the section on XRD analysis of the $\text{PtL}^{16}\text{Cl}_2/\text{PtL}^{16}\text{Cl}_4$ mesophase.

Characterization of the $\text{PtL}^n\text{Cl}_2/\text{PtL}^n\text{Cl}_4$ mesophases proceeded in two parts. Initially, the traditional methods for characterizing mesophases (e.g. optical microscopy, DSC, and XRD analyses) were explored. The second portion of this work focused on luminescence spectroscopy. Previous work on the photophysical properties of Pt aromatic complexes is mentioned as it becomes relevant to the discussion of the $\text{PtL}^n\text{Cl}_2/\text{PtL}^n\text{Cl}_4$ luminescence at the end of this chapter. Electronic structure calculations for PtL^1Cl_2 and PtL^1Cl_4 are discussed to aid in identification of the excited states responsible for the luminescence properties.

4.2 Experimental

4.2.1 General Laboratory Procedures and Instrumentation

The syntheses for the PtL^nCl_2 and PtL^nCl_4 complexes are given in Chapter 3, as are the descriptions of the instrumentation for ^1H NMR and UV-vis absorbance spectroscopies and DSC. The precision in temperature measurement for the DSC analyses is high; however, the complicated process of weighing, mixing, and heating samples, along with the effects of heating viscous mixtures leads to a ± 3 °C variation in transition temperatures, as has been previously documented with other binary systems.¹⁵⁶ The transition enthalpies also

demonstrate similar variability. In order to minimize the kinetic effects of slow mixing, a 2 °C/min heating/cooling rate was utilized for some DSC measurements, but no difference was observed from those results obtained at 10 °C/min.

4.2.2 Variable Temperature Powder X-ray Diffraction

The instrumentation for all powder XRD measurements, except the room temperature analysis of the 1:1 PtL¹⁶Cl₂/PtL¹⁶Cl₄ alloy, is discussed in Chapter 3. The 1:1 PtL¹⁶Cl₂/PtL¹⁶Cl₄ molecular alloy was heated to 130 °C and quenched with liquid nitrogen according to the procedure given below. The powdered sample was placed on an open plate and mounted in the Cu K α beam of a Rigaku Multiflex powder diffractometer. The instrument and beamstop were carefully aligned to give the maximum possible low-angle range (approximate minimum 2Θ , 2°).

4.2.3 Luminescence Emission Measurements

Luminescence measurements were obtained on a Spex 1403 0.85 m Double Spectrometer with Hamamatsu R928/115 PMT detector using the 514 nm line of an argon ion laser as the excitation source. Samples were prepared for analysis by two methods. In the first, finely ground powder samples were packed tightly into 1 mm diameter glass tubes. Multiple samples were then aligned on a sliding frame and sequentially placed in front of the laser beam for measurement. In the second method, utilized for both room temperature and low temperature vacuum work, samples were tightly packed into 1 mm diameter depressions of a copper block and were then covered with a quartz window. The sample holder was placed in a vacuum chamber and evacuated to $\sim 3 \times 10^{-6}$ torr with a diffusion pump system.

For low temperature work, the copper block was cooled via an Air Products closed-cycle refrigerator inside the vacuum chamber. A temperature of 30 K was maintained by a Lakeshore temperature controller via a thermocouple attached to the copper block adjacent to the sample depressions.

4.2.4 Luminescence Lifetime Measurements

Experiments were conducted by time-correlated photon counting using the 846 nm output of a mode-locked Spectra Physics Tsunami Ti:sapphire oscillator which was frequency doubled in a BBO crystal to produce ~ 1 ps pulses at 423 nm. The repetition rate of the 76-MHz pulse train was reduced using an acousto-optic modulator so the time between excitation pulses was $\geq 5\times$ the natural lifetime of the sample. Emission is collected at 90° with respect to excitation, passed through a 0.25-m monochromator, and monitored with a microchannel plate photomultiplier tube at 614 nm. Samples were finely chopped, packed tightly into 1 mm diameter glass tubes, and placed in an aluminum block, which had been machined with windows for the laser beam. The block was heated or cooled to maintain the correct temperature for analyses, and the temperature was measured by an Omega Products thermal couple placed in an empty tube adjacent to the sample tube.

4.2.5 PtLⁿCl₂/PtLⁿCl₄ Sample Preparation

All samples were extensively dried under vacuum in the presence of P₂O₅ prior to carrying out measurements. Samples should be stored in the dark to minimize the possibility of photodecomposition over long times. In order to minimize error in weighing, powdered mixtures of the samples were prepared in ~ 100 mg batches by combining stoichiometric

amounts of PtL^nCl_2 and PtL^nCl_4 and chopping the mixture finely with a razor blade. Grinding is not recommended as a method of mixing the samples due to their soft and greasy character. The ratio of PtL^nCl_2 to PtL^nCl_4 is confirmed by ^1H NMR analysis. The self-assembled alloys were prepared by first confirming the proper ratio of $\text{PtL}^n\text{Cl}_2/\text{PtL}^n\text{Cl}_4$ by ^1H NMR spectroscopy, and then suspending small vials containing the samples for at least 1 h in a pre-equalibrated oil bath. To preserve the mesophase ordering, the samples were then quenched by placing them in liquid nitrogen. To prevent the sample vials from shattering, they were lowered slowly into the liquid nitrogen bath. This safety measure resulted in a slight cooling of the vials before quenching occurred. For that reason, the samples were heated to 10-20 °C above the temperature for mesophase formation ($\text{PtL}^{12}\text{Cl}_2/\text{PtL}^{12}\text{Cl}_4$: 102 °C, $\text{PtL}^{16}\text{Cl}_2/\text{PtL}^{16}\text{Cl}_4$: 108 °C, $\text{PtL}^{20}\text{Cl}_2/\text{PtL}^{20}\text{Cl}_4$: 89 °C) determined by DSC analyses.

4.2.6 DFT Calculations

The basis sets and parameters utilized for the calculations were previously discussed in Section 2.2.7. The geometries of PtL^1Cl_2 and PtL^1Cl_4 were allowed to reach energy minimization without restricting bond lengths or angles.

4.3 Results and Discussion

4.3.1 Determination of the Mesogenic Range for $\text{PtL}^n\text{Cl}_2/\text{PtL}^n\text{Cl}_4$ Molecular Alloys

Initial experiments by optical microscopy demonstrated the relatively high viscosity of PtL^nCl_2 and PtL^nCl_4 ($n = 12, 16, 20$) even near their respective clearing temperatures. The high viscosity presents a kinetic barrier to forming a single bimetallic mesophase from the microcrystalline powders.

Due to the large overlap in the temperatures for the individual Pt^{II} and Pt^{IV} mesogenic phases, PtL¹⁶Cl₂/PtL¹⁶Cl₄ was the first system explored. This alloy will be discussed as a representative example of the other molecular alloys, PtL¹²Cl₂/PtL¹²Cl₄ and PtL²⁰Cl₂/PtL²⁰Cl₄. Figure 4-4 shows the DSC trace over two heating/cooling cycles for a 1:1 mixture of PtL¹⁶Cl₂ and PtL¹⁶Cl₄. The viscosity of the mesophases and the macroscale separation of the PtL¹⁶Cl₂ and PtL¹⁶Cl₄ complexes prior to heating produced different results for the first DSC cycle than for all subsequent cycles. A 1:1 mixture of individual PtL¹⁶Cl₂ and PtL¹⁶Cl₄ powders softens but does not flow under optical analysis at ~70-75 °C (Figure 4-5 a), which correlates to the endotherms observed in the DSC trace. Crystalline to lamellar transitions are observed for the individual species (83 and 69 °C for PtL¹⁶Cl₂ and PtL¹⁶Cl₄, respectively) near this temperature range. If the PtL¹⁶Cl₂ and PtL¹⁶Cl₄ mesophases are sheared together, there is visual evidence of mixing, but it is not known if a single mesophase is formed on forcible mixing or if separate, though smaller, PtL¹⁶Cl₂ and PtL¹⁶Cl₄ domains remain.

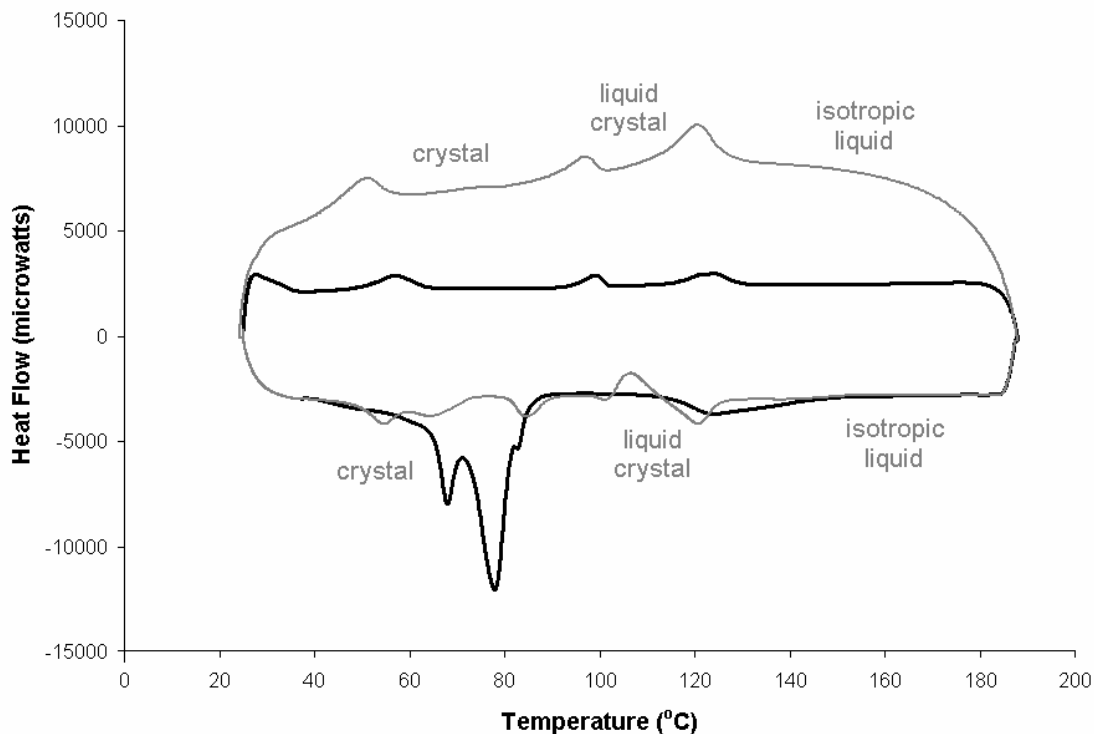


Figure 4-4. DSC trace for 1:1 PtL¹⁶Cl₂/PtL¹⁶Cl₄; 1st heating and cooling (black), 2nd heating and cooling (grey); phases are given for the 2nd cycle.

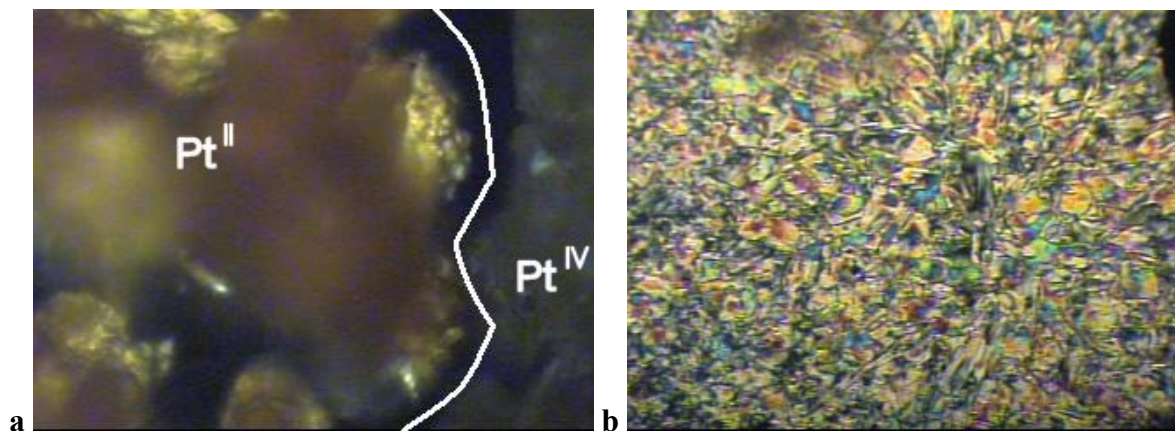


Figure 4-5. Mesogenic phases of PtL¹⁶Cl₂ and PtL¹⁶Cl₄ prior to shearing at 106 °C (a), and the single 1:1 PtL¹⁶Cl₂/PtL¹⁶Cl₄ mesophase during the second heating at 118 °C (b); under cross-polarization.

In the DSC trace during the second heating cycle, an exothermic transition is observed at 108 °C, and on all subsequent cycles the transition occurs with the same change

in enthalpy. During the first heating, the size of the exotherm is variable, depending on how well the PtL^nCl_2 and PtL^nCl_4 species are mixed. The texture under cross-polarization for the mesophase marked “liquid crystalline” in the DSC trace (Figure 4-4) is shown in Figure 4-5 **b**. This texture is obtained spontaneously after multiple heating and cooling cycles or after shearing of the separate $\text{PtL}^{16}\text{Cl}_2$ and $\text{PtL}^{16}\text{Cl}_4$ mesophases together during the first heating cycle. The difficulty in forming this phase during the first heating cycle is attributed to kinetic barrier to mixing provided by the high sample viscosity. As discussed in the next section, this mesophase has a hexatic-columnar (Col_H) structure and will be referred to as the Col_H alloy for the rest of this discussion.

The clearing temperature of the Col_H alloy is very sensitive to contamination and to the $\text{Pt}^{\text{II}}/\text{Pt}^{\text{IV}}$ ratio. As will be discussed below, a partial clearing to produce a mixture of liquid crystalline and isotropic domains is observed before complete clearing for compositions that are not 1:1 $\text{PtL}^n\text{Cl}_2/\text{PtL}^n\text{Cl}_4$. The 1:1 $\text{PtL}^{16}\text{Cl}_2/\text{PtL}^{16}\text{Cl}_4$ molecular alloy clears completely in a single transition at 121 °C.

Similar exothermic transitions were observed for all cooling cycles. The $\text{PtL}^{16}\text{Cl}_2/\text{PtL}^{16}\text{Cl}_4$ Col_H alloy become liquid crystalline beginning at 120 °C according to the DSC trace, but optical analysis occasionally gives supercooling of up to 10 °C. In some trials, a uniform texture similar to the mosaic texture shown in Figure 4-5 **b** was obtained for the alloy on cooling from the isotropic liquid. In other samples, separate domains of different textures were obtained. In all cases, shearing resulted in a uniform mosaic or finely textured phase. At 97 °C the sample solidifies maintaining the texture observed in the liquid crystalline phase, and a corresponding exotherm is observed in the DSC.

Due to the focus on MX chain formation, the Col_H alloy was of special interest because of its uniform texture under optical microscopic analysis and the apparent formation of a single phase throughout the sample. The other phases (except the isotropic liquid) generally show evidence of macroscopic phase separation. Analogous DSC results are obtained for the PtL¹²Cl₂/PtL¹²Cl₄ and PtL²⁰Cl₂/PtL²⁰Cl₄ when the Pt^{II} and Pt^{IV} components are mixed in a 1:1 ratio as shown in Figure 4-6. An exotherm corresponding to the formation of a uniform molecular alloy is observed on the 2nd heating cycle. It should be noted that the exotherm for PtL¹²Cl₂/PtL¹²Cl₄ is small and broad. Upon cooling the PtL¹²Cl₂/PtL¹²Cl₄ mixture appears to solidify without first forming a liquid crystalline phase, possibly due to experimental difficulties with cooling the sample slowly. The molecular alloy is more stable for the PtL¹⁶Cl₂/PtL¹⁶Cl₄ and PtL²⁰Cl₂/PtL²⁰Cl₄ samples. Table 4-1 gives the temperature range over which the Col_H mesophase is stable for the various molecular alloys. Longer alkyl chain lengths lower the temperature for alloy formation and lead to a larger stable range. The maximum stable temperature for the mesophase is nearly constant over an eight carbon variation in alkyl chain length. This lack of alkyl chain length dependence for the clearing temperature supports the hypothesis that the headgroup interactions control the ordering in the molecular alloy mesophase.

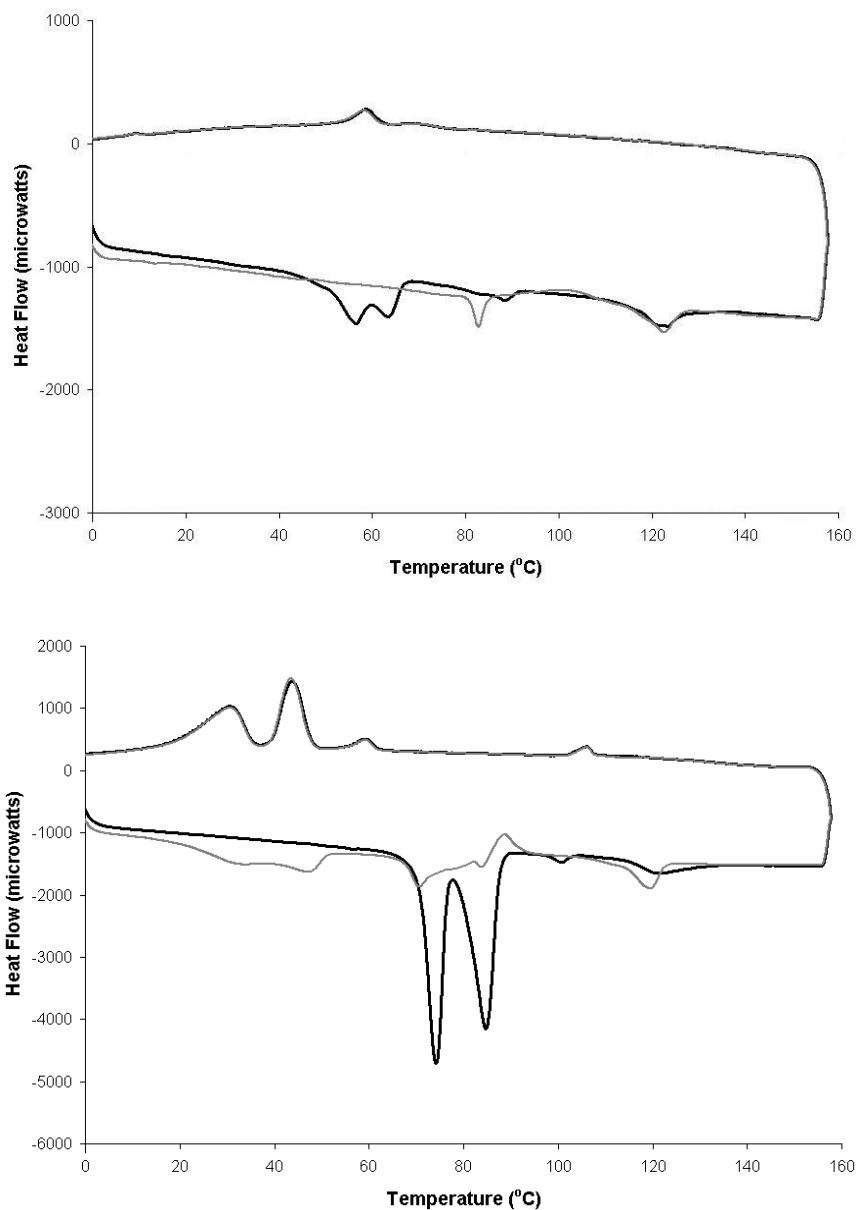


Figure 4-6. DSC traces for 1:1 mixtures of $\text{PtL}^{12}\text{Cl}_2/\text{PtL}^{12}\text{Cl}_4$ (top) and $\text{PtL}^{20}\text{Cl}_2/\text{PtL}^{20}\text{Cl}_4$ (bottom); 1st heating/cooling cycle (black), 2nd heating/cooling cycle (grey).

Table 4-1. Stable temperature range upon heating for the CoI_H molecular alloy of 1:1 $\text{PtL}^n\text{Cl}_2/\text{PtL}^n\text{Cl}_4$ as determined by DSC.

Alloy	Stable Temperature Range Limits (°C)	
	Lower	Upper
$\text{PtL}^{12}\text{Cl}_2/\text{PtL}^{12}\text{Cl}_4$	102	123
$\text{PtL}^{16}\text{Cl}_2/\text{PtL}^{16}\text{Cl}_4$	108	121
$\text{PtL}^{20}\text{Cl}_2/\text{PtL}^{20}\text{Cl}_4$	89	119

To examine the stability of the CoI_H alloy, a series of off-stoichiometry samples of $\text{PtL}^{16}\text{Cl}_2/\text{PtL}^{16}\text{Cl}_4$ were prepared. The most interesting feature of the DSC trace in these mixtures is the appearance of a new endothermic transition at $140\text{ }^\circ\text{C}$ (shown for 1.5:1 and 0.55:1 $\text{PtL}^{16}\text{Cl}_2/\text{PtL}^{16}\text{Cl}_4$, Figure 4-7). Under optical analysis, a partial clearing of the off-stoichiometric samples was observed at $\sim 120\text{-}124\text{ }^\circ\text{C}$ to give a mixture of isotropic and mesogenic phases, followed by complete clearing of the sample at $\sim 140\text{ }^\circ\text{C}$. Table 4-2 gives the enthalpy changes associated with the $\sim 140\text{ }^\circ\text{C}$ transition as a function of the ratio of $\text{PtL}^{16}\text{Cl}_2/\text{PtL}^{16}\text{Cl}_4$. The enthalpy change is greatest for samples that deviate most from 1:1 stoichiometry. No transition at $\sim 140\text{ }^\circ\text{C}$ is observed for 1:1 mixtures.

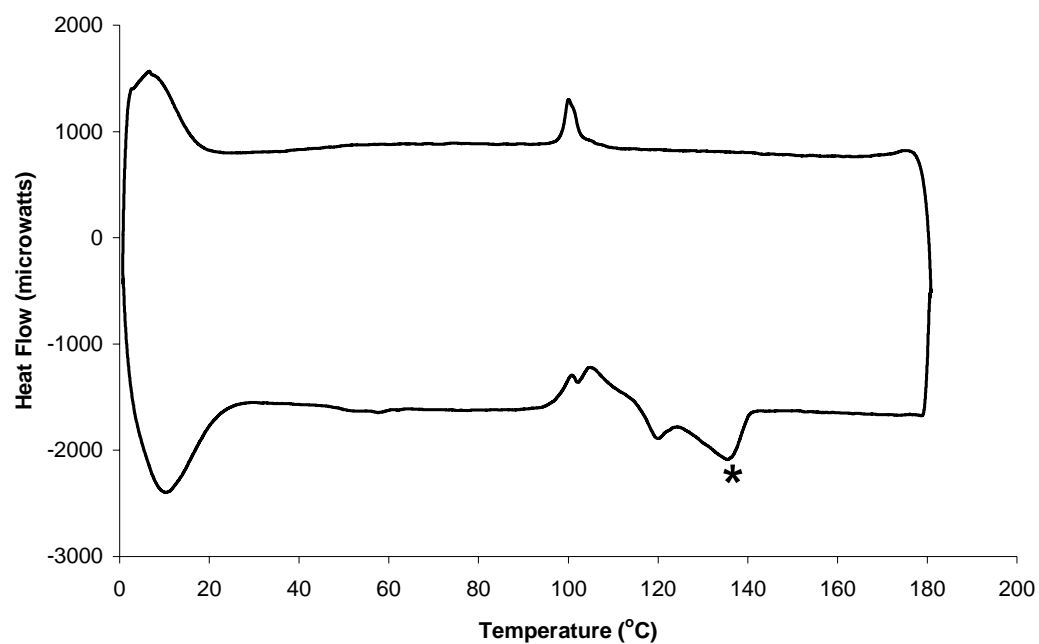
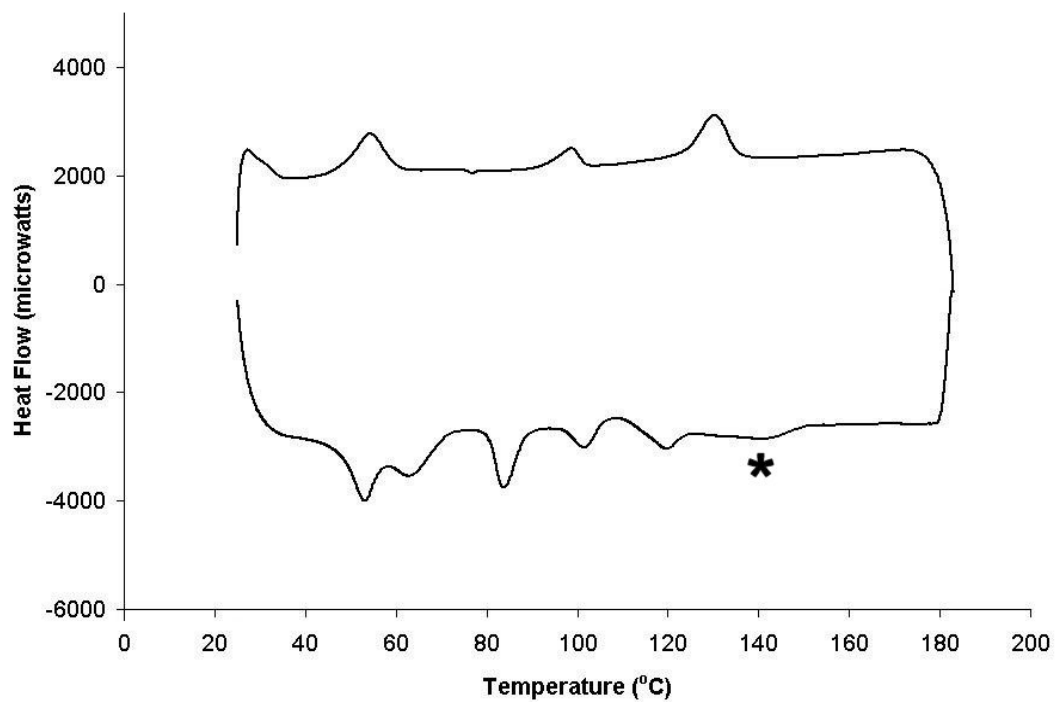


Figure 4-7. DSC trace for 1.5:1 PtL¹⁶Cl₂/PtL¹⁶Cl₄ (top) and 0.55:1 PtL¹⁶Cl₂/PtL¹⁶Cl₄ (bottom) showing the new endotherm (*), which is not observed for 1:1 PtL¹⁶Cl₂/PtL¹⁶Cl₄; 2nd heating shown.

Table 4-2. Enthalpy change upon clearing for various ratios of PtL¹⁶Cl₂/PtL¹⁶Cl₄ as determined by DSC.

PtL ¹⁶ Cl ₂ /PtL ¹⁶ Cl ₄	Temperature (°C)	ΔH (mJ/mg)
0.55:1	139	7 ^[a]
0.81:1	145	4 ^[a]
1:1	[a]	[b]
1.3:1	139	0.19
1.5:1	140	1.54
1.8:1	137	2 ^[a]

^[a] endotherm is broad and overlaps with the adjacent endotherm; values are estimated

^[b] second clearing endotherm is not observed, sample clears at 121 °C

The enthalpy at ~140 °C is only observed when the PtL¹⁶Cl₂/PtL¹⁶Cl₄ ratio is not 1:1; therefore the PtL¹⁶Cl₂ or PtL¹⁶Cl₄ in excess of the 1:1 Pt^{II}/Pt^{IV} ratio is most likely the origin of this phase change. At ~120 °C, the eutectic mixture of 1:1 PtL¹⁶Cl₂/PtL¹⁶Cl₄ forms an isotropic liquid. As the temperature increases, the excess PtL¹⁶Cl₂ or PtL¹⁶Cl₄ begins to dissolve into the isotropic phase (1:1 PtL¹⁶Cl₂/PtL¹⁶Cl₄ eutectic mixture), and a broad transition is observed. At ~140 °C the excess component becomes freely soluble in the isotropic mixture. Optical analysis demonstrates that at the clearing temperature of PtL¹⁶Cl₄ (143 °C), PtL¹⁶Cl₂ dissolves easily into the PtL¹⁶Cl₄ isotropic liquid. Because of the PtL¹⁶Cl₂ solubility in PtL¹⁶Cl₄ at 143 °C, no ordered phases would be expected to form above 143 °C for the PtL¹⁶Cl₂/PtL¹⁶Cl₄ compositions analyzed. The appearance of a second clearing endotherm for off-eutectic samples is similar to the eutectic melting behavior observed for many binary systems. One component melts with sufficient amounts of the second component to reach the eutectic composition, then a broad melting transition is observed for the excess of the second component.¹⁵⁶

If a true eutectic liquid crystalline phase is formed from 1:1 PtL¹⁶Cl₂/PtL¹⁶Cl₄, then the transition for the formation of the phase (the exothermic transition at ~108 °C) should

also show a single phase transition for the 1:1 sample. The off-stoichiometry samples, however, should show more complicated DSC behavior in addition to the exotherm for formation of the CoI_H alloy at ~ 108 °C due to the formation of multiple phases. For all samples analyzed, a transition is observed at ~ 108 °C. The phase behavior becomes more complicated as the $\text{Pt}^{\text{II}}/\text{Pt}^{\text{IV}}$ ratio further deviates from 1:1 (see Appendix II); however the phase behavior of the samples below 108 °C differs depending on whether the excess component is $\text{PtL}^{16}\text{Cl}_2$ or $\text{PtL}^{16}\text{Cl}_4$ (see Figure 4-7). The differences in intermolecular interactions in neat samples of $\text{PtL}^{16}\text{Cl}_2$ and $\text{PtL}^{16}\text{Cl}_4$ (Chapter 3) would be expected to give different thermal behavior. Many binary mixtures demonstrate different phases depending on which component is in excess of the eutectic composition.^{153, 156, 158}

Because the samples with excess $\text{PtL}^{16}\text{Cl}_2$ display less complicated thermal behavior, they will be discussed first. Based the clearing behavior, as a function of the ratio of Pt^{II} to Pt^{IV} , the eutectic composition was suspected to be 1:1 $\text{PtL}^{16}\text{Cl}_2/\text{PtL}^{16}\text{Cl}_4$. To test this hypothesis, various amounts of excess $\text{PtL}^{16}\text{Cl}_2$ were added to the 1:1 $\text{PtL}^{16}\text{Cl}_2/\text{PtL}^{16}\text{Cl}_4$ samples, and the enthalpy change associated with formation of the CoI_H alloy was compared to the number of moles of alloy in the samples (Table 4-3). The enthalpy change associated with formation of the CoI_H alloy is determined by integrating the area under the exotherm at 108 °C. The molar mass of alloy is taken to be 994.61 g/mol for alloy formula unit of $[\text{PtL}^{16}\text{Cl}_3]$. This corresponds to the suspected 1:1 $\text{PtL}^{16}\text{Cl}_2/\text{PtL}^{16}\text{Cl}_4$ composition of the alloy. As can be observed in Figure 4-8, the enthalpy change associated with the transition roughly correlates with the number of moles of alloy, supporting the hypothesis that the alloy composition is indeed 1:1 $\text{PtL}^{16}\text{Cl}_2/\text{PtL}^{16}\text{Cl}_4$. The large degree of variability for this fit, as evidenced by the deviation in the 1:1 $\text{PtL}^{16}\text{Cl}_2/\text{PtL}^{16}\text{Cl}_4$ samples, is due to a variety of factors

that may affect the enthalpy change. These factors include the viscosity of the samples, difficulties in obtaining precise sample ratios, and the current inability to determine the effect of interactions with the excess $\text{PtL}^{16}\text{Cl}_2$.

Table 4-3. Enthalpy change for the formation of $\text{PtL}^{16}\text{Cl}_2/\text{PtL}^{16}\text{Cl}_4$ molecular alloys.

$\text{PtL}^{16}\text{Cl}_2/\text{PtL}^{16}\text{Cl}_4$	Sample mass (mg)	ΔH (mJ/mg)	ΔH (kJ/mol alloy) ^[a]
1:1	10.1	3.71	3.7
1:1	9.4	4.50	4.5
1:1	8.0	3.42	3.4
1.3:1	5.1	0.72	0.8
1.5:1	9.8	1.10	1.4
1.8:1	4.9	4.54	6.3

^[a] molecular mass of the alloy is taken for the formula unit $[\text{PtL}^{16}\text{Cl}_3]$ and is 994.61 g/mol

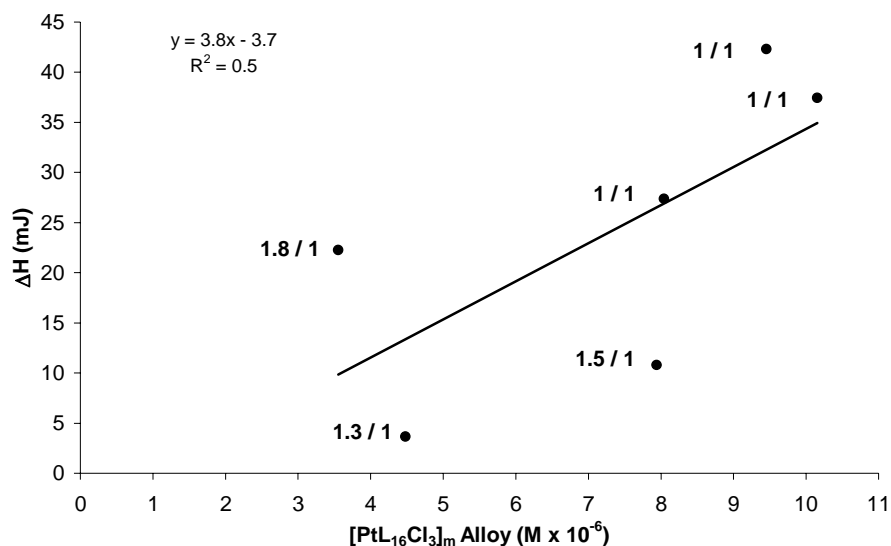


Figure 4-8. Enthalpy change associated with formation of the CoI_H alloy for various ratios of $\text{PtL}^{16}\text{Cl}_2/\text{PtL}^{16}\text{Cl}_4$ as a function of the number of moles of alloy; ratio of $\text{PtL}^{16}\text{Cl}_2/\text{PtL}^{16}\text{Cl}_4$ adjacent to each point.

Eutectic behavior is also observed when examining the DSC traces of the off-stoichiometry samples that are enriched in $\text{PtL}^{16}\text{Cl}_4$ (see Figure 4-7 and Appendix II). As shown in Figure 4-7, the 0.55:1 $\text{PtL}^{16}\text{Cl}_2/\text{PtL}^{16}\text{Cl}_4$ sample displays more complicated thermal

behavior than those samples that are $\geq 50\%$ PtL¹⁶Cl₂. An exothermic transition is observed for samples of $< 50\%$ PtL¹⁶Cl₂ at ~ 102 °C, prior to the formation of the Col_H alloy at ~ 108 °C. Due to the proximity of this exotherm to the exotherm for formation of the Col_H alloy, the enthalpy change for formation of the Col_H alloy could not be analyzed as it was for the samples with excess PtL¹⁶Cl₂ (Table 4-3 and Figure 4-8). It is suspected that the exotherm at ~ 102 °C may correspond to the formation a PtL¹⁶Cl₂/PtL¹⁶Cl₄ molecular alloy of a composition other than 1:1 PtL¹⁶Cl₂/PtL¹⁶Cl₄; however, without further analysis by XRD this cannot be confirmed. As MX chain formation in a 1:1 molecular alloy was the focus of the research, XRD analysis focused on samples of 1:1 composition.

4.3.2 Structure of the PtL¹⁶Cl₂/PtL¹⁶Cl₄ Alloy Mesophase as Determined by XRD

The Col_H structure of the molecular alloy was determined from the XRD pattern obtained for a 1:1 mixture of PtL¹⁶Cl₂/PtL¹⁶Cl₄ as given in Figure 4-9. Due to its proximity to the X-ray beam, the (100) reflection could not be observed. The large number of low angle reflections corresponding to the progression a , $(\sqrt{3})^{-1}a$, $2^{-1}a$, $(\sqrt{7})^{-1}a$, $3^{-1}a$ supports assignment of the mesophase as Col_H.⁴⁹ The packing expected for the Col_H mesophase along with the various dimensions are shown in the figure. Calculation of a powder pattern using a simplified unit cell, in this case a single Pt atom in a P-6 cell and the dimensions $a = b = 35.1$ Å, $c = 10.2$ Å, $\alpha = \beta = 90^\circ$, $\gamma = 120^\circ$, gives good agreement with the observed data. The observed reflections are expected to have a progressively greater broadening for the higher order reflections. The higher angle reflections, corresponding to very short correlation distances, are expected to be so broad that the reflections are no longer apparent due to the inverse relationship of correlation distance and peak width.⁴⁹ For these reasons many of the

higher order reflections are not expected to be observed for the mesogenic phase.

Assignments of various reflections and the unit cell dimensions are given in Table 4-4.

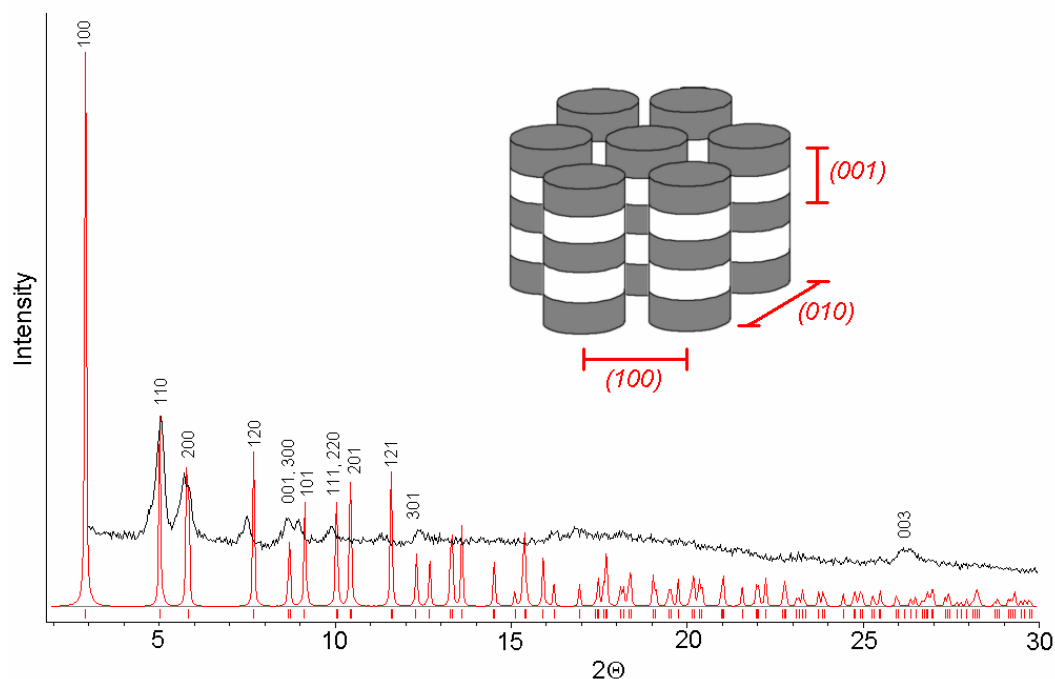


Figure 4-9. X-ray diffraction pattern for CoI_H 1:1 $\text{PtL}^{16}\text{Cl}_2/\text{PtL}^{16}\text{Cl}_4$ molecular alloy mesophase at 110 °C (top) and calculated powder pattern based on a P-6 unit cell of dimensions $a = b = 35.16 \text{ \AA}$, $c = 10.2 \text{ \AA}$, $\alpha = \beta = 90^\circ$, $\gamma = 120^\circ$ (bottom) showing proposed assignment of the major reflections.

Table 4-4. Calculated and observed reflections for the $\text{PtL}^{16}\text{Cl}_2/\text{PtL}^{16}\text{Cl}_4$ molecular alloy at 110 °C.

$Q (\text{\AA}^{-1})$	$d_{\text{meas.}} (\text{\AA})$	$d_{\text{calc.}} (\text{\AA})$	hkl
[a]	[a]	35.1	100
0.361	17.4	17.6	110
0.408	15.4	15.2	200
0.536	11.7	11.5	120
0.619	10.2	10.2	001
0.637	9.9	9.8	101
0.705	8.9	8.8	111, 220
0.803	7.8	7.5	400
0.884	7.1	7.2	301
1.35		4.9 (broad)	
1.858	3.4	3.4	003

P-6: $a = 35.1 \text{ \AA}$, $b = 35.1 \text{ \AA}$, $c = 10.2 \text{ \AA}$, $\alpha = \beta = 90^\circ$, $\gamma = 120^\circ$

^[a] reflection cannot be observed due to proximity to the X-ray beam.

As can be seen in Figure 4-10, the PtL¹⁶Cl₂/PtL¹⁶Cl₄ alloy mesophase is not a mixture of the two individual mesophases. Reflections that are not observed for the individual species are marked (*). Because the mesogens themselves are the same size in the individual and binary mesophases and because the shape and size of a mesogen are major factors in determining the mesophase packing, some similarities are expected for the XRD patterns of the alloy and those of its components. However, the large number of new reflections and the degree to which all the observed reflections may be accounted for by formation of a Col_H mesophase (Figure 4-9) point to formation of a single molecular alloy mesophase rather than a mixture of PtL¹⁶Cl₂ and PtL¹⁶Cl₄ mesophases.

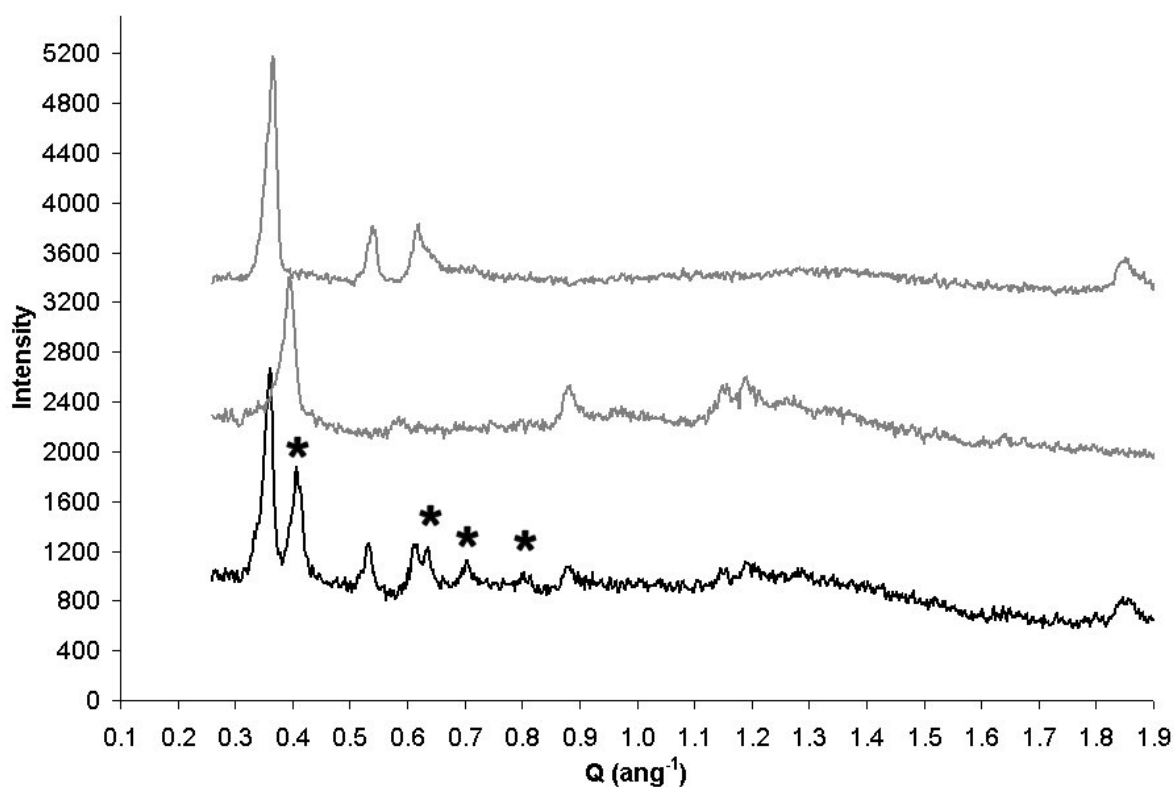


Figure 4-10. XRD patterns for PtL¹⁶Cl₂ at 110 °C (top), PtL¹⁶Cl₄ at 120 °C (middle), and the PtL¹⁶Cl₂/PtL¹⁶Cl₄ Col_H alloy at 110 °C (bottom); reflections not observed for the individual complexes (*).

Though a Col_H phase is observed, there are several possibilities for production of a hexatic phase in a 1:1 $\text{PtL}^{16}\text{Cl}_2/\text{PtL}^{16}\text{Cl}_4$ alloy. The two extremes, as diagramed in Figure 4-11, are either the hexagonally ordered columns corresponding to MX chains which alternate Pt^{II} and Pt^{IV} sites (left) or the individual columns composed solely of Pt^{II} or Pt^{IV} moieties, where the $[\text{PtL}^{16}\text{Cl}_2]_m$ and $[\text{PtL}^{16}\text{Cl}_4]_m$ columns are randomly distributed through the hexatic phase (center). The formation of a Col_H mesophase with randomly distributed $[\text{PtL}^{16}\text{Cl}_2]_m$ and $[\text{PtL}^{16}\text{Cl}_4]_m$ columns is unlikely because the dissimilar axial dimensions of $\text{PtL}^{16}\text{Cl}_2$ and $\text{PtL}^{16}\text{Cl}_4$ would result in differences in the packing of the $[\text{PtL}^{16}\text{Cl}_2]_m$ and $[\text{PtL}^{16}\text{Cl}_4]_m$ columns. In molecular alloys that do form mesophases of randomly distributed columns (like $[(\text{CH}_3(\text{CH}_2)_n\text{CO}_2)_2\text{Rh}]_2/[(\text{CH}_3(\text{CH}_2)_n\text{CO}_2)_2\text{Cu}]_2$ alloy,¹⁶⁰ Figure 4-2), the two mesogens have similar dimensions.



Figure 4-11. Possible methods of formation for a Col_H mesophase of 1:1 $\text{PtL}^{16}\text{Cl}_2/\text{PtL}^{16}\text{Cl}_4$; MX chain interactions within $[\text{PtL}^{16}\text{Cl}_2\text{-PtL}^{16}\text{Cl}_4]_m$ columns (left), and random distribution of individual $[\text{PtL}^{16}\text{Cl}_2]_m$ and $[\text{PtL}^{16}\text{Cl}_4]_m$ columns (center).

4.3.3 $\text{PtL}^{16}\text{Cl}_2$ Absorbance Spectrum and DFT Calculations

Resonance Raman spectroscopy is the most frequently utilized technique to probe for the presence of MX chain interactions when single crystal X-ray data cannot be obtained. A

strong resonance progression is observed in the Raman spectrum of MX chain systems when the excitation wavelength corresponds to the energy for Pt^{II} to Pt^{IV} electron transfer along the chain.²² Due to the luminescence of PtLⁿCl₂ and PtLⁿCl₄ complexes at the available laser wavelengths, Raman spectroscopy was not possible. However, as will be discussed in Section 4.3.5, luminescence of the PtLⁿCl₂ and PtLⁿCl₄ complexes provides a probe for the self-assembly of the PtL¹⁶Cl₂/PtL¹⁶Cl₄ molecular alloy. Initial absorbance and fluorescence experiments focused on characterizing PtL¹⁶Cl₂ and PtL¹⁶Cl₄ individually, and those results are discussed in this section and the next. Subsequent sections discuss the analysis of PtL¹⁶Cl₂/PtL¹⁶Cl₄ mixtures before and after self-assembly of the Col_H alloy.

The UV-vis absorbance spectrum for PtL¹⁶Cl₂ in chloroform solution is shown in Figure 4-12 along with a simplified molecular orbital diagram for a square-planar complex. The spectrum of PtL¹⁶Cl₂ is in good agreement with the reported analysis of the complex in methylene chloride solution.⁴⁷ Strong absorbances for PtL¹⁶Cl₂ are observed at 244, 306, and 430 nm, and shoulders at 260, 340, and 408 nm. As a good understanding of the absorbance spectra is expected to aid in the identification of the electronic state responsible for the luminescence, the absorbance spectra are analyzed in detail. Previously, the 306 and 340 nm absorptions were assigned as spin-allowed ligand centered (¹LC) transitions.⁴⁷ The 244 and 260 nm transitions are also expected to be LC. These transitions were not reported by Pucci et al., presumably due to the solvent cut-off wavelength. Although quantitative data cannot be obtained at these wavelengths, qualitative data can be obtained in chloroform from 240 to 260 nm.¹⁶¹ These higher energy absorptions are likely $\pi \rightarrow \pi^*$ transitions involving the ligand. The 408 nm transition is unassigned in the literature, but given the absence of such an absorbance for the free ligand and the molar absorptivity of 5490 M⁻¹cm⁻¹, the transition is

suspected to involve either a ligand-to-metal (LMCT) or metal-to-ligand (MLCT) charge transfer. The 430 nm absorbance and its shoulder have been assigned as $^3\text{MLCT}$ and $^1\text{MLCT}$ transitions, respectively.⁴⁷ This assignment was based on previous analysis of the lowest energy excited states of $\text{Pt}(\text{bpy})\text{Cl}_2$, $\text{Pt}(5,5'\text{-Me}_2\text{bpy})\text{Cl}_2$, and $\text{Pt}[3,3'\text{-(MeO}_2\text{C)}_2\text{bpy}]\text{Cl}_2$, which were assigned as LF for the former two complexes and MLCT for the latter.^{162, 163} The solid-state structures of PtL^1Cl_2 and $\text{PtL}^{16}\text{Cl}_2$ more closely resemble that of the planar $\text{Pt}(5,5'\text{-Me}_2\text{bpy})\text{Cl}_2$, than the non-planar structure of $\text{Pt}[3,3'\text{-(MeO}_2\text{C)}_2\text{bpy}]\text{Cl}_2$ which arises from steric repulsions between the methyl ester substituents.¹⁶³

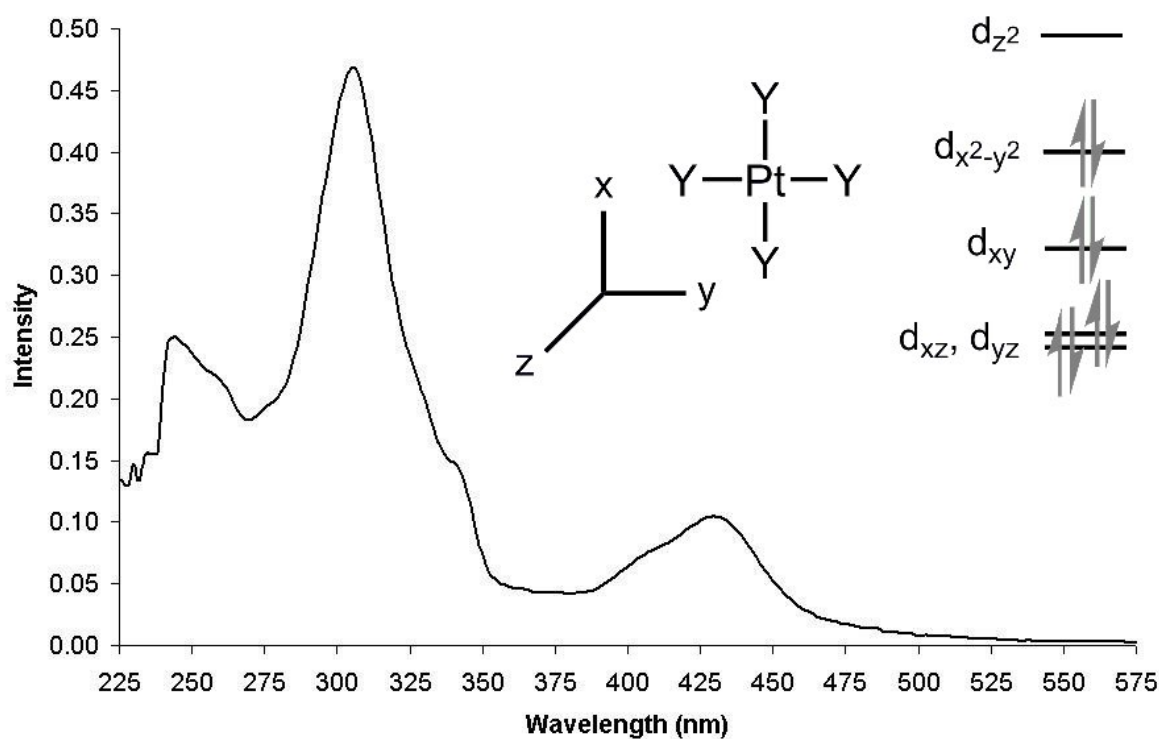


Figure 4-12. UV-vis absorbance spectrum for 12.5 μM $\text{PtL}^{16}\text{Cl}_2$ in CHCl_3 and the d orbital diagram expected for a generic square-planar complex.

To better understand the photophysical data, a series of molecular orbital calculations were performed with Gaussian using a density functional theory approach. A gas-phase model was utilized. The bond distances and angles obtained from energy minimizations of PtL¹Cl₂ and PtL¹Cl₄ are compared with those obtained from the single crystal structures of PtL¹Cl₂ and Pt(bpy)Cl₄ (Table 4-5). The greatest discrepancy between the model and the single crystal structure is found in the axial Pt-Cl bond distance, which is calculated to be ~0.08 Å longer than is observed. The other calculated bond lengths are within ~0.04 Å of the observed bond lengths. Previous work has shown that for PtL⁸Cl₂, PtL¹⁶Cl₂, and PtL²⁰Cl₂ the photophysical data was independent of chain length.⁴⁷ On that basis, the simple PtL¹Cl₂ model complex is expected to behave similarly to PtL¹⁶Cl₂, at least in chloroform solution where intermolecular packing is not an issue.

Table 4-5. Bond distances and angles for PtL¹Cl₂ (**a**) and PtL¹Cl₄ (**b**) as determined by Gaussian DFT calculation compared to single crystal X-ray diffraction data for similar species.

a	PtL ¹ Cl ₂ ^[a]	PtL ¹ Cl ₂ calculated
Pt-N (Å)	2.009 ^[b]	2.03
Pt-Cl (Å)	2.299 ^[b]	2.34
Cl-Pt-Cl (°)	88.44(6)	89.9
N-Pt-Cl (°)	95.61 ^[b]	94.9
N-Pt-N (°)	80.4(3)	80.3

^[a] determined by single crystal X-ray diffraction Chapter 3
^[b] av value

b	Pt(bpy)Cl ₄ ^[c]	PtL ¹ Cl ₄ calculated
Pt-N (Å)	2.041 ^[b]	2.07
Pt-Cl _{ax} (Å)	2.318 ^[b]	2.40
Pt-Cl _{eq} (Å)	2.307 ^[b]	2.35
Cl _{eq} -Pt-Cl _{eq} (°)	89.1(1)	89.3
N-Pt-Cl _{eq} (°)	94.9 ^[b]	95.4
N-Pt-N (°)	81.3(4)	79.8
N-Pt-Cl _{ax} (°)	89.2 ^[b]	89.1

^[c] determined by single crystal X-ray diffraction¹⁴⁴

The calculated orbitals and their energies are shown in Figure 4-13, while Figure 4-14 is a molecular orbital diagram showing the relative energies of the orbitals and their symmetries. The d orbitals are referred to by their more familiar square-planar symmetry designations and the molecular orbitals are designated based on their most significant component. The orbital symmetries in the C_{2v} point group of the molecule are also given in the figure. The highest occupied molecular orbital (HOMO) is calculated as the antibonding combination of $d\pi^*$ and $p_z(\text{Cl})$ orbitals. The lowest unoccupied molecular orbital (LUMO) is calculated to be the $d\pi^*$ and $\pi^*(L^1)$ antibonding combination, with most of the orbital character being based on the bipyridine ligand. Significantly for determination of the state responsible for the solid-state luminescence, the mainly $\pi^*(L^1)$ LUMO is lower in energy than the $d\sigma^*$ orbital, as was expected based on previous results with the $3,3'-(\text{MeO}_2\text{C})_2\text{bpy}$ complex.¹⁶³ As expected from the generic square-planar MO diagram, the $d\pi^*$ orbitals are filled, and a $d\sigma^*$ orbital is the LUMO+3. The ligand coordination results in a d_{z^2} orbital stabilized below the $d\pi^*$ orbitals. Applying a solvent correction raises the energy of this orbital.

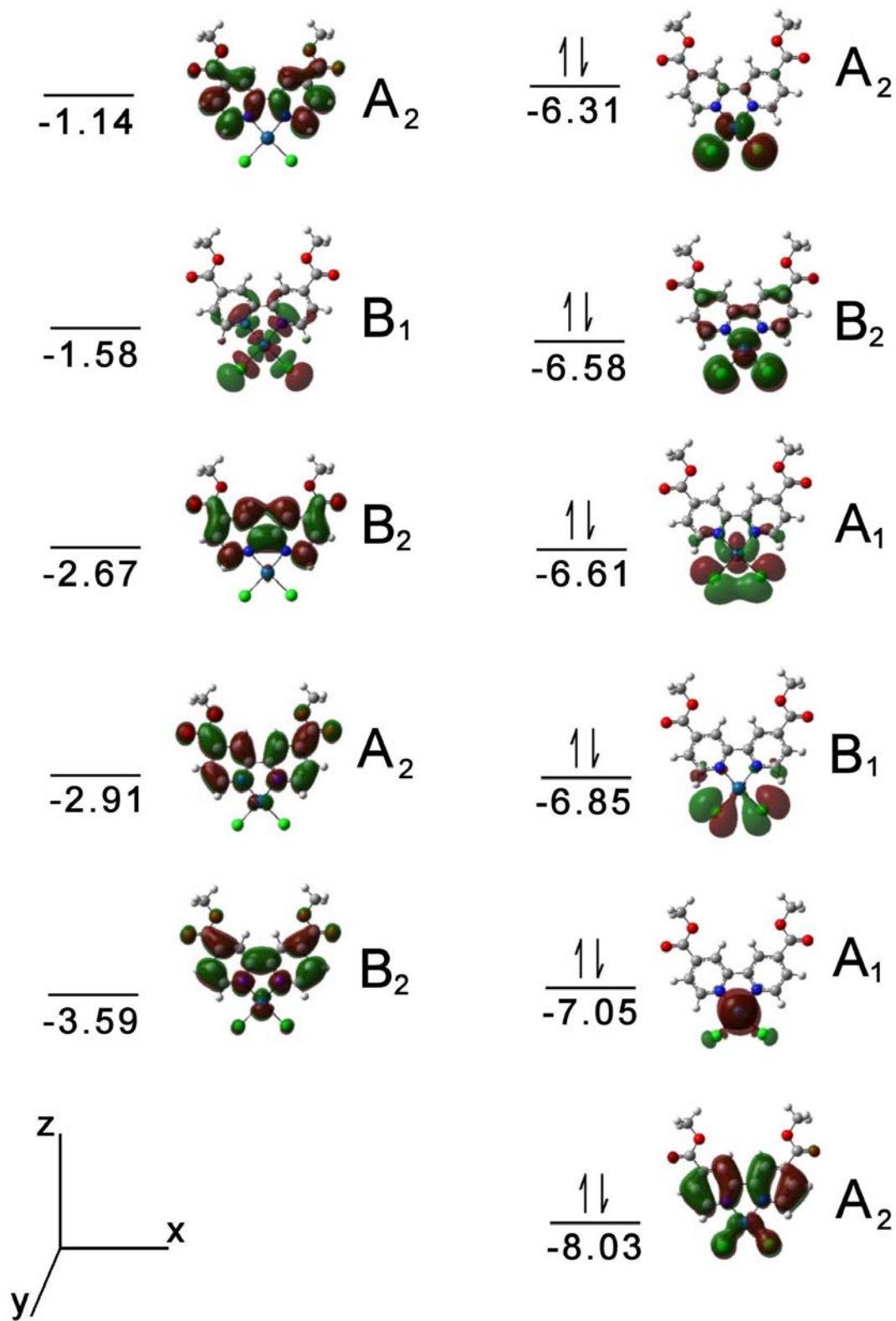


Figure 4-13. Calculated molecular orbitals for PtL^1Cl_2 ; orbital energies in eV, orientation in the C_{2v} symmetry of the molecule shown.

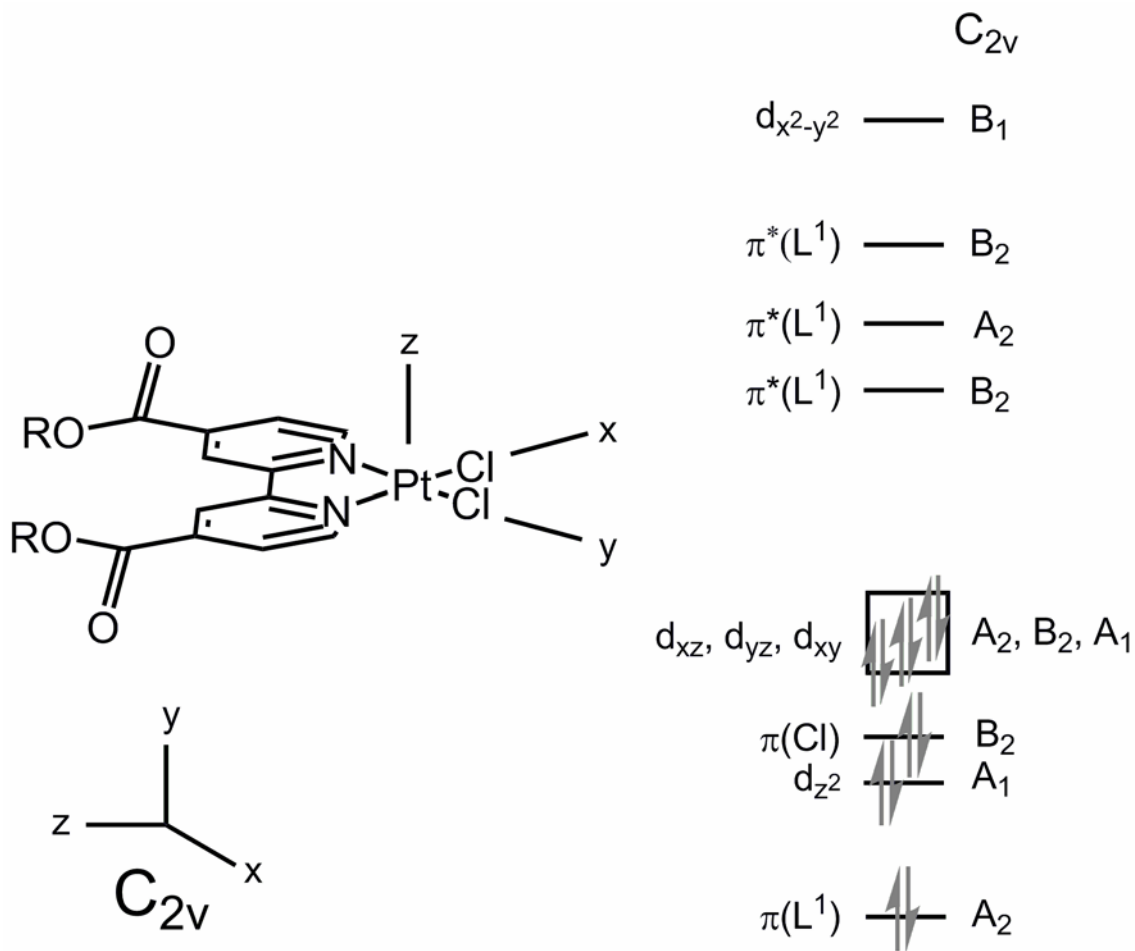


Figure 4-14. Molecular orbital diagram for PtL^1Cl_2 as determined using Gaussian; orientation at the molecule refers to the usual square-planar coordinate system.

The proposed assignments of the $PtL^{16}Cl_2$ absorbances can be compared to the transition energies and molecular orbitals of PtL^1Cl_2 . Although the energy differences between the molecular orbitals are only a crude estimate of the absorbance energies, a good correspondence is observed between the PtL^1Cl_2 model and the absorbances observed for $PtL^{16}Cl_2$ (Table 4-6). Assignment of the low energy absorbance as MLCT rather than LF is made based on the more significant ligand π^* contribution in the antibonding combination of $d\pi^*$ and $\pi^*(L^1)$ character of the LUMO. The calculated lowest energy transition is 456 nm

for HOMO→LUMO. This compares well to the observed 408 and 430 nm absorbances for PtL¹⁶Cl₂. Previous work by Connick and coworkers¹⁶³ on Pt[3,3'-(MeO₂C)₂bpy]Cl₂ and Pucci et al.⁴⁷ on PtL¹⁶Cl₂ assigned the lowest energy excited states as MLCT derived for both complexes. The calculated molecular orbital energies for PtL¹Cl₂ conform to these results.

Table 4-6. UV-vis absorbance maxima and molar absorptivities for PtL¹⁶Cl₂ in CHCl₃ and calculated orbital energy differences for PtL¹Cl₂.

PtL ¹⁶ Cl ₂ - observed			PtL ¹ Cl ₂ - calculated			
nm (ε M ⁻¹ cm ⁻¹)	λ _{max} eV		ΔE		molecular orbitals ^[a]	
			nm	eV		
244 (10600)	5.08	π→π*	192	6.45	HOMO-5→LUMO+3	LMCT (π→d _{x²-y²})
260 (11500)	4.77	π→π*	231	5.36	HOMO-5→LUMO+2	π→π*
306 (15900)	4.05	π→π*	243	5.12	HOMO-5→LUMO+1	π→π*
340 (4450)	3.65	MLCT	247	5.03	HOMO-1→LUMO+3	LF (d _{yz} →d _{x²-y²})
408 (5490)	3.04	MLCT	262	4.73	HOMO→LUMO	LF (d _{xz} →d _{x²-y²})
430 (7330)	2.89	MLCT	279	4.44	HOMO-5→LUMO	π→π*
			338	3.02	HOMO-2→LUMO	d _{xy} →π*
			415	2.99	HOMO-1→LUMO	d _{yz} →π*
			456	2.72	HOMO→LUMO	MLCT (d _{xz} →π*)

^[a] molecular orbitals shown in Figure 4-13

4.3.4 Luminescence Spectroscopy of Pt^{II} Complexes

Solid-state emission spectroscopy of Pt^{II}-diimine complexes is complicated by a variety of factors. For square-planar Pt^{II}-diimine complexes, the lowest energy excited state may be LF, intraligand π→π*, or MLCT, and a great variety of excimer interactions are possible due to the close Pt-Pt and π-π interactions.¹⁶⁴ Excimers, excited state dimers, form when an excited state species reacts to form a dimer with a closely adjacent species. Pt(trpy)Cl⁺ (trpy = terpyridine)¹⁶⁵ and [Pt(phen)₂]Cl₂ (phen = phenanthroline)¹⁶⁶ show

emission from π - π^* excimers. Both complexes also luminesce from monomeric excited states, and $\text{Pt}(\text{trpy})\text{Cl}^+$ forms additional luminescent Pt-Pt excimers. Solid-state supramolecular interactions also affect the lowest energy excited state. For example, the yellow polymorph of $\text{Pt}(\text{bpy})\text{Cl}_2$ gives ^3LF based emission, but Pt-Pt interactions in the red polymorph lead to $^3\text{MLCT}$ based emission.¹⁶² There have been no reports of polymorphism which affects the luminescence emission of $\text{Pt}(\text{bpy})\text{Cl}_4$. As will be discussed below, this potential for polymorphism complicates the solid-state luminescence spectra of $\text{PtL}^{16}\text{Cl}_2$ and $\text{PtL}^{16}\text{Cl}_4$.

The emission spectra ($\lambda_{\text{ex.}} = 514 \text{ nm}$) obtained from microcrystalline samples of $\text{PtL}^{16}\text{Cl}_2$ and $\text{PtL}^{16}\text{Cl}_4$ are given in Figure 4-15. The emission maximum for $\text{PtL}^{16}\text{Cl}_2$ is 614 nm at room temperature under ambient conditions. This difference from the reported 640 nm emission⁴⁷ for sample dispersed in a KBr pellet is likely due to the sample concentration. Diluting the sample 1:1 with free ligand (L^{16}), gives a shift in the emission maximum to 626 nm (Figure 4-15). The free ligand does not fluoresce at the experimental excitation wavelength.

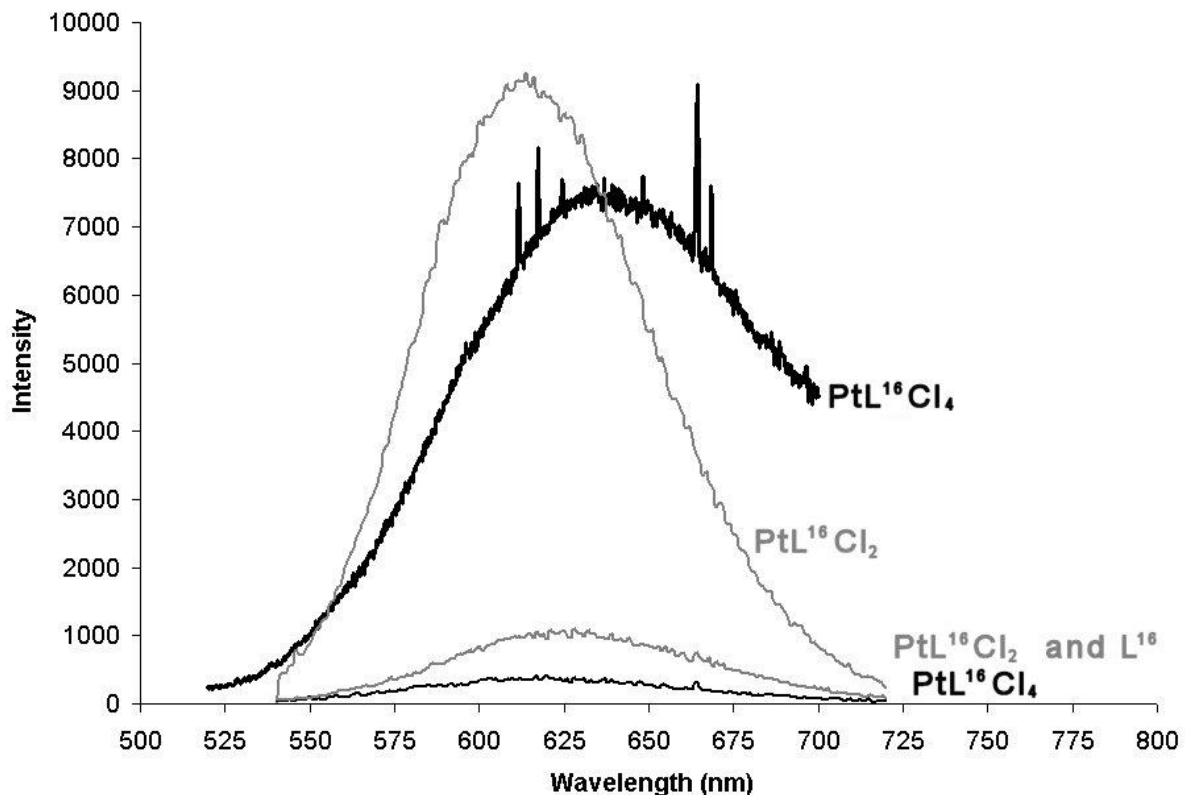


Figure 4-15. Solid-state emission spectra for PtL¹⁶Cl₄, PtL¹⁶Cl₂, and 1:1 PtL¹⁶Cl₂ and L¹⁶; $\lambda_{\text{ex}} = 514$ nm excitation, measured under reduced pressure (thick line); measured under ambient conditions (thin line), relative intensities un-normalized.

The most notable difference between the solution and solid-state absorbances is the ability to use a 514 nm excitation wavelength. As shown in the absorbance spectrum, PtL¹⁶Cl₂ does not absorb significantly in solution at 514 nm, although the broad edge of the 430 nm absorbance is observed at very high concentration. Previous work on PtL¹⁶Cl₂ showed a large shift in the emission maximum from 482 nm in CH₂Cl₂ solution to 640 nm for KBr pellet microcrystalline samples, which is attributed to Pt-Pt stacking interactions in the solid state.⁴⁷

The broad featureless emission for PtL¹⁶Cl₂ (Figure 4-15) is consistent with emissions arising from either ³LF (d→d) or MLCT excited states, as has been observed for similar Pt

complexes.^{115, 117, 164} Work by Miskowski and coworkers has shown that Pt[3,3'-(MeO₂C)₂-bpy]Cl₂ has a lowest energy triplet metal-to-ligand charge transfer (³MLCT) excited state, and an asymmetric emission peak is observed for emission from the MLCT state.¹⁶² The calculations and solution absorbance data support assignment of the PtL¹⁶Cl₂ excited state as MLCT derived as was previously reported in the literature.⁴⁷

Further research needs to be carried out to determine if similarly to Pt(bpy)Cl₂, PtL¹⁶Cl₂ can display polymorphs which affect the emission spectra. Visual inspection of samples provides some evidence for polymorphism. Samples precipitated from chloroform have a pale orange color, while samples cooled from the neat isotropic liquid have a red-orange color, and the isotropic liquid is an intense red.

The Gaussian model of PtL¹Cl₂ does not account for either the Pt-Pt or π - π stacking interactions that were previously discussed as resulting in excimer effects and changes in the giving rise to for emission. PtL¹Cl₂ emits in the solid-state at 658 nm (298 K) and 664 nm (77 K), but it is non-emissive in room temperature CH₂Cl₂ solution.¹³⁰ While the absolute energy differences determined from the molecular orbital calculations are not applicable to the solid-state luminescence behavior, the composition of the molecular orbitals and their relative energies are useful. The molecular orbital compositions may be used to rationalize the decrease in the HOMO→LUMO gap when comparing solution and solid-state absorbances. Any d orbital with a component along the Pt-Pt axis will be affected by the formation of solid-state Pt-Pt interactions. A destabilization of the HOMO, which has no significant bipyridine character but considerable $d\pi^*$ and $\pi^*(Cl)$ character, is expected. The $\pi^*(L^n)$ LUMO, meanwhile, would be affected by the formation of π - π interactions in the solid-state.

The emission wavelengths and lifetimes for microcrystalline samples including PtL¹⁶Cl₂ are given in Table 4-7. The tabulated data includes the emission properties of PtL¹⁶Cl₂, PtL¹⁶Cl₄, and various mixtures of these species and the free ligand, L¹⁶. The emission lifetimes of PtL¹⁶Cl₄ and the mixed samples are discussed in subsequent sections. Emission lifetimes were determined by fitting the decay curve (Figure 4-16) to a biexponential function. A 7.14 ns luminescence lifetime is observed for the PtL¹⁶Cl₂ powder at room temperature. This lifetime is considerably shorter than the emission lifetime of the red polymorph of Pt(bpy)Cl₂ (250 ns) or Pt[3,3'-(MeO₂C)₂bpy]Cl₂ (350 ns, 300 K); the yellow form of Pt(bpy)Cl₂ is non-emissive at 300 K.¹⁶² At this time, the reason for the decreased lifetime in comparison to these other species is not known, but differences in vibrational quenching modes caused by the supramolecular ordering of the alkyl chains in PtL¹⁶Cl₂ solid are suspected.

Table 4-7. Solid-state emission wavelengths and lifetimes of various L¹⁶, PtL¹⁶Cl₂, and PtL¹⁶Cl₄ samples.

Sample	Preparation	λ_{\max} (nm)	$\tau^{[c]}$ (ns)	$\tau^{[c]}$ (ns)
L ¹⁶	RT, powder	none ^[a]		
PtL ¹⁶ Cl ₂	RT, powder	614 ^[a]	0.673 ^[d]	7.14
1:1 PtL ¹⁶ Cl ₂ and L ¹⁶	heated and quenched	626 ^[a]	23.5	118
PtL ¹⁶ Cl ₄	RT, powder	619 ^[a]	15.6	157
PtL ¹⁶ Cl ₄	RT, powder	634 ^[b]		
1:1 PtL ¹⁶ Cl ₂ and PtL ¹⁶ Cl ₄	RT, mixture	608 ^[a]	108	564
1:2.4 PtL ¹⁶ Cl ₂ and PtL ¹⁶ Cl ₄	RT, mixture	622 ^[b]		
1:1 PtL ¹⁶ Cl ₂ /PtL ¹⁶ Cl ₄ alloy	heated and quenched	650 ^{[a],[e]}		
1:1 PtL ¹⁶ Cl ₂ /PtL ¹⁶ Cl ₄ alloy	heated and quenched	680 ^{[b],[e]}		
1:2.1 PtL ¹⁶ Cl ₂ /PtL ¹⁶ Cl ₄ alloy	heated and quenched	628 ^[b]		

^[a] RT under ambient conditions in a glass tube sample holder, $\lambda_{\text{ex}} = 514$ nm.

^[b] RT under reduced pressure in a brass and quartz sample holder, $\lambda_{\text{ex}} = 514$ nm.

^[c] RT under ambient conditions in a glass tube sample holder, $\lambda_{\text{ex}} = 423$ nm, $\lambda_{\text{obs}} = 614$ nm, fitted to a biexponential decay.

^[d] Due to emission from the glass sample holder

^[e] Very broad low intensity emission

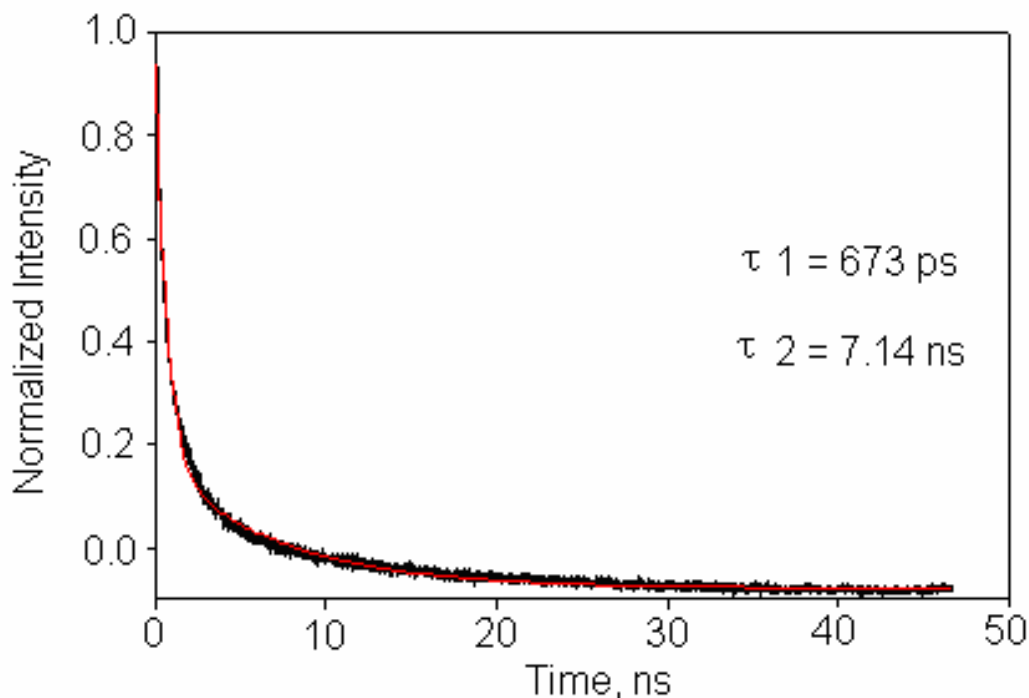


Figure 4-16. Decay curve for the luminescence of $\text{PtL}^{16}\text{Cl}_2$ at room temperature (black) with the lifetimes determined by fitting the curve to a biexponential decay (red); $\lambda_{\text{ex}} = 423 \text{ nm}$; $\lambda_{\text{obs}} = 614 \text{ nm}$.

4.3.5 $\text{PtL}^{16}\text{Cl}_4$ Luminescence Spectroscopy and DFT Calculations

The PtL^nCl_4 complexes have the same C_{2v} symmetry as their Pt^{II} precursors. The addition of the axial chloride ligands affects the metal orbital energies and prevents the formation of Pt-Pt interactions in the solid-state. The UV-vis absorbance spectrum for $\text{PtL}^{16}\text{Cl}_4$ is given in Figure 4-17. The molecular orbital diagram for a generic d^6 -octahedral complex is also shown. The high energy ligand-based π - π^* absorbances are similar to those of $\text{PtL}^{16}\text{Cl}_2$ and the free ligand L^{16} , and are observed at 246 and 260 nm. A shoulder with low molar absorptivity is observed at 272 nm. The absorbance at 322 nm is likely a metal-perturbed LC absorbance, which is moved to higher energy in the $\text{PtL}^{16}\text{Cl}_4$ complex than in the $\text{PtL}^{16}\text{Cl}_2$ by addition of the axial chloride ligands.

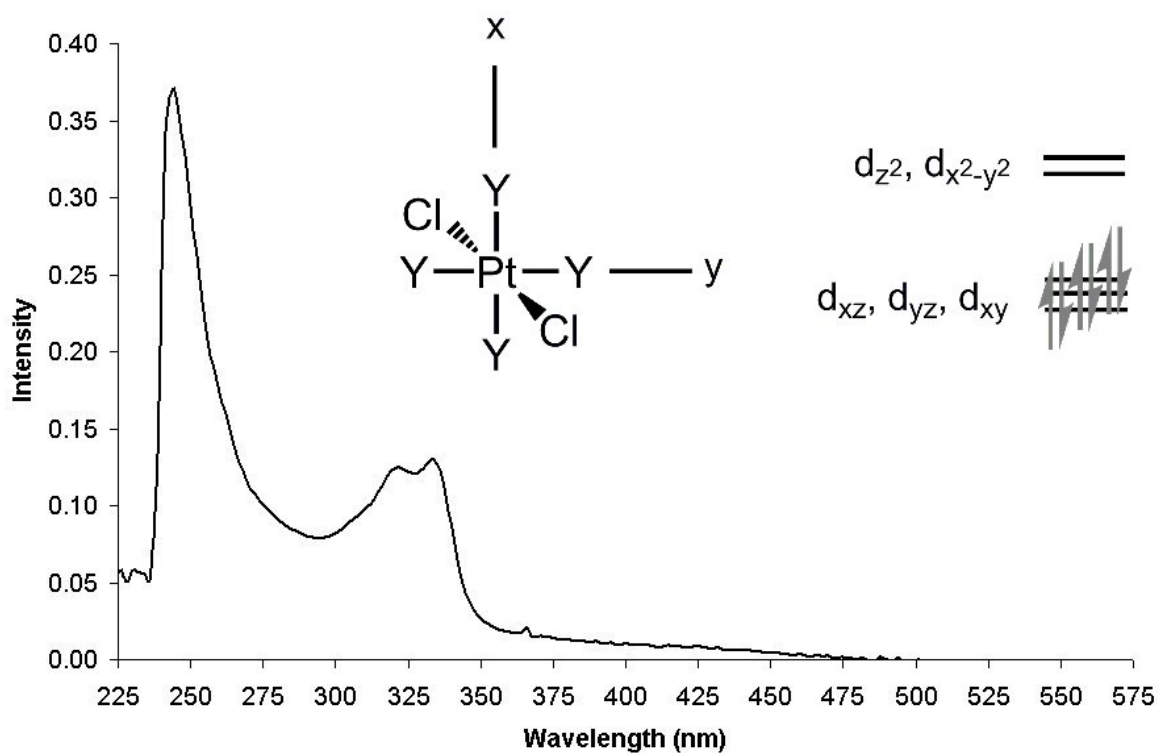


Figure 4-17. Absorbance spectrum for $8.9 \mu\text{M PtL}^{\text{I}}\text{Cl}_4$ in CHCl_3 with simplified molecular orbital diagram for a generic octahedral complex.

The molecular orbitals for $\text{PtL}^{\text{I}}\text{Cl}_4$ calculated using Gaussian are given in Figure 4-18. A molecular orbital diagram showing the effects of the ligands on the generic molecular orbital diagram (Figure 4-17) is shown in Figure 4-19. In Figure 4-19, the relative energies of the orbitals calculated for $\text{PtL}^{\text{I}}\text{Cl}_2$ and $\text{PtL}^{\text{I}}\text{Cl}_4$ are shown. As with $\text{PtL}^{\text{I}}\text{Cl}_2$, the HOMO is calculated to be $d\pi^*$ and $\pi^*(\text{Cl})$ in character. The LUMO is largely $\pi^*(\text{L}^{\text{I}})$ with a small $d\pi^*$ contribution. The $d\sigma^*$ orbitals are unfilled as would be expected for the Pt^{IV} coordination geometry.

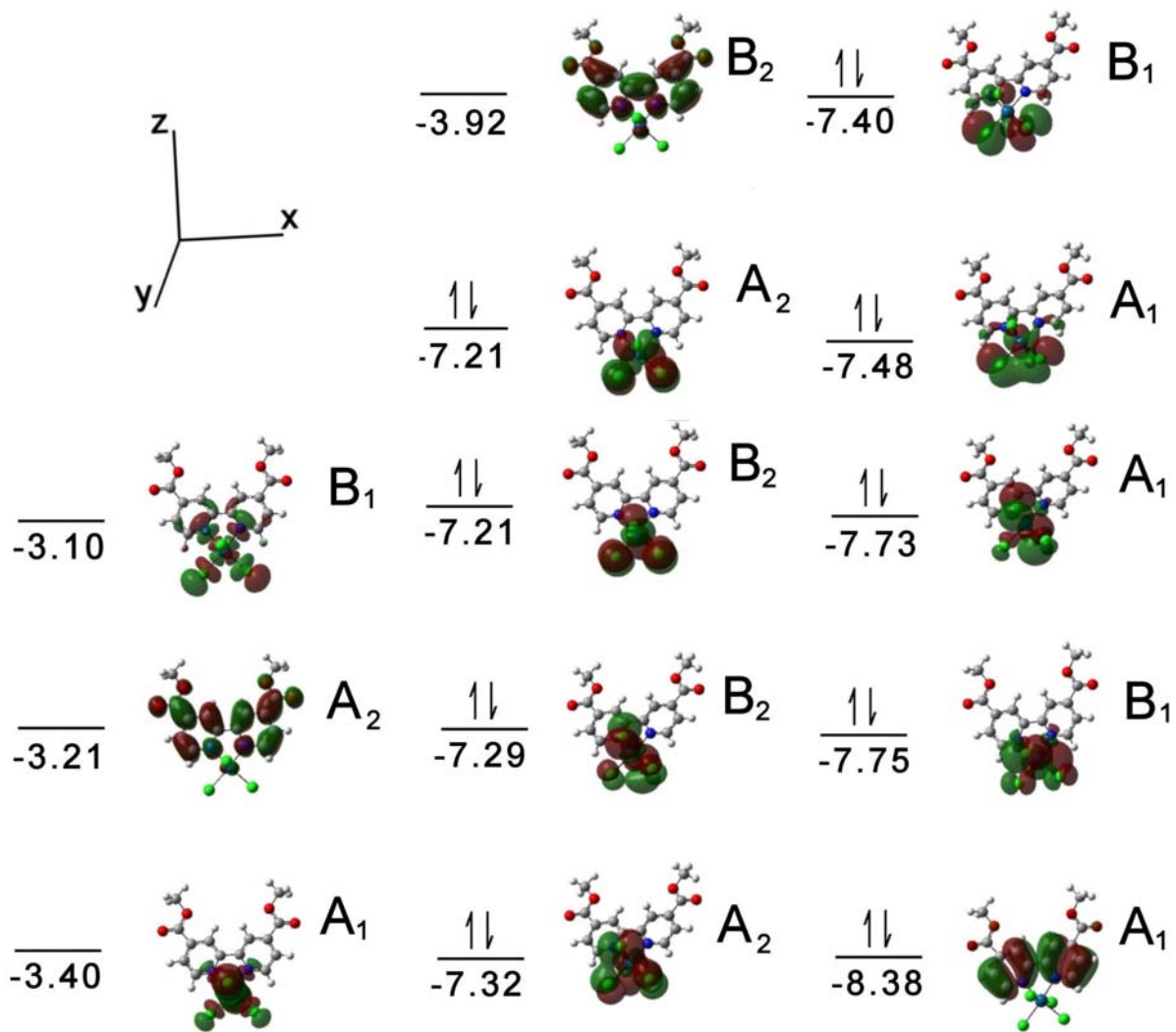


Figure 4-18. Calculated molecular orbitals for PtL¹Cl₄; orbital energies in eV.

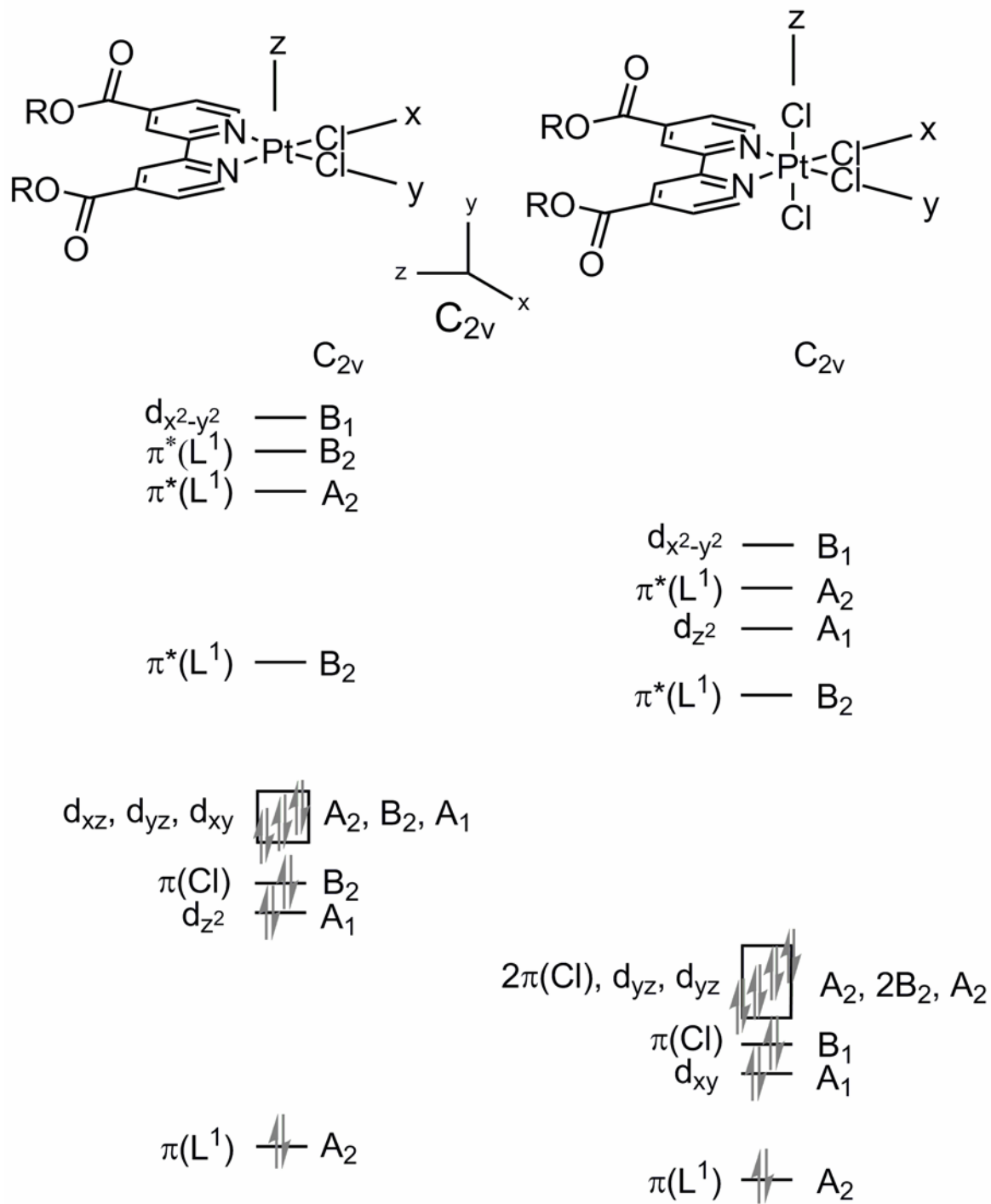


Figure 4-19. Molecular orbital diagram for PtL^1Cl_2 (left) and PtL^1Cl_4 (right) as determined using Gaussian; orientation at the molecule refers to the usual square-planar coordinate system.

The stabilization of the HOMO afforded higher oxidation state of the Pt^{IV} complex leads to a larger calculated HOMO→LUMO gap than observed for Pt^{II}. The calculated energies for PtL^ICl₄ are compared to those observed for PtL¹⁶Cl₄ in Table 4-8. Again, while the observed absorbance energies do not directly correspond to the orbital energy differences, the calculated energy differences are consistent with the observed absorbances of PtL¹⁶Cl₄.

Table 4-8. UV-vis absorbance maxima and molar absorptivities for PtL¹⁶Cl₄ in CHCl₃ and calculated orbital energy differences for PtL^ICl₄.

PtL ¹⁶ Cl ₄ - observed			PtL ^I Cl ₄ - calculated			
λ_{\max}			ΔE		molecular orbitals ^[a]	
nm (ϵ M ⁻¹ cm ⁻¹)	eV		nm	eV		
246 (37200)	5.04	$\pi \rightarrow \pi^*$	240	5.17	HOMO-8 \rightarrow LUMO+2	LMCT ($\pi \rightarrow d_{x^2-y^2}$)
260 (20600)	4.77	$\pi \rightarrow \pi^*$	249	4.98	HOMO-8 \rightarrow LUMO+1	$\pi \rightarrow \pi^*$
272 (8580)	4.56	$\pi \rightarrow \pi^*$	278	4.46	HOMO-8 \rightarrow LUMO	$\pi \rightarrow \pi^*$
322 (10700)	3.85	MLCT	296	4.19	HOMO-2 \rightarrow LUMO+2	LF ($d_{yz} \rightarrow d_{x^2-y^2}$)
334 (11200)	3.71	$\pi(\text{Cl}) \rightarrow \pi^*$	310	3.56	HOMO-5 \rightarrow LUMO	MLCT($d_{xy} \rightarrow \pi^*$)
			319	3.89	HOMO-2 \rightarrow LUMO+1	LF ($d_{yz} \rightarrow d_{z^2}$)
			377	3.29	HOMO \rightarrow LUMO	$\pi(\text{Cl}) \rightarrow \pi^*$

^[a] molecular orbitals shown in Figure 4-18

The solid-state photophysics of PtL¹⁶Cl₄ also demonstrates behavior that may indicate sensitivity to the solid-state morphology. Two different emission maxima are obtained depending on sample preparation as shown in Figure 4-15. Analyzing a sample in a purged vacuum apparatus gives a 634 nm emission, while under ambient conditions in air a 619 nm emission maximum is observed. NMR analysis does not show any decomposition of the PtL¹⁶Cl₄ samples. A possible explanation for this behavior is the formation of a hydrate. XRD data show a structural change for samples stored in air compared to those which have been carefully dried (Figure 4-20). At this time, the particulars of this rearrangement are not well understood, but the broad reflections observed for the sample stored in air seems to

support a more disordered structure, possibly the result of partial hydration. Hydration dependant emission maxima have been observed for $[\text{Pt}(\text{phen})_2]\text{Cl}_2$.¹⁶⁶ It is likely that the 634 nm emission is from anhydrous $\text{PtL}^{16}\text{Cl}_4$ as this measurement was taken under dynamic vacuum. This emission wavelength is very similar to the 639 nm emission of solid-state $\text{Pt}(\text{bpy})\text{Cl}_4$.¹⁶⁷ It is worth noting that the $\text{Pt}(\text{bpy})\text{Cl}_4$ emission is assigned as originating from a ^3LF state, but with the data currently available, an unambiguous assignment of the $\text{PtL}^{16}\text{Cl}_4$ excited state cannot be made. The emission lifetime for $\text{PtL}^{16}\text{Cl}_4$ is determined to have a long component of 157 ns and a short component of 15.6 ns when fitting the decay curve to a biexponential function. The ^3LF emissive state of $\text{Pt}(\text{bpy})\text{Cl}_4$ was determined to have a lifetime of 11,000 ns.¹⁶⁷

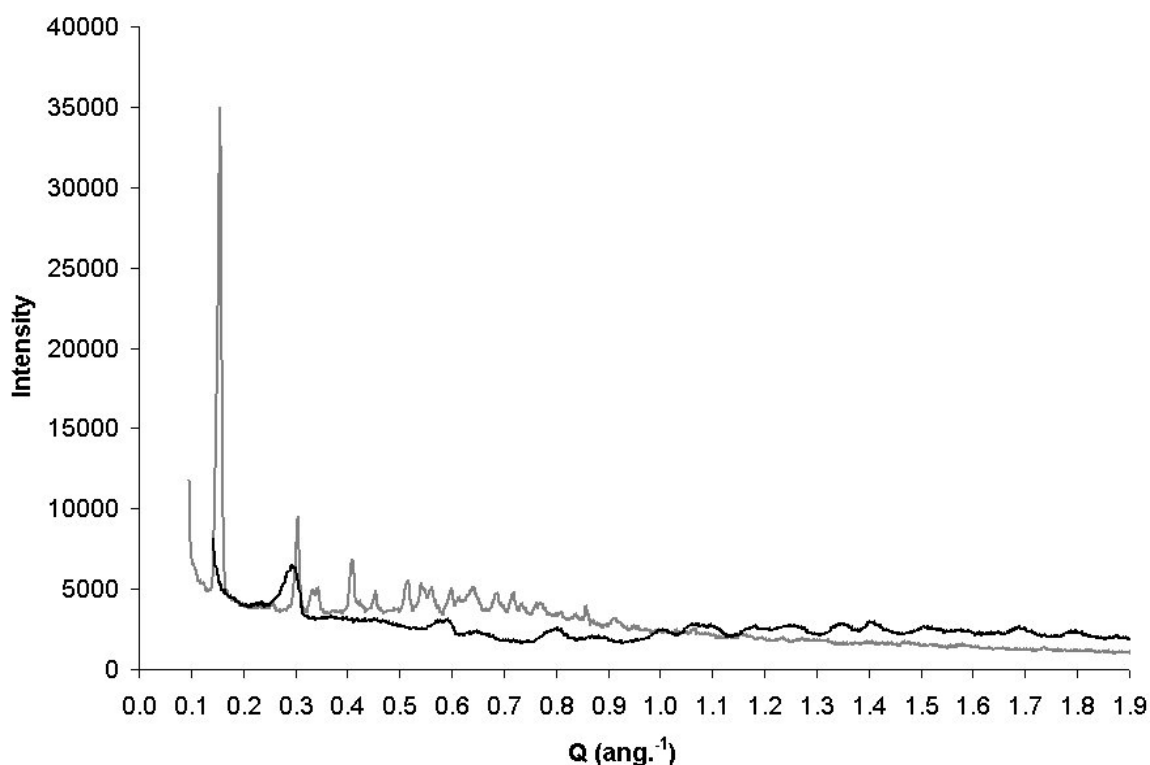


Figure 4-20. Powder XRD pattern for $\text{PtL}^{16}\text{Cl}_4$ for anhydrous sample (grey) and sample stored in air (black).

4.3.6 Luminescence Enhancement for Non-Assembled $\text{PtL}^{16}\text{Cl}_2/\text{PtL}^{16}\text{Cl}_4$ Mixture

To study the dependence of the luminescence emission on self-assembly, samples were first prepared in which no self-assembly could occur by mixing finely powdered samples of $\text{PtL}^{16}\text{Cl}_2$ and $\text{PtL}^{16}\text{Cl}_4$. The unexpected result is an enhancement in the emission intensity as shown in Figure 4-21. Without a sphere of enclosure, these results are not strictly quantitative, but reasonable agreement for the degree of enhancement is obtained using two different experimental setups, demonstrating that the enhancement is real. Initially, the enhancement was believed to be caused by a reduction in excimer quenching of the $\text{PtL}^{16}\text{Cl}_2$ emission upon dilution of the sample with Pt^{IV} . If that were the case, diluting $\text{PtL}^{16}\text{Cl}_2$ with free ligand (L^{16}) should also produce the same enhancement. As shown in Figure 4-15, enhancement in the emission is not observed from a 1:1 mixture of $\text{PtL}^{16}\text{Cl}_2$ and L^{16} .

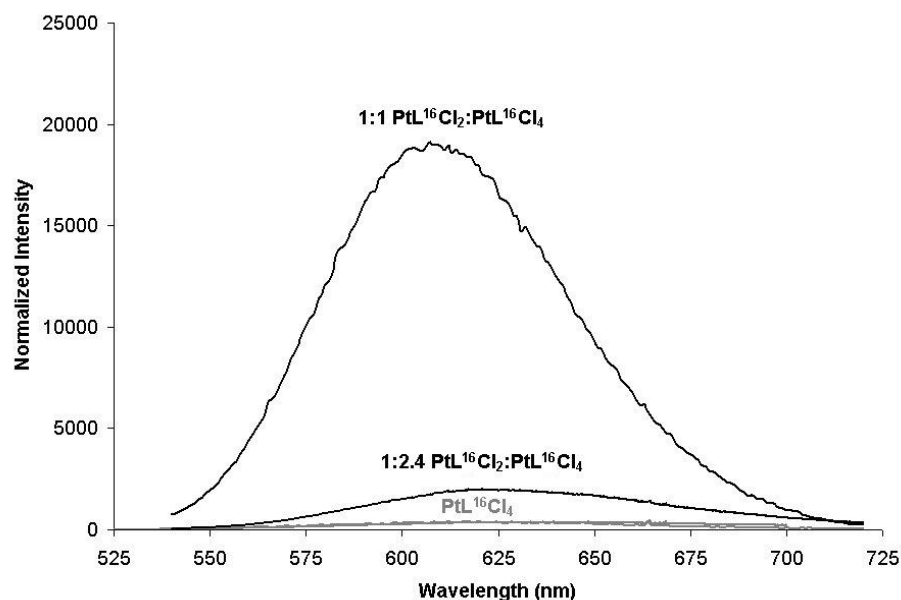


Figure 4-21. Normalized luminescence emission spectra for various heterogeneous mixtures of $\text{PtL}^{16}\text{Cl}_2$ and $\text{PtL}^{16}\text{Cl}_4$ powders; $\lambda_{\text{ex}} = 514 \text{ nm}$, $\text{PtL}^{16}\text{Cl}_4$ spectrum included for scale.

Additionally, analysis of the luminescence lifetimes (Table 4-7) shows a much longer lived excited state is responsible for emission in the mixture of Pt^{II} and Pt^{IV} than for either of the individual species. A biexponential fit to the decay curve gives lifetimes of 108 and 564 ns for the PtL¹⁶Cl₂/PtL¹⁶Cl₄ mixture. The 108 ns emission similar to that of the 157 ns lifetime observed for Pt^{IV} alone. Due to the fitting of the data to a biexponential function only two lifetime values are obtained; therefore, the much shorter emission lifetime of isolated PtL¹⁶Cl₂ would not be observed. Thus, the possibility that the PtL¹⁶Cl₂ complexes are also be undergoing the same emission behavior as is observed for the isolated species in addition to participating in this new emission behavior cannot be ruled out.

Three major observations were used to construct a working model for the luminescence enhancement: (1) the enhancement was specific to the PtL¹⁶Cl₂/PtL¹⁶Cl₄ mixture and did not occur for PtL¹⁶Cl₂/L¹⁶, (2) the longer emission lifetime supports a different excited state for the mixture than for the individual species, and (3) intermolecular electron transfer from PtL¹⁶Cl₂ to PtL¹⁶Cl₄ is energetically favorable. The following model (Figure 4-22) is consistent with the above observations and will be used as a working model for further experiments to explore the observed emission enhancement in mixtures of PtL¹⁶Cl₂ and PtL¹⁶Cl₄. The Pt^{II} complex is initially excited (Figure 4-22 **a**), and electron transfer or energy transfer occurs to give an excited state PtL¹⁶Cl₄ species (**b**). In the case of electron transfer, as shown in the figure, the PtL¹⁶Cl₄ complex could be reduced to an excited-state Pt^{III} species. This new excited-state Pt^{III} species, which is not produced by direct excitation of PtL¹⁶Cl₄, could then undergo radiative decay (**c**).

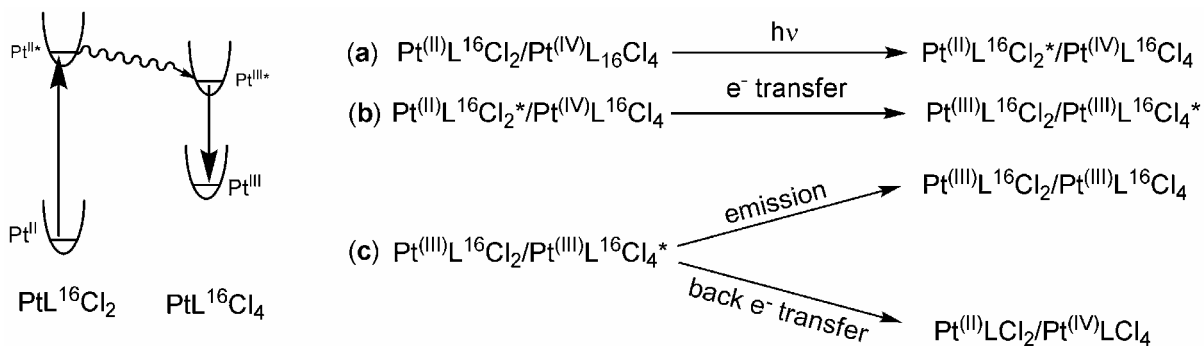


Figure 4-22. Possible mechanism for solid-state luminescence enhancement in heterogeneous mixtures of $\text{PtL}^{16}\text{Cl}_2$ and $\text{PtL}^{16}\text{Cl}_4$ where the final step (c) is dominated by radiative emission; oxidation state after each step of the mechanism shown adjacent to the energy well.

4.3.7 Luminescence Quenching in $\text{PtL}^{16}\text{Cl}_2/\text{PtL}^{16}\text{Cl}_4$ Molecular Alloys

To analyze the emission behavior of the molecular alloy, mixtures of $\text{PtL}^{16}\text{Cl}_2$ and $\text{PtL}^{16}\text{Cl}_4$ were heated to a temperature compatible with self-assembly and then quenched in liquid nitrogen to maintain the supramolecular ordering of the Col_H alloy. Figure 4-23 gives the XRD pattern for the quenched 1:1 $\text{PtL}^{16}\text{Cl}_2/\text{PtL}^{16}\text{Cl}_4$ molecular alloy in comparison to the pattern obtained in the liquid crystalline regime. Note that in both cases the edge of the X-ray beam is observed at low Q , causing the large increase in signal intensity. The intense low angle reflection observed for the quenched sample corresponds to the hexagonally ordered dimension of 36.5 Å, which is 35.1 Å for the mesophase at 110 °C. The quenching method does not perfectly maintain the quasi-long range ordering of the mesophase, as evidenced by the very broad reflection from 0.3-0.5 Å⁻¹, but does maintain at least a portion of the hexagonal ordering.

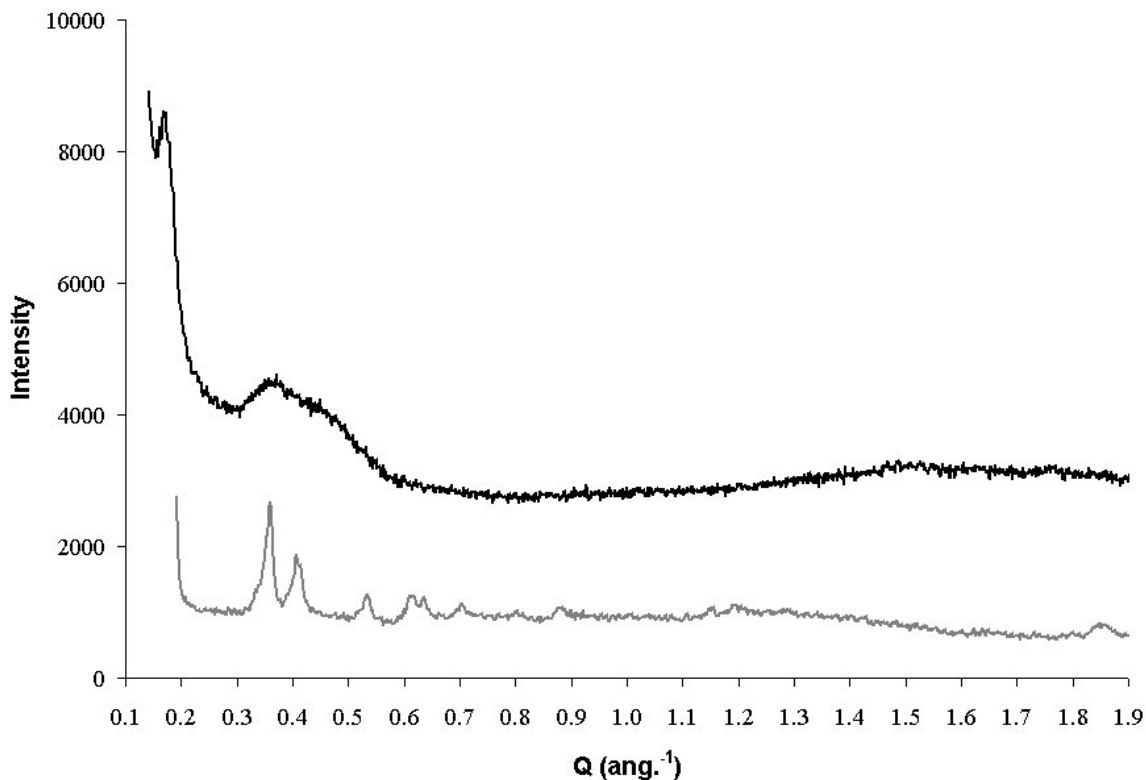


Figure 4-23. XRD patterns for the 1:1 PtL¹⁶Cl₂/PtL¹⁶Cl₄ molecular alloy; at 110 °C (bottom), RT after the sample is heated to 130 °C and quenched with liquid nitrogen (top). The X-ray beam edge appears at low Q as a sharp increase in intensity. Two different instruments were utilized resulting in different minimum observable Q.

The molecular alloy samples give almost complete quenching of the luminescence as shown in Figure 4-24. The observed quenching is quite different from the enhance luminescence observed from the unassembled mixture of PtL¹⁶Cl₂ and PtL¹⁶Cl₄ powders. The quenching experiment was performed using two different sample holders and qualitative agreement is obtained for the degree of quenching as shown by the two low intensity spectra in the figure. The degree of luminescence quenching is dependent on the ratio of PtL¹⁶Cl₂/PtL¹⁶Cl₄, with the most complete quenching obtained at a 1:1 ratio. At this time, sufficient data has not been obtained to determine if there is a direct correlation between the

amount of excess Pt^{IV} and the degree of quenching. Further experiments utilizing a sphere of enclosure are needed to obtain more quantitative data.

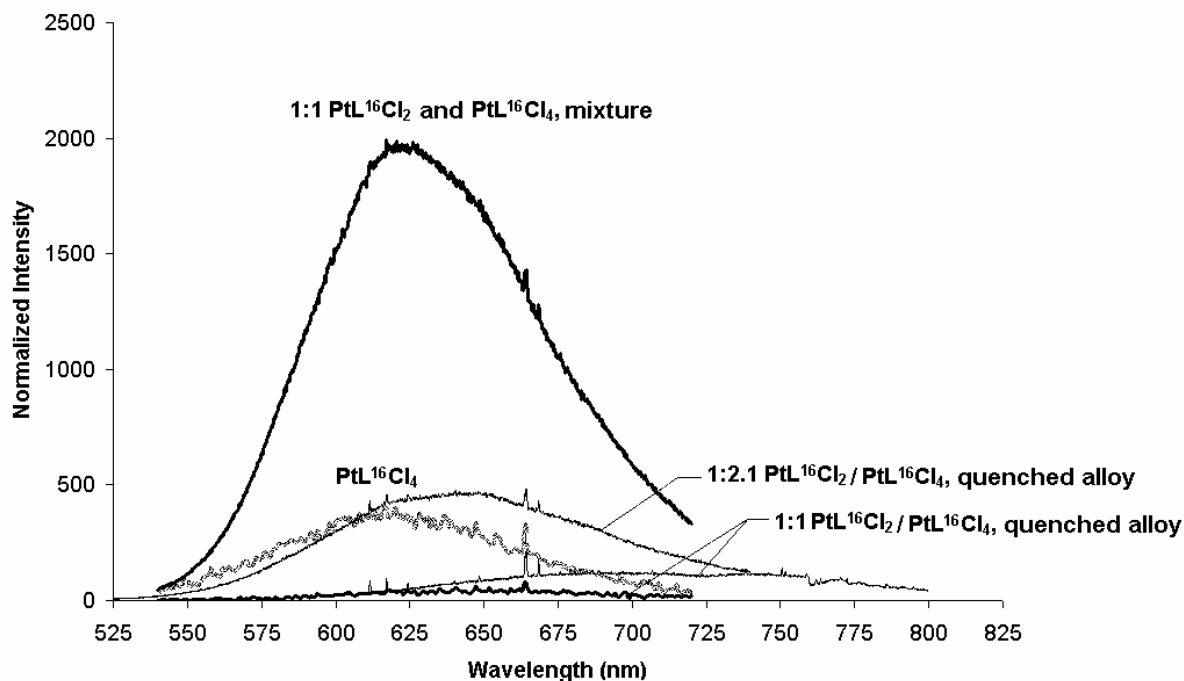


Figure 4-24. Normalized room temperature emission spectra for various $\text{PtL}^{16}\text{Cl}_2$ and $\text{PtL}^{16}\text{Cl}_4$ mixtures; $\lambda_{\text{ex}} = 514 \text{ nm}$, $\text{PtL}^{16}\text{Cl}_4$ spectrum included for scale; samples analyzed in glass tubes under ambient conditions (thick lines), samples analyzed under reduced pressure in a quartz and brass sample holder (thin lines), prepared by heating fine powders to $130 \text{ }^\circ\text{C}$ and quenching with liquid nitrogen (quenched alloy), prepared by mixing fine powders at room temperature (mixture).

The possibility was explored that the quenching of the $\text{PtL}^{16}\text{Cl}_2/\text{PtL}^{16}\text{Cl}_4$ alloy was due to the increased disorder of the alloy compared to the individual $\text{PtL}^{16}\text{Cl}_2$ and $\text{PtL}^{16}\text{Cl}_4$ microcrystalline powders. As a control experiment, the luminescence of $\text{PtL}^{16}\text{Cl}_2$ as a microcrystalline powder is compared to a sample of $\text{PtL}^{16}\text{Cl}_2$ that had been heated to $130 \text{ }^\circ\text{C}$ and quenched with liquid nitrogen (Figure 4-25). Luminescence quenching is observed, presumably due to the increased disorder in the phase, but no change is observed in the 614 nm emission maximum. As was described in Chapter 3, the packing in crystalline $\text{PtL}^{16}\text{Cl}_2$ is

similar to the mesophase packing, but the mesophase has more disordered alkyl chain packing and shorter correlation distances. After taking into account the luminescence quenching as a result of forming a more disordered phase, the PtL¹⁶Cl₂/PtL¹⁶Cl₄ alloy luminescence is still significantly less intense than that of the heated and cooled PtL¹⁶Cl₂ sample.

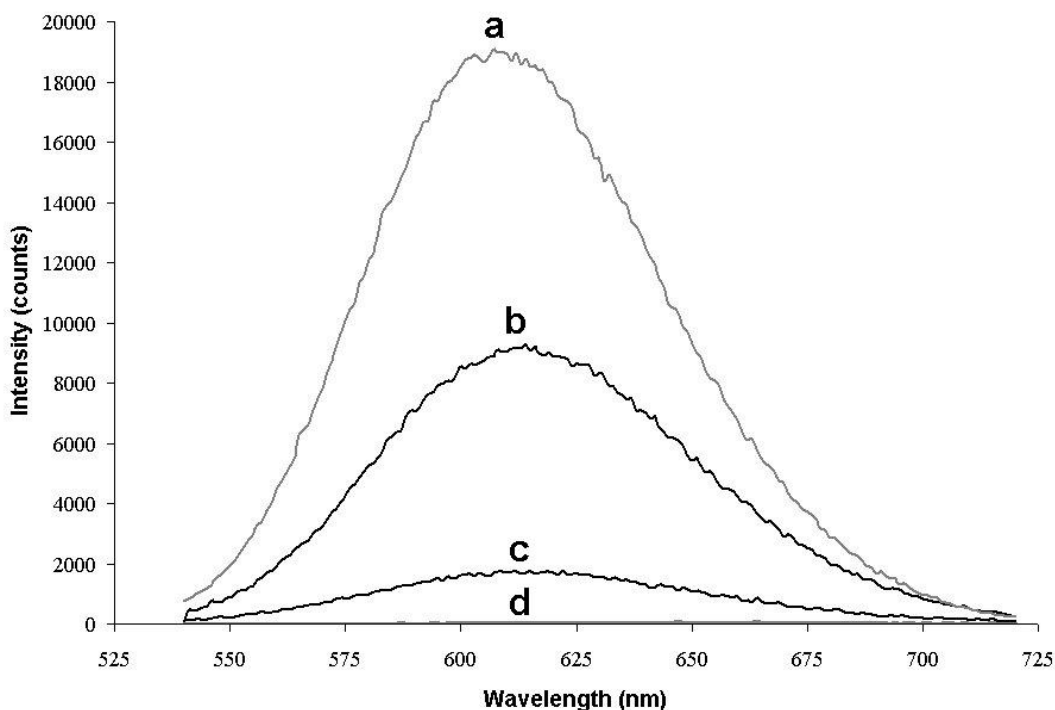


Figure 4-25. Solid-state emission spectra for various powders: 1:1 PtL¹⁶Cl₂ and PtL¹⁶Cl₄ powders mixed at RT (**a**), PtL¹⁶Cl₂ powder (**b**), PtL¹⁶Cl₂ heated to 130 °C and quenched with liquid nitrogen (**c**), and 1:1 PtL¹⁶Cl₂/PtL¹⁶Cl₄ heated to 130 °C and quenched with liquid nitrogen (**d**, at baseline); $\lambda_{\text{ex}} = 514$ nm.

Experiments were performed to determine if luminescence lifetimes could be measured for the mesophases at elevated temperatures. All observed lifetimes were <3 ns, and are attributed to emission from the glass of the sample holder. No emissions from PtL¹⁶Cl₂, PtL¹⁶Cl₄, or the PtL¹⁶Cl₂/PtL¹⁶Cl₄ alloy are observed in the mesogenic phase, presumably due to vibrational relaxation of the excited states at elevated temperatures.

The luminescence quenching is attributed to formation of $\text{Pt}^{\text{II}}\cdots\text{Cl}-\text{Pt}^{\text{IV}}$ columnar interactions in the molecular alloy mesophase (Figure 4-26). The interactions open a pathway for vibrational quenching of the excited state along the $\text{Pt}^{\text{II}}\cdots\text{Cl}-\text{Pt}^{\text{IV}}$ axis. The formation of MX chain interactions increases similarity of the Pt^{II} and Pt^{IV} orbital energies. Excitation of the $\text{PtL}^{16}\text{Cl}_2$ species and electron transfer to $\text{PtL}^{16}\text{Cl}_4$ can occur as in the heterogeneous mixture of $\text{PtL}^{16}\text{Cl}_2$ and $\text{PtL}^{16}\text{Cl}_4$ powders (Figure 4-27 a and b). However, in the self-assembled samples, Pt-Cl vibrations, which can be expected to occur with electron or energy transfer from Pt^{II} to Pt^{IV} along an MX chain, increase the potential for non-radiative back electron transfer. The non-radiative pathway (Figure 4-27 c) becomes dominant, and quenching of the luminescent emission results. While this result does not definitively prove the columnar ordering in the mesophase is driven by formation of MX chain interactions, it is consistent with such interactions.

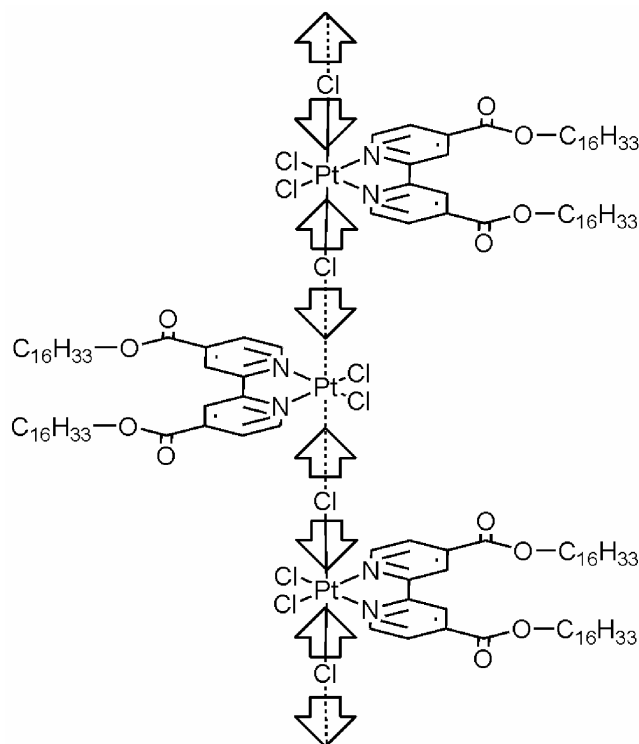


Figure 4-26. Axial vibrational mode for quenching of the charge transfer excited state.

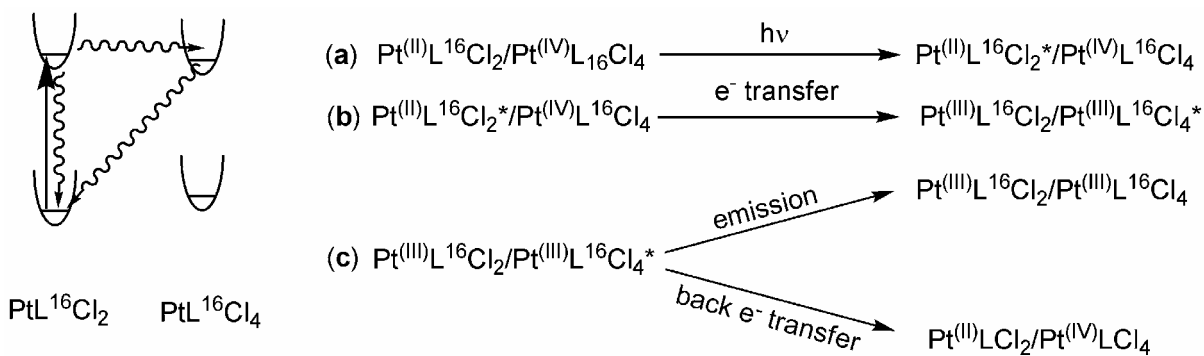


Figure 4-27. Possible vibrational relaxation mechanism for solid-state luminescence quenching of the $\text{PtL}^{16}\text{Cl}_2/\text{PtL}^{16}\text{Cl}_4$ molecular alloy where the final step (c) is dominated by back electron transfer.

4.3.8 Low Temperature Solid-State Luminescence

Preliminary experiments have been carried out to determine the luminescence behavior at low temperature. Frequently, luminescent transitions that are minimized by vibrational relaxation at room temperature are observable at low temperature. The emission spectra for $\text{PtL}^{16}\text{Cl}_4$ and $\text{PtL}^{16}\text{Cl}_2/\text{PtL}^{16}\text{Cl}_4$ mixtures at 30 K are shown in Figure 4-28, and the emission maxima are given in Table 4-9. To minimize experimental time, preliminary scans were taken to determine emissive regions and subsequent scans focused on those regions.

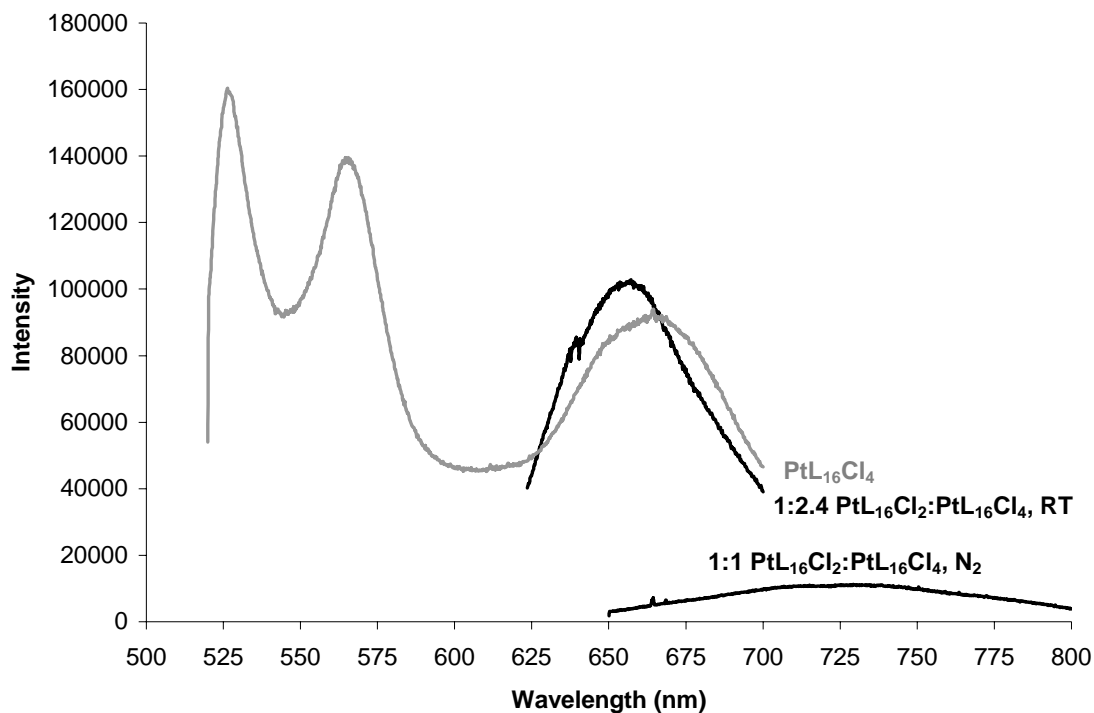


Figure 4-28. Low temperature solid-state emission spectra for $\text{PtL}^{16}\text{Cl}_4$ and various mixtures of $\text{PtL}^{16}\text{Cl}_4/\text{PtL}^{16}\text{Cl}_4$; $\lambda_{\text{ex}} = 514 \text{ nm}$, all samples held in a brass and quartz sample holder at 30 K and 3×10^{-6} torr, prepared by heating fine powders to 130 °C and quenching with liquid nitrogen (N_2), prepared by mixing fine powders at room temperature (RT).

Table 4-9. Solid-state emission maxima of $\text{PtL}^{16}\text{Cl}_4$ and $\text{PtL}^{16}\text{Cl}_2/\text{PtL}^{16}\text{Cl}_4$ mixtures in various states of self-assembly at 30 K and $\sim 3 \times 10^{-6}$ torr, $\lambda_{\text{ex.}} = 514 \text{ nm}$.

Sample	$\lambda_{\text{max.}}$ (nm)	Excited State
1:2.4 $\text{PtL}^{16}\text{Cl}_2/\text{PtL}^{16}\text{Cl}_4$, RT ^[a]	658	CT
1:1 $\text{PtL}^{16}\text{Cl}_2/\text{PtL}^{16}\text{Cl}_4$, N_2 ^[a]	728	MLCT
$\text{PtL}^{16}\text{Cl}_4$	526	$\pi \rightarrow \pi^*$
	567	$\pi \rightarrow \pi^*$
	665	MLCT

^[a] Sample preparation Figure 4-28

The most notable difference in comparing the room-temperature and low-temperature data (Figures 4-21 and 4-24 to Figure 4-28) is the appearance of higher energy emissions at

526 and 567 nm for PtL¹⁶Cl₄. These emissions may originate from $\pi \rightarrow \pi^*$ excited states. Work with [Pt(trpy)Cl]⁺ derivatives, capable of solid-state Pt-Pt and π - π stacking interactions similar to PtL¹⁶Cl₂, has determined that different states give rise to room temperature and low temperature emissions.^{165, 168} The high energy emission peaks are very similar to those emissions observed for [Pt(bpy)(en)]²⁺ and Pt(bpy)₂²⁺, which are assigned to emission from a ³(π - π^*) excited state. The shift in the emission wavelength for PtL¹⁶Cl₄ to 665 nm (30 K), from 634 nm (RT), is consistent with excimer emission originating from a charge transfer excited state. The red shift in emission wavelength upon cooling is consistent with a cooling induced contraction of the crystal lattice, which decreases the distance between PtL¹⁶Cl₄ moieties and moves the excimer luminescence to a lower energy than observed at room temperature.¹⁶⁴

Luminescence quenching for the 1:1 PtL¹⁶Cl₂/PtL¹⁶Cl₄ molecular alloy formed by heating the sample to 130 °C and quenching with liquid nitrogen is observed at 30 K as well as at room temperature. More counts are obtained from sample at low temperature than at room temperature (over the same number of scans), which is consistent with competition between luminescence and a non-emissive vibrational relaxation pathway (Figure 4-27) as was discussed in the previous section. At low temperature, the vibrational relaxation is disfavored, so more relaxation occurs via the luminescent pathway.

4.4 Conclusions

Col_H liquid crystalline molecular alloys of PtLⁿCl₂/PtLⁿCl₄ (n = 12, 16, 20) have been prepared and characterized by DSC, XRD, and optical methods. Characterization is consistent with columnar ordering through supramolecular MX chain interactions in the

mesophase. The solid-state luminescence properties of $\text{PtL}^{16}\text{Cl}_4$ and mixtures of $\text{PtL}^{16}\text{Cl}_2/\text{PtL}^{16}\text{Cl}_4$ in various states of self-assembly have been explored. The heterogeneous mixture of $\text{PtL}^{16}\text{Cl}_2$ and $\text{PtL}^{16}\text{Cl}_4$ was found to give enhanced intensity luminescence over the individual components with longer emission lifetime than either individual species. An electron transfer mechanism, featuring $\text{PtL}^{16}\text{Cl}_2$ excitation and emission from $\text{PtL}^{16}\text{Cl}_4$ was proposed to account for the enhancement. Samples of the molecular alloy of $\text{PtL}^{16}\text{Cl}_2/\text{PtL}^{16}\text{Cl}_4$, which had been quenched with liquid nitrogen after self-assembly to preserve the supramolecular ordering of the mesophase, showed quenching of the luminescence intensity. The observed quenching is consistent with the availability of a vibrational relaxation pathway along the $\text{Pt}^{\text{II}}\cdots\text{Cl}-\text{Pt}^{\text{IV}}$ chain in the self-assembled material.

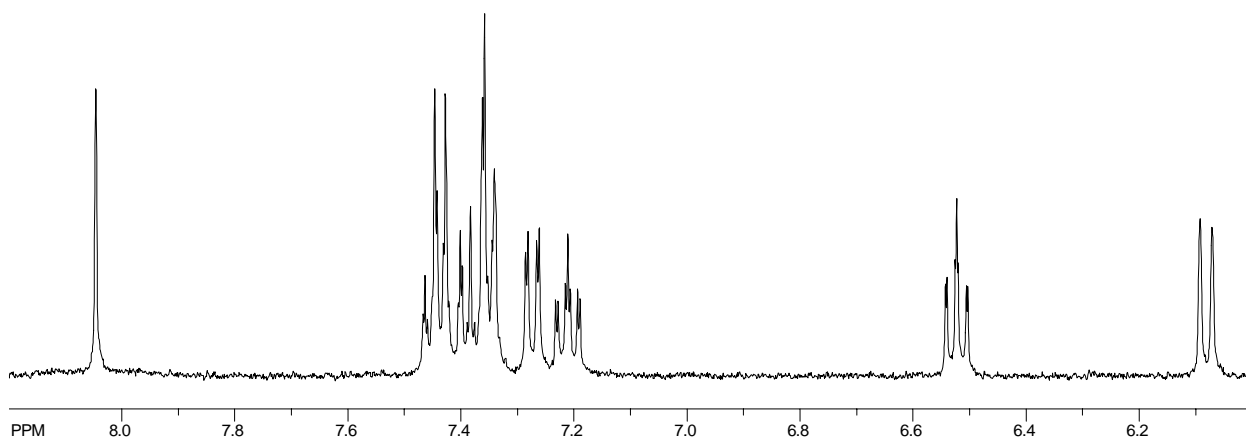
This metallomesogenic molecular alloy $\text{PtL}^n\text{Cl}_2/\text{PtL}^n\text{Cl}_4$ provides a new system for studying supramolecular interactions in binary liquid crystalline phases. This research has demonstrated formation of a Col_H liquid crystalline molecular alloy of $\text{PtL}^n\text{Cl}_2/\text{PtL}^n\text{Cl}_4$ ($n = 12, 16, 20$), and characterization of the alloy by XRD, DSC, and optical microscopy is consistent with formation of MX chain interactions. This is the first system explored for potential MX chain interactions in a liquid crystalline phase. As further work developing methods to control the alignment of large domains of the $\text{PtL}^n\text{Cl}_2/\text{PtL}^n\text{Cl}_4$ mesophases continues, the potential exists for production of useful anisotropically conductive materials. The self-assembly dependant luminescence provides the possibility for interesting photochemical applications. In this era of supramolecular ordering, and materials such as the $\text{PtL}^n\text{Cl}_2/\text{PtL}^n\text{Cl}_4$ molecular alloys present new horizons for both inorganic and liquid crystalline chemistry.

APPENDIX I

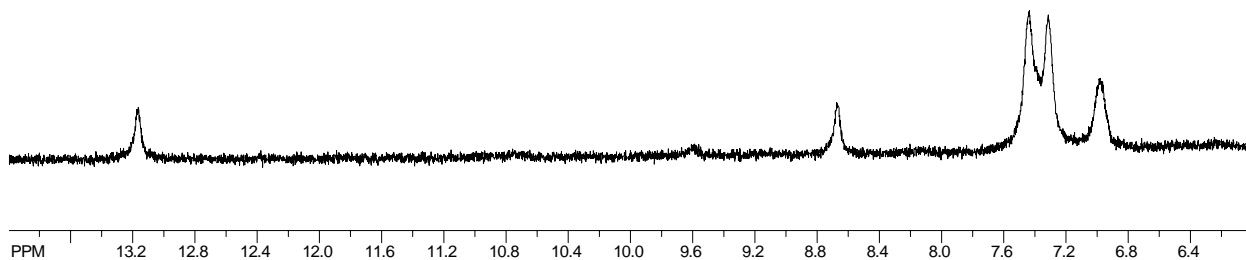
^1H NMR data for $\text{Pt}(\text{sal-Ph})_2$, $\text{Ni}(\text{sal-Ph})_2$, $\text{Pt}(\text{sal-Ph})_2\text{Cl}_2$, and $\text{Pt}(\text{sal-Ph})_2\text{Br}_2$

Instrumentation information, chemical shifts, and coupling constants may be found in the experimental section of Chapter 2.

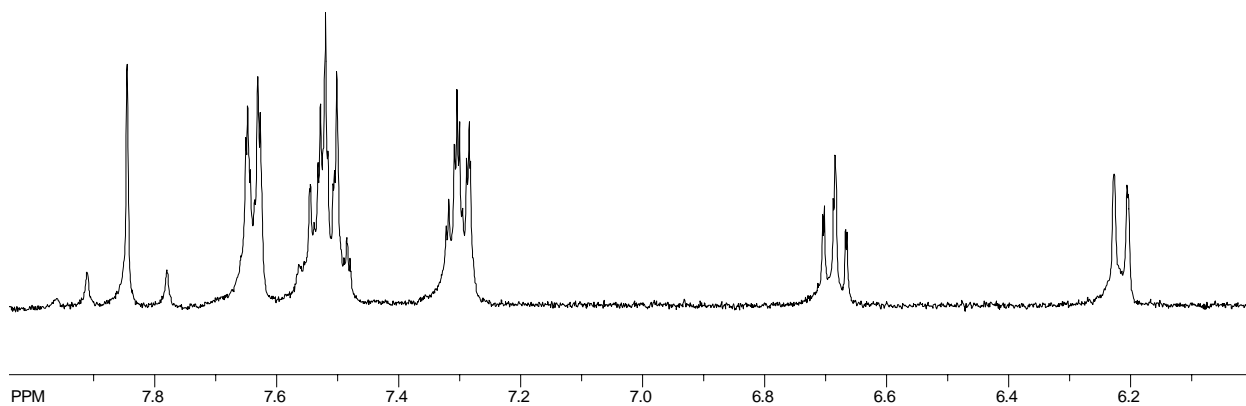
$\text{Pt}(\text{sal-Ph})_2$ – 400 MHz (CD_2Cl_2)



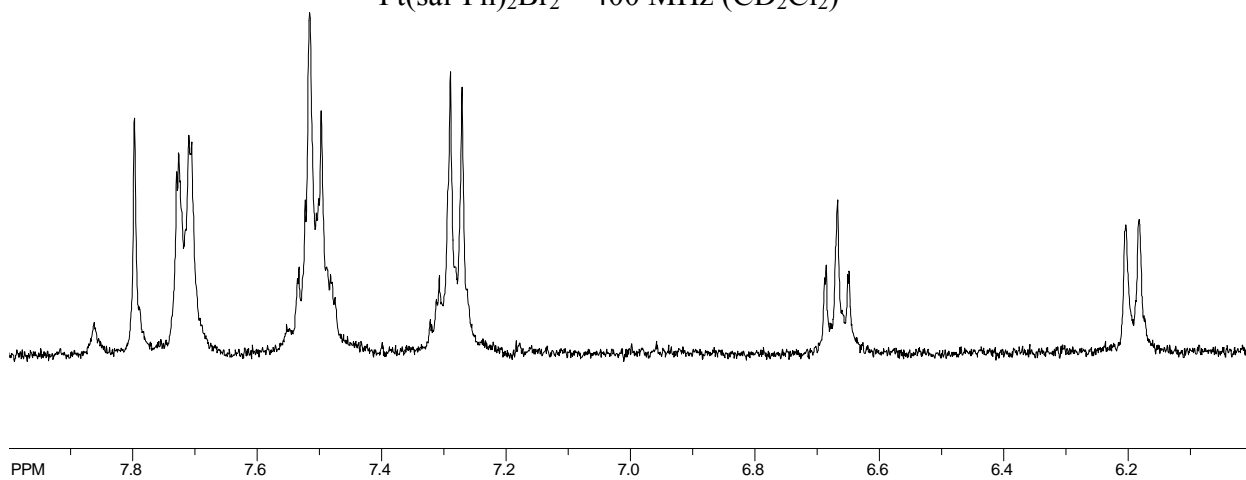
$\text{Ni}(\text{sal-Ph})_2$ – 400 MHz (CD_2Cl_2)



Pt(sal-Ph)₂Cl₂ – 400 MHz (CD₂Cl₂)



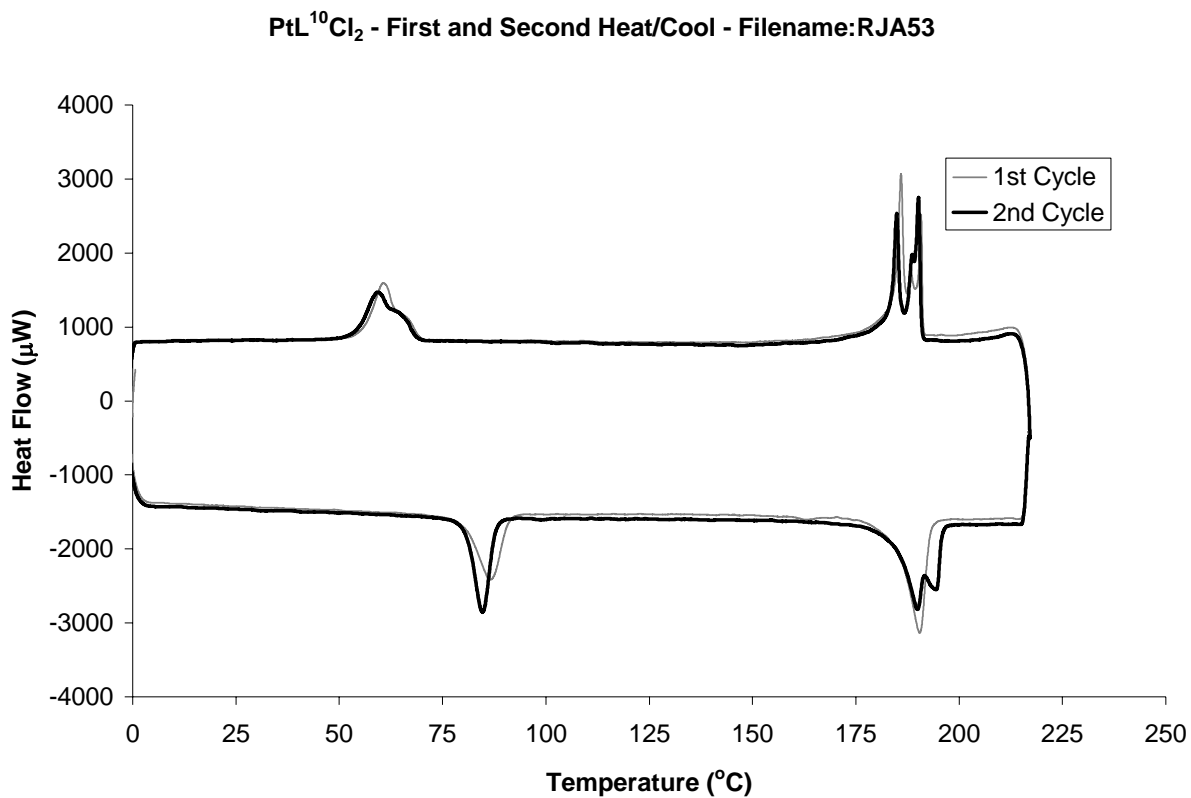
Pt(sal-Ph)₂Br₂ – 400 MHz (CD₂Cl₂)



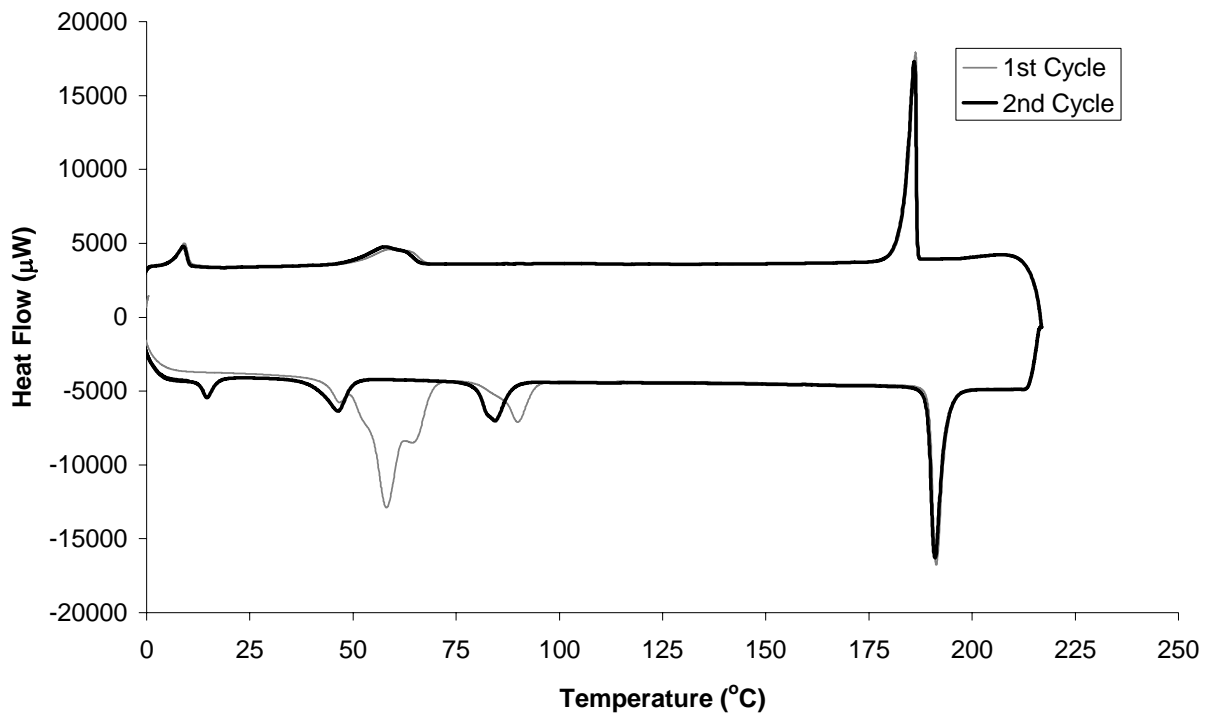
APPENDIX II

Differential Scanning Calorimetry Traces for Various PtL^nCl_2 , PtL^nCl_4 , CdL^nCl_2 , and $\text{Re}(\text{CO})_3\text{L}^n\text{Br}$ Complexes and $\text{PtL}^{16}\text{Cl}_2/\text{PtL}^{16}\text{Cl}_4$ Mixtures

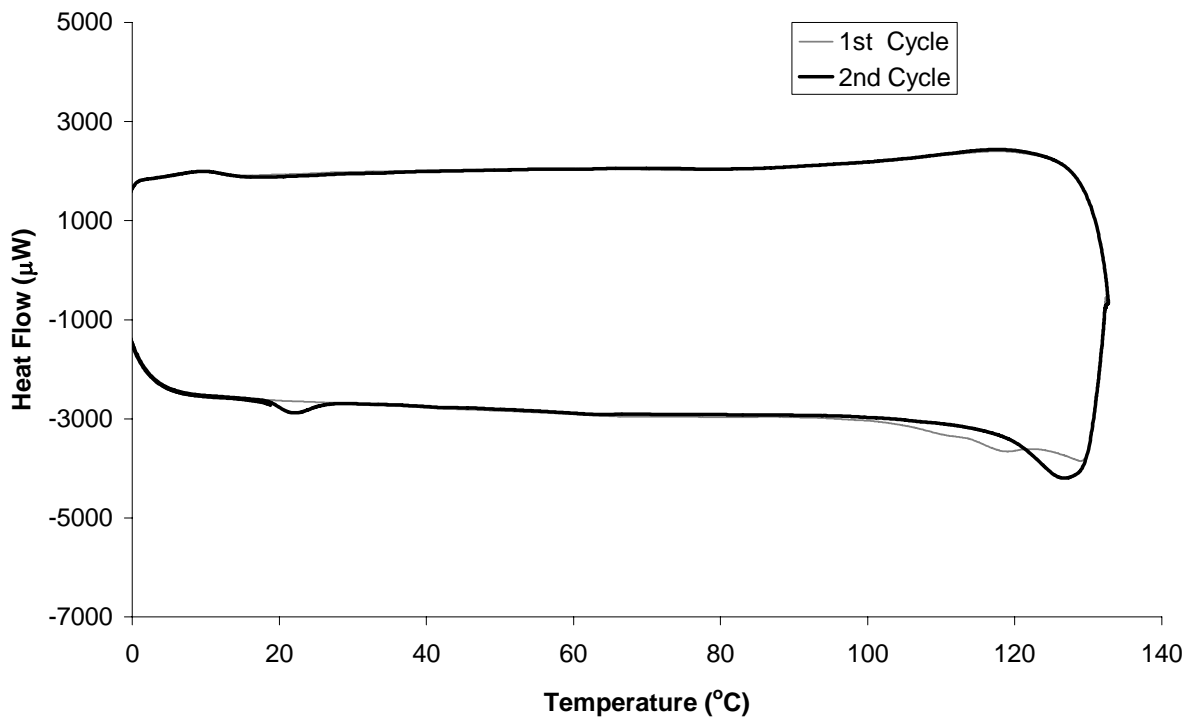
Sample preparation discussed in the experimental sections of Chapters 3 and 4. Instrumentation discussed in Chapter 3.



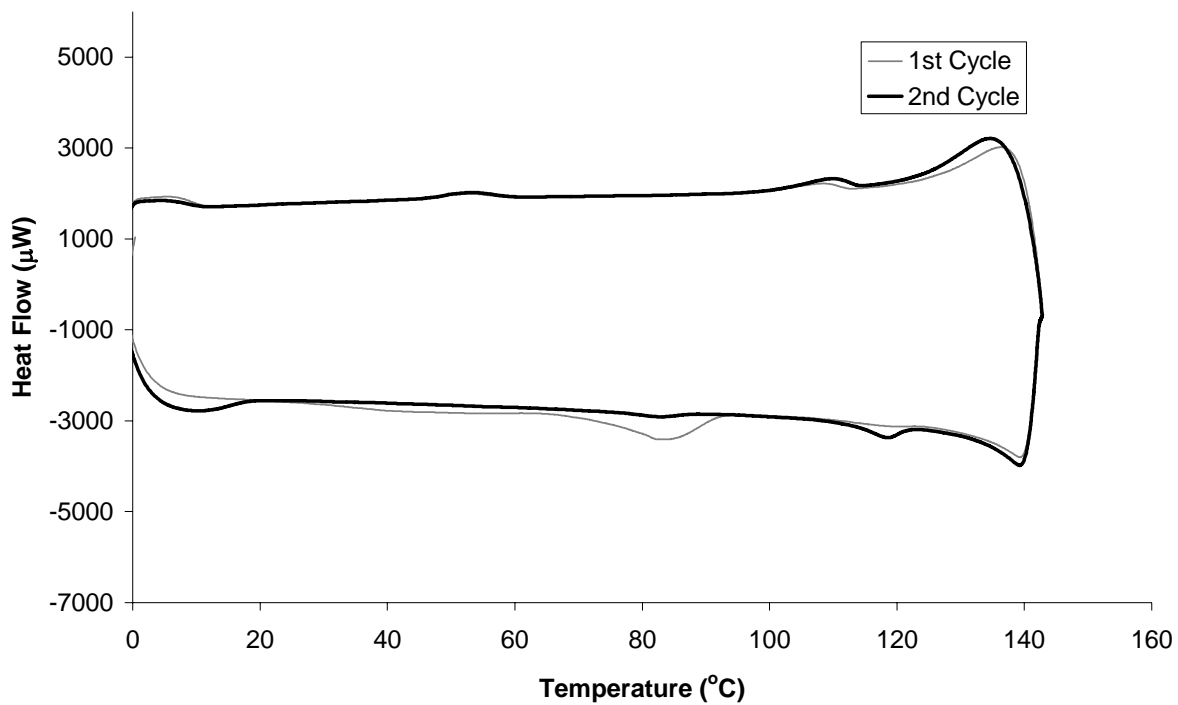
PtL¹²Cl₂ - First and Second Heat/Cool - Filename: RJA57



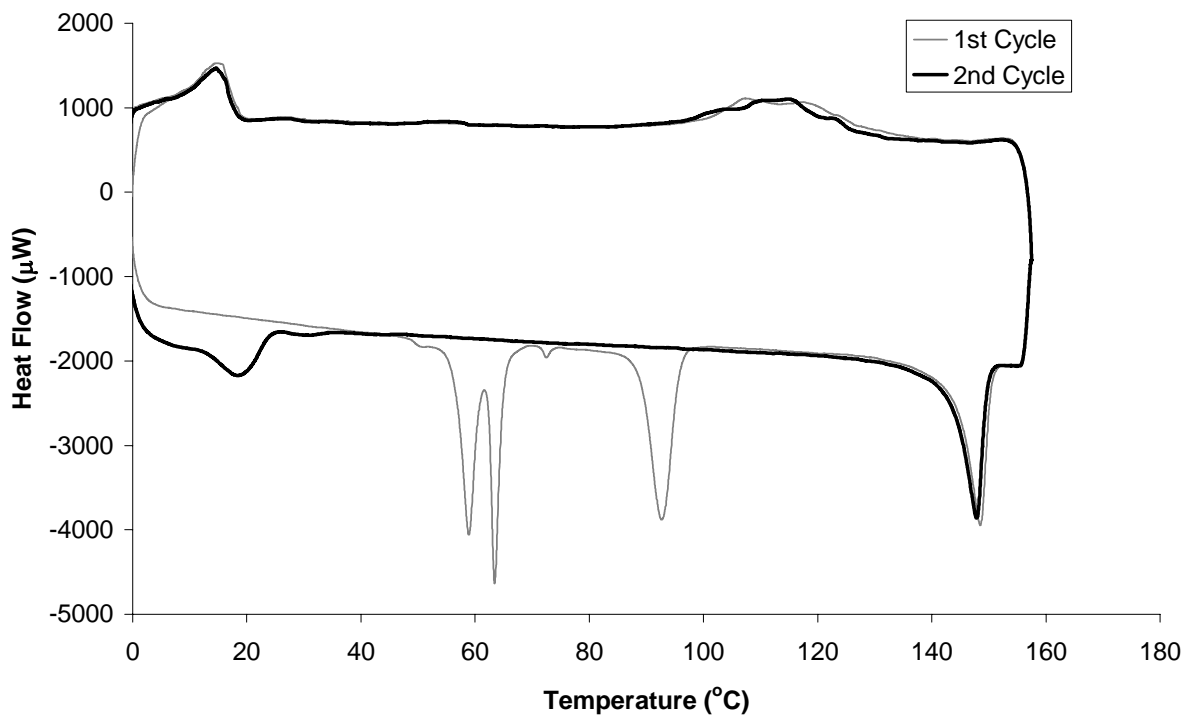
PtL⁸Cl₄ - First and Second Heat/Cool - Filename: RJA41



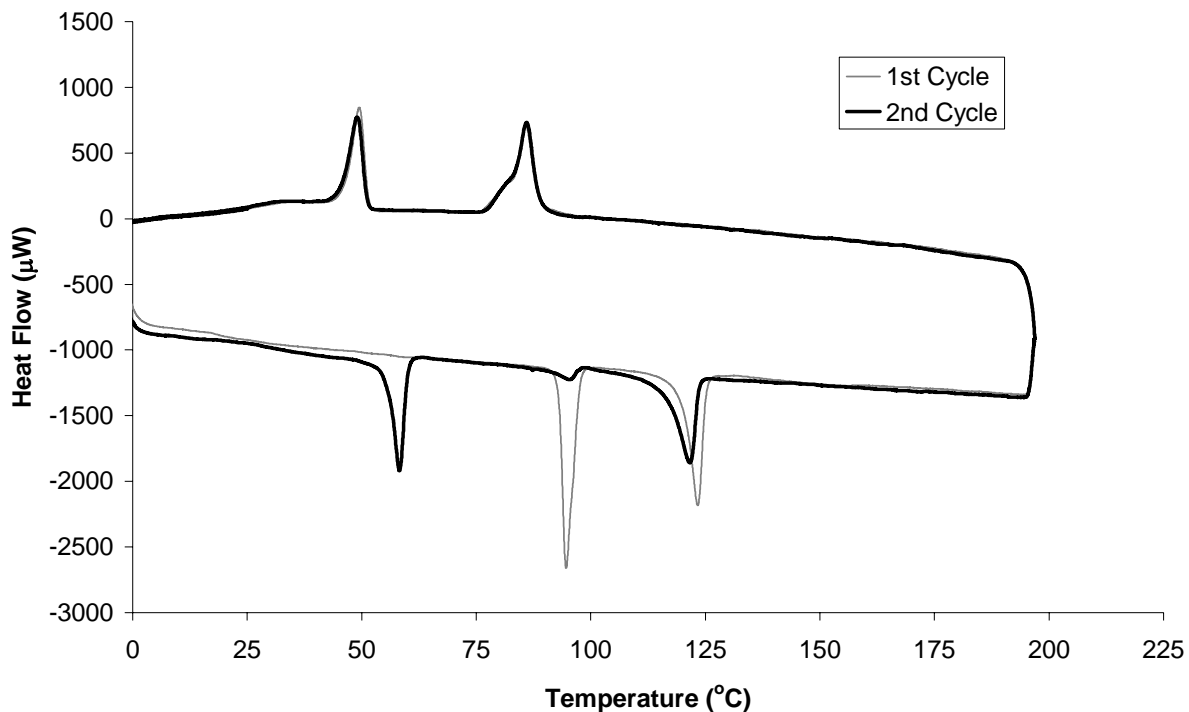
PtL ¹⁰Cl₄ - First and Second Heat/Cool - Filename: RJA44



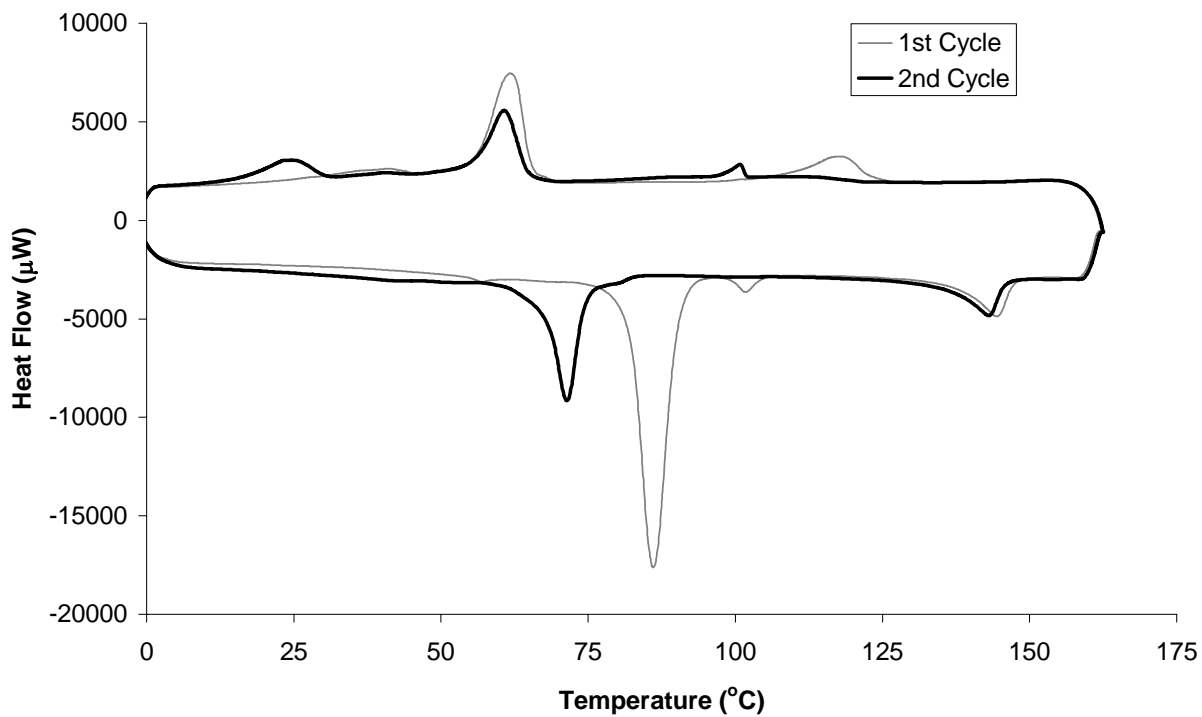
PtL ¹²Cl₄ - First and Second Heat/Cool - Filename: RJA62



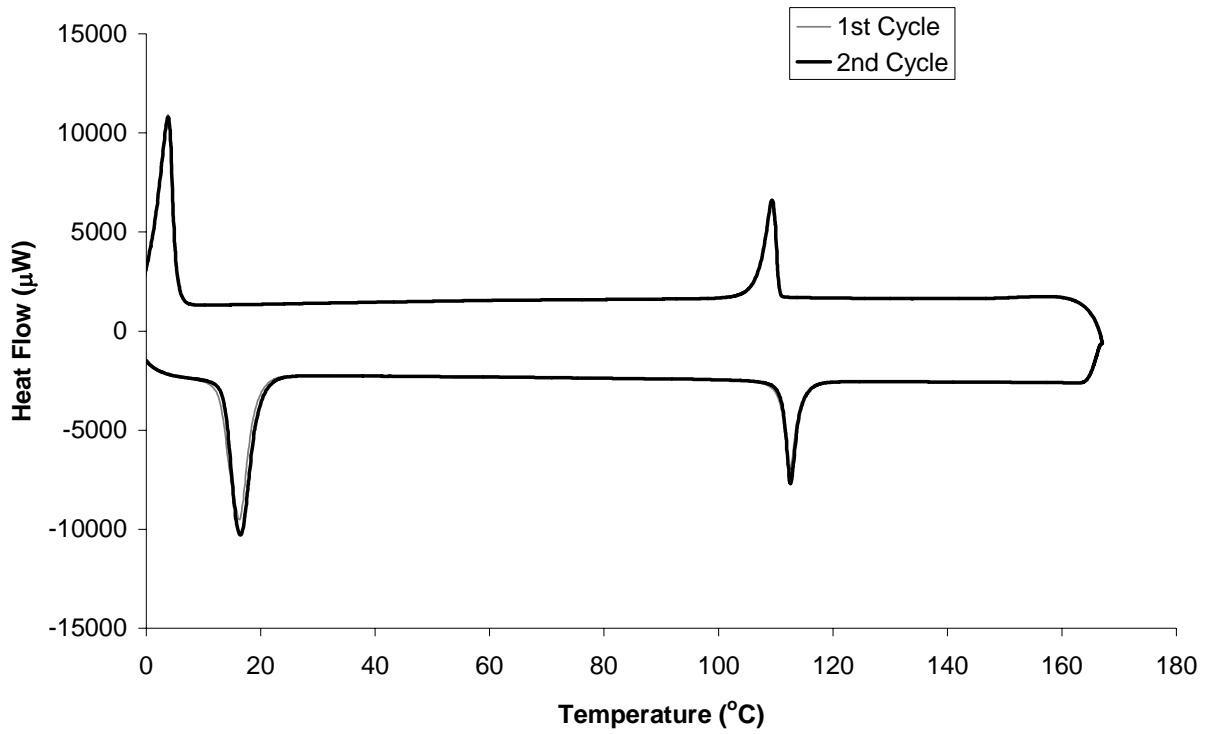
Re(CO)₃L¹²Br - First and Second Heat/Cool - Filename: RJA96



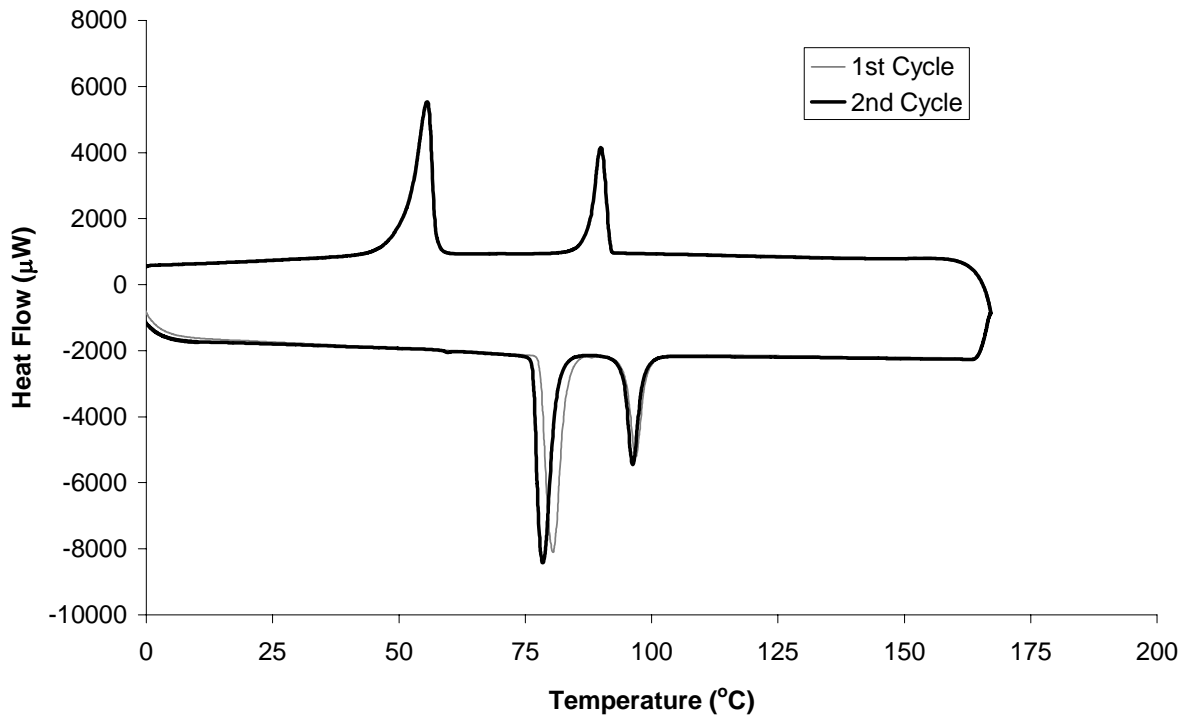
PtL²⁰Cl₄ - First and Second Heat/Cool - Filename: RJA50



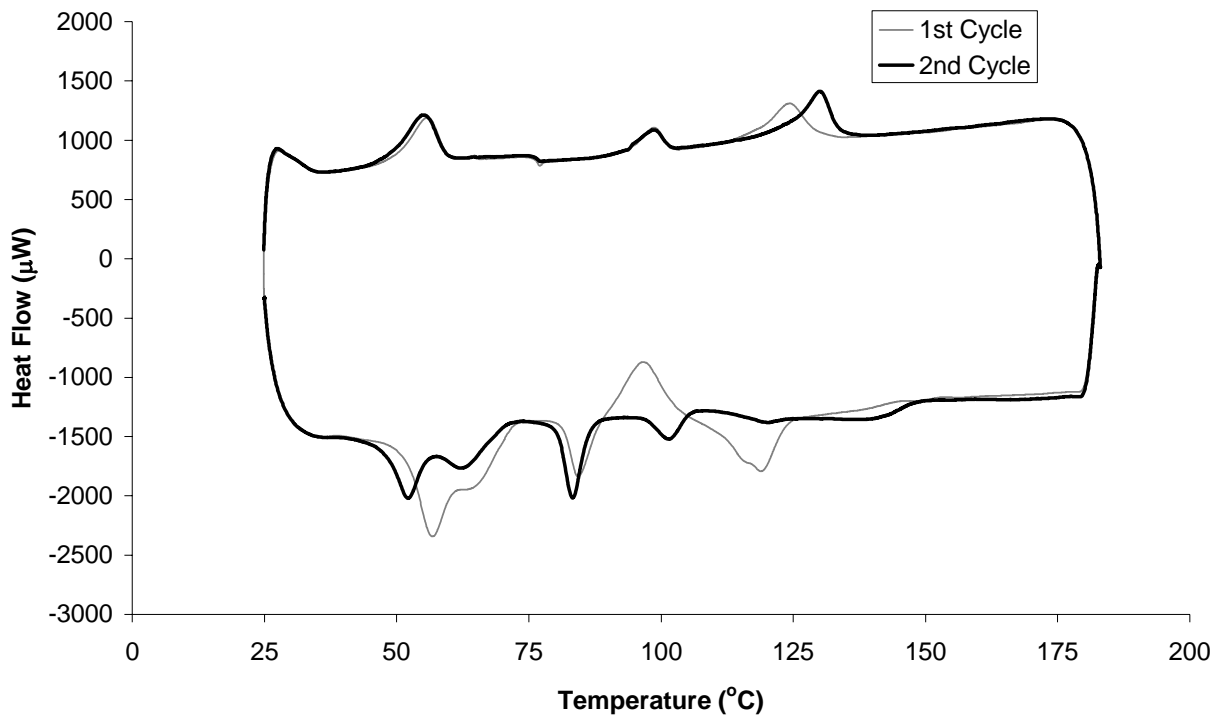
CdL¹²Cl₂ - First and Second Heat/Cool - Filename: RJA89



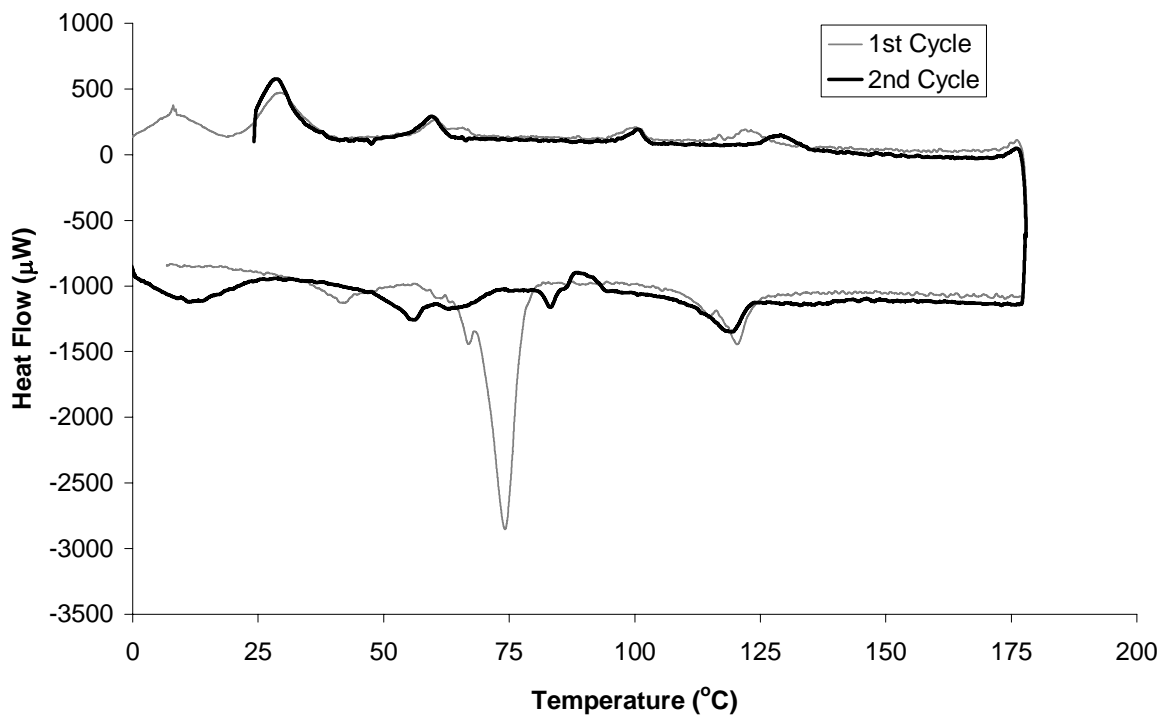
CdL¹⁸Cl₂ - First and Second Heat/Cool - Filename: RJA93



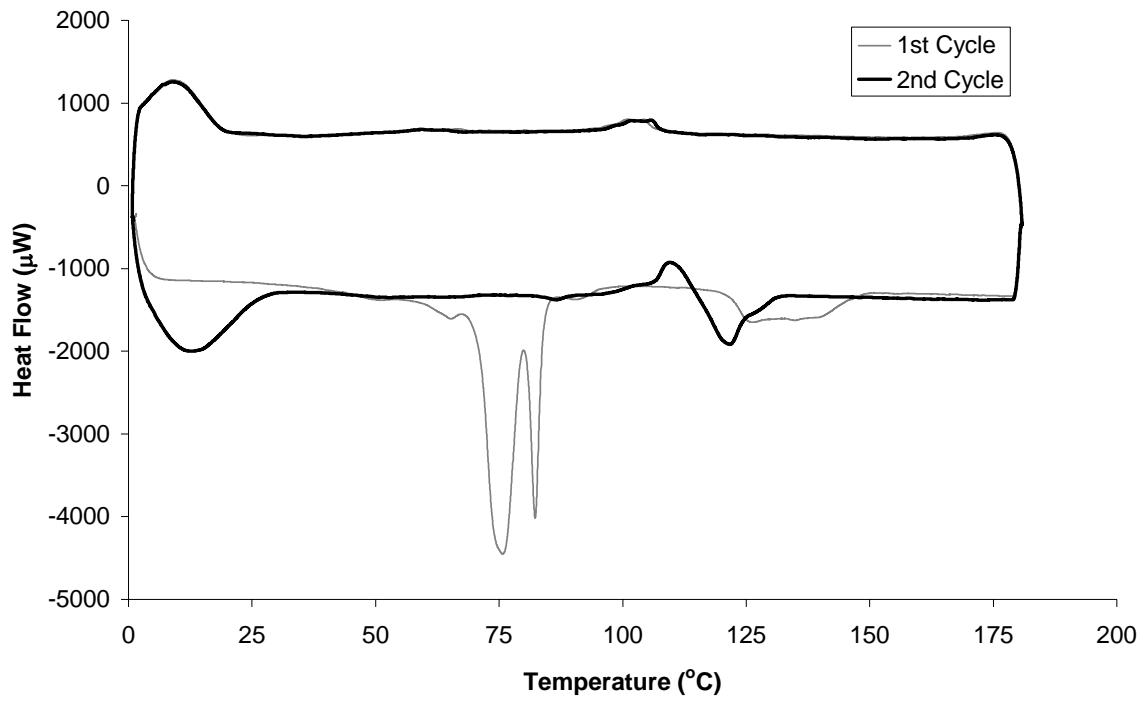
1.3:1 PtL¹⁶Cl₂/PtL¹⁶Cl₄ - First and Second Heat/Cool - Filename: RJA15



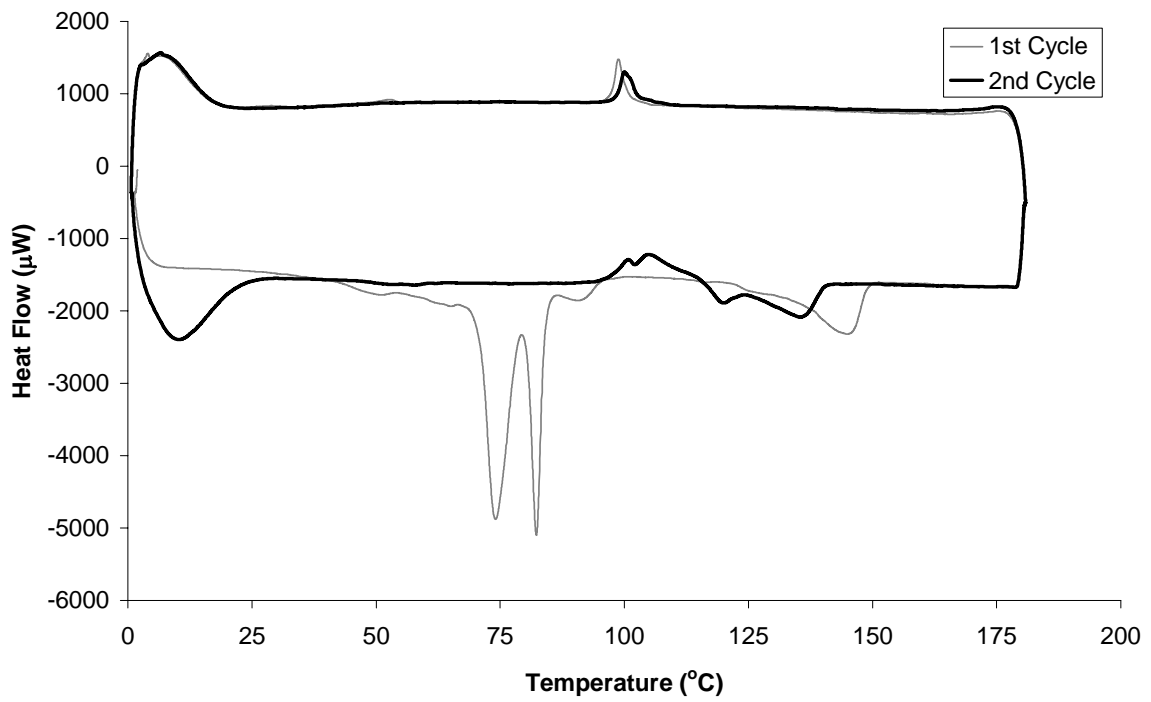
1.8:1 PtL¹⁶Cl₂/PtL¹⁶Cl₄ - First and Second Heat/Cool - Filename RJA24



0.81:1 PtL¹⁶Cl₂/PtL¹⁶Cl₄ - First and Second Heat/Cool - Filename RJA102



0.55:1 PtL¹⁶Cl₂/PtL¹⁶Cl₂ - First and Second Heat/Cool - Filename RJA101

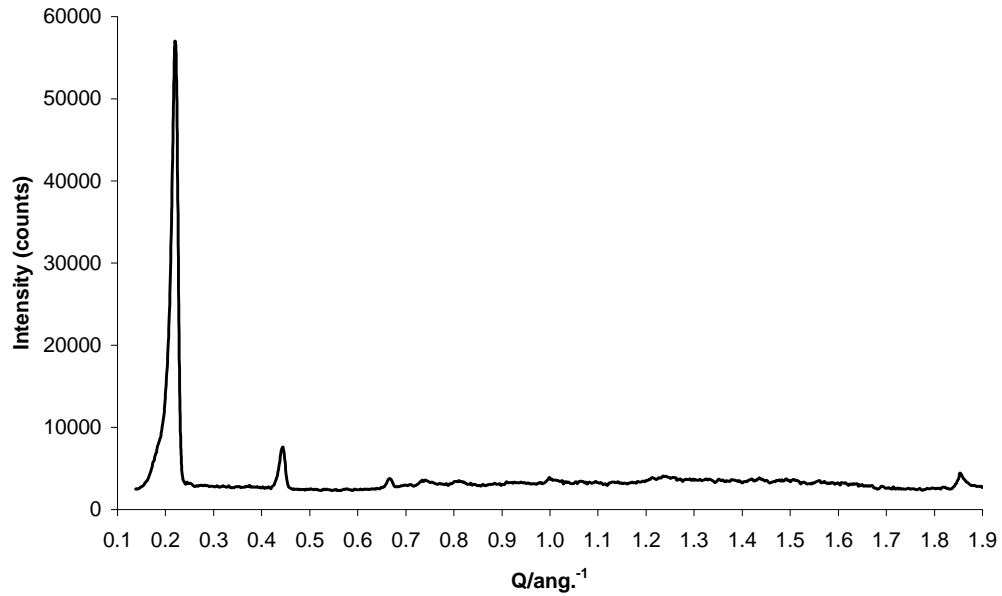


APPENDIX III

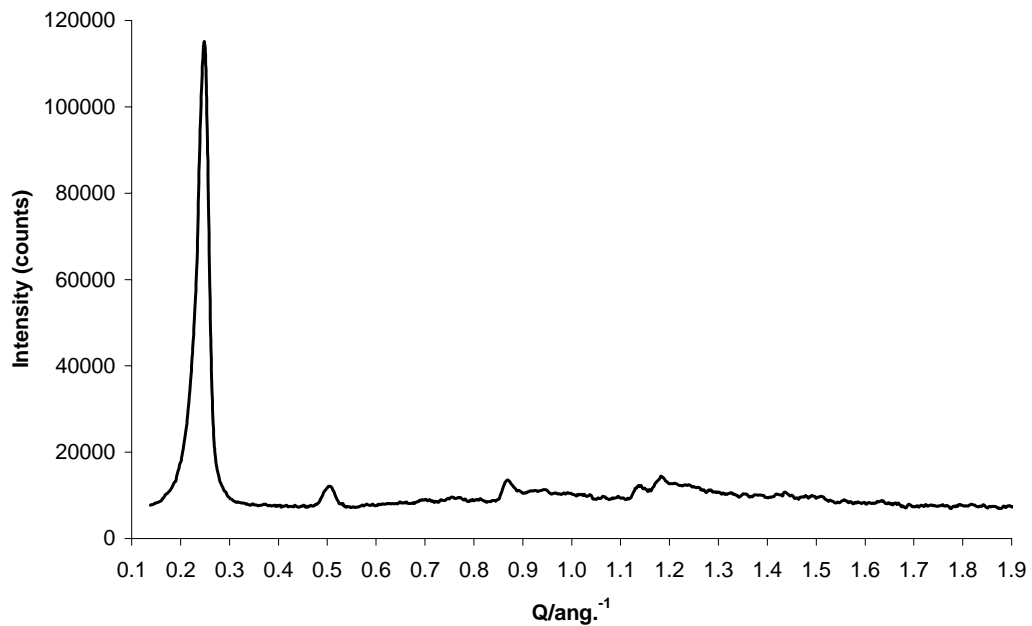
X-ray Diffraction Data for Various PtL^nCl_2 and PtL^nCl_4 Complexes

Experimental conditions and instrumentation are discussed in section 3.2.8 Variable Temperature Powder X-ray Diffraction.

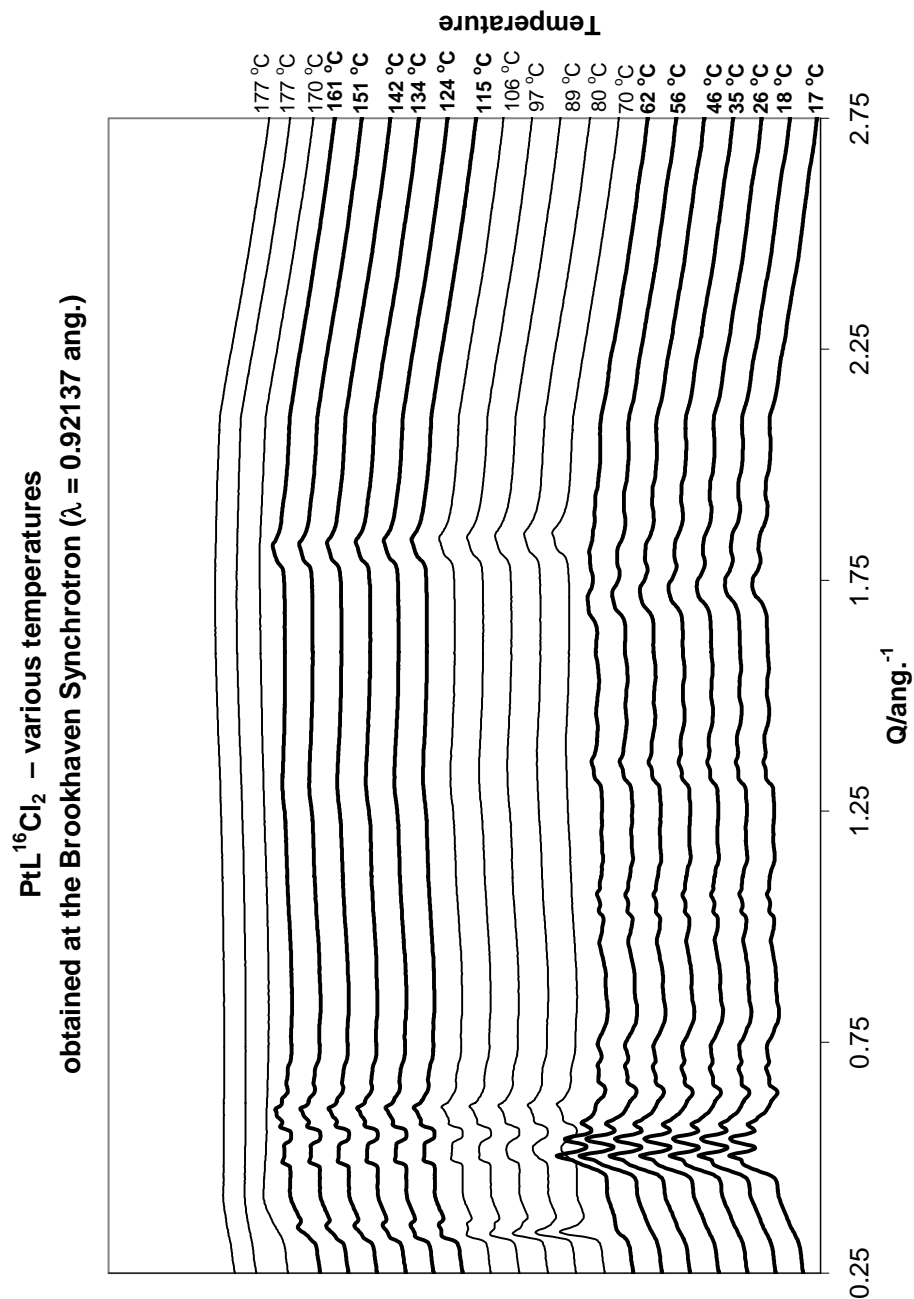
$\text{PtL}^{12}\text{Cl}_2$ - room temperature



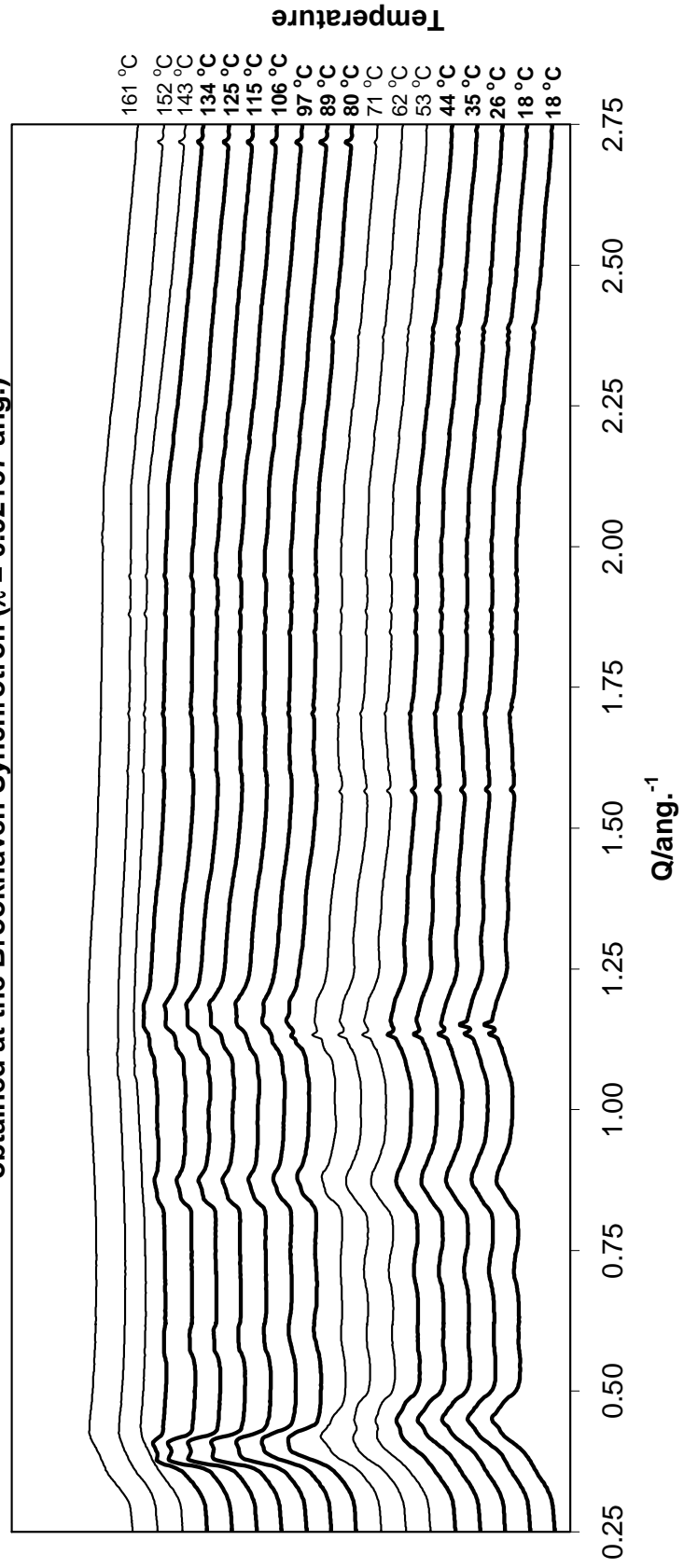
$\text{PtL}^{12}\text{Cl}_4$ - room temperature



Time-resolved variable-temperature XRD experiments were performed at the X7B beamline of the National Synchrotron Light source at Brookhaven National Laboratory. Instrumentation and the heating apparatus have been discussed previously.¹⁶⁹ Samples were placed in sealed glass capillaries for analysis. Temperatures were calibrated using the known transition temperatures of an external silicon standard.



**PtL¹⁶Cl₄ – various temperatures
obtained at the Brookhaven Synchrotron ($\lambda = 0.92137$ ang.)**



REFERENCES

- (1)Vogtle, F., *Supramolecular Chemistry*. J. Wiley: Chichester, 1991.
- (2)Lehn, J. M., *Supramolecular Chemistry, Concepts and Properties*. VCH: Weinheim, 1995.
- (3)*Comprehensive Supramolecular Chemistry*. Pergamon: Oxford, 1996.
- (4)Schneider, H.-J.; Yatsimirski, A. K., *Principles and Methods in Supramolecular Chemistry*. John Wiley and Sons: New York, 2000.
- (5)Steed, J. W.; Atwood, J. L., *Supramolecular Chemistry*. John Wiley and Sons: New York, 2000.
- (6)Constable, E. C. *Chem. Ind.* **1994**, (2), 56.
- (7)Barberá, J.; Rakitin, O.; Ros, M.; Torroba, T. *Angew. Chem. Int. Ed., Engl.* **1998**, 37(3), 296.
- (8)Giroud-Godquin, A.-M.; Maitlis, P. M. *Angew. Chem. Int. Ed. Engl.* **1991**, 30, 375.
- (9)Espinete, P.; Esteruelas, M.; Oro, L. A.; Serrano, J. L.; Sola, E. *Coord. Chem. Rev.* **1992**, 117, 215.
- (10)Hudson, S. A.; Maitlis, P. M. *Chem. Rev.* **1992**, 93, 861.
- (11)Keller, H. J., Linear Chain Platinum Haloamines. In *Extended Linear Chain Compounds*, Miller, J. S. Ed. Plenum Press: New York, 1982; Vol. 1, pp 357.
- (12)Kawamori, A.; Aoki, R.; Yamashita, A. *J. Phys. C.* **1985**, 18, 5487.
- (13)Martin, D. S. J., Optical Properties of Linear Chain Haloamine Platinum Complexes. In *Extended Linear Chain Compounds*, Miller, J. S. Ed. Plenum Press: New York, 1982; Vol. 1, pp 409.
- (14)Werner, A. *Z. anorg. Chem.* **1896**, 12, 46.
- (15)Wolffram, H. Ueber Athlaminhaltige Platinbasen. Albertus-Universitaet Zu Koenigsberg, Koenigsberg, Prussia, 1900.
- (16)Jensen, K. A. *Z. anorg. Allgem. Chem* **1936**, 229, 252.
- (17)Clark, R. *Chem. Soc. Rev.* **1984**, 13(3), 219.
- (18)Clark, R. *Chem. Soc. Rev.* **1990**, 19(2), 107.

- (19) Miller, J.; Epstein, A. *Prog. Inorg. Chem.* **1976**, *20*, 43.
- (20) Robin, M.; Day, P., In *Advances in Inorganic and Radiochemistry*, Emeleus, H. Ed. Academic Press: New York, 1967; Vol. 10, pp 247.
- (21) Hush, N., In *Progress in Inorganic Chemistry*, Cotton, F. Ed. Wiley: New York, 1967; Vol. 8, pp 357, 91.
- (22) Clark, R., Raman and resonance raman spectroscopy of linear chain complexes. In *Advances in Infrared and Raman Spectroscopy*, Clark, R.; Hester, R. Eds. Wiley-Heyden: Chichester, 1984; Vol. 11, pp 95, and citations therein.
- (23) Clark, R.; Croud, V.; Wills, R. *Acta Cryst.* **1989**, *B45*, 147.
- (24) Weber-Milbrodt, S. *Phys. Rev. B* **1992**, *45*, 6435.
- (25) Kawashima, T. *Inorg. Chem.* **2001**, *40*, 6651.
- (26) Kamoto, H.; Yamashita, A. *Bull. Chem. Soc., Jpn.* **1998**, *71*, 2023.
- (27) Interrante, L.; Browall, K. *Inorg. Chem.* **1974**, *13(5)*, 1162.
- (28) Interrante, L.; Browall, K.; Bundy, F. *Inorg. Chem.* **1974**, *13(5)*, 1158.
- (29) Yung, C. *Inorg. Chem.* **2001**, *40*, 5934.
- (30) Kawashima, T. *Synth. Met.* **1999**, *103*, 2648.
- (31) Saalfeld, F. E.; DeCorpo, J. J.; Wyatt, J. R., Mass Spectroscopy of Low-Dimensional Materials. In *Extended Linear Chain Compounds*, Miller, J. S. Ed. Plenum Press: New York, 1982; Vol. 1.
- (32) Clark, R. *Chem. Soc. Rev.* **1984**, *13(3)*, 219, and citations therein.
- (33) Summa, G. M.; Scott, B. A. *Inorg. Chem.* **1980**, *19*, 1079.
- (34) Wallen, J.; Brosset, C.; Vannerberg, N. B. *Arkiv Kemi* **1961**, *A18*, 541.
- (35) Browall, K. N.; Kasper, J. S.; Interrante, L. V. *Acta Cryst.* **1974**, *B30*, 1649.
- (36) Ryan, T. D.; Rundle, R. E. *J. Am. Chem. Soc.* **1961**, *83*, 2814.
- (37) Clark, R.; Croud, V. B. *J. Chem. Soc., Dalton Trans.* **1988**, 73.
- (38) Clark, R.; Croud, V. B.; Khokhar, A. R. *Inorg. Chem.* **1987**, *26*, 3284.

- (39)Clark, R.; Kurmoo, M.; Buse, K. D.; Keller, H. J. *Z. Naturforsch Teil B* **1980**, *35*, 1272.
- (40)Tschierske, C. *J. Mater. Chem.* **2001**, *11*, 2647.
- (41)Mery, S.; Haristoy, D.; Nicoud, J.-F.; Guillon, D.; Diele, S.; Monobe, H.; Shimizu, Y. *J. Mater. Chem.* **2002**, *12*, 37.
- (42)Mori, A.; Yokoo, M.; Hashimoto, M.; Ujiie, S.; Diele, S.; Baumeister, U.; Tschierske, C. *J. Am. Chem. Soc.* **2003**, *125*, 6620.
- (43)El-ghayoury, A.; Douce, L.; Skoulios, A.; Ziessel, R. *Angew. Chem. Int. Ed. Eng.* **1998**, *37*(9), 1255.
- (44)Thompson, N. J.; Iglesias, R.; Serrano, J. L.; Baena, M. J.; Espinet, P. *J. Mater. Chem.* **1996**, *6*(11), 1741.
- (45)Bruce, D. W.; Lalinde, E.; Styring, P.; Dunmur, D. A.; Maitlis, P. M. *J. Chem. Soc., Chem. Commun.* **1986**, 581.
- (46)Kaharu, T.; Matsubara, H.; Takahashi, S. *J. Mater. Chem.* **1991**, *1*(1), 145.
- (47)Pucci, D.; Barberio, G.; Crispini, A.; Francescangeli, O.; Ghedini, M.; La Deda, M. *Eur. J. Inorg. Chem.* **2003**, (19), 3649.
- (48)Zheng, H.; Lai, C. K.; Swagger, T. *Chem. Mater.* **1994**, *6*(2), 101.
- (49)Seddon, J. M., Structural Studies of Liquid Crystals by X-ray Diffraction. In *Handbook of Liquid Crystals*, Demus, D.; Goodby, J.; Gray, G. W.; Spiess, H. W.; Vill, V. Eds. Wiley-VCH: New York, 1998; Vol. 1, pp 635.
- (50)Clark, R. *Chem. Soc. Rev.* **1990**, *19*(2), 107, and citations therein.
- (51)Dahm, C. E.; Peters, D. G. *Anal. Chem.* **1994**, *66*, 3117.
- (52)Choi, Y. K.; Park, J. K.; Jeon, S. *Electroanal.* **1999**, *11*, 134.
- (53)Losada, J.; del Peso, I.; Beyer, L.; Hartung, J.; Fernandez, V.; Mobius, M. *J. Electroanal. Chem.* **1995**, *398*, 89.
- (54)Losada, J.; del Peso, I.; Beyer, L. *J. Electroanal. Chem.* **1998**, *447*, 147.
- (55)Costamagna, J.; Vargas, J.; Latorre, R.; Alvarado, A.; Mena, G. *Coord. Chem. Rev.* **1992**, *119*, 67, and references therein.

- (56)Vilas-Boas, M.; Freire, C.; de Castro, B.; Christensen, P.; Hillman, A. R. *Inorg. Chem.* **1997**, *36*, 4919, and references therein.
- (57)Lanza, J. Synthesis and Investigation of the Properties of Transition-Metal-Linked Homopolymers and Block Copolymers of Styrene and Dimethylsiloxane. University of North Carolina at Chapel Hill, Chapel Hill, 1999.
- (58)Reiffer, U. *Trans. Met. Chem.* **1980**, *5*, 272.
- (59)Uchiyama, T.; Toshiyasu, Y.; Nakamura, Y.; Miwa, T.; Kawaguchi, S. *Bull. Chem. Soc. Jpn.* **1981**, *54*, 181.
- (60)Yamada, S.; Nishikawa, K.; Yamasaki, K. *Bull. Chem. Soc., Jpn.* **1963**, *36*, 483.
- (61)Syamal, A.; Gupta, B. K. *Indian J. Chem. A* **1984**, *23A*, 260.
- (62)Holm, R.; Swaminathan, K. *Inorg. Chem.* **1962**, *1(3)*, 599.
- (63)Frisch, M. J.; Trucks, G. W.; Schlegel, H. B.; Scuseria, G. E.; Robb, M. A.; Cheeseman, J. R.; Montgomery, J., J. A.; Vreven, T.; Kudin, K. N.; Burant, J. C.; Millam, J. M.; Iyengar, S. S.; Tomasi, J.; Barone, V.; Mennucci, B.; Cossi, M.; Scalmani, G.; Rega, N.; Petersson, G. A.; Nakatsuji, H.; Hada, M.; Ehara, M.; Toyota, K.; Fukuda, R.; Hasegawa, J.; Ishida, M.; Nakajima, T.; Honda, Y.; Kitao, O.; Nakai, H.; Klene, M.; Li, X.; Knox, J. E.; Hratchian, H. P.; Cross, J. B.; Bakken, V.; Adamo, C.; Jaramillo, J.; Gomperts, R.; Stratmann, R. E.; Yazyev, O.; Austin, A. J.; Cammi, R.; Pomelli, C.; Ochterski, J. W.; Ayala, P. Y.; Morokuma, K.; Voth, G. A.; Salvador, P.; Dannenberg, J. J.; Zakrzewski, V. G.; Dapprich, S.; Daniels, A. D.; Strain, M. C.; Farkas, O.; Malick, D. K.; Rabuck, A. D.; Raghavachari, K.; Foresman, J. B.; Ortiz, J. V.; Cui, Q.; Baboul, A. G.; Clifford, S.; Cioslowski, J.; Stefanov, B. B.; Liu, G.; Liashenko, A.; Piskorz, P.; Komaromi, I.; Martin, R. L.; Fox, D. J.; Keith, T.; Al-Laham, M. A.; Peng, C. Y.; Nanayakkara, A.; Challacombe, M.; Gill, P. M. W.; Johnson, B.; Chen, W.; Wong, M. W.; Gonzalez, C.; Pople, J. A. *Gaussian 03*, Revision C.02; Gaussian, Inc.: Wallingford CT, 2004.
- (64)Cui, Q.; Musaev, D. G.; Morokuma, K. *Organomet.* **1997**, *16*, 1355.
- (65)Dunning, T. H., Jr.; Hay, P. J., In *Modern Theoretical Chemistry*, Schaefer, H. F., III Ed. Plenum: New York, 1976; Vol. 3, pp 1.
- (66)Schlegel, H. B.; Frisch, M. J. *Int. J. Quant. Chem.* **1995**, *54*, 83.
- (67)Hay, P. J.; Wadt, W. R. *J. Chem. Phys.* **1985**, *87*, 270.
- (68)Wadt, W. R.; Hay, P. J. *J. Chem. Phys.* **1985**, *82*, 284.
- (69)Hay, P. J.; Wadt, W. R. *J. Chem. Phys.* **1985**, *82*, 299.

- (70)Dennington II, R.; Keith, T.; Millam, J.; Eppinnett, K.; Hovell, W. L.; Gilliland, R. *GaussView 3.09*, Semichem, Inc.: Shawnee Mission, KS, 2003.
- (71)Kaplan, S. F.; Kukushkin, V. Y.; Shova, S.; Sowinska, K.; Wagner, G.; Pombeiro, A. J. *J. Inorg. Chem.* **2001**, *4*, 1031.
- (72)Connelly, N. G.; Geiger, W. E. *Chem. Rev.* **1996**, *96*, 877.
- (73)Koten; Terheijden; Beek, V.; Wehman-Ooyevaar *Organomet.* **1990**, *9*, 903.
- (74)Kamenar, B.; Kaitner, B.; Ferguson, G.; Waters, T. N. *Acta. Cryst., C* **1990**, *46*, 1920.
- (75)Sacconi, L.; Ciampolini, M. *J. Am. Chem. Soc.* **1963**, *85*, 1750.
- (76)Fox, M. R.; Orioli, P. L.; Lingafelter, E. C.; Sacconi, L. S. *Acta. Cryst.* **1969**, *17*, 1159.
- (77)Interrante, L. V.; Browall, K. W. *Inorg. Chem.* **1974**, *13*(5), 1162.
- (78)Whangbo, M.-H.; Foshee, M. J. *Inorg. Chem.* **1981**, *20*, 113.
- (79)Ohmori, H.; Matsumoto, A.; Masui, M. *J. Electrochem. Soc.* **1977**, 1849.
- (80)Goldsby, K.; Blaho, J.; Hoferkamp, L. *Polyhedron* **1989**, *8*(1), 113.
- (81)Audebert, P.; Capdevielle, P.; Maumy, M. *New J. Chem.* **1991**, *15*, 235.
- (82)Losada, J.; del Peso, I.; Beyer, L. *Inorg. Chim. Acta* **2001**, *321*, 107.
- (83)Gili, P.; Martin Reyes, M. G.; Martin Zarza, P.; Guedes, D. A.; Silva, M. F. C.; Tong, Y.-Y.; Pombeiro, A. J. L. *Inorg. Chim. Acta.* **1997**, *255*, 279.
- (84)Costamagna, J.; Lillo, L. E.; Matsuhira, B.; Nosedá, M. D.; Villagran, M. *Carbohydrate Res.* **2003**, *338*(15), 1535.
- (85)Losada, J.; del Peso, I.; Beyer, L.; Hartung, J.; Fernandez, V.; Mobius, M. *J. Electroanal. Chem.* **1995**, *398*, 89.
- (86)Patel, R. S.; Bailer, J. C., Jr. *J. Inorg. Nucl. Chem.* **1971**, *33*, 1339.
- (87)Lever, A. B. P.; Wilshire, J. P. *Can. J. Chem.* **1976**, *56*, 2514.
- (88)Bergman, R. D.; Dorfman, J. R.; Bordner, J.; Rillema, D. P.; McCarthy, P.; Shields, G. D. *J. Inorg. Biochem.* **1982**, *16*, 47.
- (89)Goldsby, K. *J. Coord. Chem.* **1988**, *19*, 83.

- (90)Vilas-Boas, M.; Freire, C.; de Castro, B.; Christensen, P.; Hillman, A. R. *Inorg. Chem.* **1997**, *36*, 4919.
- (91)Audebert, P.; Capdevielle, P.; Maumy, M. *New J. Chem.* **1992**, *16*(6), 697.
- (92)Audebert, P.; Capdevielle, P.; Maumy, M. *Synth. Met.* **1991**, *41*, 3049.
- (93)Goldsby, K. A.; Hoferkamp, L. A. *Chem. Mater.* **1989**, *1*, 348.
- (94)Vilas-Boas, M.; de Castro, B.; Hillman, A. *J. Phys. Chem. B* **1998**, *102*, 8533.
- (95)Dahm, C. E.; Peters, D. G. *J. Electroanal. Chem.* **1996**, *406*(1-2), 119.
- (96)Ozalp-Yaman, S.; Kasumov, V. T.; Onal, A. M. *Polyhderon* **2005**, *24*, 1821, and references therein.
- (97)Vilas-Boas, M.; Freire, C.; de Castro, B.; Hillman, A. R. *J. Phys. Chem., B* **1998**, *102*, 8533.
- (98)Kotocova, A.; Sima, J. *Chem. Papers* **1994**, *48*(3), 176.
- (99)Chjo, K. H.; Jeong, B. G.; Kim, J. H.; Jeon, S.; Rim, C. P.; Choi, Y. K. *Bull. Korean Chem. Soc.* **1997**, *18*(8), 850.
- (100)Kimizuka, N. *Adv. Mater.* **2000**, *12*(19), 1461.
- (101)Kimizuka, N.; Oda, N.; Kunitake, T. *Inorg. Chem.* **2000**, *39*, 2684.
- (102)Yamashita, M.; Manabe, T.; Inoue, K.; Kawashima, T.; Okamoto, H.; Kitagawa, H.; Mitani, T.; Toriumi, K.; Miyamae, H.; Ikeda, R. *Inorg. Chem.* **1999**, *38*, 1894.
- (103)Pucci, D.; Barberio, G.; Crisipini, A.; Ghedini, M.; Francescangeli, O. *Mol. Cryst. Liq. Cryst* **2003**, *395*, 325.
- (104)Schierske, C. T. *J. Mater. Chem.* **1998**, *8*(7), 1485.
- (105)Hegmann, T.; Kain, J.; Diele, S.; Pelzl, G.; Tschierske, C. *Angew. Chem. Int. Ed.* **2001**, *40*(5), 887, and citations therein.
- (106)Pratibha, R.; Madhusudana, N. V.; Sadashiva, B. K. *Science* **2000**, *288*, 2184.
- (107)Percec, V.; Johansson, G.; Heck, J.; Ungar, G.; Batty, S. V. *J. Chem. Soc. Perkin Trans.* **1993**, 1411.
- (108)Tomazos, D.; Out, G.; Heck, J. A.; Johansson, G.; Percec, V. *Liq. Cryst.* **1994**, *16*(3), 509.

- (109)Lai, C. K.; Serrette, A. G.; Swager, T. M. *J. Am. Chem. Soc.* **1992**, *114*, 7948.
- (110)Serrette, A. G.; Swager, T. M. *J. Am. Chem. Soc.* **1993**, *115*, 8879.
- (111)Serrette, A. G.; Lai, C. K.; Swager, T. M. *Chem. Mater.* **1994**, *6*, 2252.
- (112)Donnio, B.; Guillon, D.; Deschenaux, R.; Bruce, D. W., Metallomesogens. In *Comprehensive Coordination Chemistry II*, Fujita, M.; Powell, A.; Creutz, C. A. Eds. Elsevier Pergamon: Boston, 2004; Vol. 7.
- (113)Cocker, T. M.; Bachman, R. E. *Mol. Cryst. Liq. Cryst.* **2003**, *408*, 1.
- (114)Pratibha, R.; Madhusudana, N. V.; Sadashiva, B. K. *Science* **2000**, *288*, 2184-7.
- (115)Webb, D. L.; Rossiello, L. A. *Inorg. Chem.* **1971**, *10(10)*, 1.
- (116)Houlding, V. H.; Miskowski, V. M. *Coord. Chem. Rev.* **1991**, *111*, 145.
- (117)Hoggard, P. E.; Albin, M. *Inorg. Chem.* **1981**, *20(12)*, 4413.
- (118)Tschiersle, C. *Annu. Rep. Prog. Chem. Sect. C* **2001**, *97*, 191.
- (119)Swager, T. M.; Zheng, H. *Mol. Cryst. Liq. Cryst.* **1995**, *260*, 301.
- (120)Gimenez, R.; Manrique, A.; Uriel, S.; Barbera, J.; Serrano, J. L. *Chem. Commun.* **2004**, *18*, 2064.
- (121)Ghedini, M.; Pucci, D.; Crispini, A.; Barbaerio, G. *Organometallics* **1999**, *18*, 2116.
- (122)Ghedini, M.; Pucci, D.; Barberio, G. *Liq. Cryst.* **2000**, *27(10)*, 1277.
- (123)Beagley, P.; Starr, E. J.; Bacsá, J.; Moss, J. R.; Hutton, A. T. *J. Organomet. Chem.* **2002**, *645*, 206.
- (124)Zhou, Y.-F.; Xu, Y.; Yaun, D.-Q.; Hong, M.-C. *Acta. Crystallogr., E. Struct. Rep. Online* **2003**, *59*, m821.
- (125)Kocian, O.; Mortimer, R. J.; Beer, P. D. *Tetrahedron Lett.* **1990**, *31*, 5069.
- (126)Gillaizeau-Gauthier, I.; Odobel, F.; Alebbi, M.; Argazzi, R.; Costa, E.; Bignozzi, C.; Qu, P.; Meyer, G. *Inorg. Chem.* **2001**, *40*, 6073.
- (127)Sprintschnik, G.; Sprintschnik, H.; Kirsch, P.; Whitten, G. *J. Am. Chem. Soc.* **1977**, *99(15)*, 4947.

- (128)Taniguchi, M.; Ueno, N.; Okamoto, K.; Karthaus, O.; Shimomura, M.; Yamagishi, A. *Langmuir* **1999**, *15*(22), 7700.
- (129)Kelly, L. A.; Rodgers, M. A. *J. Phys. Chem.* **1994**, *98*, 6377.
- (130)Tzeng, B.-C.; Chan, S.-C.; Chan, M.; Che, C.-M.; Cheung, K.-K.; Peng, S.-M. *Inorg. Chem.* **2001**, *40*, 6699.
- (131)McGarrah, J.; Eisenberg, R. *Inorg. Chem.* **2003**, *42*, 4355.
- (132)Garelli, N.; Vierling, P.; Fischel, J. L.; Milano, G. *Eur. J. Med. Chem.* **1993**, *28*(3), 235.
- (133)Wrighton, M.; Morse, D. L. *J. Am. Chem. Soc.* **1974**, *96*(4), 998.
- (134)Gaballa, A.; Wagner, C.; Schmidt, H.; Steinborn, D. *Z. Anorg. Allg. Chem.* **2003**, 629, 703.
- (135)Huang, X.-C.; Zhang, L.-Y.; Ng, S. W. *Acta. Cryst., Sect. E, Struct. Rep. Online* **2004**, *60*, m332.
- (136)Uppadine, L.; Keene, F.; Beer, P. *J. Chem. Soc., Dalton Trans.* **2001**, *14*, 2188, and citations therein.
- (137)Osborn, R. S.; Rodgers, D. *J. Chem. Soc., Dalton Trans.* **1974**, 1002.
- (138)Canty, A. J.; Skelton, B. W.; Traill, P. R.; White, A. H. *Aust. J. Chem.* **1992**, *35*, 417.
- (139)Barbera, J., X-ray studies of metallomesogens. In *Metallomesogens Synthesis, Properties and Applications*, Serrano, J. L. Ed. Wiley-VCH: New York, 1996; pp 323.
- (140)Stout, G. H.; Jenson, L. H., *X-ray Structure Determination A Practical Guide*. 2 ed.; Wiley & Sons: New York, 1989.
- (141)Dierking, I., Polarizing Microscopy. In *Textures of Liquid Crystals*, Wiley - VCH: 2003; pp 33-41, 163-212.
- (142)Sleven, J.; Cardinaels, T.; Binnemans, K. *Liq. Cryst.* **2002**, *29*(11), 1425.
- (143)Kilian, D.; Knawby, D.; Athanssopoulou, M. A.; Trzaska, S. T.; Swager, T. M.; Wrobel, S.; Haase, W. *Liq. Cryst.* **2000**, *27*(4), 509.
- (144)Hambley, T. W. *Acta. Cryst. Sect. C, Cryst. Struct. Commun.* **1986**, *42*, 49.
- (145)Almond, M. J.; Beer, M. P.; Drew, M. G. B.; Rice, D. A. *Organomet.* **1991**, *10*, 2072.
- (146)Bushnell, G. W.; Stobart, S. R. *Can. J. Chem.* **1980**, *58*, 574.

- (147)Ivan Chenko, A. V.; Oromilov, S. A.; Zemskova, S. M.; Baidina, I. A. *Zh. Strukt. Khim.* **2000**, *41*, 106.
- (148)Santos, R. A.; Gruff, E. S.; Harbison, G. S. *J. Am. Chem. Soc.* **1990**, *112*, 9257.
- (149)Rowe, K. E.; Bruce, D. W. *J. Chem. Soc., Dalton Trans.* **1996**, 3913.
- (150)Rowe, K. E.; Bruce, D. W. *Mol. Cryst. Liq. Cryst.* **2003**, *2003(396)*, 141.
- (151)Cheda, J. A. R.; Ortega, F.; Sanchez Arenas, A.; Cosio, A.; Fernandez-Garcia, M.; Fernandez-Martin, F.; Roux, M. V.; Turrion, C. *Pure Appl. Chem.* **1992**, *64(1)*, 65.
- (152)Seghrouchni, R.; Skoulios, A. *J. Phys. II France* **1995**, *5*, 1385.
- (153)Baxter, D. V.; Chisholm, M. H.; Lynn, M. A.; Putilina, E. F. *Chem. Mater.* **1998**, *10*, 1758.
- (154)Styring, P. Neutral and ionic metal-containing liquid crystals. Ph.D., University of Sheffield, Sheffield, 1988.
- (155)Rourke, J. P.; Fanizzi, F. P.; Salt, N. J. S.; Bruce, D. W.; Dunmur, D. A.; Maitlis, P. M. *J. Chem. Soc. Chem. Commun.* **1990**, 229.
- (156)Ballesteros, B.; Coco, S.; Espinet, P. *Chem. Mater.* **2004**, *16*, 2062.
- (157)Binnemans, K.; Lodewyckx, K.; Donnio, B.; Guillion, D. *Chem. Eur. J.* **2002**, *8*, 1101.
- (158)Jongen, L.; Hinz, D.; Meyer, G.; Binnemans, K. *Chem. Mater.* **2001**, *13*, 2243.
- (159)Mirnaya, T. A.; Prisyazhnyi, V. D.; Shcherbakov, V. A. *Russ. Chem. Rev.* **1989**, *58(9)*, 821, and citations therein.
- (160)Ibn-Elhaj, M.; Guillon, D.; Skoulios, A.; Maldivi, P.; Giroud-Godquin, A.-M.; Marchon, J.-C. *J. Phys. II France* **1992**, *2*, 2237.
- (161)Noyes, J. G.; Asher, J.; Jones, O. C.; Phillips, G. F. Eds. *UV-visible spectroscopy in Kaye and Laby Tables of Physical and Chemical Constants*, 1995, Web Edition; National Physical Laboratory, http://www.kayelaby.npl.co.uk/chemistry/3_8/3_8_7.html (06 April 2006).
- (162)Miskowski, V. M.; Houlding, V. H.; Che, C.-M.; Wang, Y. *Inorg. Chem.* **1993**, *32*, 2518.
- (163)Connick, W. B.; Miskowski, V. M.; Houlding, V. H.; Gray, H. B. *Inorg. Chem.* **2000**, *39*, 2585.

(164)Delahayes, S.; Loosli, C.; Liu, S.-X.; Decurtins, S.; Lebat, G.; Neels, A.; Loosli, A.; Ward, T. R.; Hauser, A. *Adv. Funct. Mater.* **2006**, *16*, 286, and citations therein.

(165)Bailey, J. A.; Hill, M. G.; Marsh, R. E.; Miskowski, V. M.; Schaefer, W. P.; Gray, H. B. *Inorg. Chem.* **1995**, *34*, 4591.

(166)Miskowski, V. M.; Houlding, V. H. *Inorg. Chem.* **1989**, *1989*(28), 1529.

(167)Balashev, K. P.; Simon, J.; Ford, P. C. *Inorg. Chem.* **1991**, *30*, 859.

(168)Moore, J. J.; Nash, J. J.; Fanwick, P. E.; McMillin, D. R. *Inorg. Chem.* **2002**, *41*(6), 6387.

(169)Liu, H.; Sullivan, R. M.; Hanson, J. C.; Grey, C. P.; Martin, J. D. *J. Am. Chem. Soc.* **2001**, *123*, 7564.